

SATELLITE SCATTEROMETERS: CALIBRATION USING A  
GROUND STATION AND STATISTICAL MEASUREMENT  
THEORY

by

Peter K. Yoho

A dissertation submitted to the faculty of

Brigham Young University

in partial fulfillment of the requirements for the degree of

Doctor of Philosophy

Department of Electrical and Computer Engineering

Brigham Young University

December 2003

Copyright © 2003 Peter K. Yoho

All Rights Reserved

BRIGHAM YOUNG UNIVERSITY

GRADUATE COMMITTEE APPROVAL

of a dissertation submitted by

Peter K. Yoho

This dissertation has been read by each member of the following graduate committee and by majority vote has been found to be satisfactory.

\_\_\_\_\_  
Date

\_\_\_\_\_  
David G. Long, Chair

\_\_\_\_\_  
Date

\_\_\_\_\_  
Randall W. Beard

\_\_\_\_\_  
Date

\_\_\_\_\_  
Michael A. Jensen

\_\_\_\_\_  
Date

\_\_\_\_\_  
Travis E. Oliphant

\_\_\_\_\_  
Date

\_\_\_\_\_  
Karl F. Warnick

BRIGHAM YOUNG UNIVERSITY

As chair of the candidate's graduate committee, I have read the dissertation of Peter K. Yoho in its final form and have found that (1) its format, citations, and bibliographical style are consistent and acceptable and fulfill university and department style requirements; (2) its illustrative materials including figures, tables, and charts are in place; and (3) the final manuscript is satisfactory to the graduate committee and is ready for submission to the university library.

---

Date

---

David G. Long  
Chair, Graduate Committee

Accepted for the Department

---

Michael A. Jensen  
Graduate Coordinator

Accepted for the College

---

Douglas M. Chabries  
Dean, College of Engineering and Technology

## ABSTRACT

# SATELLITE SCATTEROMETERS: CALIBRATION USING A GROUND STATION AND STATISTICAL MEASUREMENT THEORY

Peter K. Yoho

Electrical and Computer Engineering

Doctor of Philosophy

Satellite scatterometers have recently gained popularity due to their unique ability to measure global geophysical data on a daily basis. Increased interest in scatterometry mandates improved design and calibration of these instruments. This dissertation presents new techniques for scatterometer calibration and addresses issues related to the design of future instruments and applications. First, the use of a calibration ground station is considered. A new methodology is established for calibration of SeaWinds, NASA's current scatterometer, using a receive-only ground station. Principles of the methodology are implemented, new analysis techniques developed, and important results obtained for instrument timing, frequency, power, position, and pointing. Second, an investigation into methods for calibration of measurement surface location is conducted. Two new approaches are proposed and results of both approaches using SeaWinds data are provided. Third, measurement correlation, a critical issue related to new scatterometer designs, particularly those which significantly oversample the surface is considered. General statistical expressions for

measurement correlation are derived and analysis of the effects on data variance is presented. Finally, a new data simulation model is developed to support instrument and application development. New applications require sophisticated models which are general, yet accurate, enabling them to rapidly and easily simulate data from multiple instruments. The model generates data which is statistically equivalent (in a mean and variance sense) to actual scatterometer measurements by separately accounting for the two main forms of variation present in scatterometer data, multiplicative fading and additive noise, and also accounting for correlation between measurements. The model is valuable for a variety of data applications including image generation and high resolution wind retrieval.

## ACKNOWLEDGMENTS

This work is dedicated to my wife, Polly, who recognized before I did that a doctorate was what I should do. She provided much patience and support, even when she needed me most.

I would also like to acknowledge my advisor, Dr. David G. Long, who has been a very patient and concerned mentor. Thank you.





# Contents

|   |              |
|---|--------------|
| <b>Acknowledgments</b>                      | <b>vii</b>   |
| <b>List of Tables</b>                       | <b>xiii</b>  |
| <b>List of Figures</b>                      | <b>xviii</b> |
| <b>1 Introduction</b>                       | <b>1</b>     |
| 1.1 Definition of the Problem . . . . .     | 2            |
| 1.2 Research Contributions . . . . .        | 5            |
| 1.3 Dissertation Outline . . . . .          | 8            |
| <b>2 Background</b>                         | <b>9</b>     |
| 2.1 Scatterometer Operation . . . . .       | 10           |
| 2.1.1 Fan-Beam Designs . . . . .            | 11           |
| 2.1.2 SeaWinds Pencil-Beam Design . . . . . | 14           |
| 2.2 Calibration Ground Stations . . . . .   | 15           |
| 2.2.1 CGS History . . . . .                 | 15           |
| 2.2.2 The SeaWinds CGS . . . . .            | 16           |
| 2.3 Summary . . . . .                       | 18           |
| <b>3 Calibration Methodology</b>            | <b>21</b>    |
| 3.1 Data Capture . . . . .                  | 22           |
| 3.2 Data Processing . . . . .               | 26           |
| 3.3 Data Analysis . . . . .                 | 27           |
| 3.4 Calibration Reporting . . . . .         | 30           |
| 3.5 Summary . . . . .                       | 30           |

|          |  |            |
|----------|--|------------|
| <b>4</b> | <b>Calibration Methodology - Approach and Implementation</b>         | <b>33</b>  |
| 4.1      | Parameter Identification . . . . .                                   | 33         |
| 4.1.1    | Foundation . . . . .   | 33         |
| 4.1.2    | Calibration Elements . . . . .                                       | 36         |
| 4.2      | Implementation Overview . . . . .                                    | 41         |
| 4.3      | Observation and Identification . . . . .                             | 44         |
| 4.4      | Summary . . . . .  | 49         |
| <b>5</b> | <b>Results from the SeaWinds Calibration Ground Station</b>          | <b>51</b>  |
| 5.1      | Model Development . . . . .  | 52         |
| 5.2      | Telemetry Analysis . . . . .   | 53         |
| 5.3      | Blind Calibration . . . . .  | 59         |
| 5.4      | Comprehensive Estimation . . . . .                                   | 71         |
| 5.5      | Summary . . . . .  | 97         |
| <b>6</b> | <b>Measurement Location Calibration</b>                              | <b>101</b> |
| 6.1      | Coastal Validation . . . . .   | 101        |
| 6.2      | Antenna Pattern Reconstruction . . . . .                             | 112        |
| 6.3      | Summary . . . . .  | 119        |
| <b>7</b> | <b>Correlation of Scatterometer Measurements</b>                     | <b>121</b> |
| 7.1      | Interaction and Statistics of Multiple Measurements . . . . .        | 122        |
| 7.1.1    | Surface Scattering for Distributed Targets . . . . .                 | 122        |
| 7.1.2    | Scatterometer Signals . . . . .                                      | 123        |
| 7.1.3    | Instrument Measurement . . . . .                                     | 124        |
| 7.1.4    | Measurement Statistics . . . . .                                     | 127        |
| 7.2      | Noisy Signal Measurements . . . . .                                  | 130        |
| 7.3      | Analysis of the Signal Covariance Expression . . . . .               | 133        |
| 7.3.1    | Footprint Resolution ( $\bar{V}^a$ ) . . . . .                       | 134        |
| 7.3.2    | Range Resolution ( $\bar{V}^f$ ) . . . . .                           | 136        |
| 7.4      | Multiple Pulse Measurements and the Effects of Correlation . . . . . | 138        |

|          |  |            |
|----------|--|------------|
| 7.4.1    | Incoherent Measurements . . . . .                                    | 139        |
| 7.4.2    | Coherent Measurements . . . . .                                      | 142        |
| 7.5      | Summary . . . . .  | 142        |
| <b>8</b> | <b>Simulating Measurement Variations</b>                             | <b>145</b> |
| 8.1      | Data Collection . . . . .  | 146        |
| 8.2      | Modeling Scatterometer Measurement Variation . . . . .               | 148        |
| 8.3      | Summary and Application . . . . .                                    | 152        |
| <b>9</b> | <b>Summary and Conclusion</b>  | <b>153</b> |
| 9.1      | Contributions . . . . .  | 154        |
| 9.1.1    | Ground Station Calibration . . . . .                                 | 154        |
| 9.1.2    | Measurement Location Calibration . . . . .                           | 156        |
| 9.1.3    | Multiple Measurement Statistics . . . . .                            | 156        |
| 9.1.4    | Noise Modeling . . . . .   | 157        |
| 9.2      | Future Work . . . . .  | 157        |
| 9.2.1    | Future Calibration Ground Stations . . . . .                         | 157        |
| 9.2.2    | Measurement Location Tools . . . . .                                 | 158        |
| 9.2.3    | Noise Model Application . . . . .                                    | 159        |
| <b>A</b> | <b>Issues Related to SeaWinds CGS Calibration</b>                    | <b>163</b> |
| A.1      | Ground Station Self-Calibration . . . . .                            | 163        |
| A.2      | Blind Calibration Results . . . . .                                  | 167        |
| A.2.1    | Timing Calibration . . . . .   | 167        |
| A.2.2    | Frequency Calibration . . . . .                                      | 173        |
| A.2.3    | Power Calibration . . . . .  | 177        |
| <b>B</b> | <b>Derivation of Multiple Measurement Statistics</b>                 | <b>181</b> |
| B.1      | Expectation of Surface Backscattered Voltage . . . . .               | 181        |
| B.1.1    | Second-Order Expectation . . . . .                                   | 181        |
| B.1.2    | Fourth-Order expectation . . . . .                                   | 181        |
| B.2      | Single Pulse, Antenna Resolution, Signal-only Measurements . . . . . | 183        |

|       |  |     |
|-------|--|-----|
| B.2.1 | Expected Value . . . . .   | 183 |
| B.2.2 | Correlation . . . . .  | 183 |
| B.2.3 | Covariance . . . . .   | 185 |
| B.3   | Single Pulse, Range Resolution, Signal-only Measurements . . . . .       | 186 |
| B.3.1 | Expected Value . . . . .   | 186 |
| B.3.2 | Correlation . . . . .  | 186 |
| B.3.3 | Covariance . . . . .   | 187 |
| B.4   | Single Pulse, Range Resolution, Signal Plus Noise Measurements . . . . . | 187 |
| B.4.1 | Expected Value . . . . .   | 187 |
| B.4.2 | Correlation . . . . .  | 188 |
| B.4.3 | Covariance . . . . .   | 191 |
| B.5   | Single Pulse, Range Resolution, Unbiased Measurements . . . . .          | 191 |
| B.5.1 | Correlation Between Noise and Noisy Measurement . . . . .                | 191 |
| B.5.2 | Correlation of Measured Noise . . . . .                                  | 191 |
| B.5.3 | Correlation . . . . .  | 192 |
| B.5.4 | Covariance . . . . .   | 192 |
| B.6   | Analysis of Signal Covariance Expressions . . . . .                      | 193 |
| B.6.1 | Footprint Resolution $\bar{V}^a$ . . . . .                               | 193 |
| B.7   | Derivation of Multiple Measurement Statistics . . . . .                  | 194 |
| B.7.1 | Incoherent Variance . . . . .  | 194 |
| B.7.2 | Incoherent Correlation . . . . .   | 195 |
| B.7.3 | Incoherent Covariance . . . . .  | 195 |
| B.8   | Double Integral Simplification . . . . .                                 | 196 |

**Bibliography** **206**

## List of Tables

|     |  |    |
|-----|--|----|
| 4.1 | Selected SeaWinds technical mission requirements . . . . .                       | 34 |
| 4.2 | Primary effect of errors on measurement location . . . . .                       | 37 |
| 5.1 | Definitions and values of terms used in calculation of $P_{cgs}^{rec}$ . . . . . | 70 |
| 5.2 | Values of terms used in calculation of $P_{sw}^{rec}$ . . . . .                  | 71 |
| 5.3 | Selected results of CGS calibration of SeaWinds . . . . .                        | 99 |



## List of Figures

|      |   |    |
|------|---|----|
| 1.1  | Global representation of SeaWinds measurements . . . . .  | 2  |
| 2.1  | Azimuthal dependence of the Geophysical Model Function. . . . .   | 11 |
| 2.2  | Historical characteristics of space-borne scatterometers . . . . .  | 12 |
| 2.3  | Coverage geometry for SeaWinds. . . . .   | 13 |
| 2.4  | Artist’s rendering of SeaWinds. . . . .   | 14 |
| 2.5  | CGS capture geometry. . . . .   | 18 |
| 2.6  | Sample CGS data capture. . . . .  | 19 |
| 3.1  | Flow diagram of the SeaWinds simulation model . . . . .   | 29 |
| 4.1  | Geometry used to define reference directions for SeaWinds . . . . .   | 36 |
| 4.2  | Cluster diagram depicting the interrelationships between $\sigma^\circ$ , measure-<br>ment location, and the five basic elements. . . . . | 38 |
| 4.3  | Backscatter error as a function of instrument pointing . . . . .  | 40 |
| 4.4  | Received power of a sample CGS capture. . . . .   | 42 |
| 5.1  | Reported spacecraft position as a function of frame . . . . .   | 56 |
| 5.2  | Change in spacecraft position as a function of frame . . . . .  | 57 |
| 5.3  | Difference of frame timetags as a function of frame. . . . .  | 58 |
| 5.4  | Timetag improvement through interpolation . . . . .   | 59 |
| 5.5  | Simulation of pulse width determination . . . . .   | 62 |
| 5.6  | Simulation of pulse width at multiple signal-to-noise ratios . . . . .  | 63 |
| 5.7  | Sample CGS data set with overlaid arrival time filter output . . . . .  | 64 |
| 5.8  | Pulse arrival time simulation results . . . . .   | 65 |
| 5.9  | Monte Carlo frequency simulation for carrier and chirp rate . . . . .   | 67 |
| 5.10 | Calculated range as a function of telemetry frame . . . . .   | 74 |
| 5.11 | Arrival time differences between CGS data and model simulations . . . . .   | 75 |

|      |   |     |
|------|---|-----|
| 5.12 | Difference in timetag slope between linearly fit CGS data and telemetry reported values . . . . .               | 77  |
| 5.13 | Mean arrival time difference for each capture between model estimated arrival and CGS recorded values . . . . . | 78  |
| 5.14 | Frequency difference of CGS and simulation model, single capture . . . . .                                      | 80  |
| 5.15 | Frequency difference of CGS and simulation model, entire mission . . . . .                                      | 82  |
| 5.16 | Simulated CGS sweep showing the effects of yaw error . . . . .  | 84  |
| 5.17 | Simulated CGS sweep showing the effects of roll and pitch . . . . .   | 85  |
| 5.18 | Objective function for roll and pitch . . . . .   | 86  |
| 5.19 | Simulation of attitude perturbations . . . . .  | 88  |
| 5.20 | Simulated and received CGS power, example capture . . . . .   | 89  |
| 5.21 | Results of minimum variance attitude fit . . . . .  | 89  |
| 5.22 | Subjective fit of CGS power data . . . . .  | 90  |
| 5.23 | Inner beam power differences for an outer beam capture . . . . .  | 91  |
| 5.24 | Azimuth sensitivity of the CGS . . . . .  | 92  |
| 5.25 | Elevation sensitivity of the CGS . . . . .  | 93  |
| 5.26 | Power difference vs. mission day (total) . . . . .  | 95  |
| 5.27 | Power difference vs. mission day (ascending and descending) . . . . .   | 96  |
| 5.28 | Power difference vs. mission day (outer beam and inner beam) . . . . .  | 97  |
| 6.1  | Orientation of measurement footprint and range resolved slices . . . . .  | 103 |
| 6.2  | Illustration of the effect of measurement orientation on image-based measurement location validation . . . . .  | 103 |
| 6.3  | Gridded slice image of Puerto Rico . . . . .  | 105 |
| 6.4  | SIR enhanced $\sigma^\circ$ image of Puerto Rico . . . . .  | 106 |
| 6.5  | SIR-enhanced $\sigma^\circ$ image of southern Florida, the Bahamas and Cuba . . . . .                           | 107 |
| 6.6  | SIR enhanced image of an descending pass subtracted from an ascending pass . . . . .                            | 109 |
| 6.7  | SIR enhanced image of an aft looking descending pass subtracted from a fore looking ascending pass . . . . .    | 110 |



|      |  |     |
|------|--|-----|
| 6.8  | SIR enhanced image of a fore looking descending pass subtracted from an aft looking ascending pass . . . . .                             | 111 |
| 6.9  | SeaWinds' outer beam antenna pattern . . . . .   | 113 |
| 6.10 | CGS reconstruction of the transmit antenna pattern I . . . . .   | 114 |
| 6.11 | CGS reconstruction of the transmit antenna pattern II . . . . .  | 116 |
| 6.12 | Scatter plot of measurement location error . . . . .   | 117 |
| 6.13 | Distance error results for each quality rating . . . . .   | 118 |
| 6.14 | Distribution of quality factors . . . . .  | 119 |
| 7.1  | Simplified geometry of a scatterometer footprint . . . . .   | 125 |
| 7.2  | Generalized signal flow graph of a scatterometer measurement . . . . .   | 130 |
| 7.3  | Radar ambiguity function for a LFM pulse . . . . .   | 135 |
| 7.4  | Plot of $\bar{V}_{kl}^a$ at $90^\circ$ azimuth as a function of $l - k$ for the HYDROS instrument . . . . .                              | 137 |
| 7.5  | Illustration of antenna rotation effects on Doppler bandwidth . . . . .  | 138 |
| 7.6  | Contour plot of normalized variance as a function of SNR and azimuth offset in decibels for HYDROS at $90^\circ$ azimuth angle . . . . . | 141 |
| 8.1  | Simplified signal flow model for scatterometer measurements . . . . .  | 147 |
| A.1  | Distribution and spectrum of a CGS noise source sample . . . . .   | 165 |
| A.2  | Noise power as a function of mission day . . . . .   | 166 |
| A.3  | Histogram showing the distribution of pulse width estimation . . . . .   | 168 |
| A.4  | Histograms of pulse width estimates for multiple orbit conditions . . . . .  | 169 |
| A.5  | Scatter plot showing the effect of SNR on PRI estimates . . . . .  | 170 |
| A.6  | Histogram of PRI observations for one data capture . . . . .   | 171 |
| A.7  | Mean capture PRI as a function of mission day . . . . .  | 172 |
| A.8  | PRI difference separated by pass direction . . . . .   | 172 |
| A.9  | Estimated carrier frequency and chirp rate as a function of SNR . . . . .  | 173 |
| A.10 | CGS reported center frequency as a function of mission day . . . . .   | 175 |
| A.11 | Example of chirp rate estimation . . . . .   | 175 |
| A.12 | Chirp rate as a function of mission day . . . . .  | 176 |
| A.13 | Peak power of each capture as a function of mission day . . . . .  | 177 |

|  |     |
|--|-----|
| A.14 Peak received power as a function of mission day, separated into orbit passes . . . . . | 179 |
| A.15 Peak received power as a function of mission day, separated by beam                     | 180 |
| B.1 Double integral simplification. . . . .  | 196 |

# Chapter 1

## Introduction

The purpose of remote sensing is to gather information about the physical condition of a location which is difficult, impractical, or undesirable to visit. Examples of remote sensing range from a simple thermometer measuring air temperature outside a window to a complex instrument in space observing arctic ice movement. Satellite remote sensing has become popular in the last decade because a satellite instrument possesses the ability to frequently orbit the entire globe, remotely observing surface and atmospheric conditions on a daily basis, and because the accuracy of data from satellites frequently exceeds those of surface-based measurements.

A particular type of remote sensing, satellite-based instrument which has gained prominence is a microwave scatterometer. Satellite scatterometers are primarily designed to measure wind speed and direction near the ocean surface [8, 21]. They also have demonstrated an ability to perform functions such as tracking the location of icebergs, measuring snow melt cycles in polar regions, monitoring the extent of tropical flooding, and studying wind-caused movement of sand dunes, among others [6, 29, 32, 33, 40, 43, 45, 67]. Scatterometers operate on a simple principle: they transmit microwave energy which bounces off an object, in most cases the Earth's surface, and measure the amount of energy that returns to the instrument. If the surface is rough, the microwaves bounce in a variety of directions, with some of the energy bouncing, or scattering, back in the direction of the instrument. This type of reflection is termed backscatter. By measuring the amount of backscatter from a surface, its electromagnetic properties can be inferred, which, in turn, can be related to physical features such as near-surface wind. Though the method is highly indirect, it is reliably accurate [39].

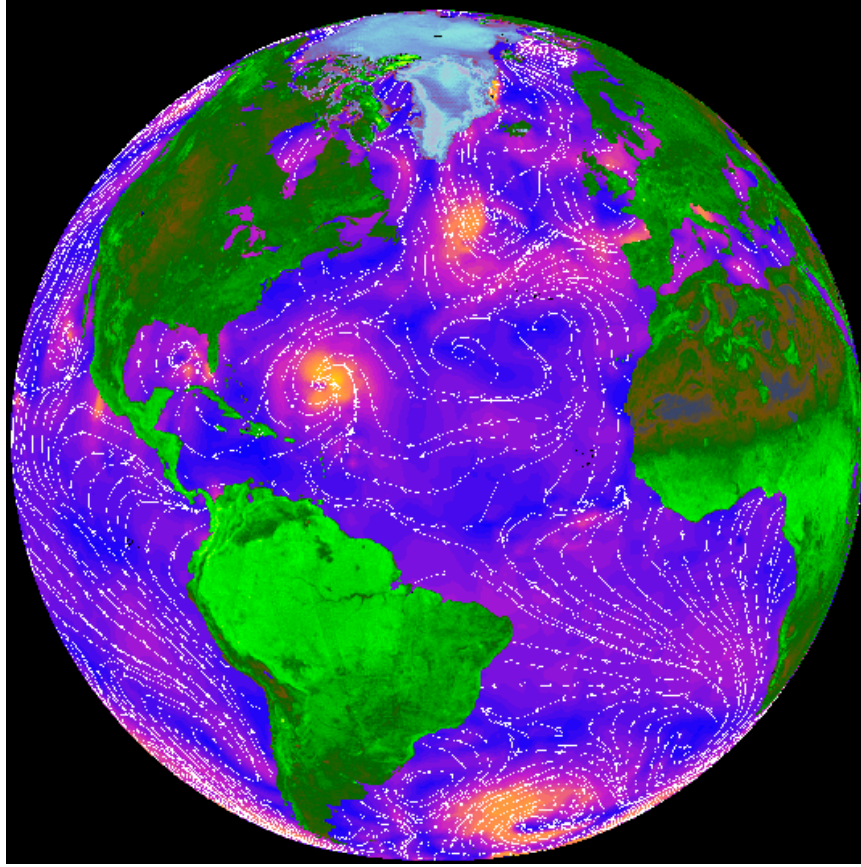


Figure 1.1: An image promoting the capabilities of SeaWinds. Each of the colors and shades are directly related to backscatter values recorded by the instrument. The ocean shades represent wind speed derived from backscatter, with the contour lines showing wind direction. Land hues reflect vegetation types. The various colors in the polar region are representative of water density and snow and ice type [46].

## 1.1 Definition of the Problem

Every instrument since satellite scatterometry originated has endeavored to improve the quality, accuracy, and availability of data. Current conditions have magnified these desires due to a wealth of recently envisioned applications. This dissertation addresses four topics related to improving the design and calibration of satellite scatterometers.

First, NASA's current scatterometer, SeaWinds, has been launched and requires on-orbit calibration. All previous instruments have used fan-beam antenna

configurations, while SeaWinds is fundamentally different in that it uses a pencil-beam approach to scan the surface. While a few existing calibration approaches are valid for SeaWinds' configuration, all were designed for fan-beam instruments. The limited number of existing multi-platform techniques necessitates development of new approaches to accommodate SeaWinds' new measurement approaches. Specifically, precise calibration of instrument power, position, pointing, timing, and frequency, is required for accurate, reliable data. One useful technique to assess scatterometer calibration is a calibration ground station, or CGS. The CGS approach is unique in its ability to provide calibration values independent of the information which is measured and reported by the instrument. This separation allows the CGS to validate results of other methods and also provide information that is otherwise unavailable. To improve instrument performance through calibration, this dissertation develops a new methodology for scatterometer calibration using a passive calibration ground station. It then implements the method, and obtains valuable results. The observed parameters are used to verify instrument operation to ensure that it meets its functional requirements. In addition to this validation, the values obtained also characterize the instrument performance. One of the key results obtained from the CGS relates to timing. SeaWinds CGS calibration detected a one second bias in reported timing improving the measured location of backscatter values by over 7 km.

The second issue addressed by this dissertation is calibration of the specific surface location where measurements are taken. New applications of scatterometer data are focusing on resolution, requiring accurate calibration of the location of measurements. While SeaWinds' performance is excellent, meeting the location accuracy requirement of 10 km, emerging applications such as high resolution wind and imaging techniques desire data accuracy beyond the specifications of instrument design, up to 2.5 km. Precise calibration of measurement location is accomplished using several methods, two new methods are presented in this dissertation. The first method of measurement location calibration uses data images of coastal boundaries to validate reported values. Backscatter measurements made by scatterometers are sensitive to the type of surface measured - land and ocean have very different signatures. Known

coastal locations provide truth data for monitoring discrepancies in measurement location. Comparing reported backscatter and location values to known islands and coast lines allows estimates of measurement location to be made. The second method is based, in part, on the CGS calibration approach. It uses the principles of antenna directivity measurement to estimate SeaWinds' transmit antenna pattern from CGS data. Measurement location estimates are then determined by calculating the boresight of the reconstructed pattern and relating it to the CGS location. Values presented in the dissertation show a mean measurement location error of approximately 5 km, independent of the error caused by the one second timing error, as a result this bias can be accounted for and data accuracy improved to desired levels.

After discussing calibration related issues, the third topic considered in the dissertation focuses on design issues for future instruments. Based on SeaWinds' success, more capable instruments are planned. These new instruments seek to improve data resolution and accuracy over SeaWinds by implementing more sophisticated processing schemes and increasing antenna sizes and pulse rates. Higher pulse rates create an oversampling effect which introduces the issue of correlation between measurements. This topic has been irrelevant to previous instruments and thus has never been addressed in the literature. Correlation initially poses a threat to higher resolution designs by increasing the variance of measurements and thus the precision of backscatter estimates. To better understand how correlation effects scatterometer measurements, the dissertation derives expressions for measurement correlation and relates these expressions to practical effects of measurement correlation on instrument performance, using SeaWinds and a new instrument, HYDROS, as examples. The data shows that SeaWinds pulses are effectively uncorrelated, while consecutive HYDROS pulses have a correlation coefficient greater than 0.3.

The fourth topic considered by this dissertation is the simulation of scatterometer measurements for new instrument and application design. Two forms of measurement variation exist in scatterometry - fading and noise. Fading is multiplicative in nature and related to the surface backscatter amplitude. Noise is additive, caused by thermal excitement and environmental radiation. Previous simulation models do

not separately account for the two variational forms. The dissertation addresses this problem by developing a new simulation model which is able to separately and accurately account for both forms of variation, as well as correlation between measurements. The model is easily implemented, providing a practical tool for simulating data in application development by improving simulation accuracy and reducing development times.

Consideration of these topics advances the field of scatterometer design and development by providing solutions to four current issues. Calibration plays a key role in accurate and precise instrument operation. Better understanding of low-level parameters such as timing and frequency and their new effect on reported data is necessary to not only improve data quality, but to also provide feedback for new instrument designs. Calibration of high-level parameters such as measurement location directly improves data quality. Better understanding of measurement correlation allows new designs to consider more advanced measurement approaches and precisely assess tradeoffs between key instrument parameters. Improved modeling of instrument data allows new instrument designs and new data applications to be rapidly and more accurately simulated.

## **1.2 Research Contributions**

Investigation of issues related to instrument design and calibration results in several contributions to the discipline of satellite scatterometry. The following section highlights several of the fundamental achievements.

The first major contribution of the dissertation is the development of the CGS calibration methodology and associated implementation for SeaWinds. The methodology enhances the ability of a ground station to assist in instrument calibration by detailing the effect of specific parameters on instrument performance. The system-level approach developed for the SeaWinds CGS determines which instrument parameters effect the signal observed by the CGS and which parameters are uniquely identifiable. It provides a way to estimate instrument timing, frequency, position,

pointing, and power using a device which is isolated from the satellite. While the dissertation presents an implementation of the methodology for the SeaWinds scatterometer, the methodology has broad application to general scatterometer design and improves future CGS and instrument designs [64].

A critical component of the CGS approach involves development of the SeaWinds Calibration Simulation Model which models CGS data based on reported instrument telemetry. The model allows for perturbations of telemetry parameters, providing a method to accurately simulate CGS data. The model is valuable for several applications, including CGS-based calibration and measurement location estimation. Further, it can be used as part of image generation code to create images based on perturbed inputs such as attitude.

The next major contribution is the calibration results, obtained from implementation of the methodology for SeaWinds. The successful implementation and operation of a calibration ground station represents a significant accomplishment, as no prior ground station has operated as successfully as the SeaWinds CGS. The results demonstrate the ability of the method, the utility of the CGS, and the excellent calibration of SeaWinds. Results include estimates of several timing and frequency parameters to levels of precision which are magnitudes better than previously determined. Other timing and power parameters are calibrated which were previously inestimable. As a whole, the results show that SeaWinds is well calibrated, stable, and operating as expected on both the QuikSCAT and ADEOS II satellites. The effect of precise calibration results from the CGS allows operators to quickly focus their efforts on areas which are limiting to data accuracy and resolution. The results also provide limits on precision for users and application developers, allowing them to understand the inherent constraints of data accuracy [36, 58–62].

The third major contribution relates to measurement location calibration. Measurement location, along with backscatter values, constitute the primary values reported by scatterometers. Calibration of measurement location directly effects the performance of most applications of scatterometer data. A specific focus on measurement location provides quantitative values of instrument accuracy, and defines limits



of resolution enhancement. The location calibration techniques developed here represent a significant portion of current methods. They show that the SeaWinds instruments are operating within specification for measurement location and also provide specific limits of precision for data applications such as wind speed estimation and image generation [63].

The fourth major contribution is improved understanding of design issues for new instruments, namely measurement correlation. Developed expressions for measurement correlation show that the level of correlation depends on the size of the instrument antenna and the rate at which pulses are transmitted. Moreover simulations show that at low signal to noise ratios noise variation dominates and signal correlation is not an issue, but a high signal to noise ratios correlation becomes a significant issue. Measurements made with multiple pulses are always as effective or better (in terms of variance) than single pulse measurements, but the added benefit decreases rapidly for highly correlated pulses. Expressions derived for correlation and covariance between measurements use a general measurement model which is applicable to all previous and future instruments. The expressions provide a method of evaluating the effects of variations and uncertainties on measurements and what limitations they place on precision. Derived values provide the information necessary to determine the effects of correlation on measurement variance and improve understanding of observed surface features, information which is critical for future scatterometer designs. An understanding of tradeoffs between improving resolution through surface oversampling, minimizing additive noise, and decreasing variance is also developed. Correlation between measurements requires accepting a larger variance, transmitting more power, or using more pulses than required for independent samples, the exact combination being dependent upon specific instrument requirements [65].

The fifth major contribution is the development of the noise simulation model. This new model directly benefits applications designers, allowing them to more simply simulate data fluctuations and conduct tradeoff and design analysis studies. The new model is able to generate data which is statistically equivalent (in a mean and variance sense) to actual instrument measurements by accounting for both fading

and noise while maintaining ease of implementation. Unlike previous models, the new model also accounts for correlation between measurements. The model is particularly adept at handling design tradeoffs related to signal-to-noise ratios by appropriately separating the variational forms. The model applies to new sensor and application designs by assisting in tradeoff studies which strive to maximize performance while limiting costs [66].

### **1.3 Dissertation Outline**

The dissertation is organized as follows. Chapter 2 provides background on the theory and implementation of satellite scatterometer designs, providing a brief analysis of the tradeoffs involved in measurement coverage and accuracy. It introduces the concept of CGS calibration and includes a brief history of the topic. Chapter 3 describes the methodology for the SeaWinds Calibration Ground Station. It discusses the process of extracting information from CGS data and evaluates tradeoffs involved. Chapter 4 discusses issues related to implementation of the methodology and Chapter 5 presents the results of SeaWinds CGS calibration. Chapter 6 presents the topic of measurement location calibration, Chapter 7 discusses measurement correlation issues, and Chapter 8 presents the scatterometer data simulation model. Chapter 9 summarizes key results, discusses limitations and avenues of further research, and concludes.

## Chapter 2

### Background

Scatterometry's foundation began with the development of radar in the 1920's for World War I. During the war it was noticed that radar signals were corrupted by reflections from the Earth's surface and varied with weather conditions. Later, instruments were developed to determine how well radar could measure the roughness of the ocean surface and to study ocean waves. These experiments showed that radar backscatter is proportional to wind speed and related to the azimuthal observation angle relative to wind direction. It was during this time that the term scatterometry was coined, defining the concept of using radar signals to measure the physical characteristics of a surface [54].

The idea of spaceborne scatterometers was hatched with the advent of satellites, motivated by the difficulty of deploying ground-based instruments in the open ocean. The first spaceborne scatterometer was RADSCAT, part of the Skylab experiment flown in 1973 [38]. It proved that physical phenomenon, such as ocean wind speed, could be measured from space using a scatterometer. Its success motivated the development of other spaceborne instruments, six to date, which are designed to measure near surface marine winds and formally established the discipline of satellite scatterometry.

This chapter presents a history of satellite scatterometers, how past instruments have influenced the design and objectives of SeaWinds, and how they guide development of current scatterometer data applications. The chapter overviews the process of measuring marine winds remotely and presents a brief description of the instruments flown to date. The chapter emphasizes design requirements and tradeoffs in presenting the logic behind specific portions of instrument development.

After discussing the development of satellite scatterometers, the chapter turns its focus to calibration ground stations, discussing why a ground station is an attractive option and what previous ground stations have accomplished. It then presents the SeaWinds CGS, its objectives, how it operates, and how it assists in instrument calibration.

## 2.1 Scatterometer Operation

Low elevation winds over the ocean cause waves and roughness on the surface. This roughness has a direct effect on the amount of backscatter measured by a scatterometer. To determine wind speed and direction, a relationship between the wind and the backscatter, termed  $\sigma^\circ$ , must be established. The function which defines this relationship is termed the Geophysical Model Function, or GMF. The GMF requires several inputs, including wind speed and direction, instrument azimuth angle, frequency, and polarization to estimate backscatter observed by the instrument. Scatterometry uses the inverse model to determine wind speed and direction from measured  $\sigma^\circ$  values.

To help understand the requirement on scatterometer design, it is noted that the relationship between  $\sigma^\circ$  and wind direction within the GMF can be generalized using a  $\cos(2\theta)$  function, where  $\theta$  is the azimuth angle of the instrument relative to the wind direction, shown in Figure 2.1. For every  $\sigma^\circ$  measurement there are four possible azimuth directions associated with a single wind speed. To resolve this ambiguity multiple  $\sigma^\circ$  measurements of the same area must be made using a variety of azimuth angles.

The primary objective of satellite scatterometry is to obtain estimates of near-surface wind speed and direction for the majority of the ocean surface every day. To obtain this objective several requirements are developed. First, the satellite orbit and instrument swath must be such that desired coverage is obtained. The second requirement is that multiple measurements of each surface area must be made using several azimuth angles. This section overviews several satellite scatterometers, discussing how their designs meet these objectives.

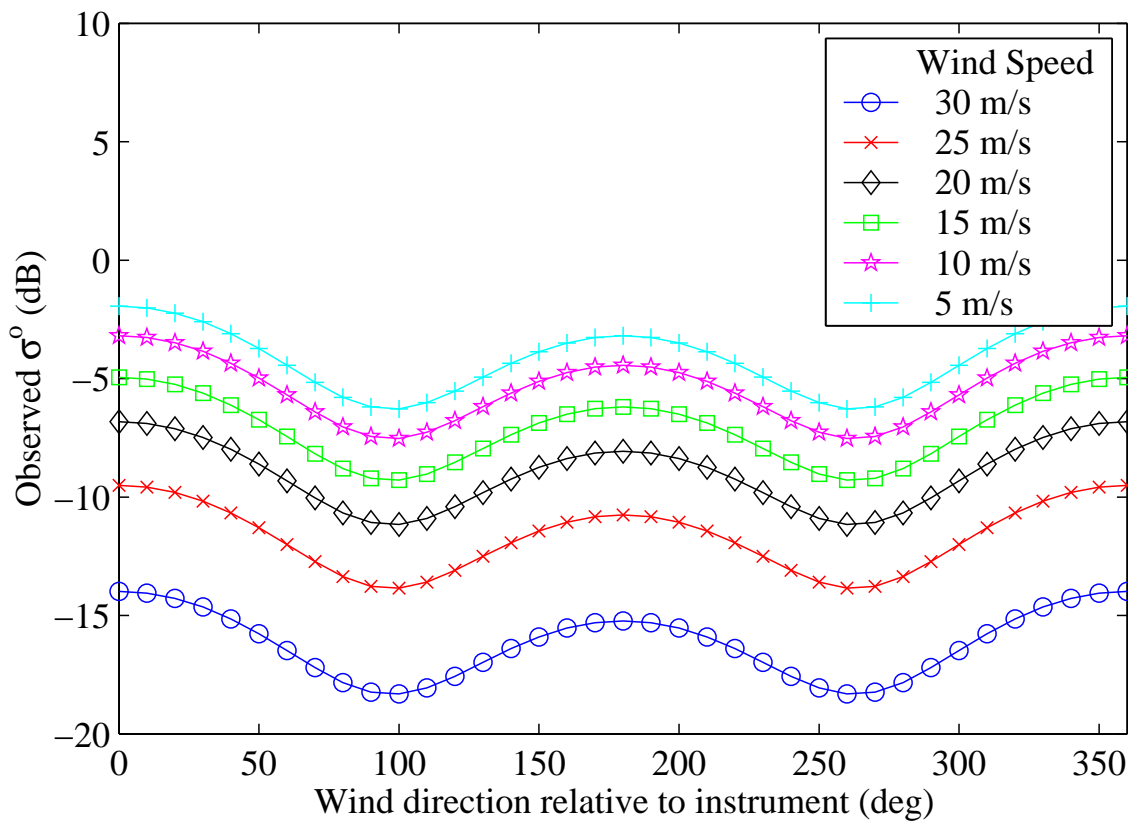


Figure 2.1: Dependence of  $\sigma^0$  on wind speed and azimuth angle [39].

### 2.1.1 Fan-Beam Designs

The first satellite scatterometer program after the Skylab experiment was the NASA SeaSat scatterometer, or SASS, which operated from 6 July to 9 October 1978 [10, 22, 25]. The instrument used four fan-beam antennas, two on each side, in an X-configuration. Each antenna was identical, having a beamwidth of  $0.5^\circ \times 25^\circ$  (see Figure 2.2). This configuration provided two azimuthal measurements, or “looks”, for each surface area and created a swath of 500 km on each side. The swath width allowed SASS to cover the entire ocean every three days. While the mission was short in duration due to a satellite power failure, it advanced the field of satellite scatterometry significantly. It proved that satellites are viable remote sensing devices

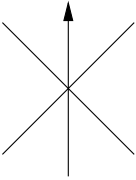
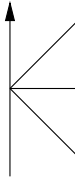
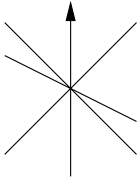
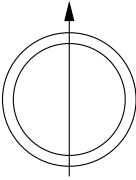
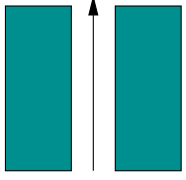

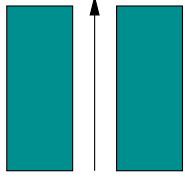
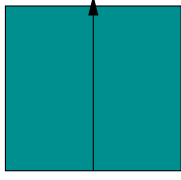
|                      | SeaSat (SASS)  | ERS-1/2   | NSCAT   | SeaWinds   |
|----------------------|--|---|---|--|
| Frequency            | 14.6 GHz   | 5.3 GHz   | 13.995 GHz  | 13.402 GHz   |
| Scan Pattern         |                   |            |                   |             |
| Polarization         | V-H, V-H   | V Only  | V, V-H, V   | V, H   |
| Incidence Angle      | 22°-55°  | 18°-47°, 24°-57°  | 18°-57°, 22°-63°  | 46°, 54°   |
| Beam Resolution      | Fixed Doppler  | Range Gate  | Variable Doppler  | Spot   |
| Resolution           | 50 km  | 50 km   | 25 km   | 25 km  |
| Swath                | <br>500 km 500 km | <br>500 km | <br>600 km 600 km | <br>1800 km |
| Daily Earth Coverage | Variable   | 41%   | 77%   | 93%  |
| Dates of Operation   | 6/78 - 10/78   | 8/91 - 1/01   | 8/96 - 6/97   | 6/99 +   |

Figure 2.2: Historical characteristics of space-borne scatterometers [29].

and that wind fields are estimable from space. It also showed that more than two azimuth looks are necessary to completely resolve directional ambiguities.

The next satellite scatterometer was built by the European Space Agency (ESA) and termed the Active Microwave Instrument (AMI) on the ERS-1 satellite (see Figure 2.2) [9,26]. ERS-1 was launched 17 July 1991 and was followed by another AMI mounted on ERS-2, launched 21 April 1995 [12, 28]. Though the AMI instruments operate at a different frequency, 5.3 GHz, as opposed to 14.6 GHz for SASS, they utilize the same design principle: fan-beam antennas to create a wide swath and multiple antennas to provide several azimuthal looks. ERS improves on the SASS design by using three antennas to obtain more azimuth looks though it only has one swath, which decreases the coverage of the instrument. The simple design of ERS

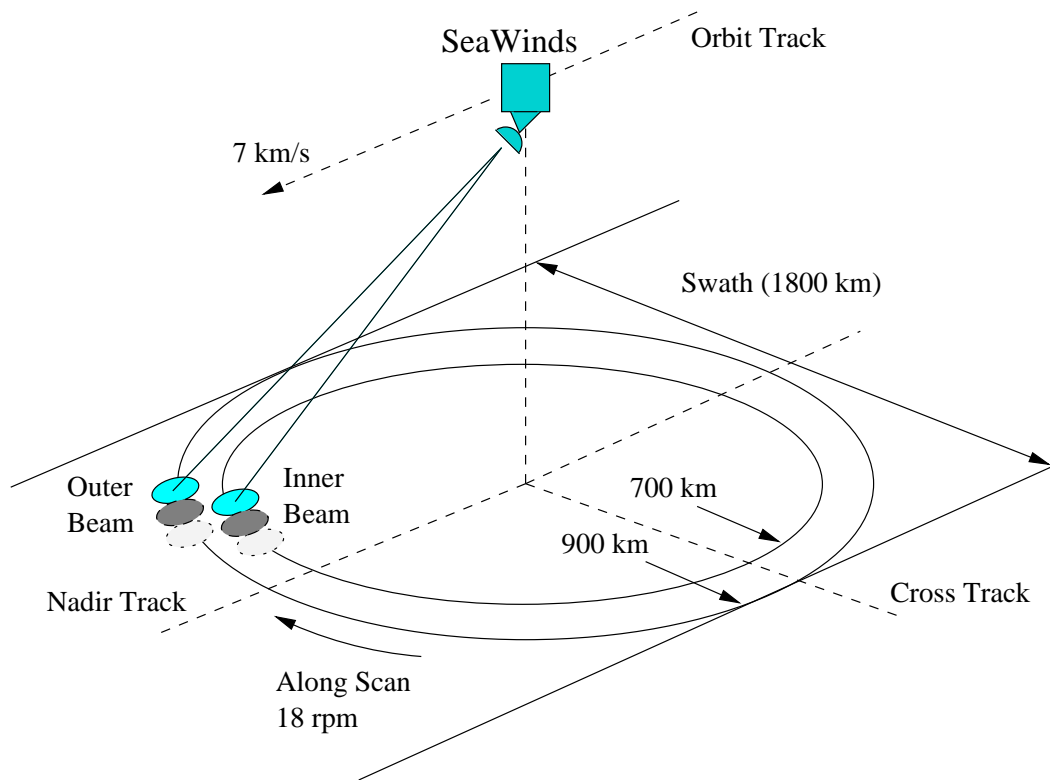


Figure 2.3: Coverage geometry for SeaWinds [51].

proves very effective. While it does not have the swath size of SASS, ERS has been accurate and durable in measuring the winds for over a decade. ERS-1 retired in March 2000, while ERS-2 remains in operation.

The second scatterometer launched by NASA, and fourth instrument overall is the NASA Scatterometer, or NSCAT, launched 17 August 1996 (see Figure 2.2) [39, 53]. Like its predecessors, NSCAT uses fan-beam antennas to create a wide swath. It has a total of six antennas, three on each side to obtain azimuth looks. The design is an improvement over SASS and AMI in that it increases the swath size, allowing it to cover 90% of the Earth every two days. It also provides a better antenna geometry than SASS to estimate wind direction. Unfortunately, due to a solar panel failure, NSCAT's mission ended on 30 June 1997.



Figure 2.4: Artist's rendering of the SeaWinds instrument aboard the QuikSCAT satellite [56].

### 2.1.2 SeaWinds Pencil-Beam Design

The third and most recent NASA scatterometer design is SeaWinds, operating on both the QuikSCAT satellite and the ADEOS II satellite [50, 51]. ADEOS II was originally the only planned SeaWinds mission. The unexpectedly short life of NSCAT and delays in the launch of ADEOS II prompted the development of QuikSCAT as a “quick recovery mission”. This history established the loose convention, which is used here, of SeaWinds on QuikSCAT being referred to as QuikSCAT, and SeaWinds on ADEOS II as SeaWinds.



The design of the SeaWinds instrument is fundamentally different from fan-beam satellite scatterometers. Rather than use multiple fan-beam antennas to create the measurement swath, it has only one antenna, a pencil-beam type, which it mechanically rotates about nadir. The combination of rotation and inclination angle of the antenna give it the advantage of a significantly larger swath (see Figures 2.2 and 2.3) and no gap in the nadir region. The rotating antenna has two feeds, creating two beams, an inner and outer, which provide four different azimuth looks for ground locations.

The fundamental shift in design from fixed fan-beam to rotating pencil beam occurred for several reasons. First, a single antenna is smaller and easier to launch into space. Once in orbit it requires no complicated deployments, a necessary and difficult task required by fan-beam systems. Second, the scanning geometry provides a wider swath and more azimuth looks. Third, the pencil-beam antenna requires no Doppler or range filtering to provide required resolution, simplifying hardware. Fourth, the data is measured using only two discrete incidence angles, as opposed to a range of angles for fan beam systems, significantly simplifying and improving inversion of the geophysical model function for wind estimation. Fifth, multiple polarizations and/or radiometric measurements are easier to implement using a rotating pencil-beam design [47, 49].

## **2.2 Calibration Ground Stations**

A ground station is a surface device that interacts with a spaceborne instrument in some way, either passively listening or transmitting information as the instrument operates overhead. Its objective is to assist in calibration of the instrument. A ground station is a popular calibration option because it is easily observed, controlled and adjusted, unlike a spacecraft which is inaccessible while in orbit.

### **2.2.1 CGS History**

Most satellite scatterometer instruments have had a calibration ground station associated with it, though objectives and operations vary significantly. The ERS instruments utilize transponder ground stations to help calibrate their attitude

and gain constants [12, 19, 27]. Acting as beacons, the transponders sense ERS pulses and reply with pulses having known properties. By measuring the beacon signal, instruments are able to be calibrated. The ERS satellites also benefit from having multiple instruments on board. While the scatterometer instrument (AMI) has three transponders of its own located in Spain, a synthetic aperture radar (SAR) instrument has three separate transponders, located in the Netherlands. Since attitude is the primary object of ERS calibration, the SAR transponders are more heavily used. While ERS attitude is able to be calibrated to within  $0.02^\circ$ , this approach allows for only extremely limited information regarding scatterometer-based calibration [9].

The NSCAT CGS functions differently than the ERS transponders. The NSCAT CGS is designed to receive pulses transmitted by NSCAT, shift the frequency and transmit the pulses back to the instrument. This system allows the CGS to measure characteristics of the NSCAT transmitted pulses, and for NSCAT to characterize its receiver using CGS repeated pulses.

When related to the SeaWinds instrument and the SeaWinds CGS, the history of ground based calibration is brief. While the ERS beacons assist the instrument in calibrating attitude, they focus on the SAR instrument and do not record any information of their own. The NSCAT CGS records some calibration information, though it has limited utility due to the short length of the NSCAT mission and significant stability issues of the NSCAT CGS. This brief ground calibration history is further limited by little published information in the open literature.

### **2.2.2 The SeaWinds CGS**

Like the instrument design, the SeaWinds CGS design departs from the established standard. It does not actively transmit pulses to the instrument, it instead passively listens and records the instrument signal, the satellite being unaware of the CGS's existence. Calibration information is obtained from this design by analyzing the CGS data and adjustments are made through delayed instrument command and data post processing.

The SeaWinds CGS is designed to focus on measuring basic parameters with extreme accuracy [3,4]. This simplification is due to the previous challenges with the NSCAT CGS as well as the completely new design of the SeaWinds instrument. The focus of CGS operation is to provide fast, accurate calibration information about basic SeaWinds operation, focusing on pulse timing, frequency, and received power levels. Advanced calibration issues are addressed primarily using other methods, though the CGS can assist with these issues.

Each time the instrument flies overhead a CGS capture occurs. The CGS predicts from ephemeris data where the instrument will be in the sky and positions its antenna accordingly. When received, the transmitted instrument signal is sampled and recorded. Depending upon the geometry of the pass, the CGS observes either a four beam crossing or a two beam crossing, as shown in Figure 2.5. A four beam crossing consists of the outer beam as the instrument approaches, the inner beam as the instrument approaches, the inner beam as the instrument recedes, and finally the outer beam as the instrument recedes. A two beam crossing occurs when the CGS is only able to observe the outer beam due to pass geometry.

The SeaWinds CGS is able to store 40 seconds of data from each CGS pass. In the case of a four beam crossing, this translates to four 10 second captures. SeaWinds' antenna rotates at a speed of 18 RPM, corresponding to three complete rotations of the antenna, termed sweeps, during each 10 second capture. Once a data pass is completed the data is segmented into 0.1 second files and stored electronically. Figure 2.6 shows a 0.2 second sample of CGS data.

First located in White Sands, New Mexico, the SeaWinds CGS began operation in June of 1999, coinciding with the launch of QuikSCAT. It operated for approximately one year, compiling a large QuikSCAT data set. In March of 2002 it was relocated, for financial reasons, to Provo, Utah where it continued its observation of QuikSCAT. It was switched to SeaWinds observation in January 2003, coinciding with the turn on of SeaWinds on ADEOS II.

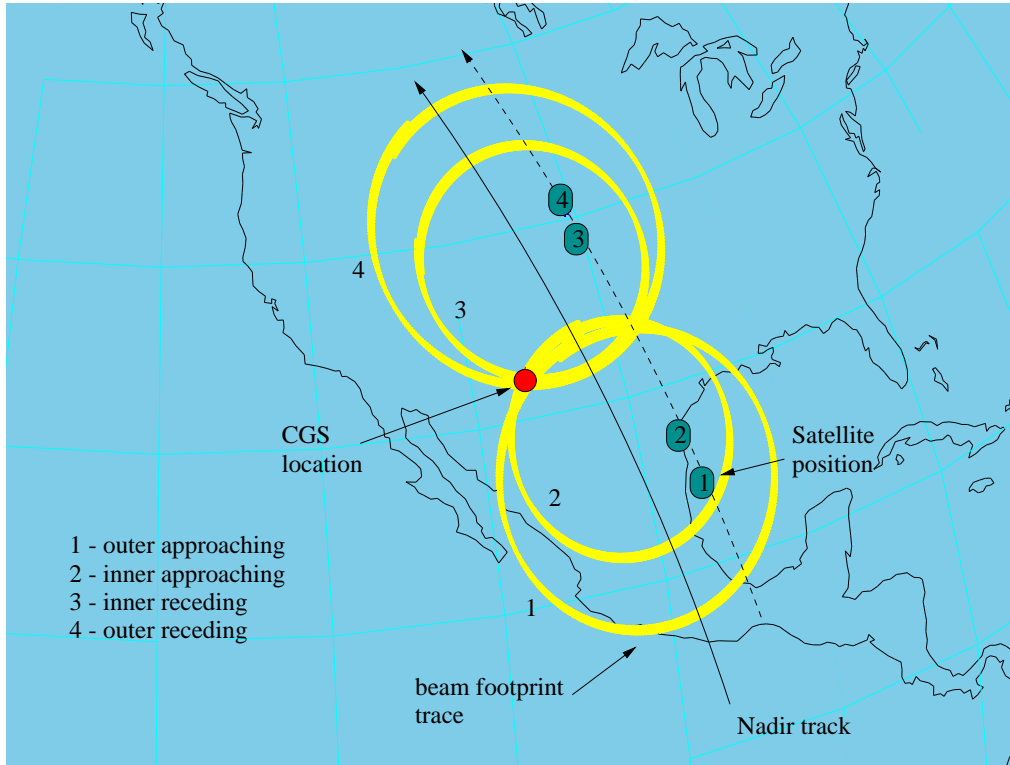


Figure 2.5: Geometry of a four beam CGS capture. The figure shows the footprint trace on the earth's surface and its intersection with the CGS for each of the four captures [5].

### 2.3 Summary

Scatterometry is a constantly evolving discipline where new advancements are constantly required to keep pace with desires and expectations. The design of SeaWinds is fundamentally different from any past instrument. The new design, while promising, requires significant calibration to validate its measurements. The new design of the SeaWinds CGS also shows promise for improving the understanding of SeaWinds operation. While the existing design in some ways constrains the extent of possible calibration options, many approaches can be taken to improve instrument operation. Likewise, new designs require continual education and understanding of theory and related issues. This dissertation addresses several of these desires.

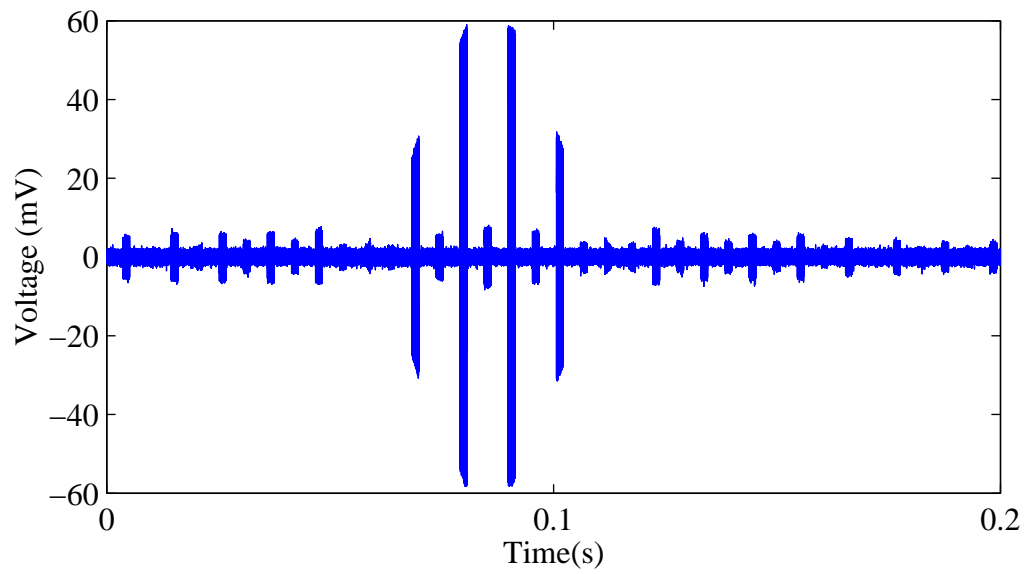


Figure 2.6: Sample CGS data capture. The figure shows the received voltage as a function of time, pulses are clearly evident. The figure displays the excellent signal-to-noise ratio present at the CGS.



## Chapter 3

### Calibration Methodology

Previous calibration ground stations associated with satellite scatterometers have been active - both receiving signals from and transmitting information to the orbiting instrument as it flies overhead. The SeaWinds' CGS is passive, or receive-only. Previous scatterometers have also been fan-beam configurations while SeaWinds is a rotating pencil-beam instrument. As such, several key issues relating to the design and implementation of the SeaWinds CGS have never been completely assessed. Moreover limited ground station related literature reveals little investigation into ground station capability, therefore a new methodology for using a receive-only ground station needs to be developed for SeaWinds calibration.

The primary objective of a passive ground station is simple: use data recorded by the ground station to calibrate instrument parameters and characterize performance. Each pulse received by the ground station contains information relating to the power, position, pointing, timing, and frequency of the instrument, the desired calibration parameters must simply be extracted from the data. The process of extracting information from the data consists of four steps. First, the instrument signal must be captured. Second, the data must be processed into an easily recognizable form. Third, the processed data is analyzed for information. Finally, calibration estimates are reported and instrument operation is modified as necessary.

This chapter develops a methodology for calibration of the SeaWinds scatterometer using the receive-only SeaWinds Calibration Ground Station. The methodology presents issues and tradeoffs for each phase of the calibration process and strategies for resolving the tradeoffs.

### 3.1 Data Capture

The first step in instrument calibration using a passive ground station is the capture of instrument data. Passive ground stations are able to estimate instrument timing, frequency, power, position, and pointing. They cannot calibrate the instrument receiver or data processing systems, nor can they observe all internal instrument control and communication. Issues related to CGS data capture include the number and location of ground stations, the frequency of data capture, and the method of data acquisition.

The first consideration is the number of calibration ground stations used. Multiple ground stations improve on a single station system by providing additional spatial and temporal coverage of instrument operation. A configuration of multiple (three to five) stations placed over several hundred kilometers, where all units are covered simultaneously by the swath of the instrument, is one option. Accurate triangulation of instrument position and coherent comparison of received signal data streams allows for calculation of pointing and position estimates. An alternative configuration is the placement of ground stations at relatively large distances, perhaps one or two in each hemisphere of the earth. The benefit of this arrangement is improved spatial and temporal sampling of instrument operation. While a distributed arrangement may provide six to eight spacecraft observations per day, a single unit or compact cluster of stations only has the ability to observe the instrument once or twice per day.

The tradeoff for the improved capability of multiple calibration units is cost. Precision ground stations are expensive to build and expensive to deploy. Each calibration unit also requires consideration of the environment of each ground station. Ocean areas, extreme temperature zones, and political climates pose significant complications, limiting available spatial diversity. For example, calibration units in polar areas are attractive due to their frequent observation of the instrument but are costly to construct and maintain.

The decision tradeoff for multiple units is the benefit in improved calibration of each ground station relative to its cost. A single ground station provides



a wealth of information, additional units provide proportionally less information, though they may be fractionally less expensive. A related issue is the capability of each station. A precision station capable of detailed calibration estimates can be more expensive to design and construct than several low-cost units. The details related to this tradeoff are dependent upon specific costs and limitations which cannot be considered here.

For SeaWinds the decision was made by the SeaWinds project to operate only a single calibration ground station. It was believed that the monetary costs of multiple units outweighed the benefits of additional stations. A single precision unit is able to make a strong contribution to instrument timing, frequency, and power measurements, while other parameters such as attitude can be calibrated using other methods. This choice is correct in the sense that timing and frequency estimates are excellent in accuracy and precision. In hindsight, better attitude estimates for SeaWinds would be possible using multiple CGS receivers arrayed in a small constellation.

The choice of a single calibration unit leads to the next consideration in data capture, which is station placement. The primary consideration in placement of a single ground station is the number of times it observes the instrument. Excluding polar regions, most geographical points are covered once per day. Based on the inclination angle of SeaWinds' orbit, some locations observe two instrument passes per day, a few have none. SeaWinds repeats its orbit every four days. Placing a single CGS unit in an area which maximizes the number of instrument observations over any four day period is desirable. Such a location is dictated by orbit geometry.

The SeaWinds project placed the CGS in White Sands, New Mexico, an ideal location with regard to orbit coverage. It receives six observations by the instrument over any given four day period, the maximum possible for SeaWinds at non-polar latitudes. Being in a desert, attenuation from rain and humidity is minimal.

Once placement of the ground station is resolved the next issue related to data capture is the design of the physical capture system, namely the receiver. The

first receiver issue is the type of antenna chosen. Tradeoffs involving antenna design are the subject of volumes of literature, though most focus mainly on beamwidth and gain. For a poor signal-to-noise ratio (SNR) at the CGS a high directivity antenna is desirable to improve the strength of the signal received. High directivity generally translates to small antenna beam widths, requiring more accuracy in antenna pointing. A large beamwidth which requires only limited pointing accuracy results in reduced SNR.

The most general receiver is an omni-directional antenna. An antenna of this kind requires no pointing at all since it has uniform gain in all directions though the maximum gain of this antenna is significantly smaller than other configurations. It is thus subject to issues such as multipath which corrupt the signal. In contrast, a directional antenna such as a horn or dish can also be used. While this type of antenna must be pointed towards the instrument, it provides significantly more gain and mitigates multipath issues. Such pointing requires knowledge of the instrument's position and a mechanism to move the antenna.

The primary issue of pointing is knowledge of the CGS's antenna position relative to instrument position in space. To properly position an antenna before a capture occurs orbital prediction is required, the specified accuracy of the antenna pointing is dependent upon the accuracy of the orbit prediction. Once the accuracy of orbit prediction is verified, required CGS pointing accuracy is specified, and a related antenna beamwidth and directivity are determined.

A second issue related to the CGS antenna is signal polarization. Most scatterometers transmit linearly polarized signals, using both vertical and horizontal polarizations. The option of differentiating signal polarization is related to required signal power and cost of additional hardware. For polarization separation two receivers are required, increasing the complexity of the system. This discrimination provides more signal power and ability to differentiate pulses of alternative polarizations. A uni-pol receiver, such as one that is circularly polarized, is easier and cheaper to design, but reduces signal power and eliminates polarization differentiation. The SeaWinds CGS employs a single, circularly polarized horn antenna.

Other issues related to receiver design include controlling the temporal stability of the ground station and accounting for the system noise figure. The precision and stability of the RF hardware directly effects the ultimate performance of the ground station. Tradeoffs relating to these factors are a balance of accuracy, simplicity, and cost.

SeaWinds' CGS design allows for inaccuracies in orbit prediction by utilizing an antenna which has a wide beamwidth. A large available signal-to-noise ratio supports this decision. The beamwidth (over  $13^\circ$  within 3 dB of the peak) allows for instrument movement during capture and reduces the effects of errors in CGS antenna pointing.

The final issue related to data capture is the amount and rate of data acquired. It is assumed that data capture occurs in a digital format using an analog-to-digital (A/D) converter. While analog capture is possible, it severely limits the quality of data and types of calibration analysis available.

In most situations it is desirable to capture instrument observations as frequently and as long as they occur. The only limitation to this principle is the data handling capacity of the ground station in processing and analysis. A given surface point is observed by the instrument for a finite amount of time over each orbit. The duration of this observation is dependent upon the instrument-based capture geometry. During this time data is captured at a particular rate. In most situations the total amount of data available (rate multiplied by duration) exceeds the limitations of the processing hardware. One way to reduce the required capacity is to reduce the sample rate by mixing the received signal to a lower frequency. The magnitude of this reduction is dependent upon the combined signal and Doppler bandwidth and also desired time resolution.

Once data rate is established, capture duration is then established, based on the capacity of the receive hardware. If the hardware can handle a capture of the full duration, the choice is simple. If this is not the case, the choice must be made of when to sample. For SeaWinds, most ground points are observed four times though some captures only see the outer beam (see Figure 2.5 regarding capture geometry).

Four beam captures have a time gap between the approaching captures and the receding captures. This represents a time when data capture might be eliminated. This choice is dependent upon the ability of the ground station hardware to restart the capturing in a relatively short time period and its accuracy in doing so.

SeaWinds CGS data capture is designed around a 41.5 MHz A/D converter. The instrument carrier frequency is 13.402 GHz, which is mixed at the ground station in two stages, 13.007 GHz and 360 MHz, to a center frequency of 35 MHz. The bandwidth of the received signal is 375 kHz with an expected variation of  $\pm 500$  kHz due to Doppler shift. The mixed signal is sampled at 41.5 MHz and decimated by a factor of 8, yielding an effective sampling rate of 5.1875 MHz. This sampling provides an effective bandwidth of just over 2 MHz and a time resolution of  $0.192 \mu\text{s}$ , adequate for the expected signal.

The CGS A/D has a buffer of 400 MB, allowing a maximum of 40 seconds of data capture for each pass using a 2 byte sample digitization factor. The critical decision given this limitation is where to allocate the 40 seconds of capture. It was decided by the SeaWinds project to perform the most straightforward allocation: 10 seconds to each beam crossing, and 20 to each beam when only the outer beam is visible. Considering that SeaWinds rotation rate is one rotation per 3.3 seconds, 10 seconds allows for capture of three full rotations. This allocation has proven adequate for effective measurement of pulse timing, frequency, and power. It is also adequate for nominal attitude estimation, though Chapter 6 demonstrates that precise pointing estimates are more effective using longer durational captures.

## 3.2 Data Processing

Once the issues of data capture have been evaluated the next step is to consider issues related to data processing. These issues are heavily dependent on the number of ground stations and the types of data captured for each pass. A single CGS configuration, like SeaWinds, greatly simplifies the processing.

The primary goal of data processing is to provide all available information from the waveform without compromising its accuracy. In general, any system which

samples the signal at an adequate rate for time and frequency resolution, is well calibrated for power stability, and has a reliable method of storing data is appropriate. Consideration must be given to each component in the design as to how it effects these parameters. More specific descriptions of the SeaWinds CGS design related to this matter can be found in [2–4].

The second issue related to data processing is management of the ground station. With the advancement of modern computers it is sufficient and perhaps desirable to have an unmanned, automated system. The SeaWinds CGS operates by obtaining instrument orbit information ahead of time, predicting the captures, digitizing the data, and posting the data to an FTP site using a network of three workstations. One workstation acts as a controller for the antenna pedestal, using orbital predict information to point the antenna in the calculated direction prior to data capture. The second workstation houses the A/D converter. It uses GPS time signals to trigger digitization of the data and processes the A/D signal into a analyzable waveform. The third workstation acts as a server. It obtains the orbit prediction data, schedules the captures, and handles the data once processed. This arrangement allows for autonomous operation and remote analysis of the data at a reduced cost compared to a manually operated system.

### **3.3 Data Analysis**

Discussion of data analysis, the third step, allows for consideration of a wide variety of viable implementations. The step consists of applying a set of algorithms to the data and extracting desired calibration parameters. The primary limitations on the analysis are the data provided by the CGS and the accuracy desired for instrument calibration.

The first consideration in analysis is the accuracy of the data used in conjunction with the CGS such as instrument telemetry. Variations and limitations in this information directly degrade the precision and accuracy of reported values. The second consideration of data analysis is determination of which parameters need to be calibrated, followed by analysis of which can be observed and identified. The number

and type of available parameters is dependent upon satellite instrument operation and the geometry between instrument and ground station. Many parameters can be observed through the recorded waveform but not uniquely identified (separately estimated). Many can be identified, but with varying levels of accuracy. Thus, the sensitivity of the received waveform to calibration inaccuracies is a critical portion of data analysis. The answers to these issues direct the basic design of the ground station and the types of analysis possible. It is desirable to estimate as many parameters as possible, but also necessary to recognize limitations and not pursue parameter estimates which are lacking in sensitivity.

When the SeaWinds CGS was first envisioned it was perceived simply as an aid in initial sensor validation; it was designed to measure basic instrument operation such as pulse timing, frequency, and power [3]. Once it became apparent that SeaWinds was operating well within specification and the CGS was performing well beyond expectations, its role was expanded to encompass sensor characterization - a comprehensive analysis of instrument performance in an attempt to operate SeaWinds at levels exceeding its initial design. As will be shown in the following chapters, the SeaWinds CGS fulfills its primary role extremely well, providing estimates of calibration parameters which are orders of magnitude better than previously possible.

The expanded role of characterization was proposed after CGS fabrication and instrument launch and thus was not fully considered in the design stage. Ideally, sensitivity and identifiability issues are analyzed prior to CGS implementation so as not to be compromised by limitations in the design. However, the CGS was designed and built before the expansion of its role, and prior to the author's involvement, resulting in some suboptimal abilities. As a result most tradeoffs addressed here are limited to determining what is possible with the existing system. The limitations of the CGS design in this expanded role are apparent, most prominently in attitude characterization. Timing inaccuracies associated with the SeaWinds instrument and its associated spacecraft (QuikSCAT and ADEOS II) limit the ability of the CGS to accurately determine the pointing of the instrument for a given pulse. This, along

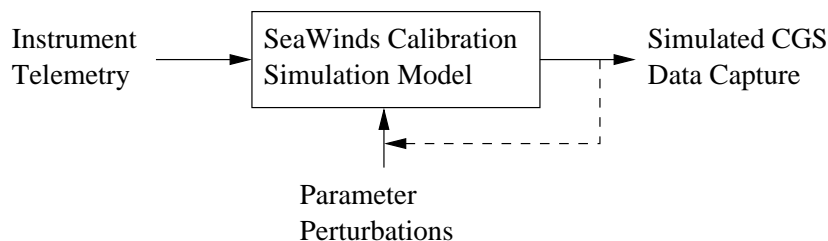


Figure 3.1: Flow diagram of the SeaWinds simulation model. The software model accepts instrument telemetry as an input as well as any desired perturbations, producing files which simulate CGS data captures. Comparison between actual CGS data and simulated data provides required feedback for the recursive estimation process, helping the model best match received data.

with limited sensitivity to attitude induced gain variations limit the precision of CGS-based attitude estimates.

The bifurcated development of the CGS's role in calibration and characterization leads to a two phased analyses. The first phase is validation of basic sensor operation. The SeaWinds sensor is designed to meet certain specifications. The primary role of the CGS is to determine if the instrument meets these specifications. For the validation phase a type of blind analysis is selected. The analysis is termed blind because only very limited information about instrument operation is assumed. While basic operation geometry and specifications are used, no telemetry relating to captured pulses is incorporated. Blind estimation is advantageous because of its simplicity and ease of implementation, algorithms assume no prior parameter distributions. Blind calibration is well suited to parameters which are directly observable and identifiable through CGS measurements of pulse timing, frequency, and power. The sensitivity to these parameters is directly related to CGS precision and not dependent upon outside information such as telemetry. Examples of blind calibration parameters include pulse width, pulse period, carrier frequency, and chirp rate. In this phase the CGS excels.

The second phase of data analysis is the extension of CGS operation to complete characterization. The approach used in extended calibration is a model-based approach. The model simulates the operation of the instrument during ground station capture by using instrument telemetry to simulate CGS data sets, as described by Figure 3.1. Analysis then compares model data to actual ground station data, providing observations of desired parameters. Parameter estimates are recursively fed back into the model until some minimum error is attained. This approach is advantageous over blind calibration because the added information increases the potential of estimating a broader range of calibration parameters and gaining a more accurate understanding of the inter-relationships between all elements of operation. The tradeoff with this approach is a significant increase in complexity. It also requires in-depth analysis of telemetry parameters. Finally, the approach requires detailed consideration of parameter sensitivity. While many parameters can be observed, not all can be uniquely identified. Examples of parameters estimated using the model-based approach include instrument frequency compensation, satellite position, and spacecraft attitude.

### **3.4 Calibration Reporting**

The final stage of the calibration methodology is the reporting of calibration analysis results. Results obtained from data analysis are reported as necessary so that instrument operation and recorded data may be modified to optimize performance.

### **3.5 Summary**

The SeaWinds CGS differs from past ground stations by being passive, requiring a new methodology for use. This section provides an overview of the philosophy and approach required to obtain calibration information from this type of ground station. It describes basic instrument operation and basic guidelines for estimating parameters related to its operation. Successful extraction of these calibration parameters requires an appropriate approach and implementation of the methodology.



While SeaWinds is the instrument of focus, the philosophy and approach presented are applicable to most scatterometers.

The SeaWinds CGS was designed and constructed prior to the development of the methodology and the expanded CGS role in calibration and characterization. Most issues related to data capture were already decided [3]. The remaining requirement is development of an approach which defines the availability, observability, and identifiability of parameters and an implementation of algorithms to provide estimates of desired calibration information.



## Chapter 4

### Calibration Methodology - Approach and Implementation

The calibration methodology described in the previous chapter is motivated specifically by the need for calibration of the SeaWinds instrument, on both the QuikSCAT and ADEOS II platforms. In developing the methodology for SeaWinds CGS calibration several issues were introduced, namely the recognition of calibration parameters and the determination of their observability and identifiability. This chapter describes the approach and implementation of the methodology for the SeaWinds CGS by considering these issues.

The chapter is divided into three sections. The first, parameter recognition, employs a top-down approach, beginning with required values for wind estimation and determining which operational elements effect these primary values. The following section thoroughly describes SeaWinds CGS data captures, relating data description to recognized parameters. This description serves as an introduction to the third section, parameter observation and identification. The remaining issue of the methodology is sensitivity. While this issue might be appropriately considered here, it is presented along with the results of CGS calibration in Chapter 5 to allow for consideration of specific values as they relate to the accuracy and precision of the model and CGS.

#### 4.1 Parameter Identification

##### 4.1.1 Foundation

Fundamentally, the only data required for scatterometer applications are  $\sigma^\circ$  values and the surface location where  $\sigma^\circ$  is recorded. From these two terms the GMF is calculated and vector winds estimated. Because of their importance, these

Table 4.1: Selected SeaWinds technical mission requirements [1].

| Parameter               | Description | Requirement |
|-------------------------|-------------|-------------|
| $\sigma^\circ$ Accuracy | Absolute    | 0.9 dB      |
|                         | Relative    | 0.2 dB      |
| Location Accuracy       | Absolute    | 25 km (rms) |
|                         | Relative    | 10 km (rms) |

two parameters are assigned specific accuracy requirements within primary mission requirements (see Table 4.1). The primary objective of calibration is to ensure that the instrument meets prescribed specifications, the goal is realized by calibrating individual parts of the instrument which effect  $\sigma^\circ$  and measurement location.

Mathematically,  $\sigma^\circ$  and measurement location can be modeled using four elements: transmitted power, signal frequency, satellite position, and instrument pointing. Calibration tools such as ground stations are designed to measure parameters related to these four elements. The CGS measures two of these parameters directly, power and frequency, and indirectly confirms position and pointing.

This section describes the process of separating instrument operation into simplified elements and the inter-relationships between the elements. It also qualitatively assesses the methods used to independently evaluate the calibration of each - which parameters can be estimated blindly by the CGS and which require the assistance of the simulation model.

### The Radar Equation

The normalized radar backscatter ( $\sigma^\circ$ ) is related to received power using the radar equation. A commonly used form is [41],

$$\sigma^\circ = \frac{P_r (4\pi)^3 R^4 L}{P_t G^2 \lambda^2 A}, \quad (4.1)$$

where  $P_r$  is the reflected power received by the instrument,  $R$  is the range from the instrument to the ground measurement location,  $L$  is a loss term incorporating system losses,  $P_t$  is the amount of power transmitted,  $G$  is the antenna gain,  $\lambda$  is the

wavelength of the transmitted energy, and  $A$  is the area illuminated by the antenna. This simplified form aids in understanding factors which influence  $\sigma^\circ$  calculation though in actual application the radar equation is not this simple. Variables such as range and gain are not constant over the entire area illuminated by the instrument. The nominal illumination area for SeaWinds is 25 km x 35 km. Within this footprint radar range varies by more than 18 km and gain varies by 3 dB. (The 3 dB beamwidth is the commonly defined value for illumination area.)

SeaWinds obtains values for  $\sigma^\circ$  using an integral form of the radar equation which accounts for these variations

$$\sigma^\circ = \frac{P_r}{X}, \quad (4.2)$$

where  $X$  is defined as

$$X = \frac{P_t}{(4\pi)^3 L} \iint \frac{G^2(d\bar{r})\lambda^2(d\bar{r})}{R^4(d\bar{r})} d\bar{r}, \quad (4.3)$$

with  $\bar{r}$  as the vector between the instrument antenna and each illuminated point on the surface. This form of the radar equation better emphasizes the relationship between instrument operation and the terms of the equation. The gain,  $G(\bar{r})$ , for each point on the ground is a function of the angle between the antenna boresight and  $\bar{r}$ . Likewise,  $R(\bar{r})$  is a function of each individual point. For most instruments, wavelength is treated as a constant and is not a function of measurement location. SeaWinds varies the transmit frequency while a pulse is being transmitted, thus the wavelength is a function of  $\bar{r}$  as well. To determine  $\sigma^\circ$  for a transmitted pulse each of the terms in (4.3) must be known for each point in the illuminated ground area.

### Measurement Location

The geographic area where a pulse impacts the Earth's surface is defined as the location of the measurement. In SeaWinds' case measurement location is a function of instrument pointing, satellite position, satellite velocity, pulse frequency, and geometric parameters of the Earth such as topography.

The combination of these factors creates coordination issues which complicate measurement location calculation. Figure 4.1 illustrates the geometry associated

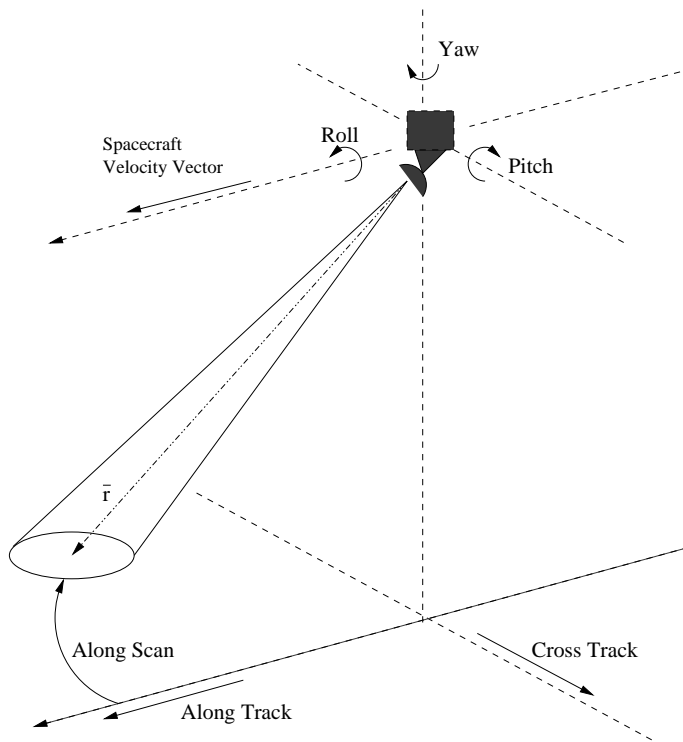


Figure 4.1: Geometry used to define  $\bar{r}$  and reference directions - roll, pitch, yaw, along track, cross track, and along scan.

with measurement location, defining the vector  $\bar{r}$ , as well as directions for spacecraft roll, pitch, and yaw, referred to as attitude. Table 4.2 describes the nominal effect of variations on measurement location.

#### 4.1.2 Calibration Elements

The values of  $\sigma^\circ$  and measurement location can be modeled as a function of the four elements: power, frequency, position, and pointing. The relationships between these parameters and their effect on  $\sigma^\circ$  and measurement location is complex. This section briefly describes their interrelationships, illustrated by Figure 4.2.

#### Power and System Gains

The first calibration element, power and system gains, incorporates the transmitted power, system gain and loss, antenna gain, and received power terms in

Table 4.2: Primary effect of errors on measurement location

| Variation | Description          | Directional Effect                       |
|-----------|----------------------|--|
| Position  | Satellite Location   | Along Track<br>Cross Track<br>Range      |
| Attitude  | Roll<br>Pitch<br>Yaw | Cross Track<br>Along Track<br>Along Scan |
| Antenna   | Alignment Error      | Along Scan                               |
| Frequency | Frequency Shift      | Range                                    |

the radar equation. Transmitted power is a function of transmitter gain and loss, which is determined by power amplification factors of the system hardware. Internal losses are calibrated before launch.

The CGS performs power calibration by monitoring the transmissions of the instrument. The power levels of each transmitted pulse are recorded, and using nominal values for satellite range and antenna gain, an estimate of transmitted power is made. Since a CGS records transmitted energy, it is not able to assist in calibrating received power for the instrument. For SeaWinds this problem is solved using an onboard calibration loop which feeds the transmitted power into the receiver. The CGS also aids in stability analysis by comparing power values over several passes.

Incorporating the simulation model into CGS calibration provides the ability to separate the transmitted power, antenna gain, and range spreading terms. By separating these terms, transmitted power no longer becomes a function of satellite position (via range loss), or instrument pointing (via antenna gain). This permits short term analysis because variations are accounted for without averaging.

### Frequency

For SeaWinds, calculating  $\sigma^\circ$  requires determining measurement location as a function of frequency. Calibration of the frequency chirp can be performed by measuring the received frequency at the ground station. A second frequency shift is

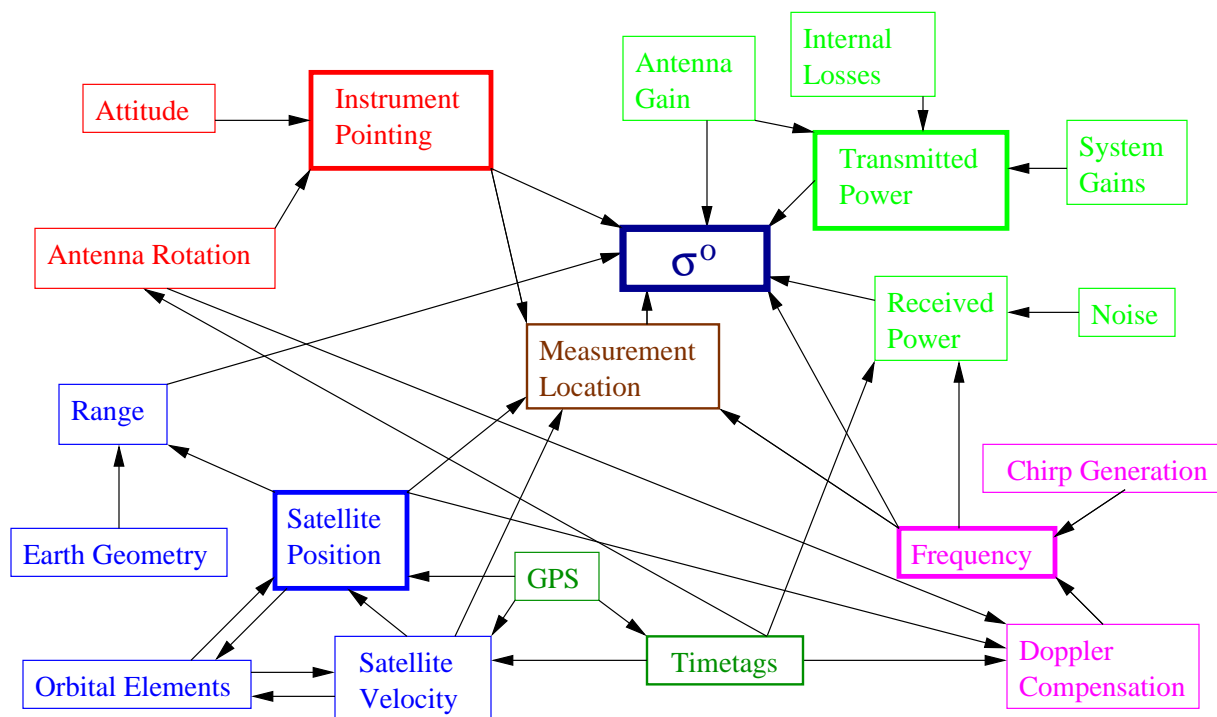


Figure 4.2: Cluster diagram depicting the interrelationships between  $\sigma^0$ , measurement location, and the five basic elements.

the Doppler effect. Transmitted pulses naturally shift in frequency when they impact the Earth, caused by the motion of the satellite relative to the Earth. This shift is a function of instrument pointing, satellite position, satellite velocity, instrument timing, and Earth topography. SeaWinds pre-calculates the Doppler shift based on the spacecraft and antenna position for a given pulse and alters the transmit frequency to account for this effect so that the received echo frequency is nominally constant.

Calibration of Doppler pre-compensation is obtained by recording the received frequency of the signal at the calibration ground station. Incorporating the simulation model allows the center frequency / Doppler pre-compensation / Doppler effect triad to be separated, impossible using CGS data alone. This separation permits specific analysis of the compensation algorithm and estimates of center frequency stability.



## Satellite Position

Accurate knowledge of satellite position is required for determining the location of each measurement, the range of the satellite to the ground, and the appropriate frequency compensation for a given pulse. SeaWinds determines satellite position using an on-board GPS receiver and associated time measurements. Position is also related to the orbital velocity of the satellite. The CGS is not able to precisely determine satellite position since range is an insensitive metric. It can validate position by confirming that data captures occur at predicted times and frequencies. The model improves capability by validating the range between satellite and CGS through confirmation of expected time delays.

## Instrument Pointing

Pointing, or attitude, is the most critical element of system calibration because extraordinary precision is necessary for acceptable  $\sigma^\circ$  accuracy. Slight variations of even a tenth of a degree significantly alter measurement location calculations and  $\sigma^\circ$  values, shown in Figure 4.3. Accurate pointing knowledge is also necessary to calculate the measurement location, range, gain, and wavelength terms of the radar equation.

Precision attitude values are obtained using ground-based targets such as ground stations. As shown in Table 4.2, variations in attitude mislocate the ground footprint. Roll and pitch values are verified by triangulating several satellite positions and instrument pointing angles with a single point on the ground. Yaw is particularly difficult to determine for SeaWinds because the rotating antenna causes the antenna azimuth pointing angle and yaw angle to be on the same axis of rotation.

Antenna azimuth is defined as the angle at which the antenna is pointing in reference to the direction of motion. It is a function of antenna motor rotation and alignment of the antenna on the motor. Before launch, the antenna motor is tested for rotational velocity and the alignment values are recorded. It is, however, impossible to completely simulate the effects of launch and additional calibration is desired once in orbit.

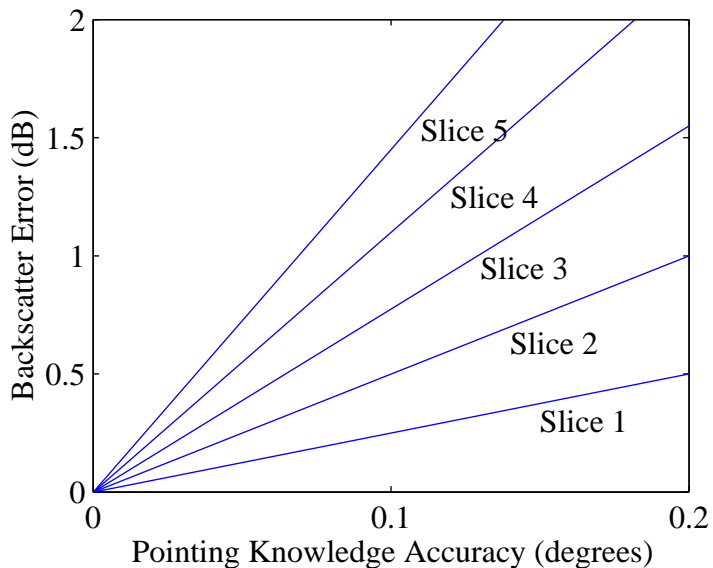


Figure 4.3: Backscatter error as a function of instrument pointing for several range resolved measurement slices. Each slice corresponds to a different range location within the antenna footprint. The figure shows that minor pointing errors cause significant deviations in calculated  $\sigma^\circ$  values. These values are compared to Table 4.1 for requirements of attitude precision [51].

Determination of antenna pointing and yaw is further complicated by timing issues. Since the antenna is rotating, the exact time of transmission of a pulse is necessary to determine the azimuth angle of the pulse. The coupling of antenna pointing, yaw, and timing make this issue most difficult in terms of achieving calibration.

The subject of attitude is a major emphasis of the model-based approach for SeaWinds. The CGS is unable to blindly estimate attitude due to its dependence on other elements. The simulation model possesses the ability to isolate the antenna gain term from transmitted power and range loss thus allowing for estimates of attitude to be made.

## Timing

In order for the SeaWinds instrument to operate correctly, all systems must be coordinated through timing. Timing relates antenna pointing to attitude. It relates satellite position and velocity to measurement location as well as received power to instrument gain. Though it is not directly implicated in the radar equation, instrument timing calibration is imperative to accurately determining  $\sigma^\circ$ , as shown in Figure 4.2.

For SeaWinds, timing information is ultimately related to measurements obtained from GPS satellites. The time values obtained from GPS are known to be accurate to within nanoseconds, more precision than is necessary [24]. Timing values, termed timetags, are the time associated with satellite operation - satellite position, antenna angle, and pulse transmit time. Ideally, timetags match the absolute reference times received from GPS. However, due to hardware delays, computer digitization, and software truncation, timetags differ from GPS time values by several milliseconds, a significant amount. Timing variation introduces errors in the gain, range, and frequency terms of the radar equation. For this reason timing is critical to system calibration.

Accurate time information can be derived using the calibration ground station. The ground station is also linked to GPS time measurements and has known internal delays. By comparing the time that pulses arrive at the ground station to the time recorded by the instrument, proper timing calibration is obtained. Without precise timing measurements, calibration of the four fundamental calibration elements, and their related parameters, is difficult. With proper information, the inter-relationships of calibration are isolated, and accurate, precise values of  $\sigma^\circ$  and measurement location are obtained.

## 4.2 Implementation Overview

To better understand specific details of implementation and the limitations of CGS analysis for SeaWinds it is helpful at this point to overview the basic format of CGS data, types of information available, and major causes of variations and

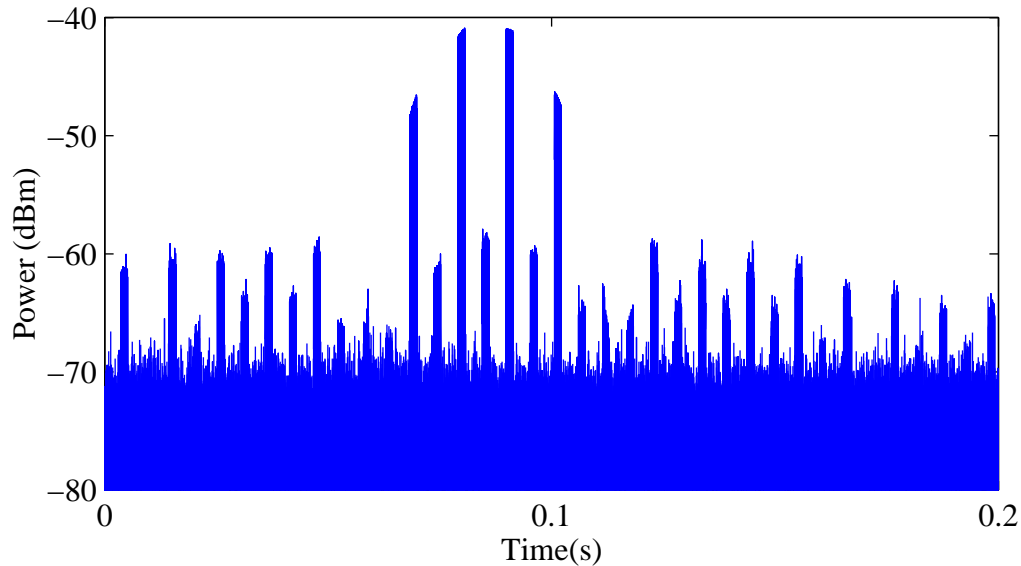


Figure 4.4: Received power of a sample 0.2 second CGS data capture. The figure shows the power recorded by the CGS as a function of time. The timing of the pulses appears steady while pulse power varies significantly. All calibration parameters are estimated from this data.

inaccuracies. The ground station is able to measure three types of properties for every pulse received: power, frequency, and timing. Combinations of these three properties allow estimates of parameters relating to the five fundamental elements to be made.

The first CGS data parameter evaluated is power. Figure 4.4 shows a 0.2 second sample CGS data capture, similar to Figure 2.6. The period, or pulse repetition increment (PRI), is 5.4 ms. Consistent power estimates are complicated by the variation of pulse power. The change in power from pulse to pulse is caused by two sources, controlled by the elements of position, power, and pointing. First, the instrument and its antenna are moving continuously. The ideal maximum CGS received power (near -40 dBm) occurs when the boresight (point of maximal antenna gain) of SeaWinds' antenna is pointing directly at the CGS and the CGS antenna boresight is pointing directly at the instrument. Any other pointing geometry results in less received power. While the CGS antenna is held stationary from pulse to

pulse, SeaWinds' antenna is moving. The gain variations shown in the figure are caused by rotation of the instrument antenna while pulses are being transmitted and during the time of CGS capture. The second source of pulse power variation is the alternating polarization between inner and outer beam, employed by SeaWinds. When the boresight of one beam is pointing near the CGS, the boresight of the other beam is not (see Figures 2.3 and 2.5) resulting in a significant reduction of power observed by the CGS for the opposing beam. This effect is seen in the Figure 4.4 by the alternating power levels. The constant change in power effects the observed CGS signal-to-noise ratio (SNR) of each pulse, defined as the average energy of each pulse divided by the average energy of the noise. While the noise power does not change over short periods of time, varying pulse powers cause the SNR of any given pulse to be different from other pulses.

CGS observed pulse frequency also varies from pulse to pulse. The movement of the instrument as it propagates in orbit induces a Doppler frequency shift on the signal which is complicated by SeaWinds compensation. The CGS observes a signal which is overcompensated in frequency and varies with each pulse. Minor timing variations also exist, caused by changes in satellite position.

Variations of CGS recorded power, frequency, and timing in each pulse caused by instrument movement obfuscate instrument uncertainties which are in the interest of calibration. In general, the orbit of SeaWinds is semi-periodic, meaning it nominally repeats itself every four days - exactly it is non-repeating. From a CGS standpoint, the non-exact repeats mean that every data capture possesses a unique geometry. Assuming ergodicity of any given sample is unwarranted due to the irregular distribution of capture look angles. These temporal and geometrical variations add significant complexity and uncertainty to instrument parameter estimation and warrant empirical parameter estimates. They also limit *a priori* knowledge of individual CGS pulses and thus minimize choices of parameter estimation algorithms.

An additional issue relating to data variation is a limitation in timing estimation, termed pulse aliasing. The CGS's circular polarized antenna makes it impossible to differentiate inner and outer beam pulses using only power information.

The satellite's ephemeris allows the CGS to determine which beam is being captured with limited time accuracy. In the case of Figure 4.4 the outer beam is primary and its pulses are received with significantly more power than inner beam pulses, allowing beam differentiation to occur. Ephemeris does not provide timing values accurate enough to align CGS data pulses with specific telemetry pulses. There exists, therefore, a like-beam aliasing of 2 PRI (10.8 ms) that is only resolved with model simulations. Blind estimation techniques are thus limited to individual pulse analysis. While the CGS provides excellent estimates of power, frequency, and timing, relating these values to instrument operation requires an accounting for these variations, discussed as individual calibration algorithms are presented in Section 5.3.

### 4.3 Observation and Identification

After the broad introduction to issues related to CGS data variation and parameter limitations, the final step of the calibration approach is to determine how the five calibration elements are observed by the CGS and whether they can be uniquely identified and estimated.

The instrument waveform received by the SeaWinds CGS is modeled as

$$\xi_r(t) = \Re \left\{ \left( \frac{\sqrt{E_t} G(t) \lambda}{L(4\pi)^{3/4} r(t)} \right) e^{j([\omega_c + \omega_{dc} + \omega_d + \frac{1}{2}\mu(t-r(t)/c)](t-r(t)/c) + \phi + \omega_c r(t)/c} + n(t) \right\} \quad (4.4)$$

where  $E_t$  is the transmitted energy,  $G(t)$  is the gain of the instrument,  $\lambda$  is the wavelength,  $L$  encompasses losses such as atmospheric attenuation (assumed to be constant for a single pulse), and  $r(t)$  is the range between instrument and ground station. The carrier frequency is  $\omega_c$ , the chirp rate is  $\mu$  and the phase is  $\phi$ . As mentioned, the frequency varies as a function of the observed Doppler shift,  $\omega_d$ , and the SeaWinds pre-compensated shift,  $\omega_{dc}$ . The speed of light is  $c$  and  $n(t)$  is additive noise. While the signal itself is real ( $\Re$ ), complex numbers are used for convenience.

The first calibration element, power, consists of transmitted and received power and internal instrument gains. Ideally, the transmitted power,  $E_t$ , is constant over every pulse. Internal gains or losses are not able to be identified uniquely by the CGS but are observed through the net transmitted energy,  $E_t$ , in the CGS receive equation.

Observation of transmitted power is simple, without it there are no received pulses. Identification is more difficult. Calibration of individual terms related to power in (4.4),  $E_t$ ,  $G(t)$ ,  $L$ , and  $r(t)$ , is impossible in a blind situation since individual values are not separable. The major cause of variation in CGS recorded power is non-boresight pointing, caused by the angle between instrument and CGS not equating to the boresight of the antenna for every pulse. Without knowledge of capture geometry, non-boresight adjustments are not accurately possible and power estimates contain significant biases in the blind analysis.

Incorporation of instrument telemetry data improves power estimates by accounting for pointing losses due to range and gain. Wavelength is assumed constant since Doppler induced changes cause less than 0.001 dB of variation. Loss terms are also assumed constant since variations are on the order of a few hundredths of a dB. While it is necessary to know the approximate value of the instrument range, errors of 1 km (which is large) effect the final estimate by 0.003 dB. These terms contrast with the large variability of the antenna gain term, which varies by as much as 40 dB over the span of the antenna, and even 10 dB from pulse to pulse as seen in Figure 4.4. Thus, transmitted power is observable and identifiable, but is dependent upon an accurate estimate of the antenna gain in the direction of the CGS.

The second element of instrument operation is frequency, consisting of six terms,  $\omega_c$ ,  $\omega_d$ ,  $\omega_{dc}$ ,  $\mu$ ,  $\phi$ , and  $\omega_c r/c$ . The frequency portion of the received signal in (4.4) is modeled as a quadratic. The curvature portion consists of the chirp rate,  $\mu$ , which is observed and identified blindly since it does not change from pulse to pulse.

The slope term is a function of three values, the center frequency, the commanded Doppler shift, and the observed Doppler:  $\omega_{est} = \omega_c + \omega_{dc} + \omega_d$ . The center frequency is driven by the instrument STALO (stable local oscillator) which is quite stable. The instrument reports values for commanded Doppler shift, while the observed Doppler is calculated using instrument position and velocity. Each parameter is estimated using frequency measurements from the CGS,  $\omega_{est}$ , and knowledge of the other two parameters.

Errors in these three frequency terms are not easily identified due to their linear relationship - on a pulse-by-pulse (blind) basis they are unidentifiable. Combinations of multiple pulses over multiple time scales allow some estimate of their value to be made. Center frequency is estimated by averaging large numbers of pulses. The received Doppler frequency is analyzed for changes caused by spacecraft position and velocity variations and the calculated Doppler is compared to changes in azimuth angle and orbit position, the terms used to calculate its value.

Since each of these terms are developed independently they are theoretically separable and thus identifiable. In reality, residual errors are expected due to the relative magnitude of the terms. The received and calculated Doppler are on the order of kilohertz, the center frequency has a gigahertz magnitude. Even small errors in the carrier are significantly larger than Doppler related values.

Finally, the phase portion of the frequency element is defined by the terms  $\phi + \omega_c r/c$ . SeaWinds uses a quadrature phase shift keying (QPSK) scheme in which it varies the transmitted phase every pulse between one of four possible values. This is combined with the phase of the Doppler compensation algorithm to define the transmitted phase,  $\phi$ . The phase shift caused by propagation,  $\omega_c r/c$ , varies as the range from instrument to CGS changes. The difficulty with estimating phase comes from the propagation phase shift. In order to estimate the phase to within  $\pi/2$  radians, the accuracy necessary to account for QPSK phase shifting, the known range value needs to be within 6 millimeters, a prohibitive value considering that the position of the instrument is specified accurate to within 150 meters and relative changes in position from pulse to pulse are on the order of 40 meters. The lack of sensitivity at the CGS to phase allows for the conclusion that while phase is clearly observed its sources are not identifiable.

The third element of instrument operation is satellite position, observed through several of the terms in the received signal (4.4) including range, gain, observed Doppler and time. For range and time, the exact position is not observed, only



the distance between spacecraft and ground station. Gain and Doppler are dependent upon actual coordinates, as they require relative velocity and the angle between instrument and ground station.

Exact errors in position are not uniquely identified using the gain term in (4.4) since gain is not invertible - a single gain term maps to many different pointing angles. Doppler is also not one-to-one invertible since it is a function of the dot product between the velocity vector and the CGS pointing vector. A combination of pulses with variable instrument gain possesses the possibility of a position estimate, providing that the group of pulses is properly referenced to the gain of the antenna. While possible, the probability is small because it requires the pointing of the instrument to be exact, an unlikely prospect. Since gain and Doppler are the only terms in the CGS received signal which use exact pointing, it is concluded that satellite position is not uniquely identifiable unless instrument pointing is ideal.

While exact position can not be determined, relative errors in position are theoretically identifiable. Range of the instrument to the ground station effects range spreading and time delay values. Range spreading is an insensitive metric, kilometer errors have an effect of less than 0.01 dB. Timing is slightly more sensitive. Given the transmit,  $t_{tx}$ , and arrival times,  $t_{arr}$ , of a given pulse, range is determined using

$$t_{arr} = t_{tx} + r/c. \quad (4.5)$$

SeaWinds CGS timing is accurate to  $0.2 \mu\text{s}$  which translates to a range accuracy of 60 meters provided that pulse transmission times are accurate.

The fourth element is pointing, observed only through the gain term - the gain of the instrument in the direction of the CGS. It is only identifiable through variations of gain from pulse to pulse using the simulation model. Instrument pointing is described by the spherical angles  $\theta$  and  $\phi$  where  $\theta$  is the azimuth angle relative to the velocity vector of the spacecraft and  $\phi$  is the elevation angle from the geocentric nadir vector. The  $(\theta_t, \phi_t)$  couplet describes the angle between the instrument and a target (in this case the ground station) in an instrument geocentric coordinate system. It is a function of the target location, and the position and velocity of the spacecraft.

The gain in the direction of the target is determined by finding the difference between  $(\theta_t, \phi_t)$  and  $(\theta_a, \phi_a)$ , the boresight pointing of the instrument antenna. For SeaWinds,  $\phi_a$  is fixed for each beam,  $\theta_a$  varies as the antenna rotates.

To determine the difference between the target angle and antenna boresight angle several coordinate transformations must be made. QuikSCAT attitude is reported geodetically (referenced to a nadir vector normal to the Earth's surface), while SeaWinds attitude is reported geocentrically (referenced to the center of mass of the Earth). Once coordinates are made consistent an evaluation of attitude induced gain variation is possible.

The fifth and final element is timing. Timing refers to pulse timing characteristics such as pulse length and pulse period, as well as absolute time values such as the transmission and arrival time of pulses. Duration parameters are estimated blindly, transmission times require incorporation of the simulation model. Timing is a necessary element so that pulses received at the CGS are aligned with those transmitted by the instrument (pulse aliasing) and so that instrument operation is coordinated. Timing errors are observed when pulse arrival times do not match up with estimates of pulse transmission time and range. The combination of multiple pulses allows for identification of both range and transmission time errors since the range change from pulse to pulse is non-linear.

To this point many parameters of operation are identified by the CGS and many more are observed. With the exception of instrument position, parameters from each element are identifiable. A list of these parameters includes: transmitted power (excluding internal gains and losses), range between spacecraft and CGS, carrier frequency, compensated Doppler frequency, observed Doppler frequency, instrument chirp rate, instrument attitude, pulse width, pulse duration, pulse arrival time and pulse transmission time. Several other parameters are observed but are not identifiable and therefore not able to be calibrated using the CGS. The remaining steps in SeaWinds CGS calibration are to validate the simulation model and develop algorithms for parameter estimation.

#### 4.4 Summary

The approach and implementation is the transition between high-level ideas and algorithm development. Implementation details such as parameter separation, observation, and identification are critical to properly selecting and applying data analysis algorithms. The conclusions drawn in this section concerning the estimability of individual parameters serve as guidelines for obtaining their values. Observability and identifiability issues also highlight critical details relating to sensitivity and considered in Chapter 5.



## Chapter 5

### Results from the SeaWinds Calibration Ground Station

This chapter presents the algorithms and results of SeaWinds calibration using the CGS. The algorithms developed are based on the ideals of the methodology, the details of the implementation, and the theory of estimation. Incorporated in the estimates are assessments of parameter sensitivity. In many cases estimated parameters are directly related to instrument operation and thus sensitivity is limited only by CGS accuracy. In other cases, where estimates are poor, sensitivity issues are covered in more depth to gain understanding.

The chapter is separated into four sections. The first section discusses implementation of the simulation model. It considers parameter estimation using a Kalman filter, citing reasons why this type of model is not appropriate for the CGS data analysis. It then describes the model that is developed for SeaWinds CGS calibration. The second section describes the telemetry used by the model and how telemetry effects model performance. The third section presents the results of blind parameter estimation, where telemetry and other information about the instrument's current state of observation is omitted. The objective of this step is to establish a calibration foundation without introducing the added uncertainty of the model and instrument telemetry - analysis is based on individual pulses. The final section of the chapter is model-based, comprehensive estimation. While the blind analysis is a simple approach, it lacks the sophistication required to estimate all parameters which are identifiable through CGS data. The objective of this fourth step is to obtain estimates for parameters which can not be accurately estimated blindly. Analysis is geared toward combining multiple pulses, sweeps, and captures.

## 5.1 Model Development

Ideally a model which is optimal for some metric, such as least-squares, is the desired approach to estimate calibration parameters. Such a model is a Kalman filter. The filter is a recursive estimator which estimates a state-vector,  $\mathbf{x}_t$ , of calibration parameters at some time  $t$ . The filter is defined using two linear equations

$$\mathbf{x}_{t+1} = A_t \mathbf{x}_t + \mathbf{w}_t, \quad (5.1)$$

$$\mathbf{y}_t = C_t \mathbf{x}_t + \mathbf{v}_t, \quad (5.2)$$

where  $\mathbf{y}_t$  is a vector of observations,  $\mathbf{w}_t$  is a state noise process, or the uncertainty in the state, and  $\mathbf{v}_t$  is observation noise. As related to the CGS,  $\mathbf{x}_t$  is a vector containing each desired calibration parameter and  $\mathbf{y}_t$  contains observed CGS values. A conventional Kalman filter requires the system to be linear. In other words, both  $\mathbf{w}_t$  and  $\mathbf{v}_t$  must be stationary and Gaussian, and  $A_t$  and  $C_t$  must be linear. Unfortunately the signal received by the CGS, modeled by (4.4), which is directly related to (5.2) in the filter, is non-linear in time and frequency due to the squaring of the exponent. This non-linearity disqualifies use of the Kalman filter for CGS calibration. A possible alternative is an extended Kalman filter which is able, in many cases, to linearly approximate non-linear systems. To do this the extended Kalman filter requires accurate initial state estimates, good numerical conditioning of state matrices, and the ability to calculate the Jacobian of  $A_t$ . Unfortunately, the extended Kalman filter is also not a viable alternative for SeaWinds CGS calibration. The marginal precision of telemetry data limits the accuracy of initial state estimates. Also, several of the terms in  $\mathbf{y}_t$  such as power are quite sensitive to minor perturbations of  $\mathbf{x}_t$ , and linearization of many of the terms in  $A_t$  is imprecise due to the relatively coarse sampling of the transmit antenna pattern during instrument pulsing.

Despite these limitations an experimental, limited capability extended Kalman filter was developed by Arden Anderson to estimate the orbit, position, and velocity of SeaWinds [5]. Performance was nominal at best. The model was hampered by the limited amount of information provided by instrument telemetry, particularly the lack of acceleration vectors. The filter also suffered from a lack of precise timing

information, causing state observation updates to occur at sporadic intervals. Implementation of the filter beyond position and velocity is further limited by the rotation of the instrument antenna, which causes non-unique geometries for CGS captures, as every rotation presents a similar capture solution.

These limitations result in the development of an alternate estimation technique. The parameter separation approach described in Chapter 4 suggests that many calibration parameters are directly estimable. This concept gives further support to the idea of a two-phased analysis where all parameters which can be estimated blindly are first calibrated, followed by use of the simulation model to estimate other parameters of interest. While not always optimal in a statistical sense, the simulation model developed uses concepts similar to the Kalman filter, providing a model of the data in the observation space (the CGS) and then using parameter estimates to recursively converge on instrument calibration.

The simulation model is designed to accurately translate telemetry data to CGS observable values and to provide a tool for inversion of simulation parameters using CGS data. The interrelationships and non-linearities which exist between the five calibration elements described make direct inversion impossible. This motivates an iterative inverse implementation. Differences between simulation and CGS data are reconciled through perturbation of telemetry parameters. The model inputs which provide the best match between data observations and simulation represents the model estimate of calibration. Recognition of observable and identifiable parameters within the CGS received waveform focus efforts on those which are most likely to require calibration and most likely to cause differences between simulation and actual data.

## 5.2 Telemetry Analysis

Comprehensive evaluation of CGS identifiable parameters using the model requires an understanding of instrument operation during the time CGS data capture occurs. This is available through telemetry. Telemetry data is the instrument's own account of its operation, it reflects how the instrument believes it is operating. If

the telemetry is accurate, simulated data coincides precisely with CGS and other calibration measurements. If not, either telemetry or calibration measurements are in error. Since calibration methods, such as CGS calibration, are designed to minimize internal error, differences between calibration results and telemetry reported values are typically attributed to inaccurate telemetry.

The simulation model strives to simulate the CGS receive waveform without introducing any more uncertainty than is present in instrument telemetry. Telemetry is limited in precision, simulations are thereby limited by this factor. For this reason the accuracy and reliability of instrument telemetry must be evaluated. The focus of this section is to assess the accuracy and consistency of telemetry data as it relates to the five calibration elements in an attempt to mitigate errors in telemetry reporting and focus on existing errors in instrument operation.

SeaWinds telemetry is reported in data files, organized by orbit number, termed revs (short for revolutions) which correspond to one complete orbit from south pole to south pole. The number of frames in each rev is variable, usually 11,250, where a frame consists of exactly 100 transmitted pulses. Most telemetry values are reported once per frame, though some are reported on a per pulse basis. Values are reported for transmitted power, instrument position and velocity, Doppler compensated frequency, attitude, and pulse timing. Spacecraft pointing, observed Doppler shift, antenna gain, and CGS range are calculated using reported values. Parameters such as position and velocity, which are reported only once per frame, require interpolation for pulse based calculations, introducing some error. Additionally, some values, such as timing, are reported after a series of transformations and variable delays within the instrument, further degrading their accuracy.

SeaWinds telemetry reports two relevant power signals, the transmitted power of each beam, once per frame. Values are nominally 49.5 dBm. They are discretized in steps of 0.05 dB and have a standard deviation of 0.025 dB. The model uses the power values reported in telemetry for each pulse in the frame.

The fundamental carrier frequency of SeaWinds is specified as constant, 13.402 GHz, and is not reported in telemetry. The Doppler shift observed at the CGS



is calculated by the model since it is unreported. The pre-compensated Doppler shift is determined using a series of onboard algorithms and lookup tables. It is calculated using

$$\omega_{dc}(\tau, \alpha) = C(\tau) + A(\tau)\cos\left(\frac{2\pi}{N}(\alpha + \delta) + P(\tau)\right) \quad (5.3)$$

where  $\alpha$  is the azimuth angle of the antenna and  $\tau$  is the orbit step of the instrument. Note, that parameter values are discretized. The orbit step is a counter which separates the orbit into 256 steps. The values of  $C$ ,  $A$ , and  $P$  represent the bias, amplitude, and phase of the Doppler compensation and are stored as lookup tables on the instrument, referenced by orbit step.  $N$  is the number of discrete azimuth steps possible for  $\alpha$ , 32768 ( $2^{15}$ ), and  $\delta$  is an azimuth angle correction term which accounts for azimuth angle change between calculation and actual transmission time. Telemetry reports azimuth angle and orbit step, allowing Doppler compensation to be calculated. Azimuth angle is reported every pulse to the nearest integer step. The precision of these steps is  $0.011^\circ$ . Analysis of telemetry data shows that the mean difference from pulse to pulse is 53 steps, corresponding to  $0.582^\circ$  per pulse. The standard deviation is much less than 1 step.

SeaWinds reports position values as determined through GPS once per frame. Position is specified accurate to within 150 meters. Figure 5.1 shows a plot of spacecraft position as a function of frame for one rev. Each of the three coordinates,  $\hat{x}$ ,  $\hat{y}$ , and  $\hat{z}$ , resemble sinusoids. The coordinate frame is Earth Centered Earth Rotating, defined with the origin at the Earth's center of mass, with  $\hat{x}$  passing through the equator and prime meridian,  $\hat{z}$  passing through the north pole, and  $\hat{y}$  establishing an orthogonal, right handed coordinate system. While the overall sinusoid curves appear smooth, closer inspection of the reported values shows a fair amount of variance in the measurements, as shown in Figure 5.2. Since the model needs position measurements every pulse rather than every frame, position values are interpolated.

Interpolation using only a few reported values proves to be inadequate for accurate position since the small variations in reported position introduce significant errors in the interpolated sample set. The CGS is in a fixed location and the point of occurrence where the spacecraft passes the CGS occurs approximately within the

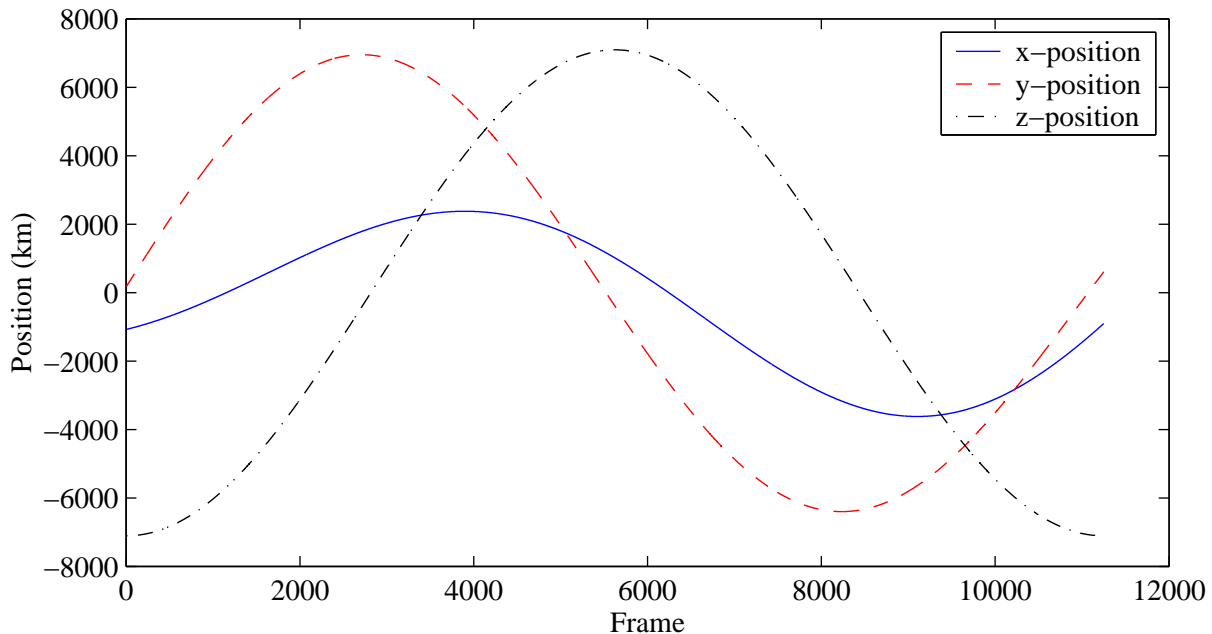


Figure 5.1: Reported spacecraft position as a function of frame for one rev.

same set of frames for each orbit, nominally 3700-4300 for ascending passes and 6700-7300 for descending passes. This allows for interpolation of a large number of frames without without having to model the entire sinusoid of each orbit coordinate reference. Over a 1000 frame period, the position coordinates are estimated using a fourth order polynomial. The improvement of this estimate over actual telemetry data is on the order of 3 meters and is instrumental in improving instrument pointing.

The fourth element is pointing. Telemetry references pointing parameters using four values: roll, pitch, yaw, and antenna azimuth. Attitude values are reported once per frame and antenna azimuth is reported each pulse. Attitude typically is reported as zero, though some deviations do occur, usually in the range of  $0.005^\circ$  for QuikSCAT. ADEOS II values are larger. The model assumes that the attitude of each pulse is equal to the reported frame value.

The fifth and final element is timing. Timetag values are reported once every frame. Ideally, timetags match their original source, GPS, which is known to be accurate to within nanoseconds [24]. However, reported timetags are derived

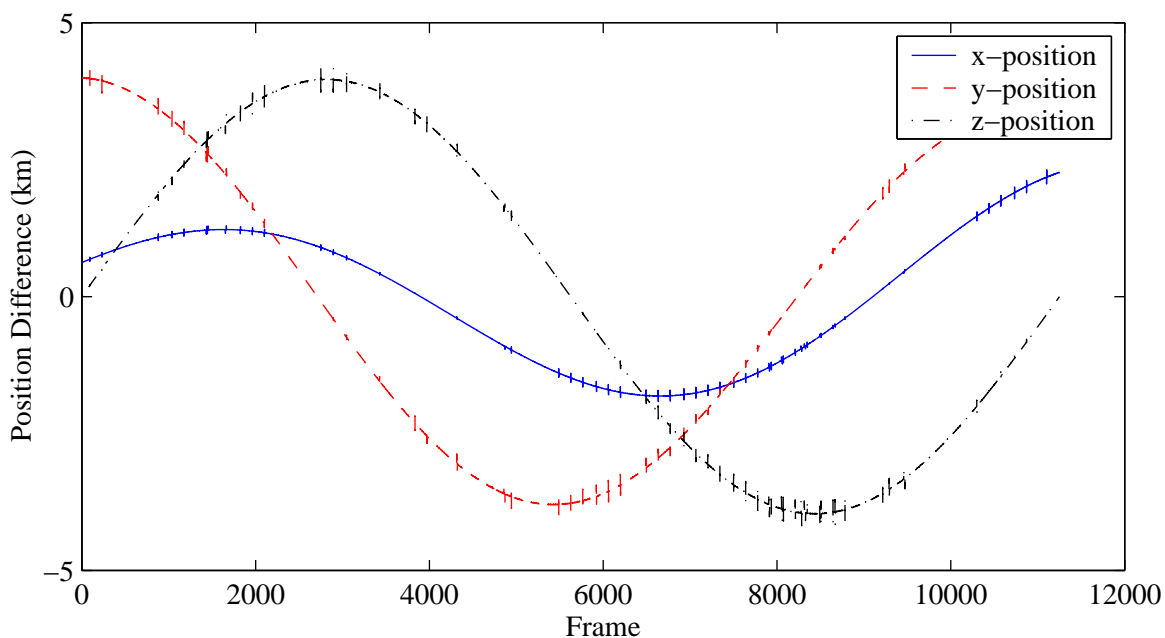


Figure 5.2: Change in spacecraft position as a function of frame for one rev.

from GPS using a series of steps which introduce delays and quantization errors. For QuikSCAT, the spacecraft clock is termed VTCW, for vehicle time code word. Once per second, the spacecraft receives the time from the onboard GPS receiver and records the corresponding VTCW. The SeaWinds instrument receives a VTCW reading once per second and records the corresponding time from its instrument clock, though not necessarily at the same time. The instrument clock's resolution is 512 counts per second, or about 2 milliseconds. Therefore, calculation of the reported frame time requires correlation of instrument time, VTCW time, and GPS time. An accurate estimate of the final frame time value is difficult to obtain due to variable internal delays which occur as the time signals are aligned. The delay time should be a stable value, though the actual delay is unknown and has some variability [44].

To assess the accuracy of timetags several of their properties are explored. Frame time values are reported once per frame to the nearest millisecond. Since one frame is exactly 100 pulses, the differences between frames should be 100 PRI (pulse repetition increment). Figure 5.3 shows the difference in frame time for a selected

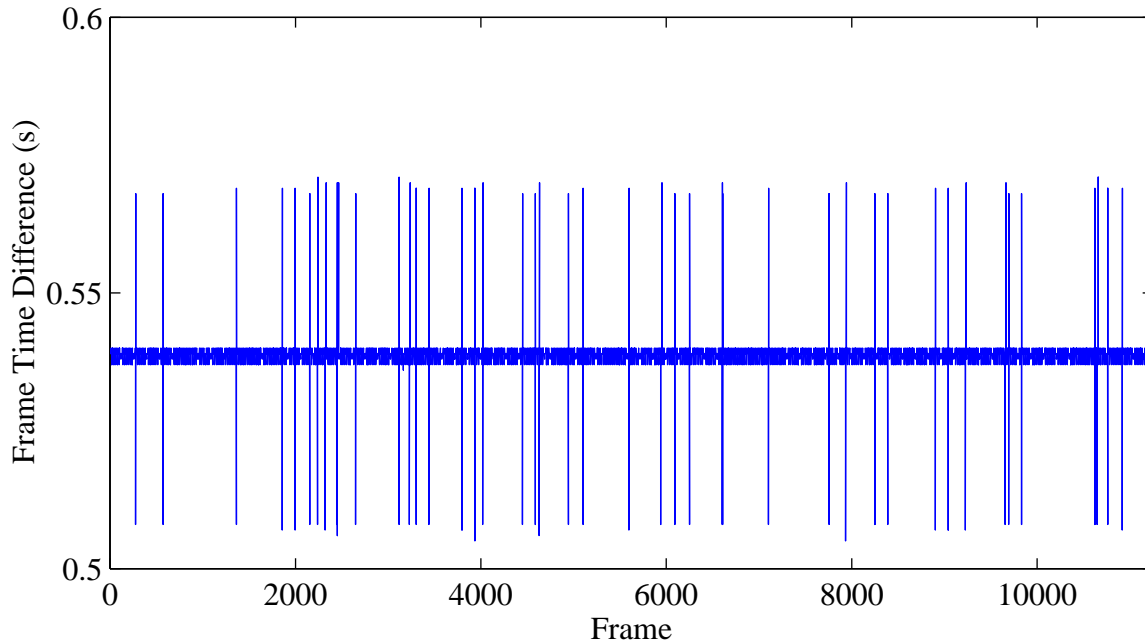


Figure 5.3: Difference of frame timetags as a function of frame.

SeaWinds rev. It shows that there exists some variation in the reported time of frames. The standard deviation of the data in the plot is 4.8 milliseconds, much larger than the deviation of the actual PRI, suggesting that the majority of the error is in the telemetry reporting. Timetag precision is improved through interpolation. Citing the stability of the instrument PRI, a linear estimate of timetag values is chosen with a variance equal to PRI the estimate variance. The suitability of this method is supported by Figure 5.4. The figure shows data compiled over 200 revs. The bumpy (larger variance) line is the mean difference of the timetags for each rev. The lower variance line shows the fitted slope for each rev. The mean of the two curves differs by only two nanoseconds, but the deviation of the fitted timetags is an order of magnitude better than the reported timetag difference and corresponds well with PRI estimates. The figure also demonstrates that timetags vary in consistency from rev to rev. While a few nanoseconds is instantaneously insignificant, differences accumulate quickly and have a significant negative effect on overall calibration.

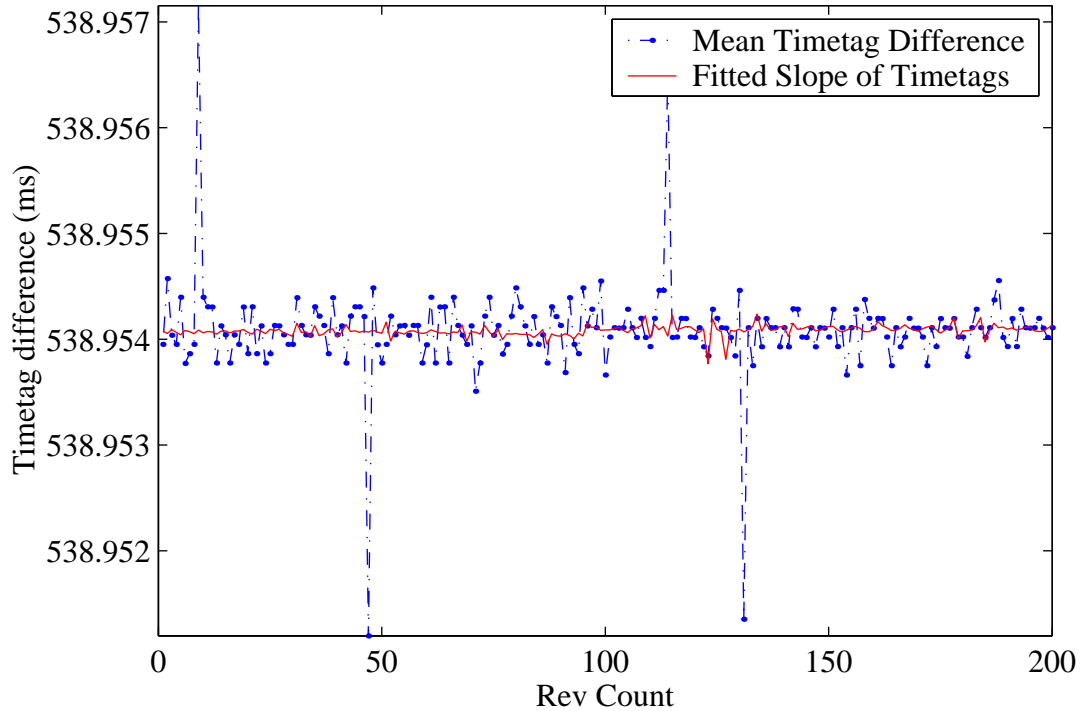


Figure 5.4: Timetag improvement through interpolation. The figure shows the mean timetag difference for 200 selected revs. It also shows the slope of a line fitted to the timetags for each rev. The variance of the line fit slopes is an order of magnitude better than the variance of the mean timetag differences.

By linearly fitting timetags, variation is minimized, though actual error is dependent upon stability of the PRI clock. The magnitude of this parameter is critical and must be one of the first extended calibration analyses performed in order to accurately estimate other parameters. The linear fit does not, however, remove any biases from the timetags. Internal delays and other biases are unidentifiable.

### 5.3 Blind Calibration

The remaining portion of the CGS methodology is application of the calibration approach and implementation, observing described limitations to develop algorithms which isolate desired parameters and estimate their value.

A prerequisite to data analysis is an assessment of the calibration and stability of the CGS itself. This analysis is found in Appendix A.1. It shows that

CGS timing values are accurate to within  $0.193 \mu\text{s}$ , which is the effective sampling rate of the A/D converter, that frequency values are accurate to 1 part in  $10^{12}$  (less than 1 Hz error for a 13 GHz signal) due to GPS disciplined phase locked loop oscillators, and that power values are accurate to within 0.15 dB using internal noise source calibration. The results also show that while timing and frequency values remain stable over time, noise power drops 1.7 dB from the beginning of the QuikSCAT mission to current time periods. This is due to decay of the ground station amplifiers and cabling over its four year life span. Commensurate drops in measured power are accounted for.

Blind calibration consists of estimating parameters which do not require outside information such as telemetry and is based only on CGS data. These prerequisites lend themselves well to maximum-likelihood-based estimates. For each parameter it designates a likelihood function based on observations and an estimate of a parameter value is chosen which maximizes this function. Mathematically, given a set of  $m$  observations,  $x_1, \dots, x_m$ , the likelihood function is

$$l(\theta, x_1, \dots, x_m) = \prod_{i=1}^m p_X(x_i|\theta) \quad (5.4)$$

where  $\theta$  is the parameter being estimated and  $p_X$  is the distribution of  $x_i$  given  $\theta$  [37]. For blind calibration a distribution for each  $x_i$ ,  $p_X(x_i|\theta)$ ,  $\mathbf{x} = [x_1, \dots, x_m]$ , must be assumed. Since no knowledge about the behavior of most parameters such as pulse timing and power is available *a priori* a Gaussian assumption is made. From this assumption it can be shown that the maximum likelihood estimate is the average of all of the observations,  $x_i$ , and the variance of the estimate is  $\frac{m-1}{m}\sigma_x^2$ , where  $\sigma_x^2$  is the variance of the observations. This approach is used to obtain estimates for timing and frequency. For power-related parameters information is available which allows for the selection of a more appropriate distribution. This section presents the algorithms used to estimate these parameters. Complete results of blind calibration are located in Appendix A.2.

## Timing

The first parameter considered is pulse timing. Timing consists of determining when pulses arrive at the CGS, how long they last, and how frequently they occur. Of these parameters, the pulse repetition interval, or PRI, is the most critical because it is generated from SeaWinds' stable local oscillator which is also used to generate the carrier frequency of the transmitted signal.

Timing estimation is optimally accomplished using a matched filter, which is a maximum likelihood estimator that attains the Cramer-Rao bound [42]. However, instrument movement and Doppler pre-compensation preclude this method from consideration in blind analysis since telemetry must be used to determine frequency compensation. Given described limitations, a simple rectangular filter for the pulse amplitude is chosen to obtain pulse width observations. The result of filtering squared received data (shown in Figure 4.4) with a rectangular window is a triangle shaped waveform. If the selected filter length is shorter than the data pulse, the output waveform shows a lower maximum value than the optimal length filter and a flat top, resembling a trapezoid. If the selected filter is too long, the output's maximum value is equal to the ideal filter's maximum and also is flat. With noise added, the peak value of an overly long filter is slightly higher than the peak of the ideal window, as shown in Figure 5.5. To assist in noise mitigation a variation of the window filter, a split gate filter, is used. This variation is defined by a rectangular window followed by a negative amplitude window, the negative portion acting as a subtracter, eliminating noise induced biasing [42].

Though this simplified method of windowing the data does not converge to the Cramer-Rao bound, optimal precision of the estimate is not necessary in this case. While pulse width calibration is necessary as a stand alone parameter, pulse width does not effect other SeaWinds systems. The width of generated pulses is controlled by SeaWinds' main STALO, which also generates the PRI and carrier frequency. As will be shown, more precise estimates for carrier and PRI are available from the CGS thus validating pulse width calibration.

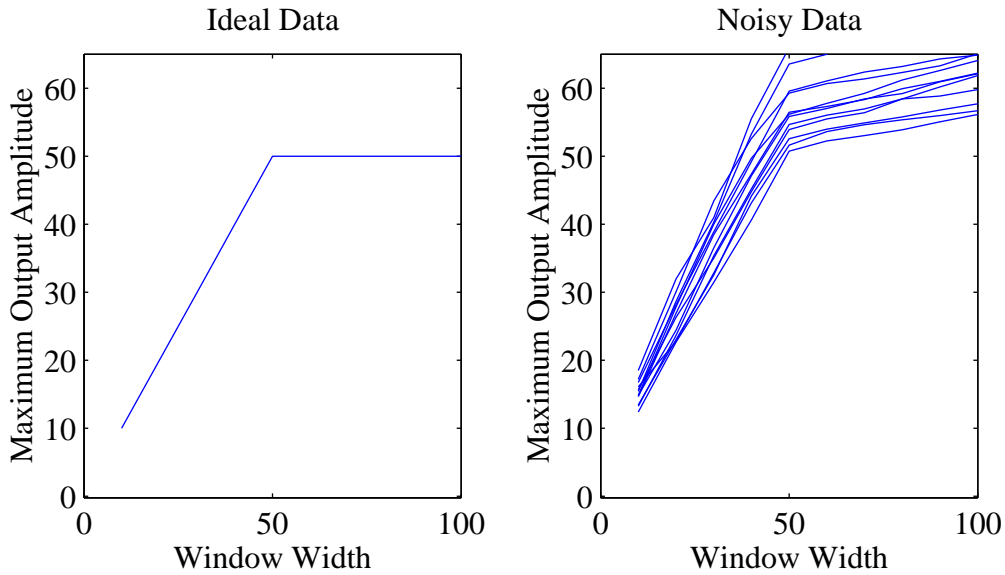


Figure 5.5: Maximum output value of a rectangular window filter of varying width using a simulated pulse 50 samples in duration. The left plot shows the noise free case, the right plot shows several Monte Carlo simulations which include noise (10 dB signal-to-noise ratio). The estimated width of the pulse is identified by the corner of the output curve.

Figure 5.6 illustrates the effectiveness of the split gate method in estimating the pulse widths in the presence of varying levels of noise. An ideal pulse is constructed, having a width of 1.5 ms (7755 samples) and is subjected to various levels of noise. The noisy pulse is filtered with various lengths of split gate filters for each SNR case. The maximum output of the filter is shown as a function of the width of the filter. The figure shows that for high signal-to-noise ratio (SNR) pulses ( $> 10$  dB SNR), the algorithm is efficient and the corner is differentiated, while at lower SNR the output corner is obfuscated by noise. Since the pulse width is expected to be stable from pulse to pulse, only high SNR pulses are selected to improve the variance of the estimate. Results of CGS timing estimates are shown in Appendix A.2.

The time that a pulse begins according to CGS data is termed its arrival time and is the second step in timing estimation. Arrival time information is used to estimate the PRI of the instrument and also plays a significant role in extended CGS



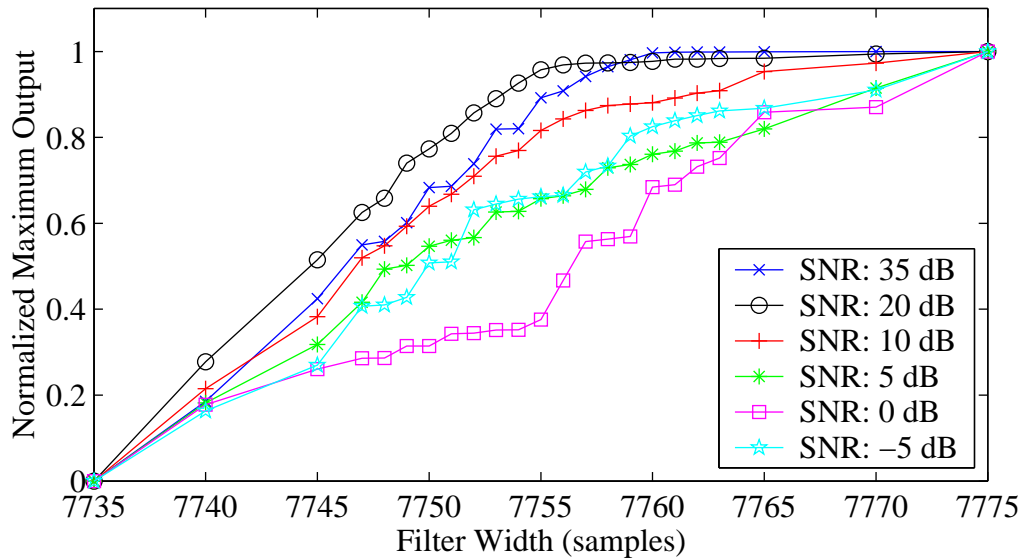


Figure 5.6: Simulation of the pulse width algorithm for various signal-to-noise ratios (SNR). The actual pulse width is located at the 'corner' of each pulse, in this case sample 7755. The figure shows that high SNR pulses exhibit cornering characteristics, while low SNR pulses show no indication of pulse termination.

calibration. Similar to pulse width estimation, pulse arrival time is observed using a rectangular window filter with the squared data stream. The result from the filter is a triangle waveform with a peak value at the moment the trailing edge of the pulse is recorded, as shown in Figure 5.7.

To estimate the accuracy of the arrival time algorithm, pulses similar to those transmitted by SeaWinds are generated using various levels of additive Gaussian noise (1.5 ms in duration, -20 to 40 dB SNR, 5.1875 MHz sample rate). The pulses are filtered with a rectangular window filter, having a duration specified by the pulse width. The time corresponding to the peak filter output is compared to the edge of the simulated pulse, differences correspond to arrival time error. Figure 5.8 shows the results of the simulation. The simulation shows that arrival time accuracy is dependent upon SNR, but not as dependent upon pulse width estimates. Results of this simulation are also used to assess the accuracy of PRI estimation algorithms,

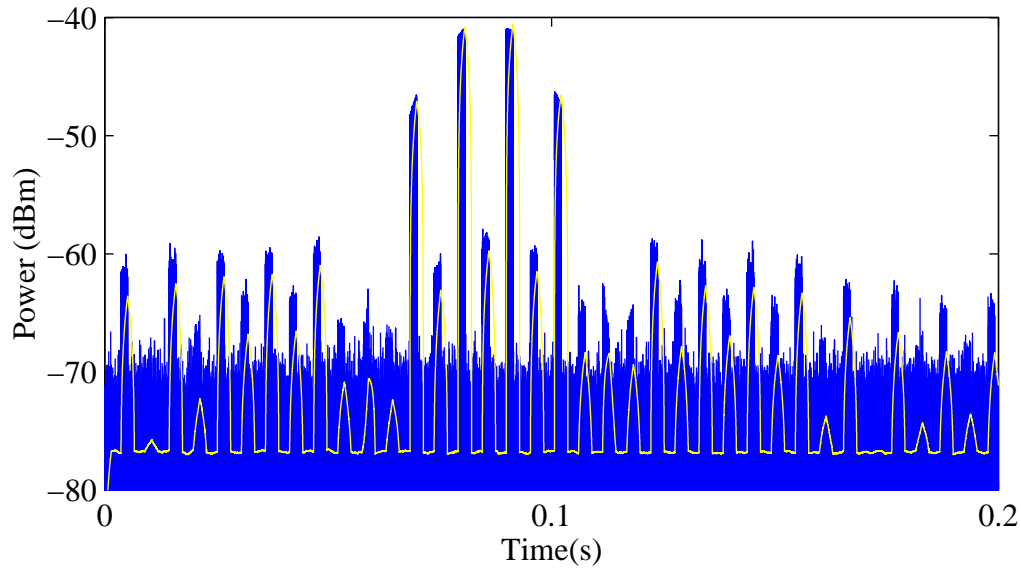


Figure 5.7: Sample CGS data set with overlaid arrival time filter output. The peak of each triangle corresponds to the end of a given pulse.

which depend on arrival time estimates. Precise values for PRI estimates are evidence of arrival time accuracy.

The last portion of timing calibration is estimation of the pulse repetition increment, or PRI. Once pulse arrival times are estimated the PRI is observed by subtracting the arrival times of two pulses. The accuracy of the observations is limited by the accuracy of the pulse arrival times and hence SNR. Like pulse width, the PRI is generally stable and estimates are not required for each pulse. This allows for minimization of the effects of SNR, decreasing the variance of PRI estimates. This process is implemented by first, only choosing pulses with high SNR. Normally consecutive CGS pulses have one pulse that is significantly lower in power than the other due to the alternating inner beam - outer beam pulse configuration of SeaWinds (see Figure 5.7). In choosing high SNR pulses, pulses which are non-consecutive are selected and the time difference is divided by the number of pulses between the chosen two. This skipping is favorable because the variance of a maximum likelihood estimate using non-consecutive pulses decreases proportionally to the number of pulses between

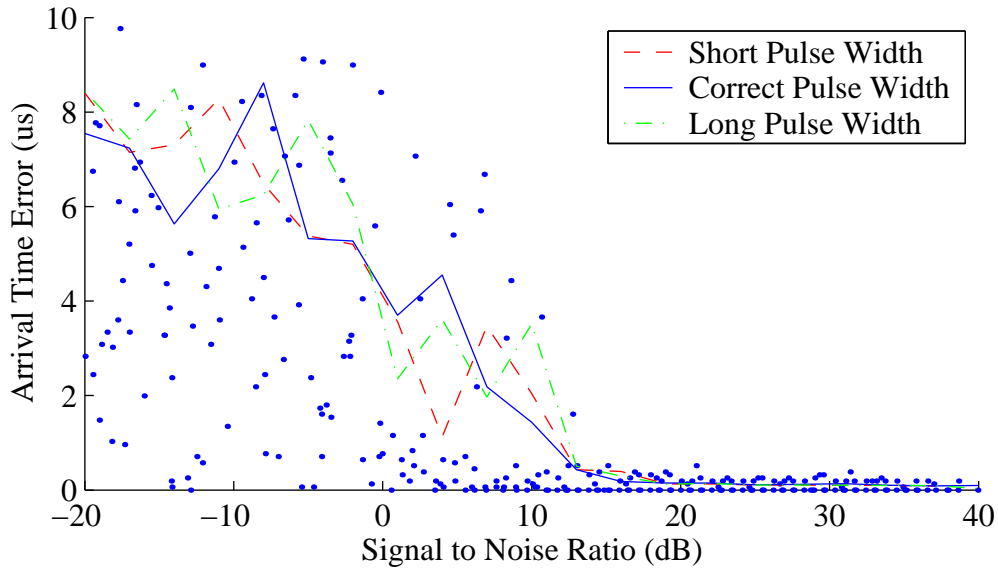


Figure 5.8: Pulse arrival time simulation results. Each data point represents the arrival error of a unique simulation using the correct pulse width. The solid line is the standard deviation of the error. The two dashed lines show the standard deviations of simulations using slightly shorter and slightly longer filtering windows. The figure shows that arrival estimates are sensitive to pulse SNR but insensitive to minor pulse width error.

the chosen two [18]. The maximum extent of this approach is limited only by the time stability of the CGS and the length of CGS captures. Generally, CGS captures have a duration of 10 seconds. During this time CGS A/D sampling is stable. Using pulses from different CGS captures introduces start and stop time uncertainties of the A/D. While these errors are not large, they are greater than desired precision. Using the length of a CGS capture as an upper bound, there are over 1800 pulses within 10 seconds, allowing a reduction of variance for a PRI estimate by three orders of magnitude over an estimate taken from consecutive pulses. Since CGS timing accuracy is within microseconds, PRI estimates with deviations of nanoseconds are expected.

Observations of pulse width and PRI are found in Appendix A.2.1. The data show excellent precision. They indicate that the estimated pulse width of both

QuikSCAT and SeaWinds is 1.494924 ms, with a standard deviation of 230 ns. They also show that the expected PRI of both instruments is 5.389527 ms, with a standard deviation of 32 ns. The accuracy and precision of these timing estimates vastly exceeds all previous calibration methods. The results not only highlight the viability of the ground station and associated algorithms, but also show that instrument movement and geometry do not preclude accurate estimates of some instrument timing parameters. The results do show the effects of instrument movement on timing, both in the pulse width estimates, and more significantly in the PRI values.

## Frequency

The second blind calibration category is frequency. A simplified form of (4.4) is

$$\xi_t(t) = \Re \{ A e^{j(\omega_c + \omega_{dc} + \omega_d + 1/2\mu t)t + \phi} \} \quad (5.5)$$

where  $A$  represents the signal amplitude, and all other terms are as previously defined. The objective of blind frequency calibration is estimation of SeaWinds' center frequency and the rate of the LFM chirp. Doppler related parameters can not be estimated without model simulation.

Several algorithms are capable of estimating desired frequency parameters exist. The one chosen for this analysis is a maximum likelihood estimate first proposed by Tretter and later expanded by Djuric and Kay [13, 52]. The algorithm is chosen because it estimates phase, frequency, and chirp rate coefficients simultaneously and because the estimate variance approaches the Cramer-Rao bound when the signal's signal-to-noise ratio is sufficient. While the SNR of every pulse varies, the vast majority of captures have several pulses with better than 0 dB SNR, many pulses exceed 20 dB SNR.

The Tretter algorithm states that the frequency of a quadratically phased sinusoid is estimated by unwrapping the phase of the sinusoid and fitting the phase to a quadratic polynomial. The coefficients of the quadratic are directly related to the frequency parameters of the signal. The phase of the CGS received signal is unwrapped by counting the zero crossings of the signal. CGS sampling provides

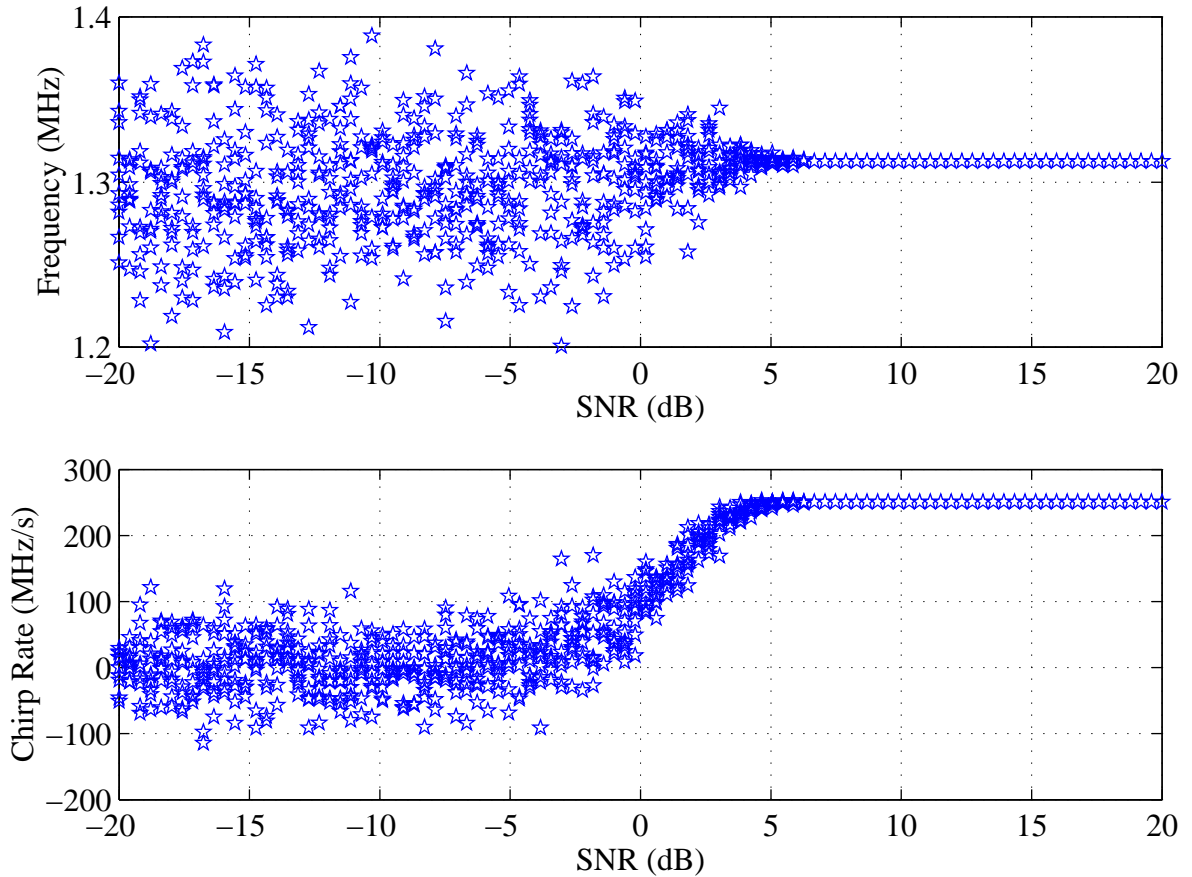


Figure 5.9: Results of a Monte Carlo frequency simulation for carrier and chirp rate. The top figure shows an independent estimate of CGS center frequency (1.3125 MHz) versus SNR, the bottom figure shows an estimate of the chirp rate (250.73 MHz/s). Both estimates converge to true values for SNR > 6 dB. The carrier estimate is unbiased while the chirp rate estimate tends to zero at low SNR.

nearly four samples per cycle, a density which is sufficient to eliminate aliasing phase unwrapping. Although noise present in the signal makes each zero cross estimate imprecise, the estimate of all pulse zero crossings, about 2000 per pulse, is unbiased and sufficiently accurate for the algorithm [13].

After the phase is unwrapped, the second step of the algorithm is to fit a quadratic curve, using least-squares, to the data. The effectiveness of this method is demonstrated through simulation. Figure 5.9 shows Monte Carlo results for estimates of center frequency and chirp rate. The simulated center frequency is 1.3125 MHz and

the simulated chirp rate is 250.73 MHz/s. The simulation shows that the results are poor for SNR below 6 dB and excellent for larger signal-to-noise ratios. The carrier estimate is unbiased, regardless of SNR, while the chirp rate estimate tends to zero, caused by a reduced change in the number of zero crossings as SNR degrades.

Actual frequency observations shown in Appendix A.2.2 closely resemble those of simulation. They show, like the simulations, that when pulses of high SNR are used, the variance of the center frequency and chirp rate estimates is minimal. The data show that the estimated carrier frequency for QuikSCAT using the White Sands location is 13.402017 GHz, for QuikSCAT in Provo it is 13.402013 GHz, and for SeaWinds it is 13.402005 GHz. The standard deviation of each estimate is 320 kHz. Chirp rate values are found to be 250.747 MHz/s for QuikSCAT at both locations and 250.743 MHz/s for SeaWinds. Recorded pre-launch values were 250.74 MHz/s for both instruments. The standard deviation of these measurements is 2.7 kHz/s. Like the timing results, these estimates display far more accuracy and precision than previously attained in scatterometer calibration, highlighting the accuracy and stability of the CGS in estimating instrument timing and frequency.

## Power

The final category of blind calibration is calculation of pulse energy, often referred to as pulse power. The main goal of the CGS in estimating pulse power is determination of how much energy is received by the CGS and if the levels correspond to what is expected based on SeaWinds' specifications. Further objectives include analysis of variations between captures, orbits, polarizations, and instruments.

Using the simplified pulse model of (5.5), power estimates focus on the amplitude,  $A$ , of each pulse, which is related to the total energy in the pulse. This is determined by integrating the squared amplitude of each pulse over its duration

$$E = \int_T |\xi_t(t)|^2 dt. \quad (5.6)$$

Comparison of power received by the CGS with power transmitted by SeaWinds requires selection of a common point of reference. The reference point

chosen here is power (per unit area) received at the CGS antenna, termed  $P^{rec}$ , and recorded in dBm (dB milliwatts). This reference is chosen mainly as a matter of convenience - it is an appropriate middle ground in the conversion process between SeaWinds' transmit power and CGS recorded voltage. It also separates CGS related terms from SeaWinds related terms in the conversion process. Power received at the CGS is determined for the digitized samples using

$$P_{cgs}^{rec} = \left( \frac{V_{ad}^2}{Z_{ad}} \right) Y_{cgs}, \quad (5.7)$$

where  $V_{ad}$  and  $Y_{cgs}$  are given by

$$V_{ad} = G_{ad}(O_{ad} + I_{ad}), \quad (5.8)$$

$$Y_{cgs} = 2 \left( \frac{4\pi}{\lambda^2} \right) \left( \frac{1}{G_{ant}G_{sys}} \right) \quad (5.9)$$

(see Table 5.1 for definitions). The  $Y_{cgs}$  term is computed using the effective area of the antenna, the directivity of the antenna, and the gain of the system. The factor of 2 accounts for the loss which a linearly polarized signal experiences using a circularly polarized antenna. This formulation is used to convert stored 12-bit digital A/D values to the desired power per unit area received at the CGS,  $P_{cgs}^{rec}$ , and is derived using the beacon equation [41, 55].

From SeaWinds' perspective, transmitted signals are converted to the common point of reference using

$$P_{sw}^{rec} = \frac{P_{gen}G_{bias}G_{pkant}}{4\pi R^2 L_{wg} L_{sas} L_{atm} L_{ant}} \quad (5.10)$$

where  $P_{gen}$  is the power transmitted to the antenna,  $G_{bias}$  is a gain bias term,  $G_{pkant}$  is the peak antenna gain,  $R$  is the range from instrument to CGS,  $L_{wg}$  is the waveguide loss aboard the instrument,  $L_{sas}$  is the SeaWinds Antenna Subsystem loss,  $L_{atm}$  is loss due to the atmosphere, and  $L_{ant}$  is loss due to non-boresight pointing of the antenna in the direction of the CGS. Values for these parameters are summarized in Table 5.2 for both QuikSCAT and SeaWinds. Using nominal values for range, and assuming boresight pointing ( $L_{ant} = 0$ ), the maximum calculated received power at the CGS for QuikSCAT is -43.01 dBm for the outer beam and -43.33 dBm for the

Table 5.1: Definition of terms for calculation of power received at the CGS, see Eq. 5.7.

| Parameter       | Description   | Value                | Variation             |
|-----------------|---|----------------------|-----------------------|
| $I_{ad}$        | Integer value stored by A/D converter   | -2048 to +2047       | $\pm 0.5$             |
| $O_{ad}$        | A/D offset used to correct bias   | -1                   | -                     |
| $G_{ad}$        | Conversion factor from A/D integer to received voltage  | 2/40950 V            | -                     |
| $V_{ad}$        | Voltage received at the A/D converter   | -0.1 V to 0.1 V      | $\pm 50 \mu\text{V}$  |
| $G_{sys}$       | Gain of the CGS RF subsystem. Includes amplifiers, mixers, cables, waveguides, and internal losses. | 56.24 dB             | $\pm 0.01$ dB         |
| $G_{ant}$       | Gain of CGS antenna   | 20.09 dB             | $\pm 0.05$ dB         |
| $\lambda$       | Wavelength of SeaWinds' pulses  | 2.239 cm             | -                     |
| $Y_{CGS}$       | Gain term used to simplify determination of $P_{cgs}^{rec}$   | 0.6794 dBm           | $\pm 0.06$ dB         |
| $Z_{ad}$        | Impedance of A/D converter  | 50 $\Omega$          | -                     |
| $P_{cgs}^{rec}$ | Power received at CGS   | -36 to $-\infty$ dBm | $\pm 0.07$ dB at peak |

inner beam. For SeaWinds, the maximum power is -43.49 dBm for the outer beam and -43.88 dBm for the inner beam.

The lack of instrument location and pointing information for blind estimation severely limits the capability of the CGS in estimating and interpreting power-related parameters. Additionally, the limit on maximum receive power, defined by (5.10), also discourages using a Gaussian distribution for the likelihood function. The assumption is therefore made that observations of CGS received power are distributed uniformly over the interval  $[0, P_{sw}^{rec}]$ . Given this distribution, it can be shown that the maximum likelihood estimate of  $P_{sw}^{rec}$  is

$$\hat{P}_{sw}^{rec} = \arg \max_i \{P_{cgs}^{rec}(i)\} \quad (5.11)$$

where  $P_{cgs}^{rec}(i)$  is the  $i^{th}$  observation of  $P_{cgs}^{rec}$ .

Appendix A.2.3 highlights the results of power estimation. The results show that in general, power received is comparable to expected levels. They also



Table 5.2: Values for terms related to calculation of power received at the CGS,  $P_{sw}^{rec}$ .

|             | QuikSCAT    |             | SeaWinds    |             |
|-------------|-------------|-------------|-------------|-------------|
|             | H-pol Value | V-pol Value | H-pol Value | V-pol Value |
| $P_{gen}$   | 49.50 dBm   | 49.50 dBm   | 49.50 dB    | 49.50 dB    |
| $G_{bias}$  | 0.40 dB     | 0.40 dB     | 0.40 dB     | 0.40 dB     |
| $G_{pkant}$ | 39.50 dB    | 40.90 dB    | 38.86 dB    | 40.46 dB    |
| $L_{wg}$    | 0.21 dB     | 0.24 dB     | 0.47 dB     | 0.52 dB     |
| $L_{sas}$   | 0.35 dB     | 0.24 dB     | 0.0 dB      | 0.0 dB      |
| $L_{ant}$   | 0 to 60 dB  | 0 to 60 dB  | 0 to 60 dB  | 0 to 60 dB  |
| $L_{atm}$   | 0.35 dB     | 0.40 dB     | 0.35 dB     | 0.40 dB     |
| $R$         | 1100 km     | 1250 km     | 1100 km     | 1250 km     |

show a gradual power decrease similar to CGS noise power. Additional observations show little difference in power between ascending captures and descending captures. The data does show a small difference between the received power of outer beam pulses versus the received power of inner beam pulses. The difference is on the order of 0.5 dB, though the imprecision of the available data limits further conclusion.

While the lack of geometry information limits the ability of the CGS in the blind power estimation, the methods and results of initial CGS calibration demonstrate success of the SeaWinds CGS. Thus, unlike previous ground stations, the SeaWinds CGS meets and exceeds its designed expectations, improving initial calibration of both QuikSCAT and SeaWinds.

#### 5.4 Comprehensive Estimation

Comprehensive estimation follows blind analysis. The objective of this portion of the analysis is to build on the solid foundation of blind estimation and expand the capabilities of the CGS to complete instrument calibration.

The comprehensive estimation algorithms build in a series of steps based on the parameter separation approach. Blind estimation is able to benefit from using large amounts of available data to decrease the variance of the estimates, while comprehensive estimation is dependent upon precise parameter separation. For this

reason Bayesian estimation techniques are employed. The principle technique of the comprehensive portion of the analysis is the recursive comparison between model simulations and CGS data. For each parameter estimate desired the model simulates a capture using a Gaussian prior distribution having a mean equal to the telemetry reported value and an infinite variance, since no quantized level of confidence exists prior to simulation. After each simulation a maximum *a posteriori*, or MAP, estimate is calculated. The MAP estimate is then recursively fed back into the model as a prior until an estimate which satisfies a pre-determined tolerance is obtained. For some parameters such as timing which are directly observable, the initial MAP estimate is sufficient and only one model iteration is required. For other parameters, such as attitude, which have non-linear dependencies, the MAP recursion requires several iterations. While this iteration process could be done simultaneously for all parameters, the parameter separation approach reduces the total number of required model simulations and allows linear parameters to be estimated prior to non-linear iteration.

To help illustrate the details of implementation, results from a sample instrument pass taken on 19 December 1999 (QuikSCAT rev 2606) are used as an example. The example capture is an outer beam only capture, with a 20 second capture occurring as the instrument approaches and a 20 second capture as it recedes. During each capture the antenna completes six complete revolutions, translating to six sweeps of the antenna footprint across the ground station's field of view.

To properly separate the parameters in implementation, the order in which each element is considered must be evaluated. Timing controls all of the instrument systems and does not require CGS power observations so it is considered first. Once timing estimates are obtained, the simulation model is perturbed using these estimates and re-simulation occurs. The next step is to estimate frequency parameters. Once frequency parameters are estimated the model is rerun with timing and frequency perturbations included. The third step is pointing estimation. Pointing estimation requires proper accounting for timing and frequency errors, including pulse aliasing, which will be described. It also requires the inclusion of CGS power observations.

Estimates of attitude require multiple perturbations of the model over roll, pitch, and yaw. Once final estimates for attitude are obtained, new simulations are used to estimate transmitted power.

## Timing

Timetag values reported in telemetry for each frame are linearly interpolated to provide estimates of the transmission time for each pulse. This interpolation is incorporated into the basic timing model (4.5) to form a simple time estimate for a given pulse,

$$\hat{t}_{arr}(p) = t_{tx}(p) + r(p)/c \quad (5.12)$$

$$= t_{tx}^b + t_{tx}^s p + r(p)/c \quad (5.13)$$

where  $t_{tx}^b$ , the timetag intercept, and  $t_{tx}^s$ , the slope, are the parameters of interest and are determined through PRI estimates, with  $p$  referencing the pulse of interest.

To better characterize range,  $r(p)$ , it is modeled as a polynomial function of time. Figure 5.10 shows the model calculated range for a sample SeaWinds rev. The solid line shows the range as a function of frame. The enlarged portion of the lines show the frames which correspond to typical CGS captures. The dashed line shows a quadratic approximation of range over the frames shown. While a higher order approximation can be used, sensitivity to higher order terms is minimal. A quadratic range polynomial is added to the arrival time estimate as

$$\hat{t}_{arr} = t_{tx}^b + t_{tx}^s p + \frac{1}{c} [(r_a p^2 + r_b p + r_c)] \quad (5.14)$$

$$= \left( t_{tx}^b + \frac{1}{c} r_c \right) + \left( t_{tx}^s + \frac{1}{c} r_b \right) p + \left( \frac{1}{c} r_a \right) p^2. \quad (5.15)$$

This model shows that the arrival times of the pulses over the span of an entire capture should exhibit a quadratic behavior. Using this information CGS observed pulse arrival times are least-squares fit to a quadratic form and estimates of timing bias, slope, and the range polynomial are obtained through their relationship to coefficients of the arrival time polynomial.

This polynomial suggests that timetag bias can not be uniquely identified from the range bias term. Based on timetag accuracy, the timetag bias is expected to

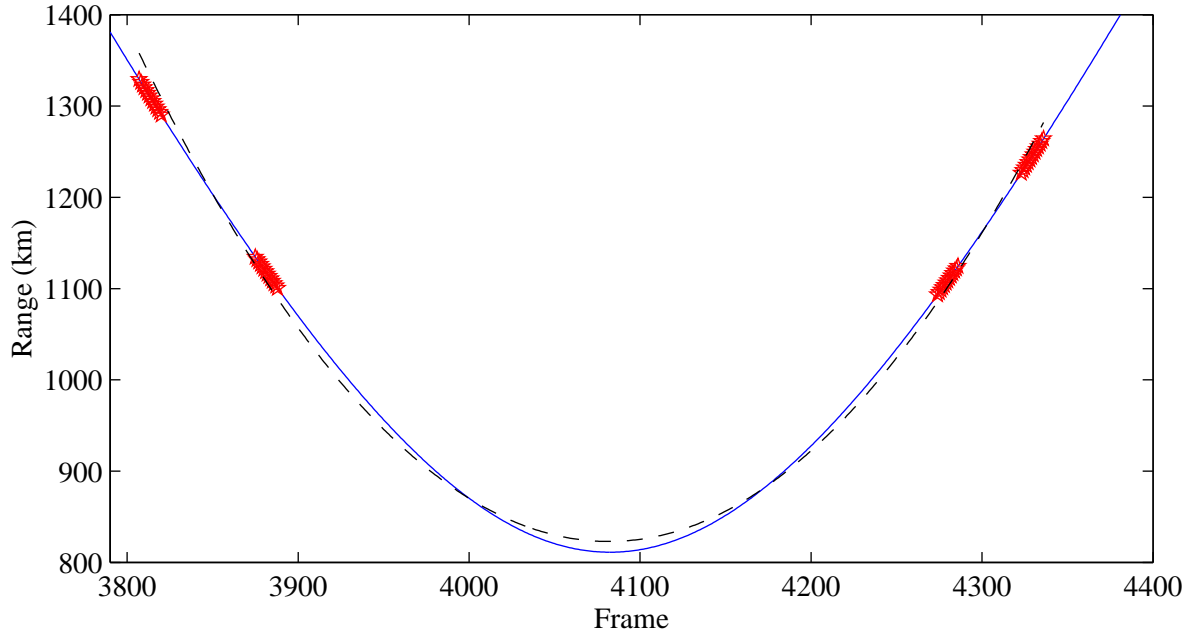


Figure 5.10: Calculated range as a function of telemetry frame. The solid line shows the calculated range from instrument to ground station. The bold segments represent the frames which correspond to CGS captures. The dashed line represents a quadratic fit to the bold range values.

be on the order of a few milliseconds; the data in Figure 5.10 suggests that the range bias term,  $r_c/c$ , is significantly smaller, on the order of microseconds. Similarly, it follows that the time slope per pulse approximates the PRI of the instrument. The slope of the range polynomial is negligible since the range to the ground station is a symmetric function. These assumptions allow simplification of the timing estimate polynomial to

$$\hat{t}_{arr} = t_{tx}^b + t_{tx}^s p + \left(\frac{r_a}{c}\right) p^2. \quad (5.16)$$

While the initial premise suggests that higher order terms of the range polynomial can be estimated from CGS data, the reality is that the magnitude of these higher order terms is extremely small when converted to timing values. They are also more susceptible to errors in arrival time estimates caused by noisy CGS data.

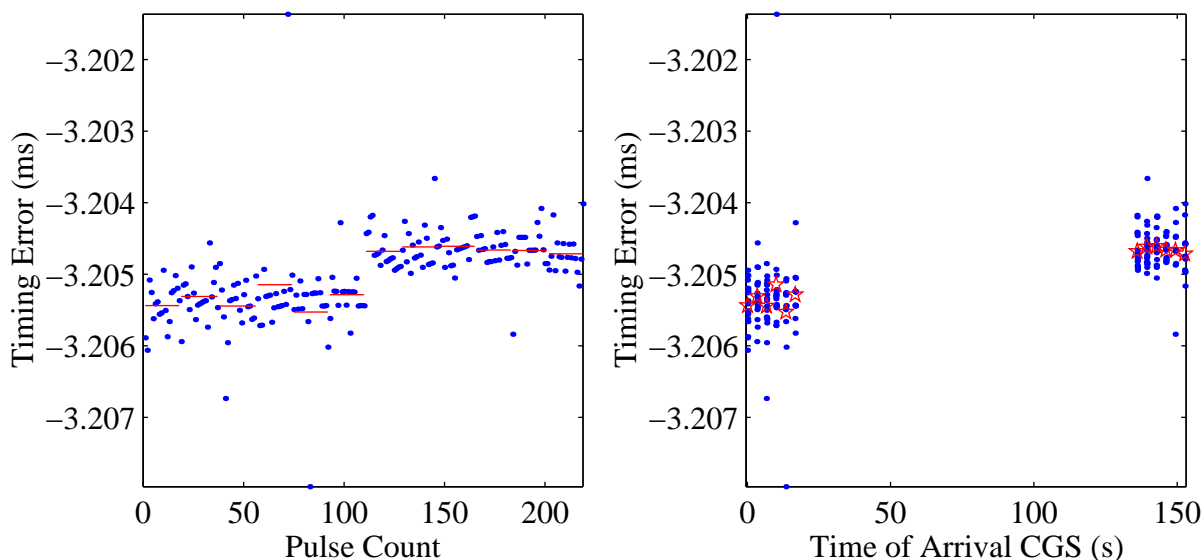


Figure 5.11: Instrument arrival time differences between CGS data and model simulations. The first figure shows the data as a function of received pulse count, the second as a function of time. Each horizontal line represents the mean time difference for each sweep. The two captures and twelve sweeps are distinguished in the first figure.

Figure 5.11 shows the difference in arrival time (in milliseconds) between what the CGS recorded and what the model predicted (before any iteration) for the 19 December 1999 example capture as a function of received pulse count and as a function of time (seconds from reception of first pulse). The figure reiterates the relative precision of the CGS sampling as well as the pulse to pulse accuracy of arrival time estimates. It also displays the difficulty of fitting a high order polynomial to the data. The MAP estimate of  $t_{tx}^b$  (which is equivalent to the observation mean when using a least-squares metric) is  $-3.205$  ms, the standard deviation of the observations is  $0.56 \mu\text{s}$ . While there are some individual pulse time differences greater than  $1 \mu\text{s}$ , they are caused by poor arrival time estimates.

The negative mean time difference between model and CGS indicates that the model predicts the pulses to arrive after they are received. This is caused by a pulse aliasing of 2 PRI (10.8 ms) that is only resolved with model simulation. For

the sample data set, the mean time difference of -3.205 ms is arrived at by aligning each CGS data pulse with the model pulse having the minimum difference in arrival time. Adjusting for aliasing, the timing difference is  $10.8 \text{ ms} + (-3.2 \text{ ms}) = 7.6 \text{ ms}$ . While this error is larger than expected, it is physically possible and is still well within SeaWinds' timing specification of 50 ms.

Once pulse time aliasing is clarified and pulses properly aligned, simulated data is regenerated. A curve fit to the regenerated sample capture data (Figure 5.11) shows that the quadratic term,  $r_a$  is on the order of  $10^{-12}$ . A fit of the telemetry reported timetags also shows a curvature of this order. The difference in curvature between data and timetags is less than  $10^{-15}$ , which implies a maximum position error of 30 meters. This value compares well against the specified accuracy of spacecraft position, 150 meters. As illustrated, range estimation is limited by timetag accuracy, CGS precision, and CGS sampling, parameters which have variances larger than predicted range effects. This lack of sensitivity requires the assumption that reported values are within specification.

The next coefficient of arrival time is timetag slope. The PRI estimate from blind estimation is 5.389527 ms, yielding an estimated timetag slope (100 PRI) of 538.9527 ms. The standard deviation of the PRI estimate is 30 ns, giving the timetag slope an estimated standard deviation of  $3.0 \mu\text{s}$ . For the sample capture, the slope of the arrival times is found to differ from the expected slope by 5 ns per frame (100 PRI), or 9.3 ns per second. Figure 5.12 shows the deviation of estimated timetag slope from the expected value for the entire CGS mission in microseconds per frame. The mean is a few nanoseconds and the variance is less than a microsecond from *a priori* values, well within expected ranges. The mean slope for SeaWinds is a bit elevated compared to QuikSCAT, suggesting a slightly different central clock rate.

Finally, the timetag bias,  $t_{tx}^b$ , is estimated using the mean time difference between CGS measured arrival times and timetag predicted arrival times for the entire capture. For the example capture the bias is 7.6 ms. The bias for the entire SeaWinds CGS mission is shown in Figure 5.13.

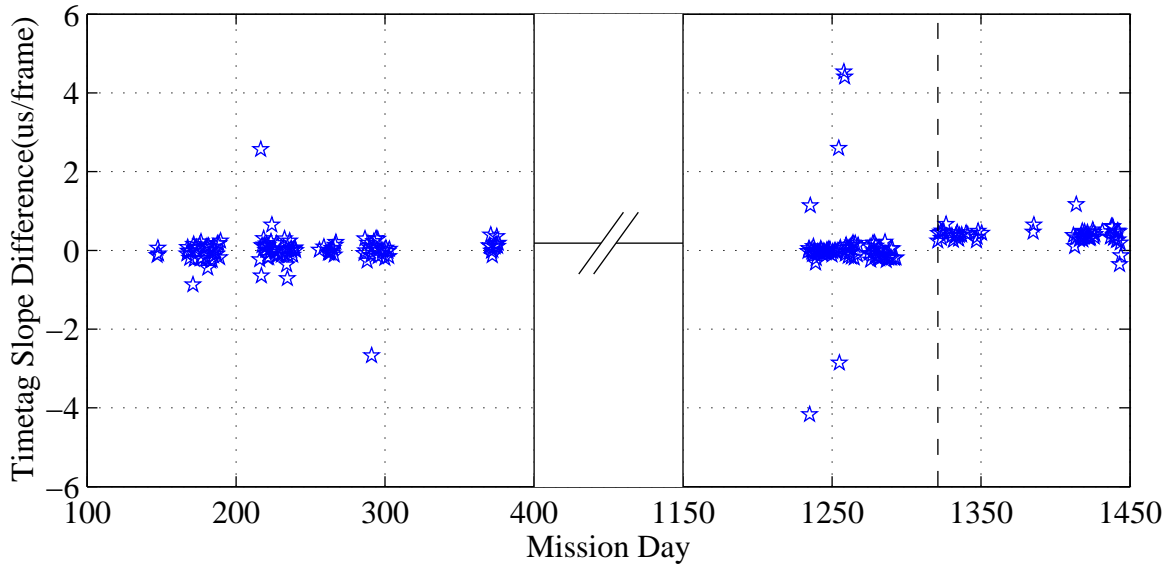


Figure 5.12: Difference in timetag slope between linearly fit CGS data and telemetry reported values. The duration of each frame is specified to be 100 PRI. The figure shows the difference between the slope of all of the captured values and the estimated 100 PRI value. It uses the convention of mission day, days since the CGS went into operation at QuikSCAT’s launch. The gap in data between day 400 and day 1150 represents the time the CGS was not capturing data. Up to day 1150 the CGS was located in White Sands, New Mexico, after day 1150 the CGS was located in Provo, Utah. the vertical line at day 1321 corresponds to SeaWinds’ turn on, January 28, 2003, when the CGS ceased to capture QuikSCAT data and began to track SeaWinds.

The timing bias depicted in Figure 5.13 shows a marked contrast between QuikSCAT and SeaWinds. The mean value of the QuikSCAT observations is 8.25 ms, the standard deviation is 0.51 ms. The mean value of the SeaWinds data is 14.43 ms, with a standard deviation of over 10 ms. Previously discussed estimates for pulse width, PRI, and time slope all show a significant stability between SeaWinds and QuikSCAT, contrasting the data in this figure. As discussed, the recorded timetag values require significant coordination between multiple timing sources. Both systems attach the actual timetags to the telemetry data after the telemetry is received at the ground, in ground post-processing. Due to the complexity of this system and a

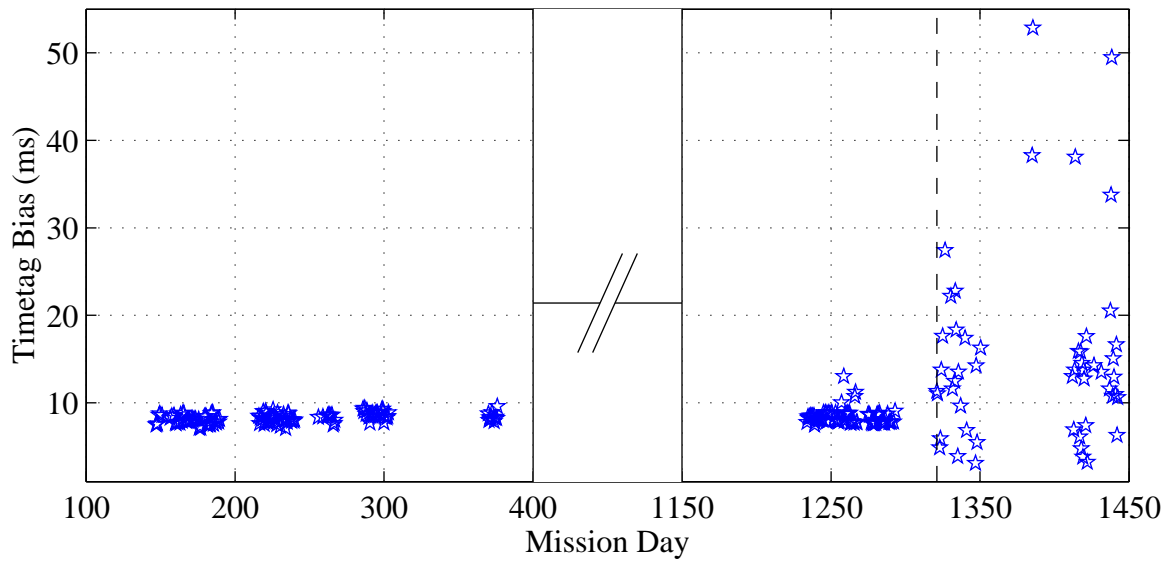


Figure 5.13: Mean arrival time difference for each capture between model estimated arrival times and CGS recorded values. Pulse time aliasing is resolved. The data shows that QuikSCAT values are stable, with a mean of 8.25 ms and a deviation of 0.51 ms. SeaWinds’ timing biases are significantly more variant, with a mean of 14.43 ms and a deviation of more than 10 ms.

lack of information, the difference in timetag biasing is attributed to post-processing issues.

Poor timetags do not necessarily indicate poor instrument operation since they are attached in post-processing, other calibration parameters reflect excellent instrument performance. Poor timing information does however make it difficult to compare measurements at different times, limiting the accuracy of other estimates such as pointing precision since timing is the backbone of the implementation.

In summary, errors present in SeaWinds timetags are estimated using CGS timing to several significant figures. The magnitude of these errors along with the inherent insensitivity of the timing data to instrument position prohibit estimation of the range, and thus position, of the spacecraft in all but the most exaggerated of circumstances. Once timing bias and slope are estimated, they are fed back into the



simulation model. However, timing inaccuracies put strict limitations on the accuracy of further calibration estimates.

## Frequency

During blind estimation the chirp rate is estimated by using a polynomial fit of the unwrapped signal. It is also shown that the initial phase of the signal is inestimable using CGS data. The remaining frequency terms for comprehensive estimation are  $\omega_c$ ,  $\omega_{dc}$ , and  $\omega_d$ .

The CGS observed Doppler frequency for pulse  $p$  is

$$\omega_d(p) = -2 \frac{u_R(p)}{\lambda} \quad (5.17)$$

where  $u_R$  is the spacecraft velocity in the CGS direction,

$$u_R(p) = \vec{U}(p) \cdot \frac{\vec{R}(p)}{\|\vec{R}(p)\|}, \quad (5.18)$$

modeled using vector spacecraft velocity  $\vec{U}(p)$  and range  $\vec{R}(p)$ . The expression for frequency (5.5) is combined with the Doppler compensation model (5.3) to provide a model for the signal center frequency received at the CGS,

$$\hat{\omega}_{est}(p) = \omega_c + C(p) + A(p) \cos \left( \frac{2\pi}{N} [\alpha(p) + \delta_\alpha] + P(p) \right) - 2 \left( \frac{u_R^b + u_R^s p}{\lambda} \right) \quad (5.19)$$

where the spacecraft velocity is modeled as linear over the region of interest. The appropriateness of this model is seen by noting that the dot product of velocity is essentially the change in range. Modeling the range as a quadratic allows the assumption of linear velocity. Errors in this approximation are at most 100 m/s over a capture, which, when divided by the wavelength, induces an error of less than 10 Hz.

Terms are rearranged to yield

$$\hat{\omega}_{est}(p) = \left( \omega_c + C(p) - 2 \frac{u_R^b}{\lambda} \right) - 2 \frac{u_R^s p}{\lambda} + A(p) \cos \left( \frac{2\pi}{N} [\alpha(p) + \delta_\alpha] + P(p) \right). \quad (5.20)$$

This expression consists, much like timing, of three, uniquely identifiable sets of terms.

While the concept of separation for this expression holds, implementation introduces several difficulties. First, the bias of the error between the data and the

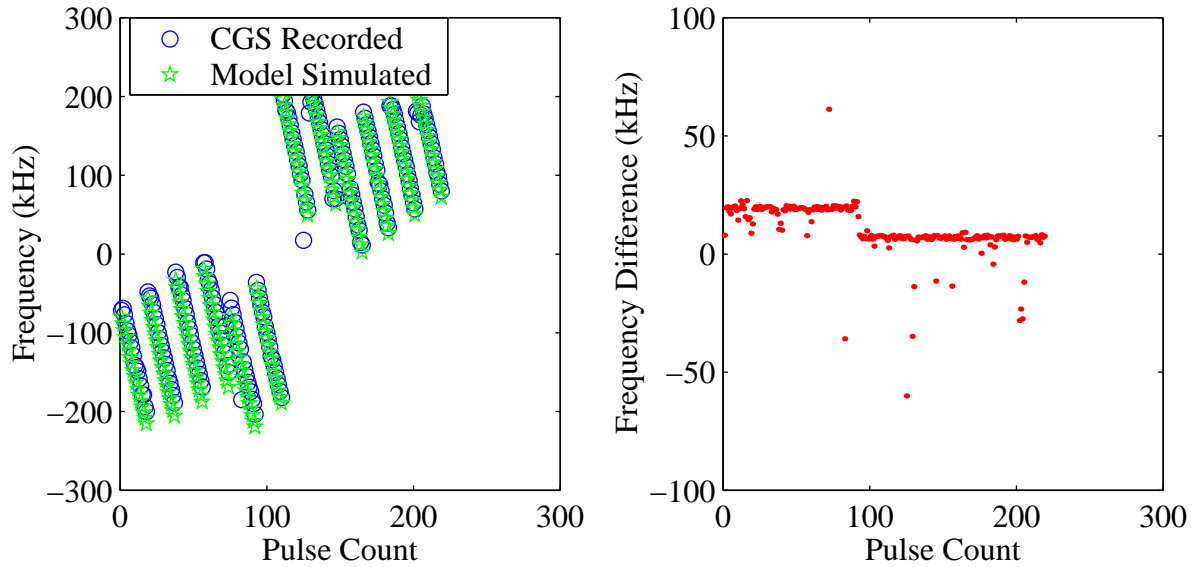


Figure 5.14: (left) CGS recorded and model simulated frequency of each pulse for one CGS data pass. (right) Difference between the model and data. With the minor exception of the observed step in the difference, the data shows good general correlation between model and data.

model frequency estimate is large relative to the other terms due to the magnitude of the instrument center frequency. Second, due to limited pulse sampling, only a small segment of each harmonic period is available, significantly decreasing azimuth sensitivity. A typical CGS sweep observation of 0.2 seconds is 6% of an antenna rotation. For side-looking azimuths, the amplitude of the sinusoid changes nearly 20% over this span, yet at forward looking azimuths the amplitude varies by less than 0.1%. Third, the variance of frequency estimates due to low pulse SNR reduce the sensitivity of the frequency slope.

Figure 5.14 shows CGS recorded frequency and model simulated frequency as a function of pulse count and the difference between the two values for the sample capture. In general there is good correspondence between the model and the data, with the mean error being 7.7 kHz. While there are some erroneous points having a difference of more than 40 kHz, these values are attributed to low SNR where the frequency estimation algorithm performs poorly. It is noted that a model simulation

which does not account for pulse aliasing increases the mean bias to 16.53 kHz, providing further evidence that the temporal dealiasing described properly aligns the pulses.

Beyond the bias, there is a significant change in the mean frequency difference, about 12 kHz, between the fifth and sixth sweep. This is notable for a number of reasons, mainly because the shift does not occur between captures, but during the first capture (the first six sweeps in this case). The linearity of the data difference suggests that the modeled velocity is not the cause of the step. Sweep to sweep variation is also negligible in the figure, showing that the azimuthal dependence of the Doppler compensation algorithm is modeled correctly. This leaves bias terms as the cause. The first bias term,  $\omega_c$ , accounts for the bias of 7.7 kHz, but is constant throughout the capture. The sharp change in frequency is therefore attributed to,  $C$ , the bias of the Doppler compensation algorithm. The  $C$  parameter is a function of orbit step, which increments 256 times over the span of an orbit, essentially changing every 24 seconds. For this capture the orbit step increments, according to telemetry, between the fourth and fifth sweep. It is likely that the model does not accurately simulate the actual implementation of the Doppler compensation algorithm. While the model is constructed using design documents, the simulation model and actual instrument software may be different in accounting for orbit step changes and determining which value of  $C$  is used for transmission.

Following analysis of the sample capture the next step is to assess long term stability of the CGS received frequency. Figure 5.15 shows the mean frequency difference between model and data for each capture over the length of the CGS mission after correcting for pulse-time aliasing. The figure shows that the data is well within tolerances established though there is some variation over the mission.

It is interesting to note that QuikSCAT frequency errors are well clustered, while the SeaWinds data is more variable. For comparison, the average Doppler compensation change from pulse to pulse (like beam) is on the order of 8-12 kHz, depending upon the geometry of the capture. While this comparison shows that the frequency difference is within 1 pulse, it also suggests that the pulse-time aliasing is

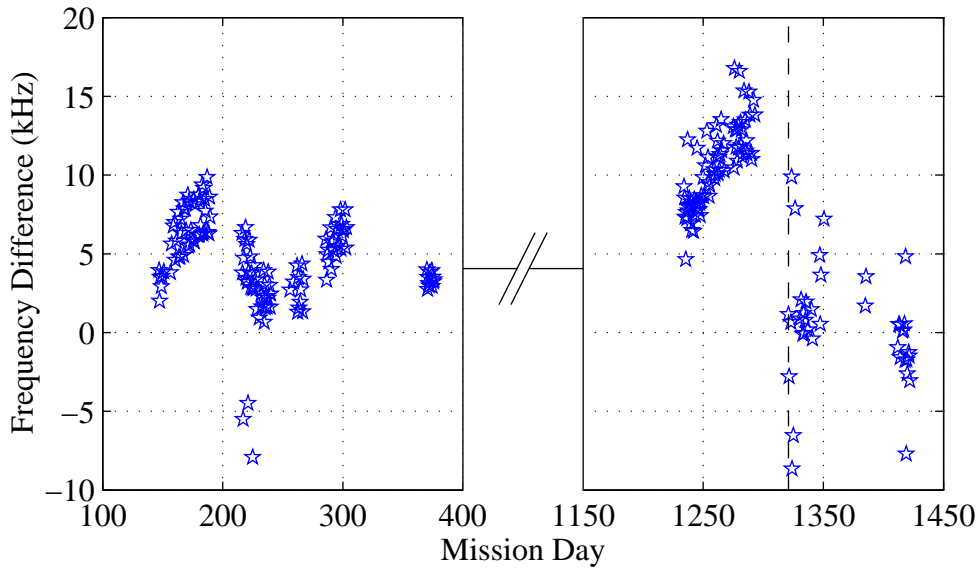


Figure 5.15: Mean frequency difference between CGS and model for each data pass over the length of the CGS mission. The data show some variability, but good temporal correlation for QuikSCAT. For SeaWinds the difference appears to be more random but within expected levels.

more complicated than just a timing bias. Discrepancies in Doppler compensation between the model simulation and instrument implementation might also explain differences of this magnitude. Unfortunately, this problem is unresolved, even after discussions with instrument software programmers.

### Pointing

Once estimates of SeaWinds frequency are made, the third step of the algorithm is to estimate instrument pointing where the observation data now includes CGS observed pulse power in addition to pulse timing and frequency. The difficulty of pointing estimation is caused by a many-to-one mapping of the instrument antenna pattern to transmitted power, meaning there are many values of  $(\theta_a, \phi_a)$  which correspond to the same antenna gain. The inverse of this system does not have a unique solution and is the primary motivator for the recursive Bayes approach. Unfortunately, pointing estimation is also limited by timing inaccuracies and the possible

inaccuracies between model and actual operation suggested by the frequency analysis. In probabilistic terms, it is impossible to estimate the maximum of  $p_A(\mathbf{a})$  or even  $p_A(\mathbf{a}|\mathbf{x})$ , where  $\mathbf{a}$  is a vector of attitude parameters, and  $\mathbf{x}$  are the observations. Instead, only  $p_A(\mathbf{a}|\mathbf{t}, \mathbf{f}, \mathbf{x})$  is available for MAP analysis (where  $\mathbf{t}$  is a vector of timing parameter estimates and  $\mathbf{f}$  is a frequency estimate vector) thus conditioning estimates on timing and frequency parameters.

To estimate pointing, instrument recording of yaw,  $\theta_y$ , is first considered. Spacecraft yaw is directly tied to the rotational azimuth angle of the instrument and as such must be separated from the recorded azimuth angle and associated timing. The azimuth angle of the antenna is defined as

$$\theta_a = 2\pi\Omega t + \theta_y \quad (5.21)$$

where  $\Omega$  is the rotation rate of the antenna,  $t$  is time, and  $\theta_y$  is the spacecraft yaw angle, converted from its reported coordinate system. This expression enumerates the limitations of  $p_A(\mathbf{a}|\mathbf{t}, \mathbf{f}, \mathbf{x})$  by showing that errors in antenna azimuth induced by timing uncertainties are inseparable from spacecraft yaw angle without knowing how timetag errors effect reported azimuth. This forces the assumption that the azimuth angle reported in telemetry for each pulse is the true azimuth angle at the moment stated by the timetag. While this may bias and possibly exaggerate yaw estimates, precise separation of this coupling is impossible.

To estimate the yaw angle of the instrument a comparison of the observed pulse power of the CGS data to model simulations for each pulse in an individual sweep is made. Figure 5.16 shows the simulated pulse power for a selected CGS sweep and the effect of yaw on pulse power ( $0.5^\circ$  yaw). The dashed curve represents actual CGS data and the solid line represents the model telemetry simulation. The related effect of roll and pitch are shown in Figure 5.17 for a roll and pitch of  $0.5^\circ$  each. The figures show that the power of each pulse is determined at several points over the duration of the pulse. This is done to provide as many estimates of power as possible without sacrificing the accuracy of CGS data.

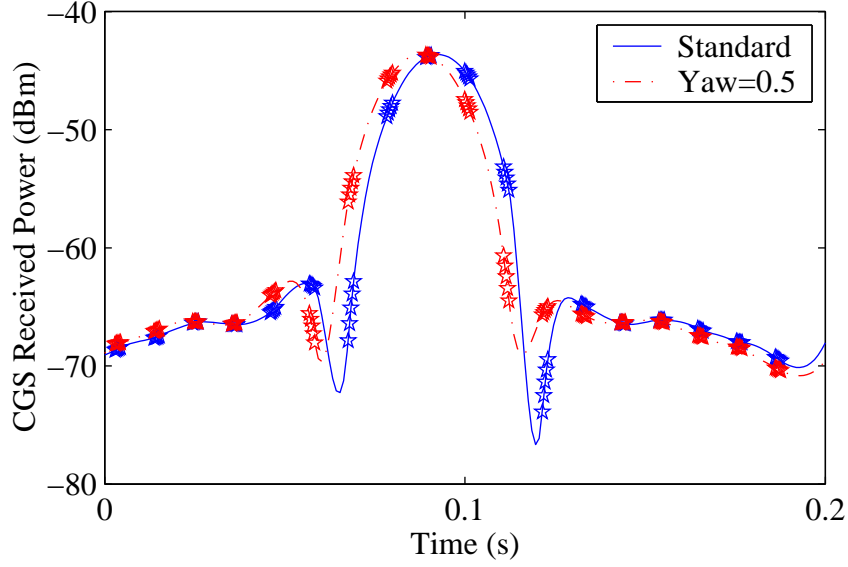


Figure 5.16: Simulated CGS sweep showing the effects of yaw error. The solid curve represents pulses received at the CGS. The dashed line represents the same pulses when possessing a  $0.5^\circ$  yaw bias. Each pulse is simulated at five points. A spline is fit to the points for clarity.

Minimization of the difference between the simulated, power of each pulse and the actual recorded power is performed using a minimum variance metric rather than the traditional least-squares metric. When the simulation of CGS power is unbiased, these two are equivalent. However, since power has not been estimated and is dependent on attitude, the desire for an unbiased estimator suggests a variance-based approach. The objective function,  $F$ , is

$$F(\theta_r, \theta_p, \theta_y) = \left( \frac{1}{\left( \sum_{m=1}^{12} N_m \right) - 1} \right) \sum_{m=1}^{12} \sum_{n=1}^{N_m} (P_{m,n}^d - \mu)^2 \quad (5.22)$$

where  $\theta_r$  is roll,  $\theta_p$  is pitch, and  $m$  is the index for each of the 12 (usually) sweeps, each sweep having  $N_m$  pulses.  $P_{m,n}^d$  is the difference in power between CGS and model data for the  $n^{\text{th}}$  pulse of the  $m^{\text{th}}$  sweep. The overall mean of the capture,  $\mu$  is given

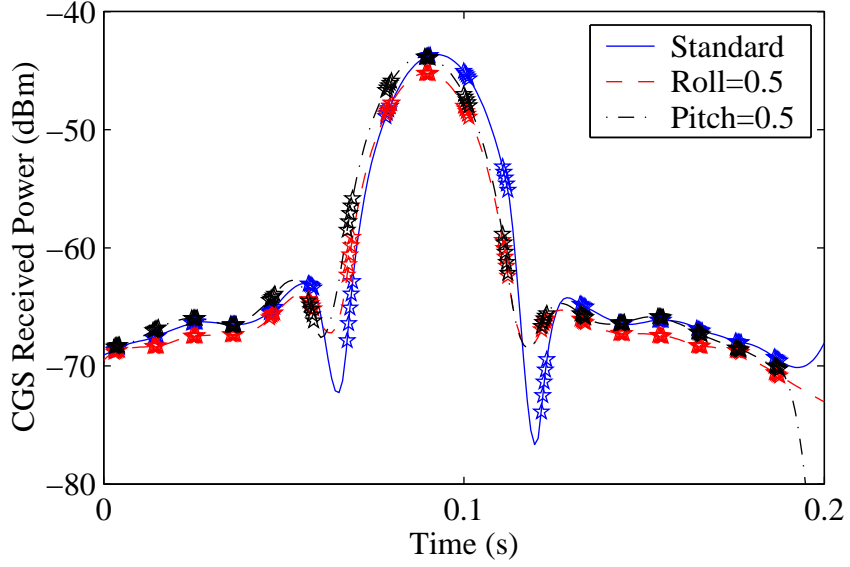


Figure 5.17: Simulated CGS sweep showing the effects of roll and pitch. The solid curve represents no attitude perturbation. The dashed line includes a  $0.5^\circ$  roll error, and the dash-dot line includes a  $0.5^\circ$  pitch error.

by

$$\mu = \left( \frac{1}{\sum_{m=1}^{12} N_m} \right) \sum_{m=1}^{12} \sum_{n=1}^{N_m} (P_{m,n}^{cgs} - P_{m,n}^{model}). \quad (5.23)$$

Estimates of  $\mathbf{a} = [\theta_r, \theta_p, \theta_y]$  are thus given by

$$\hat{\mathbf{a}} = \arg \min_{\mathbf{a}} \{F(\mathbf{a})\}. \quad (5.24)$$

To visualize the three dimensional objective function, yaw is held constant and its value as a function of roll and pitch is plotted in Figure 5.18 using simulated data. The figure shows that for large attitude errors ( $> 2.0^\circ$ ) the function is not well behaved. Attitude errors are expected to be at most  $1^\circ$  along any axis and therefore this property is overlooked. Within a range of  $\pm 1^\circ$ , the global minimum is unique and clearly identifiable.

Minimization of the objective function is performed using a simplex algorithm [57]. This is chosen over Newtonian and gradient related algorithms for time

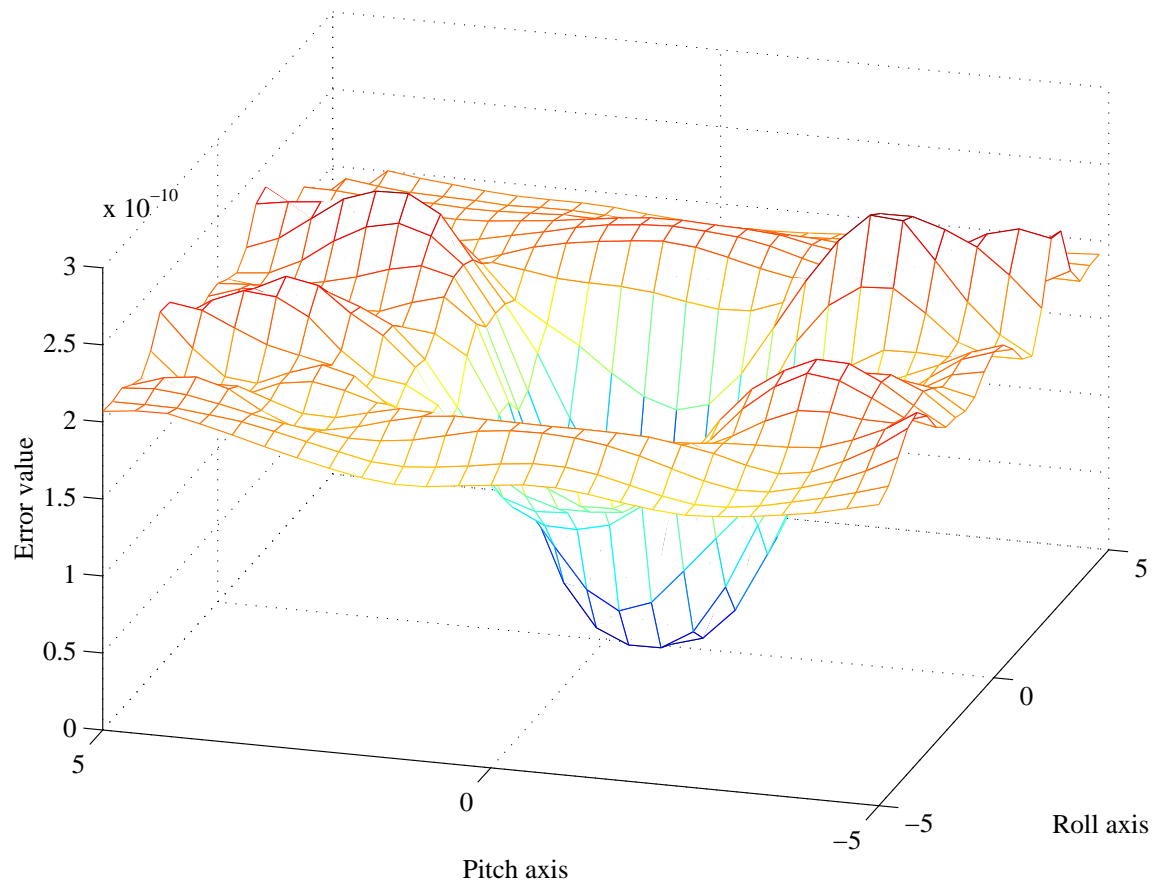


Figure 5.18: Objective function for roll and pitch. The figure shows that the function is not well conditioned for errors greater than  $2^\circ$ . It is believed that SeaWinds attitude is always within this range and thus the objective function should provide a good estimate of attitude.



related reasons. Calculation of each realization is computationally expensive. Gradient related algorithms require the knowledge of partial derivatives of the objective function. They are not analytically defined for this problem and numerical evaluation requires several iterations for each attitude perturbation.

To test the effectiveness of the objective function and minimization technique, several simulations are conducted. Each simulation is generated using the model to create a sample CGS data set. Various attitudes are selected and random noise is added at a level comparable to actual CGS levels. Figure 5.19 shows the results of four simulations, displaying the fit of roll and pitch. CGS data is generated with a pitch of  $-0.75^\circ$  and the attitude is fit by minimizing the objective function. Each of the four minimizations are started at different points,  $(\pm 1^\circ, \pm 1^\circ)$ , the perceived upper bound of attitude errors. The figure demonstrates convergence and overall effectiveness of the perturbational method.

Figure 5.20 shows real CGS received power and model simulated power for one of the 12 sweeps in the example capture of 19 December 1999 after the timing bias of 7.575 ms and frequency bias of 7.7 kHz are accounted for in the telemetry but before the pointing is estimated. The asterisks (\*) represent the actual power received by the CGS and the red circles (o) represent the model predicted power.

An estimate using the minimum variance metric for the example capture reports attitude to be  $(-0.20^\circ, 0.34^\circ, -1.02^\circ)$  for roll, pitch, and yaw. Figure 5.21 shows the power curve for this attitude estimate. Clearly the estimate is erroneous. A subjective attitude estimate is shown in Figure 5.22, the attitude being  $(-0.1^\circ, 0.1^\circ, -0.2^\circ)$ .

The three figures clearly show that in this case the minimum variance estimator provides an unrealistic value. Unfortunately, this is the case with many CGS captures. As eluded to in the CGS calibration methodology, attitude estimates using the CGS are limited in their precision. While it is shown that the algorithm converges in simulation, real data values frequently fail to realize this convergence.

Poor performance is attributed to several factors, the first being model accuracy since attitude estimates are conditioned on an accurate model. Significant

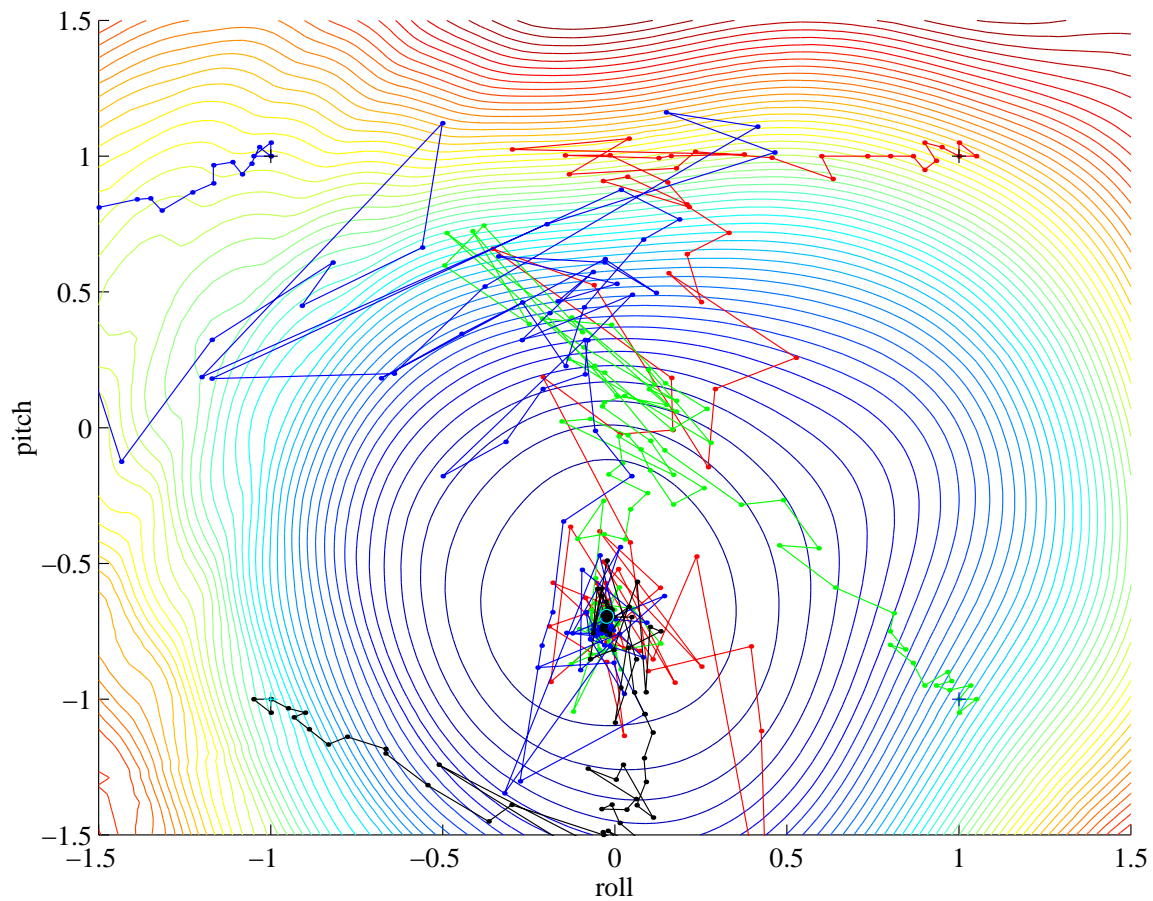


Figure 5.19: Simulation of attitude perturbations. Data is generated with a pitch of  $-0.75^\circ$ . Contours of the objective function are shown. The fitting algorithm is started at four different points,  $(\pm 1^\circ, \pm 1^\circ)$  in roll and pitch space, with the colors corresponding to each fit. The search finds the minimum of the objective function, with the path taken displayed by the figure.

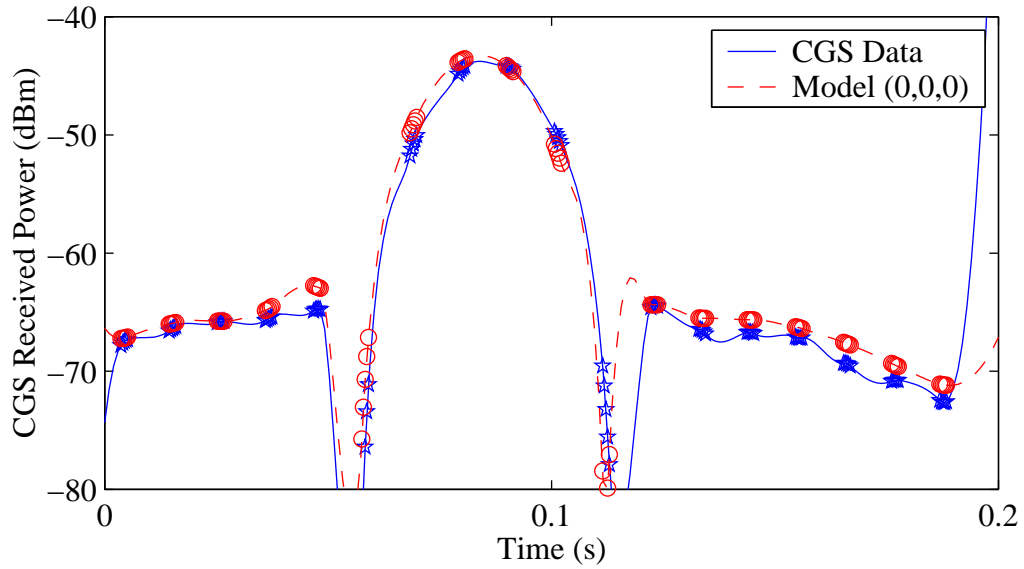


Figure 5.20: Power received by the CGS and simulated power. The asterisks (\*) represent the CGS recorded data. The circles (o) represent the model simulation after timing and frequency are accounted for. Each subplot represents one antenna sweep across the CGS. The first six subplots (sweeps) are the outer beam as it approaches the CGS, the remaining six subplots are the outer beam as it recedes from the CGS. The figure shows good overall correlation between model and CGS.

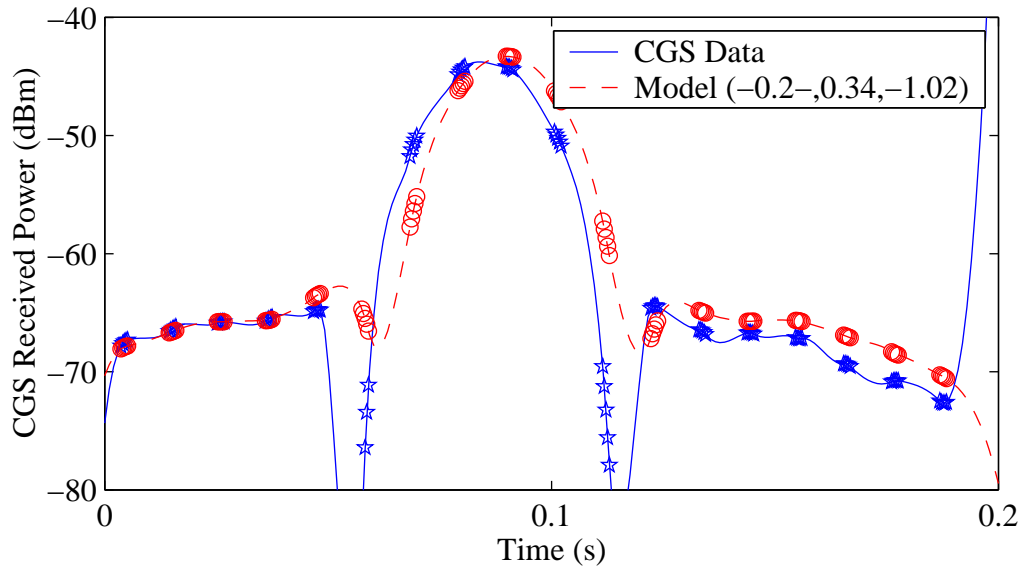


Figure 5.21: Results of the minimum variance attitude fit. The model data does not correspond nearly as well as the reported attitude data.

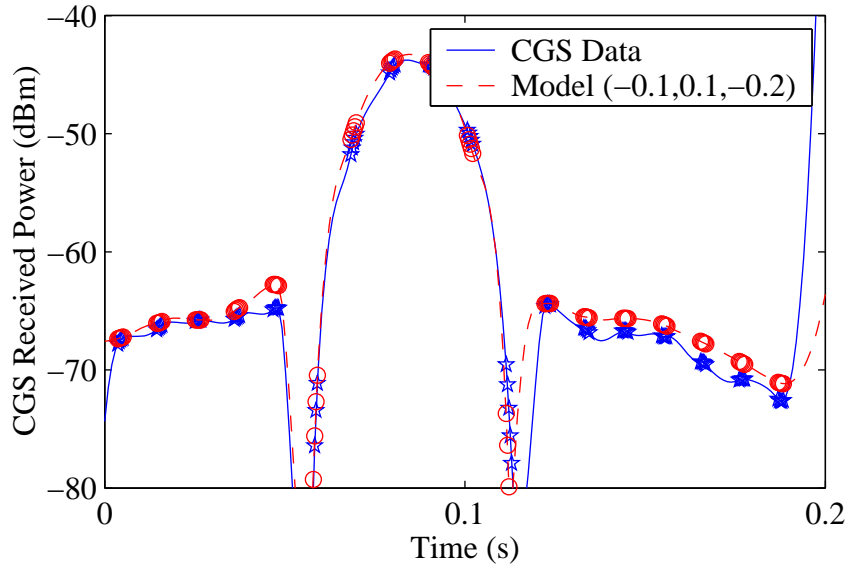


Figure 5.22: Subjective fit of CGS power data. Though the results are subjective, the model data corresponds well to the actual data. The attitude reported for this fit is  $(-0.1^\circ, 0.1^\circ, -0.2^\circ)$  for roll, pitch, and yaw.

effort is invested in the accuracy of the model, and no known major discrepancies exist. In particular, the model calculates several values which are available in other telemetry products. In every case the model is validated against this telemetry data and is found to reproduce each value with remarkable precision. Unfortunately no *in situ* truth data exist. While the model replicates reported telemetry there is no controlled way of comparing the model to actual instrument operation. Minor discrepancies are believed to be the major cause of imprecise attitude estimates.

The major model-instrument discrepancy is timing. Timing values possess a particularly large variance. While well within specification, it is impossible to obtain timing values for SeaWinds which are precise enough for desired attitude estimation, particularly yaw.

A second model-instrument discrepancy is transmitted power. The example capture (see Figure 5.22) uses only pulses from SeaWinds' outer beam. Figure 5.23 shows the inner beam CGS received power and model simulated power using an

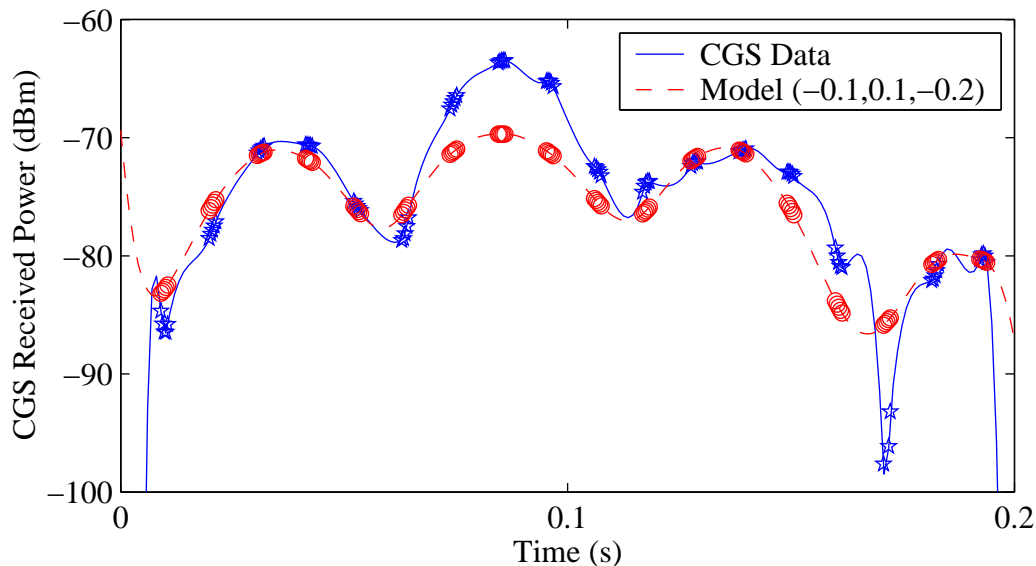


Figure 5.23: Inner beam power differences for an outer beam capture. The figure shows the discrepancies between model simulated power and CGS recorded power. Differences are believed to be mainly caused by precision limitations in the modeled antenna directivity pattern.

attitude of  $(-0.1, 0.1, -0.2)$ . The fit of the outer beam (Figure 5.22) reveals discrepancies of no more than 2.0 dB. However, the same simulation reveals discrepancies of more than 7.0 dB for the inner beam. This discrepancy suggests several things, primarily that the antenna directivity patterns reported for SeaWinds have precision limitations which effect the ability of the model to match the CGS data. This is seen not only by the inner beam but also in the lower power pulses of the outer beam. Limited precision is an inherent issue. Unfortunately it is an issue which is significant for attitude estimation.

The effect that these discrepancies have on the ability of the CGS and model to estimate attitude is described through a sensitivity analysis. Sensitivity is defined as the change in received CGS power for a given instrument perturbation. Figure 5.24 shows the simulated change in CGS observed power for azimuth offsets of  $1.0^\circ$ ,  $0.5^\circ$ ,  $0.1^\circ$ , and  $0.05^\circ$ . These values are derived by using an azimuth slice through the outer beam boresight and shifting pointing by the specified difference amount.

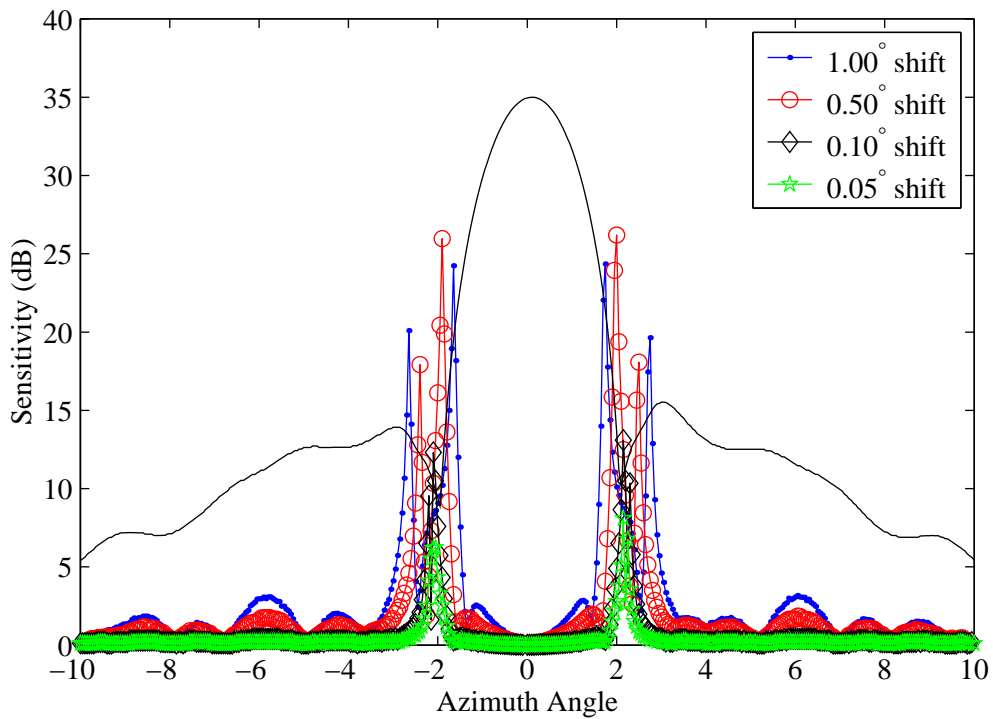


Figure 5.24: Azimuth sensitivity of the CGS for a sweep within  $1.0^\circ$  (in elevation) of boresight for offsets of  $1.0^\circ$ ,  $0.5^\circ$ ,  $0.1^\circ$ , and  $0.05^\circ$ . Sensitivity is the change in CGS received power corresponding to the specified azimuth offset. The azimuthal gain of the antenna is shown behind the plot (offset by 35 dB) for reference.

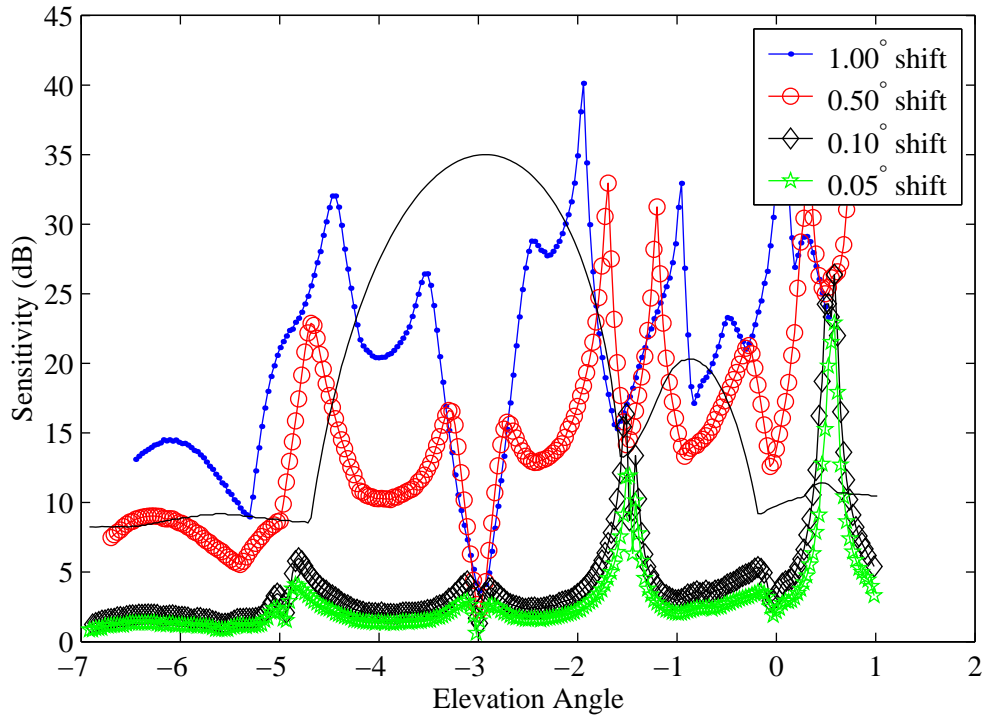


Figure 5.25: Elevation sensitivity of the CGS for a sweep within  $1.0^\circ$  (in azimuth) of boresight for offsets of  $1.0^\circ$ ,  $0.5^\circ$ ,  $0.1^\circ$ , and  $0.05^\circ$ . Sensitivity is the change in CGS received power corresponding to the specified elevation offset. The elevational gain of the outer beam antenna is shown behind the plot (offset by 35 dB) for reference.

The figure shows the peak sensitivity to be 24.3 dB, 26.2 dB, 8.1 dB, and 3.4 dB respectively. The mean change in power is 2.31 dB, 1.68 dB, 0.57 dB, and 0.34 dB. It is noted that the CGS is particularly insensitive to changes in azimuth at high gain locations, further complicating estimation.

In like manner the sensitivity of the CGS to perturbations in elevation are assessed in Figure 5.25. While the figure shows elevation sensitivity for  $\pm 4.0^\circ$ , the majority of CGS captures occur within  $\pm 1.0^\circ$ . For elevation offsets of  $1.0^\circ$ ,  $0.5^\circ$ ,  $0.1^\circ$ , and  $0.05^\circ$  within the  $\pm 1.0^\circ$  region the peak sensitivity is 18.6 dB, 16.6 dB, 4.3 dB, and 2.9 dB respectively, with mean sensitivity of 11.9 dB, 9.3 dB, 2.8 dB, and 1.9 dB. For a complete diagram of SeaWinds' transmit antenna pattern (outer beam), see Figure 6.9.

The relation between azimuth and elevation sensitivity and attitude induced offsets is dependent upon the geometry of an individual capture. Yaw is directly related to azimuth, roll and pitch are linear combinations of azimuth and elevation. Regardless of the geometry, sensitivity values are directly related to required CGS accuracy. The CGS power calibration is specified to be accurate to within 0.15 dB.

The difference between determined CGS accuracy levels and mean sensitivity levels quantify the effect of timing and power discrepancies on the CGS recorded power. The standard deviation of CGS attitude estimates is roughly  $0.27^\circ$  (data not shown). This corresponds to a mean attitude sensitivity of 4.9 dB in elevation and 1.0 dB in azimuth, azimuth is thus limiting. From these values it is concluded that the error induced on the simulated data by model imprecisions is 0.85 dB. This value is consistent with model-based estimates of transmitted power shown in the next section. The consistency of attitude and power precision values confirm the accuracy of sensitivity estimates. To estimate pointing to within  $0.1^\circ$ , the proposed objective, mean modeling error must be reduced to 0.19 dB, a difficult but achievable goal for future CGS realizations.

## Power

The final calibration parameter is power. While CGS-based attitude estimates do not possess desired precision, pointing estimates are also made by other methods. These other estimates are used as inputs to the model to facilitate power characterization. As described the MAP estimate of power using a least-squares metric is the mean value of the CGS power observations.

As with blind power estimation it is desirable to not only estimate received power of the instrument but to assess differences between orbit type and beam polarization. Figure 5.26 shows the mean difference (between model and CGS data) in power for each pass as a function of mission day using telemetry reported attitudes. The large shift in power from the White Sands CGS setup to the BYU CGS setup evident in initial CGS calibration is observed at expected levels. The mean power difference between model and CGS data for the White Sands data is 1.24 dB. The



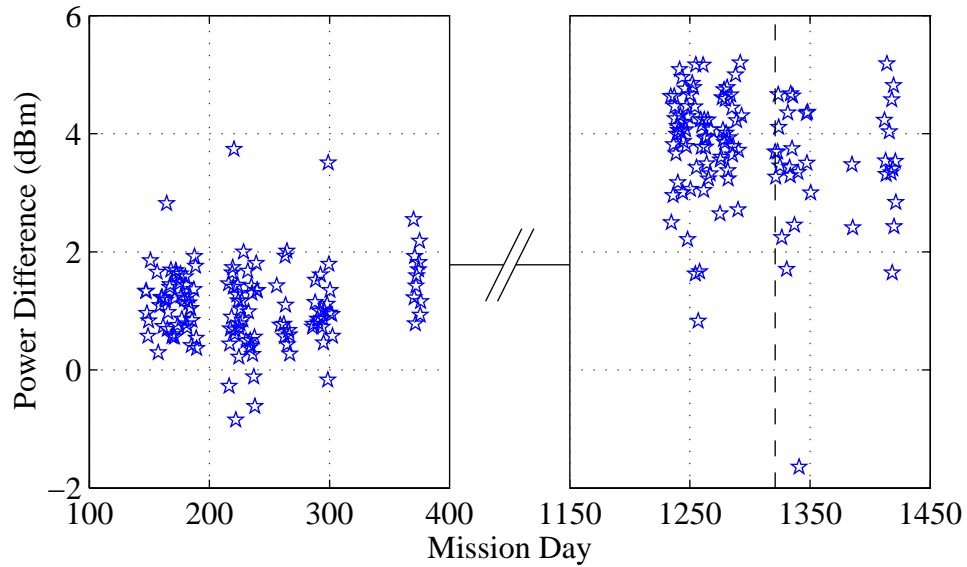


Figure 5.26: Mean power difference between CGS recorded power and model simulated power for each CGS capture as a function of mission day. The results correspond with the change in CGS recorded power from White Sands to Provo. They show that while some differences exist, the two instruments have relatively equal power levels.

mean difference for QuikSCAT at BYU is 3.71 dB. The mean power difference for SeaWinds at BYU is 3.29 dB. The standard deviation for each set is 0.73 dB, 0.86 dB, and 0.95 dB, consistent with the pointing sensitivity estimates. While the difference between White Sands and BYU has been discussed, a minor difference in received power exists between QuikSCAT and SeaWinds. This is accounted for by considering the following. First, there are a limited number of data points for SeaWinds due to the unavailability of instrument telemetry during the initial satellite calibration period. Second, the instrument is still in calibration phase and thus actual attitude does not necessarily match the telemetry reported values.

Figure 5.27 shows the power separated into ascending and descending passes. At White Sands the mean power difference is 0.24 dB, with descending being slightly larger. At BYU the orbit difference for QuikSCAT is 0.19 dB, and 0.04 dB for SeaWinds.

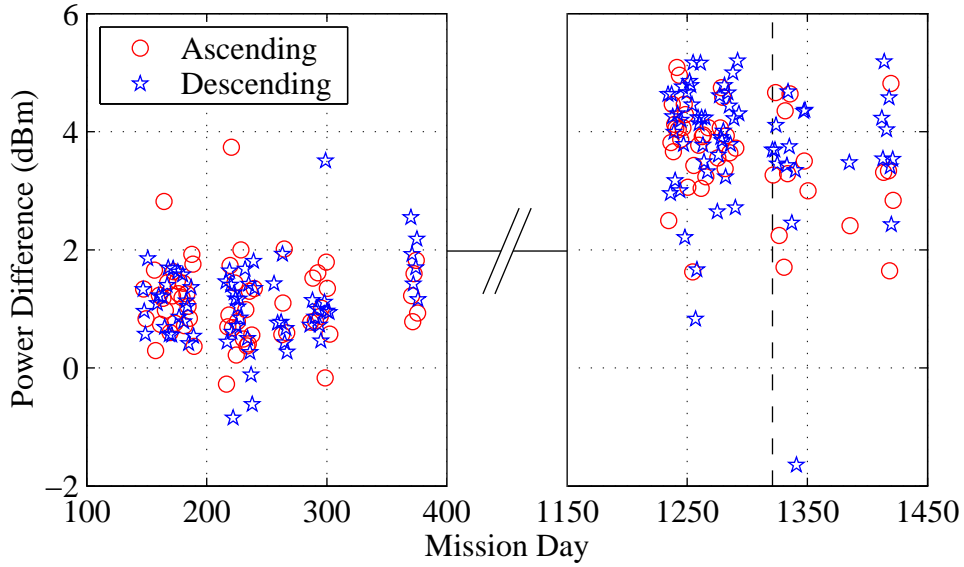


Figure 5.27: Mean power difference for each CGS capture as a function of mission day differentiated by orbit type. The data show no dependence of power on the location in the orbit where the capture occurred.

Finally, Figure 5.28 shows the received power separated into inner beam and outer beam captures. The inner beam shows a larger difference, meaning its power is less than the outer beam relative to the model. Some power difference is to be expected. Unmodeled terms such as instrument attenuation along with differences in antenna gain, instrument position and pointing, as well as excessive atmospheric attenuation all contribute to the difference. The key parameters here are first, the difference in beams and second, the cross-calibration between instruments. For QuikSCAT, the difference between beams is 1.53 dB at White Sands and 1.31 dB at BYU, the outer beam having the higher power. For SeaWinds the difference in beams is 1.39 dB, a relative difference to QuikSCAT of 0.08 dB. The deviation of each set of measurements is 1.2 dB.

The difference between the two beams is unquestionably large. Other calibration methods including the blind estimates confirm this conclusion. The large difference is attributed to discussed model inaccuracies relating to instrument timing

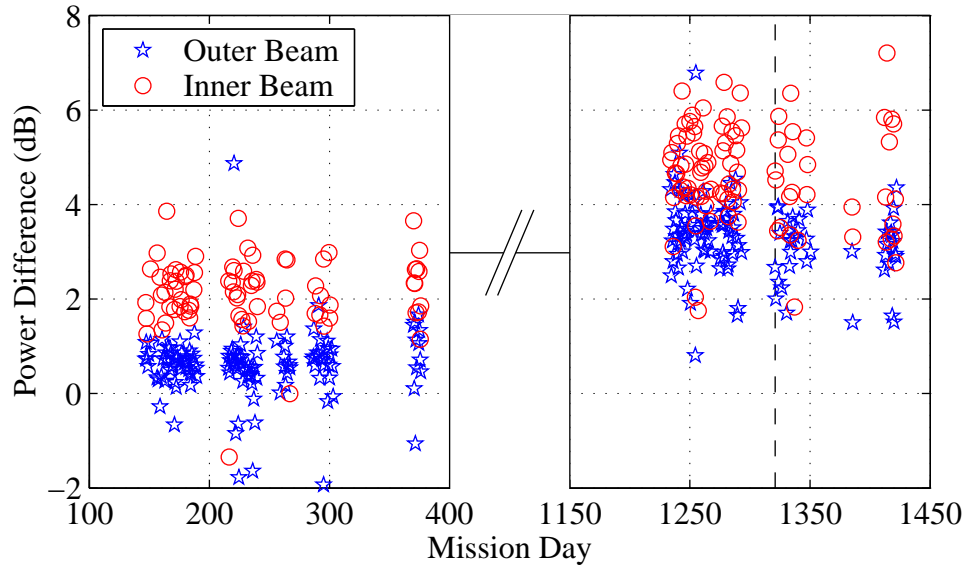


Figure 5.28: Mean power difference for each CGS capture as a function of mission day differentiated by transmitted beam. The data show a definite imbalance between inner beam and outer beam, with the inner beam corresponding better to the model simulations.

and pointing. The key observation is that values are consistent between instruments. This allows for accurate comparison of data measured with QuikSCAT to that measured by SeaWinds.

## 5.5 Summary

Previously, the SeaWinds CGS has been an underutilized option for calibration. Through the extensive development of the methodology, approach and implementation, including construction of the simulation model, the CGS is shown to be a viable calibration option. Initial calibration results show that the CGS performs in accordance with its precision design. Blind maximum likelihood estimates of timing and frequency provide excellent precision, exceeding all other previous estimates.

Unfortunately the limitations foreshadowed in the methodology concerning extended calibration appear in the results. The CGS reports that SeaWinds timing includes several inaccuracies. While these inaccuracies are in line with specified levels,

they exceed the requirements for accurate instrument characterization with CGS data. Attitude estimates displayed a precision of  $0.27^\circ$ . Sensitivity analysis shows that this level of precision relates to a 0.85 dB uncertainty in modeled power values. CGS power analysis reports similar variations.

Despite the disappointing pointing estimates, overall performance of the CGS, the methodology, and the implementation is exemplary. Table 5.3 highlights a list of key results provided by the CGS for both QuikSCAT and SeaWinds. Many of the results, particularly those relating to timing and frequency are several orders of magnitude better than any other available estimates.

The calibration results presented directly effect  $\sigma^\circ$  and measurement location performance. Observed timing errors introduce possible yaw-like biases. The mean timetag error of 8.25 ms translates to an antenna rotation of  $0.89^\circ$ , skewing the ground location of measurements by 18 km. This bias is significant when related to SeaWinds' 25 km ground footprint. Unfortunately it is impossible to know how timing directly effects spacecraft yaw due to the internal processing uncertainties described earlier (5.21). It is believed the yaw bias is on the order of  $0.20^\circ$ , more consistent with CGS attitude estimates, causing a 3.5 km ground shift. While 3.5 km is a more realistic value, it is still significant in terms of overall performance. Power measurements presented during blind calibration show a mean power bias of 0.3 dB. This value has a one-to-one relationship with reported  $\sigma^\circ$  values. In terms of application, a bias of 0.3 dB can effect estimated wind speed by up to 2 meters per second and wind direction by about  $10^\circ$ , though the exact values are related to several other variables as well.

Described limitations also highlight improvements for future instruments and ground stations. To obtain better precision in calibration, instrument timing must be improved and antenna directivity patterns must be measured with more precision. In addition, future ground stations would be well served if better pulse identification techniques were implemented such as polarization specific antennas or coded waveforms.

Table 5.3: Selected results of CGS calibration of SeaWinds. The results encompass both the blind calibration and comprehensive estimation procedures.

|                      | QuikSCAT      |                  | SeaWinds      |                  |
|----------------------|---------------|------------------|---------------|------------------|
| Category             | Value         | Deviation        | Value         | Deviation        |
| <b>Timing</b>        |               |                  |               |                  |
| Pulse Width          | 1.494924 ms   | 230 ns           | 1.494924 ms   | 230 ns           |
| PRI                  | 5.389527 ms   | 35 ns            | 5.398527 ms   | 35 ns            |
| Timetag Bias         | 8.25 ms       | 0.51 ms          | 14.43 ms      | 10 ms            |
| Timetag Slope        | 538.9527 ms   | $< 1\mu\text{s}$ | 5.38.9527 ms  | $< 1\mu\text{s}$ |
| <b>Frequency</b>     |               |                  |               |                  |
| Chirp Rate           | 250.747 MHz/s | 2.7 kHz/s        | 250.743 MHz/s | 2.7 kHz/s        |
| Center Frequency     | 13.402015 GHz | 32 kHz           | 13.402005 GHz | 32 kHz           |
| Doppler Compensation | 6.2 kHz       | 3.4 kHz          | 1.3 kHz       | 2.9 kHz          |
| <b>Power</b>         |               |                  |               |                  |
| Received Power Blind | -43.4         | -                | -44.16        | -                |
| Orbit Balance Blind  | -0.18 dB      | -                | 0.19 dB       | -                |
| Orbit Balance Model  | 0.22 dB       | -                | 0.04 dB       | -                |
| Beam Balance Blind   | 0.68 dB       | -                | 0.38 dB       | -                |
| Beam Balance model   | 1.42 dB       | -                | 1.39 dB       | -                |



## Chapter 6

### Measurement Location Calibration

Enhanced resolution imaging of measured backscatter has recently emerged as a valuable resource in measuring geophysical phenomenon. The ability of imaging applications to properly report  $\sigma^\circ$  depends upon accurate instrument calibration, primarily the calibration of measurement location. Measurement location refers to the latitude and longitude of each backscatter measurement. Erroneous measurement locations result in misplacement of physical features and significant degradation of pixel accuracy.

This chapter develops two distinct methods to assess the accuracy of scatterometer measurement location. The first method developed relates directly to the imaging of  $\sigma^\circ$  values. Backscatter values vary significantly between land and water. Boundary areas where these values converge, i.e. coast lines, provide a suitable location for estimation of location accuracy. The second method is a follow-on of CGS calibration. It uses the scatterometer calibration simulation model and CGS data to validate measurement location by reconstructing SeaWinds' transmit antenna pattern on the ground. Its direct focus on measurement location is able to overcome many of the sensitivity issues related to CGS estimation of attitude.

#### 6.1 Coastal Validation

An attractive method in validating scatterometer measurement location is data imaging. Images are an effective tool in comprehending large quantities of data and assessing overall instrument performance. Images are also an excellent medium for direct comparison of scatterometer data to coastal truth values. Properly located  $\sigma^\circ$  values displayed as an image create a picture which resembles the physical

geography of the measured scene. Mislocated values contort the scene, altering the shape and position of coast lines, lakes, and islands. More subtle mislocation reduce image clarity and contrast.

Two different variations of coastal validation using images have been developed. The first variation uses a rudimentary approach, termed gridding, which grids each measurement according to its centroid location. This approach was developed by Vincent Hsiao at the NASA Jet Propulsion Laboratory [20]. The second variation expands this approach by enhancing recorded backscatter data using the Scatterometer Image Reconstruction (SIR) algorithm [15]. The SIR algorithm uses a maximum entropy approach to synthetically enhance the resolution of the data beyond measured values. This allows for clearer definition of image boundaries and more accurate determination of measurement location.

The first step in both approaches is the choice of ground truth location. Islands and peninsulas are a clear choice for maximizing the coasts within the image. The relative size of a site is also an issue. Large locations require large amounts of data and computational time, small islands are compromised by the relatively coarse resolution of satellite scatterometers.

A second site related issue is the position of the site within the swath of the instrument. Measurements which occur at extreme azimuth angles (near  $90^\circ$ ) produce different results than do those near the nadir path ( $0^\circ$  azimuth) for pencil-beam scatterometers such as SeaWinds. As the instrument rotates its antenna the orientation of the measurement rotates as well. The effects of this rotation are exaggerated when range resolved 'slice' measurements are considered. (SeaWinds footprint is nominally 25 x 35 km. Slices are nominally 25 km x 7 km. Generally slice measurements are used for image reconstruction due to their finer resolution.) Figure 6.1 illustrates this effect. The orbit is nominally north-south. Therefore slice measurements which observe coastal areas with acute azimuth angles are oriented east-to-west, while measurements located at the edge of the swath are observed with north-to-south oriented slices.



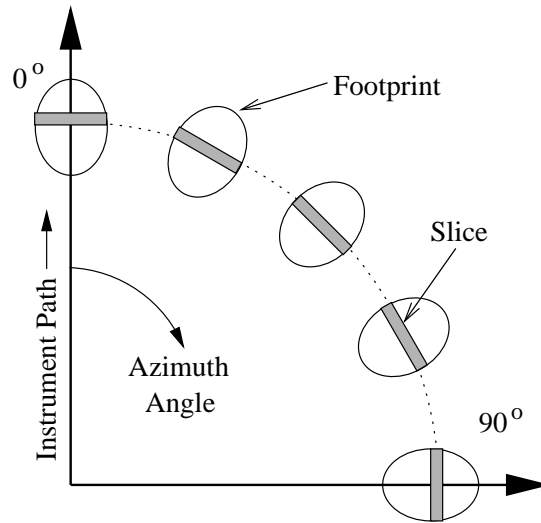


Figure 6.1: Orientation of measurement footprint and range resolved slices. The angle of each measurement relative to a fixed surface point rotates in concurrence with instrument azimuth.

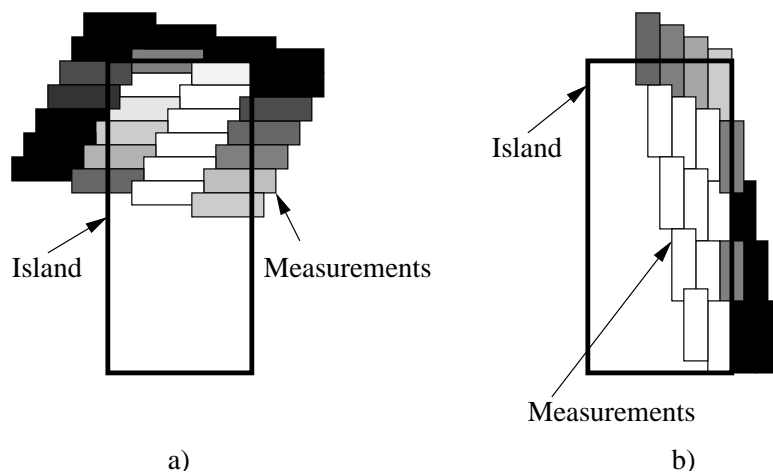


Figure 6.2: Illustration of the effect of measurement orientation on image-based measurement location validation. The left plot (a) shows slice measurements which are oriented east-west. These values accurately describe the top edge of the image but are poor estimators of the right side of the image. In comparison, the right image (b) shows north-south oriented slice measurements which accurately estimate the vertical edge, but poorly describe the top boundary.

Consideration of slice orientation relative to the site coastline is necessary due to related sensitivity issues. Figure 6.2 illustrates this phenomenon. The eastern boundary of the rectangular island is more accurately estimated by north-south measurements, while the northern boundary of the sample island is more accurately estimated using east-west measurements. A comprehensive analysis of measurement location thus requires the inclusion use of multiple areas to account for the imprecisions of measurement orientation.

The first variation of coastal imaging, the Hsiao approach, uses gridded data. A gridded image using 8 days of SeaWinds data over Puerto Rico is shown in Figure 6.3. From the data in the figure backscatter values of the ocean are discernable from values over land. However, detailed discrimination of the boundary is difficult. Many holes exist in the image due to insufficient data. The speckling effect of additive noise also reduces clarity. Measurement location estimates are obtained by calculating pixel biases, determining if pixels on the north side of the island have a greater magnitude than those on the south and so on. While the lack of a precise data image and variations of measurement orientation limit the precision of single image estimates, analysis of multiple sites over long time periods proves effective in measurement location calibration [20].

The second approach to coastal validation improves on the Hsiao approach in both choice of image construction algorithm and comparison to coastal boundaries. The Scatterometer Image Reconstruction (SIR) algorithm is specifically designed to enhance the resolution of scatterometer backscatter data by exploiting the diversity of orientation of each measurement [15]. Rather than simply grid the centroid of each measurement, each pixel is assigned a value by the algorithm based on the measurement which cover the pixel. This requires knowledge of the general measurement response function [7]. Figure 6.4 shows a SIR image of Puerto Rico using the same data set of Figure 6.3.

The application of this technique allows for sorting  $\sigma^\circ$  measurements using three criteria: polarization, orbit (ascending or descending), and look direction (fore or aft). Comparisons between various combinations of these parameters contribute

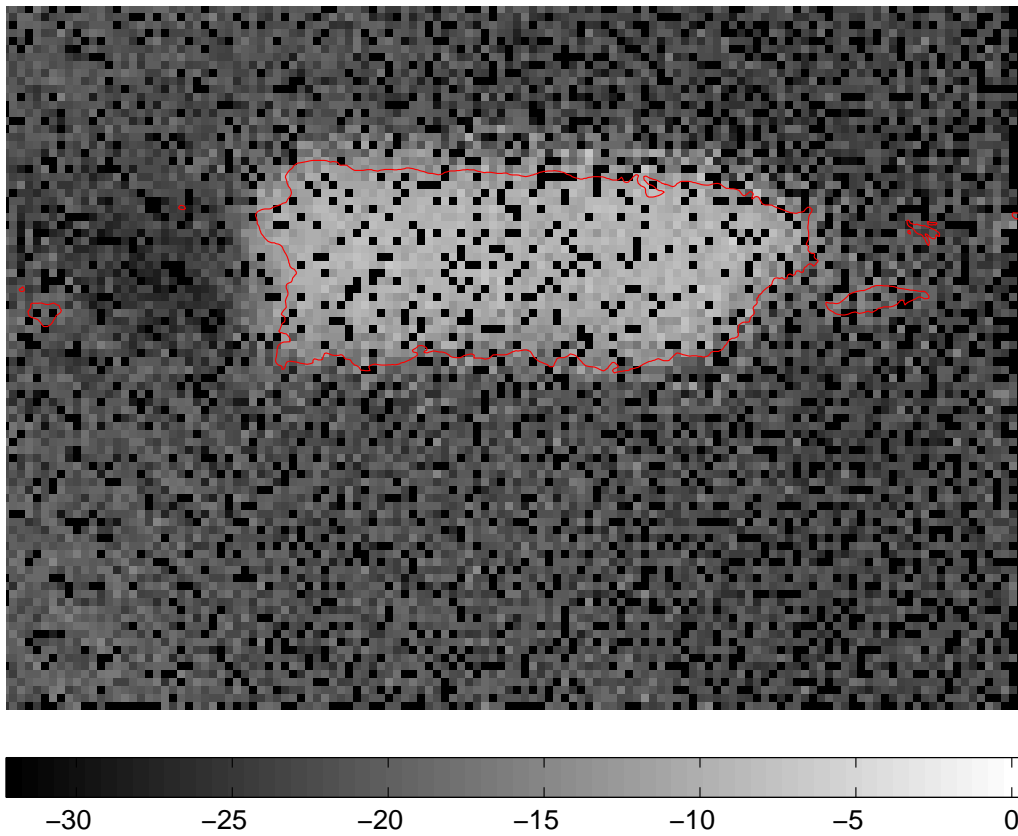


Figure 6.3: Gridded slice image of Puerto Rico. The superimposed coastline is taken from the CIA world database, pixel size is 2.5 km. The gridding technique causes holes in the image due to insufficient data and prevents noise suppression through measurement averaging.

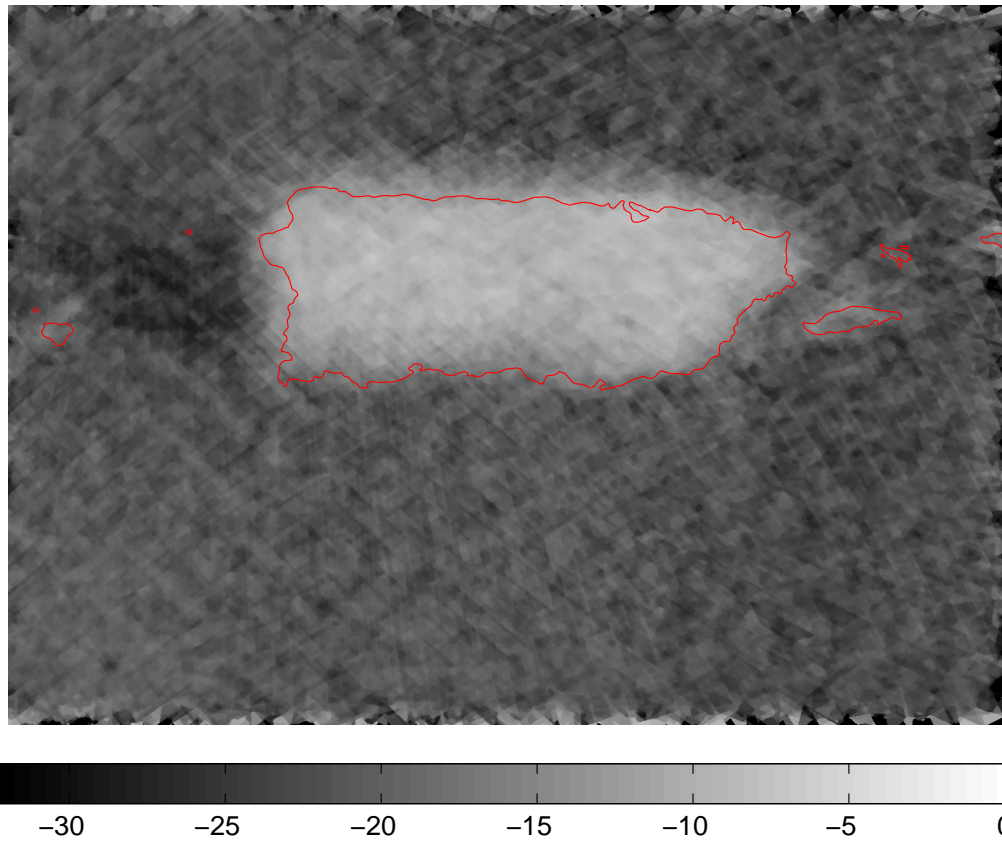


Figure 6.4: SIR enhanced  $\sigma^\circ$  image of Puerto Rico. A comparison of Figure 6.3 shows the improved resolution and edge sharpening ability of the SIR algorithm. Pixel spacing is 2.5 km.

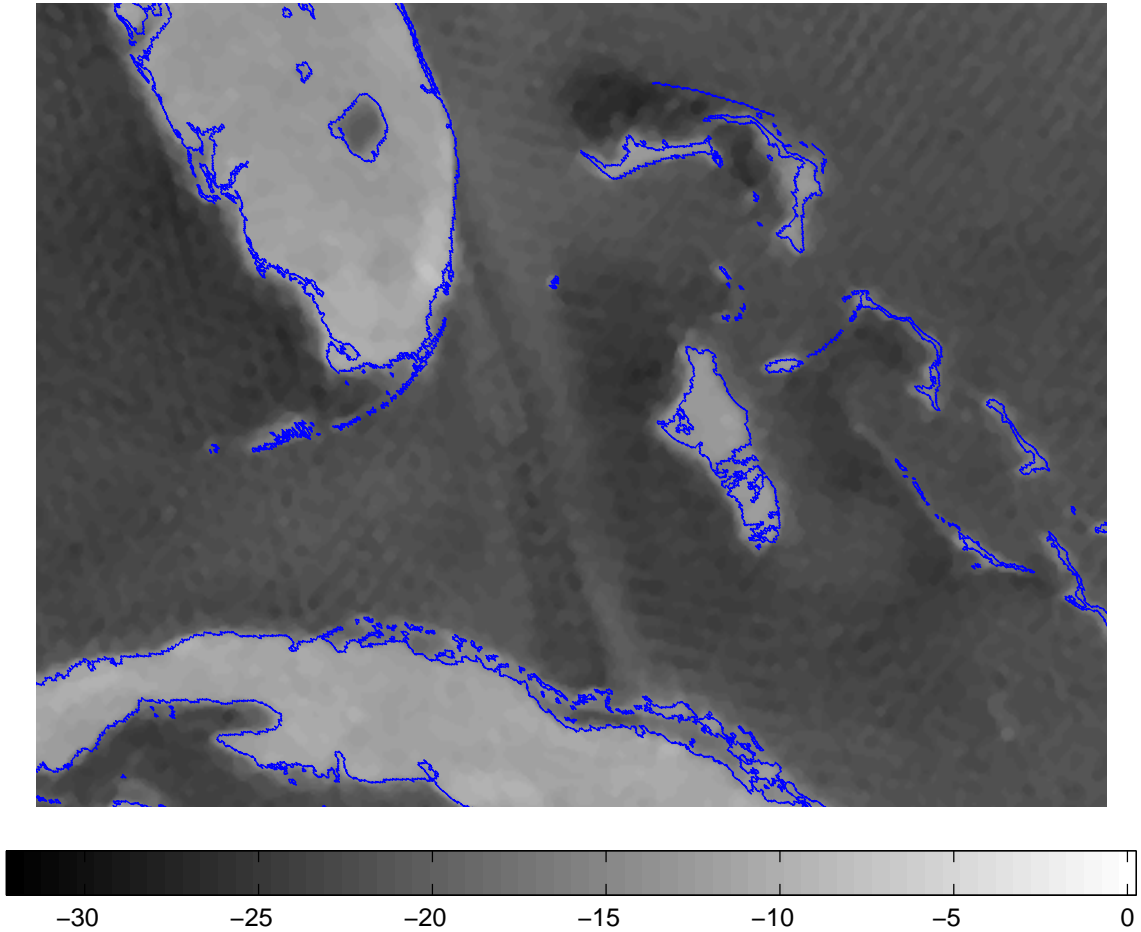


Figure 6.5: SIR-enhanced  $\sigma^\circ$  image of southern Florida, the Bahamas and Cuba, ascending orbits only, fore and aft azimuths, V-pol. Superimposed coast line added. The image is created using 28 days of QuikSCAT data, pixel size is 2.5 km.

to understanding causes of pulse mislocation by isolating measurement orientation biases.

Figure 6.5 shows a SIR enhanced  $\sigma^\circ$  image of southern Florida, the Bahamas, and Cuba. This site is selected over Puerto Rico for this example because of its size, diversity of landmass, and various coastal orientations. The image displays several principles of the SIR-based measurement location approach. First, the effects of slice orientation are visible. A distinct seam appears in the ocean parallel to the eastern coast of Florida due to the overlap of separate instrument swaths. Many of

the coast lines are crisply delimited by the superimposed coastline while other orientations are blurry. The image also demonstrates the ability of the approach to separate data into different categories (this image only uses data taken from ascending orbits).

The second improved feature of the SIR-based approach is the incorporation of difference images. Figure 6.6 shows a  $\sigma^\circ$  difference image between ascending-only data and descending-only data, highlighting differences in orbit direction. This difference image shows discrepancies of backscatter values near the Florida peninsula, northwest Cuba and southwest Andros Island, Bahamas. The black stripe on the west coast and white stripe on the east coast of Florida suggest an azimuth misalignment of about 7 km from east to west.

This observation is clarified by further refining the data selection process to also control look direction. Figure 6.7 shows the same region, subtracting descending pass, aft-looking measurements from ascending pass, fore-looking measurements. The white stripe on the east side of Florida is still present, but the black stripe is noticeably absent. Additionally the discrepancies in Cuba and the Bahamas are missing. This image is compared to its compliment, an ascending, aft looking and descending, fore looking difference image, shown in Figure 6.8. This image contains the dark strip on the west side of the Florida peninsula, but is missing the white stripe on the East side of the peninsula. The shift in the two images confirms what is suggested by Figure 6.6, that measurement location errors are present in the QuikSCAT data. In the look direction separated images (Figures 6.7 and 6.8) the discrepancy is on the order of 4 pixels, a difference of 10 km. The difference image emphasizes errors by doubling the observed difference, thus an observed 10 km error corresponds to an instrument bias of 5 km.

The technique of image comparison using parameter sorted images is effective in measurement location calibration. The 5 km discrepancy observed in these image is consistent with other methods, including the Hsiao gridding technique and is within specification for SeaWinds (see Table 4.1). Observations such as these are validated through data reprocessing. For QuikSCAT a yaw bias correction of  $0.17^\circ$  was proposed. Images created using revised telemetry confirm the accuracy of this

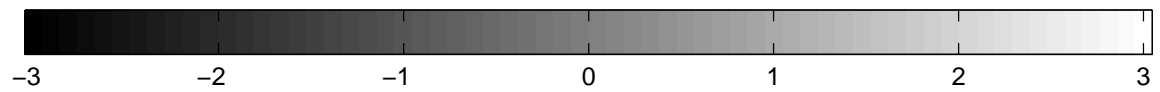
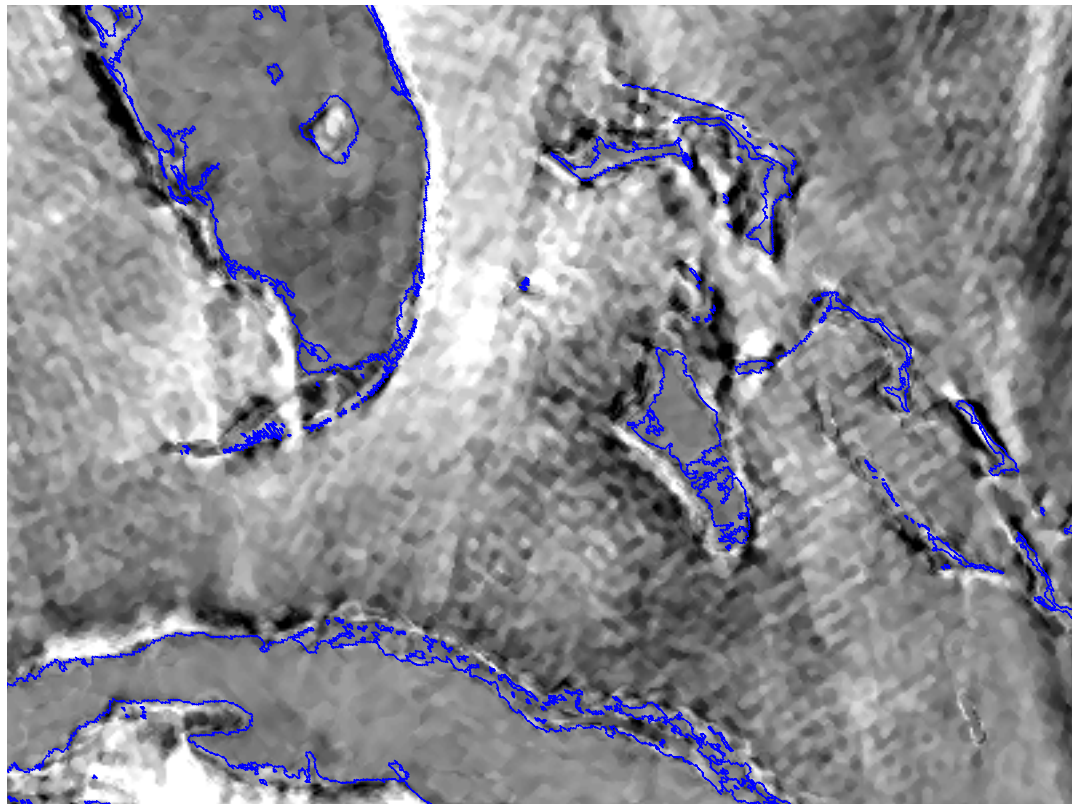


Figure 6.6: SIR enhanced image of an descending pass subtracted from an ascending pass, H-pol, combined fore and aft azimuths. Several discrepancies are observed through  $\sigma^\circ$  differences including both sides of the Florida peninsula, the northwest Cuban coast and the southwest edge of Andros Island, Bahamas.

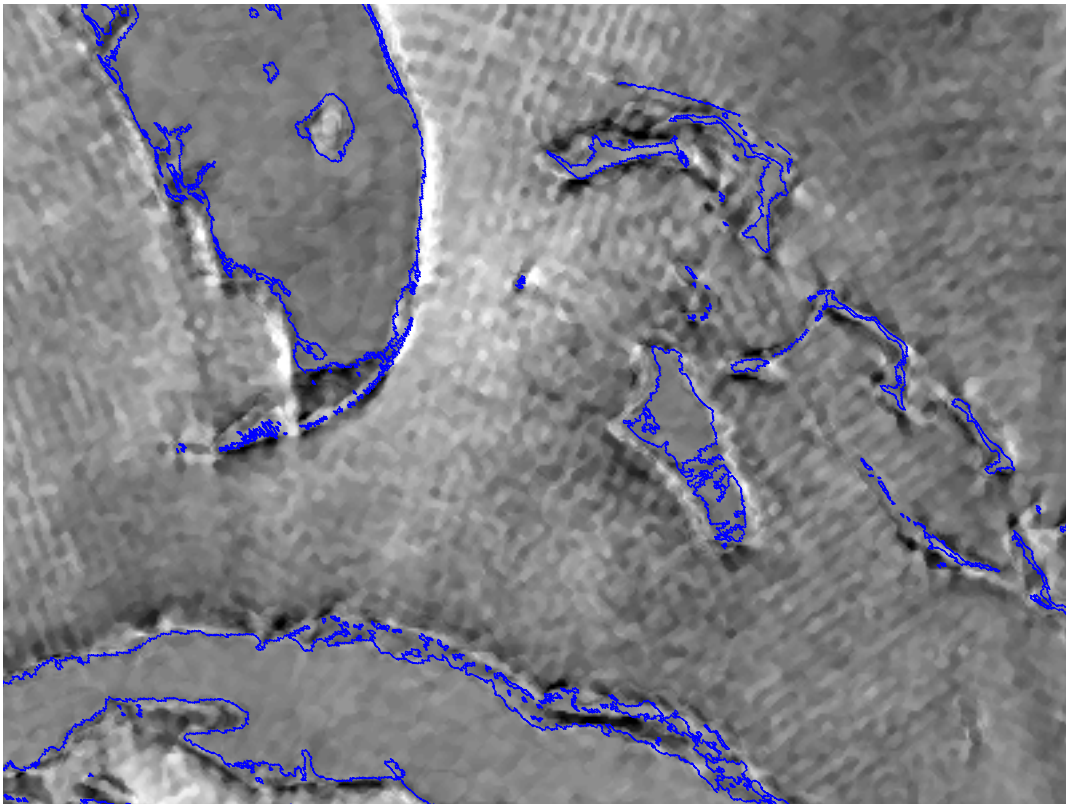


Figure 6.7: SIR enhanced image of an aft looking descending pass subtracted from a fore looking ascending pass, H-pol. With the exception of the eastern Florida coast the discrepancies observed in Figure 6.6 are noticeably absent.



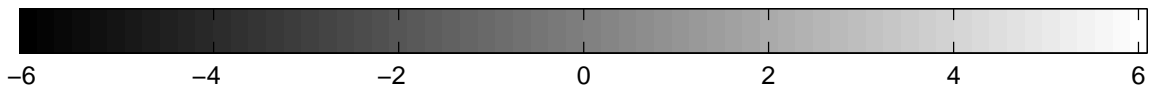
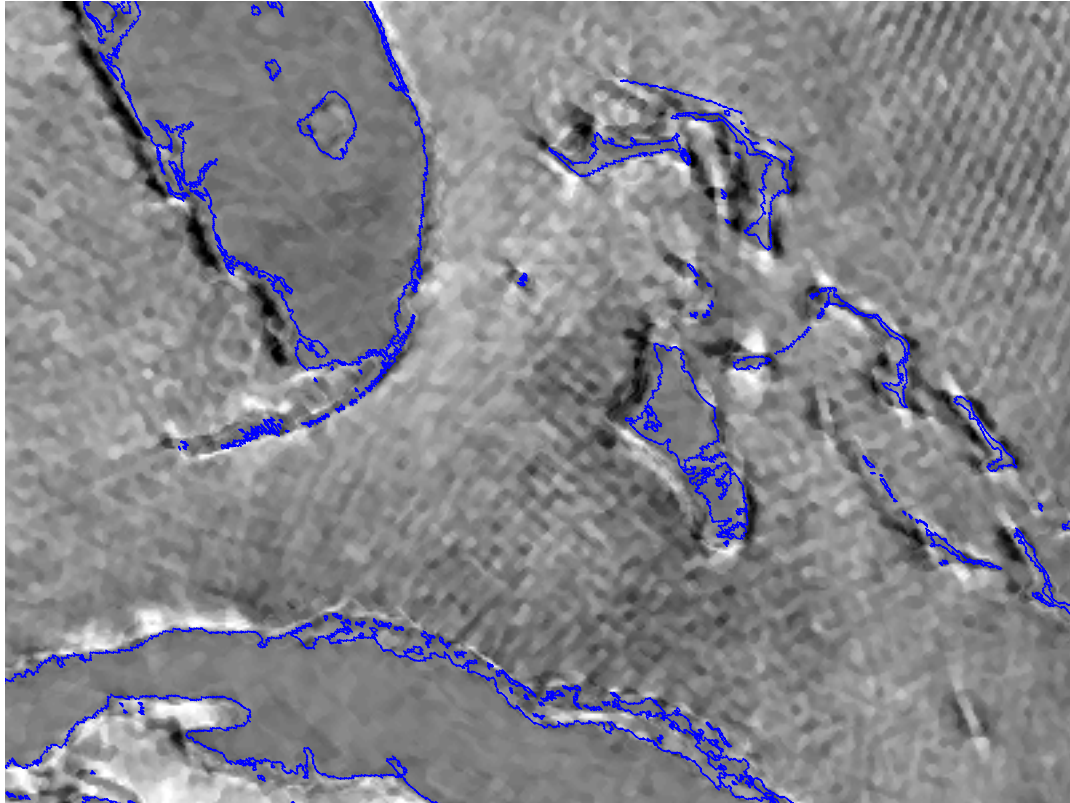


Figure 6.8: SIR enhanced image of a fore looking descending pass subtracted from an aft looking ascending pass, H-pol.

correction by displaying improved conformance with coastal edges, the residual error is zero. The intuitive simplicity of the method make it well suited for validation of instrument operation. For example, when QuikSCAT was first launched it had a timing error of 1 second, significantly mislocating measurements. Images such as these quickly and conclusively observed the mislocation.

## 6.2 Antenna Pattern Reconstruction

The second method of measurement location validation is termed the antenna pattern reconstruction method. The method utilizes SeaWinds CGS data and the SeaWinds simulation model much like the CGS calibration analysis. Its focus on measurement location allows it to use relative pulse power values measured by the CGS, rather than absolute power estimates for power calibration, thus eliminating errors caused by small power biases and minor CGS variations.

The antenna reconstruction method is similar to the measurement of an antenna directivity pattern on an antenna range. In conventional antenna pattern measurement, a transmitter is placed in a fixed position and the antenna under test is rotated while directivity values over a variety of angles are measured. Opposite to this idea, the antenna pattern reconstruction method holds the receiver (the CGS) fixed while the antenna under test (the satellite instrument) is displaced. In this situation, unlike an antenna range which employs only antenna rotation, the instrument is the transmitter and is translated due to orbit motion, and the CGS is the fixed receiver. Measurement location calibration is derived from this arrangement by calculating the boresight pointing of the test antenna for each pulse and relating it to the measured power of the calibrated antenna.

A single CGS capture constitutes one set of test measurements and consists of several (3-6) sweeps with each sweep having 15-20 pulses. For each pulse the simulation model uses reported telemetry to calculate the ground location of the antenna boresight and the pointing angle of the instrument antenna relative to the CGS, as shown in Figure 6.9. The figure shows the SeaWinds transmit antenna pattern for the outer beam as a function of azimuth and elevation angle relative

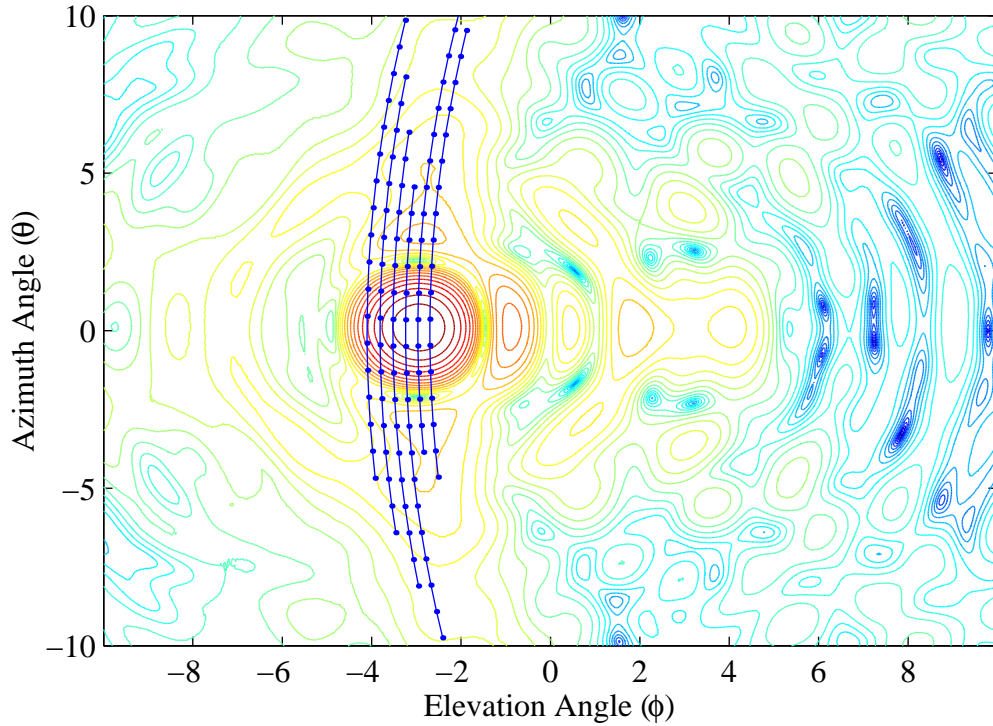


Figure 6.9: SeaWinds' outer beam antenna pattern as a function of antenna pointing angle,  $(\theta, \phi)$ . The points on the pattern correspond to the relative azimuth and elevation angles of the ground station for each pulse during a capture.

to the mechanical boresight, the electrical boresight of the V-pol antenna beam is located at  $-3^\circ$  relative elevation and  $0^\circ$  azimuth. The figure also shows the relative instrument pointing angle of the CGS for each pulse captured by the ground station during a particular capture.

Based on the antenna range example, pattern reconstruction requires associating the transmit antenna's boresight location to the power measured by the receiver. This combination is the receiver's assessment of the transmit antenna pattern. In theory, this pattern is a mirror image of the true antenna pattern (which is measured before launch on a conventional antenna range), inverted in both azimuth and elevation. If the pointing reported by the antenna under test is accurate, the boresight of the recorded pattern is centered at the location of the calibration antenna. If the reconstructed boresight is mislocated the instrument reported pointing

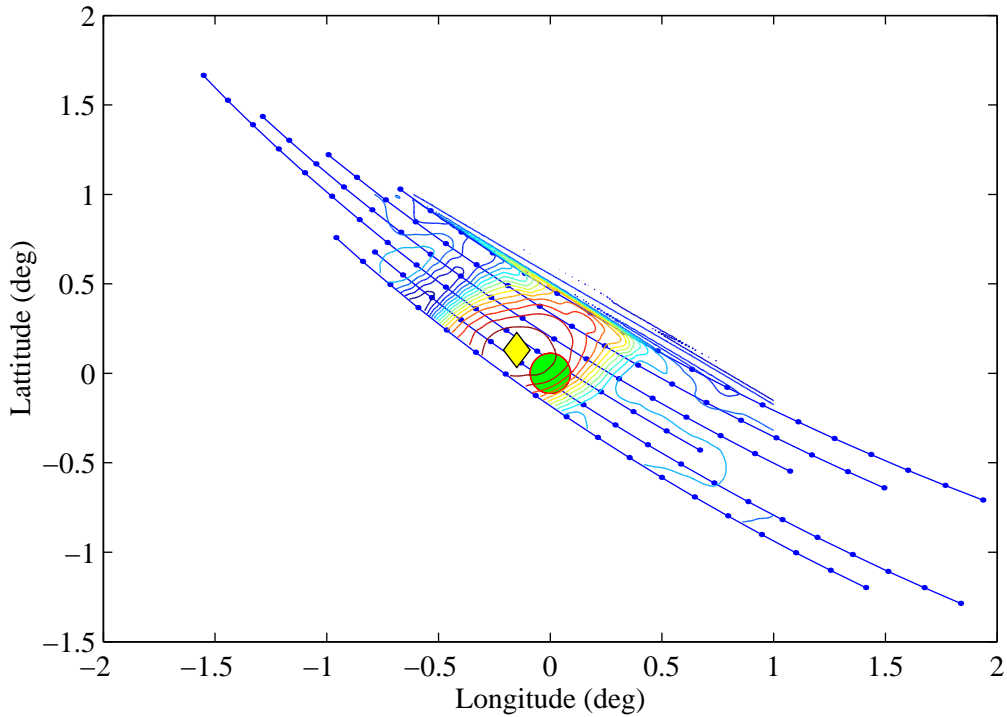


Figure 6.10: CGS reconstruction of the transmit antenna pattern with the CGS determining the elevations of each contour. The location of the CGS is represented by a large circle at the origin, all latitude and longitude values are plotted with respect to the CGS location. The lines represent the path of the transmitter on the ground, with the dots referencing its location when a pulse is transmitted. The lines are mirror images of those in Figure 6.9. The center, or boresight, of the reconstructed pattern, represented by a diamond, is based on the power measurement. The fact that the diamond and circle do not align suggests a location error of  $0.2^\circ$  longitude and  $0.1^\circ$  latitude.

is in error or the transmit antenna pattern relative to its pointing calculations is in error. Both errors cause measurement location discrepancies.

Figure 6.10 provides an example of a CGS reconstructed antenna pattern. The latitude and longitude of each measured pulse are scaled so that the location of the CGS (shown as a circle) corresponds to the origin of the figure. The lines, the same as in Figure 6.9, show the calculated location of the transmitter boresight for each pulse. The calculated boresight of the reconstructed pattern is shown as a diamond.

Errors in CGS power measurements do not effect the method so long as power measurements are consistent over the data capture. Likewise pointing variations do not effect the method as long as they are consistent from one pulse to the next. The pattern reconstruction is dependent on the spatial diversity of the sampling. As Figure 6.10 shows, there are more than enough samples to reconstruct the pattern in azimuth. However, elevation sampling is limited, caused by two factors. First, the CGS limits its capture duration since it must store data for four separate SeaWinds beam crossings for each pass. Second, the CGS must predict when to capture based on instrument ephemeris. The accuracy of this prediction is on the order of a few seconds. Antenna sweeps occur every 3 seconds, thus slight inaccuracies in orbit prediction, coupled with limited sampling duration, create the possibility of not observing the instrument boresight during capture. Figure 6.11 provides an example where the CGS failed to capture at an opportune time, resulting in a poor reconstruction of the transmit antenna pattern. Longer captures could prevent this problem.

In light of these limitations a quality rating system is developed to assist in evaluating the accuracy of the antenna pattern reconstruction method. Each reconstructed pattern is objectively evaluated according to the following criteria. Thus reported location errors from poor reconstructions are not given the credence that location errors from high quality captures receive. The quality rating system is as follows:

- 0: CGS location is outside the sweep coverage
- 1: CGS location is inside sweep coverage, but the center contour is obtuse
- 2: Center contour is acute but is not a complete circle
- 3: Complete center contour.

Using this rating system the pattern in Figure 6.11 scores a 1, and the pattern in Figure 6.10 scores a 2.

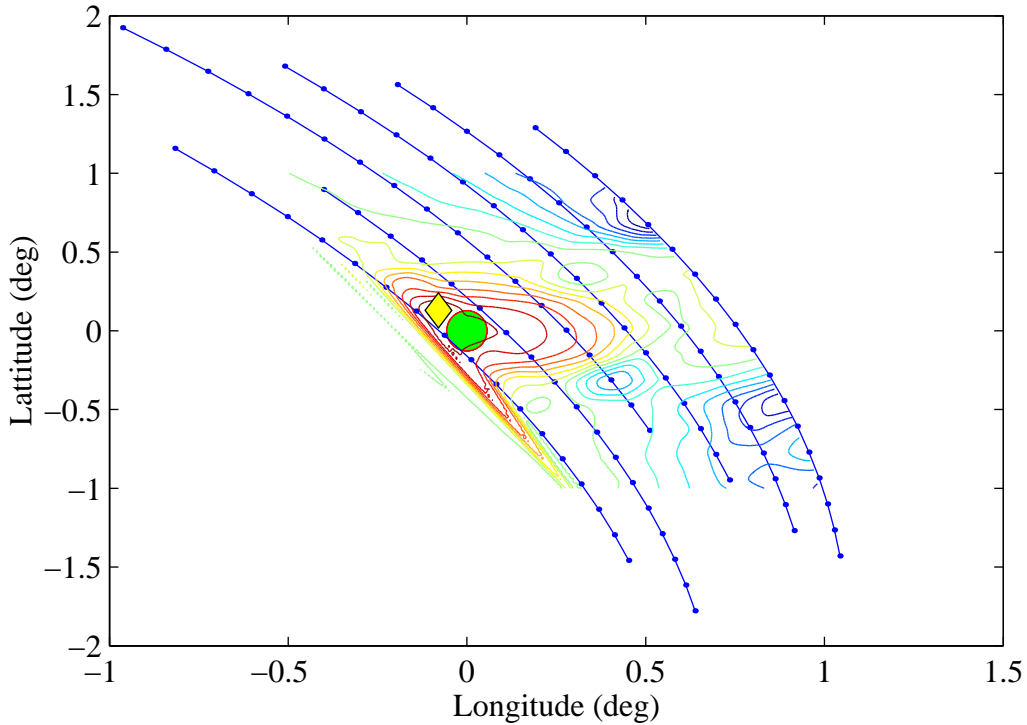


Figure 6.11: An example of a CGS reconstruction of the transmit antenna pattern where the capture did not occur at the right time, resulting in a poor reconstruction. The peak of the captured data is shown as a diamond.

Results of the method are shown in Figure 6.12, with the scatter plot showing measurement location error in latitude and longitude and the symbols representing reconstruction quality. The captures depicted in the figure correspond to a two month time span of QuikSCAT captures, all timing biases are removed. The figure shows that the measurement location results are highly correlated with pattern quality. For quality ratings of 0 or 1 the results are scattered, while the quality 2 and 3 results are clustered about the origin. The mean latitude of the entire data set is zero, while the mean longitude error is  $0.0145^\circ$ , about 1.25 km, within expected values.

These results are also shown using a histogram of distance error separated by quality in Figure 6.13. The figure shows the percentage of each distance error, separated by quality factor. The mean error of the quality 0 patterns is 20.33 km

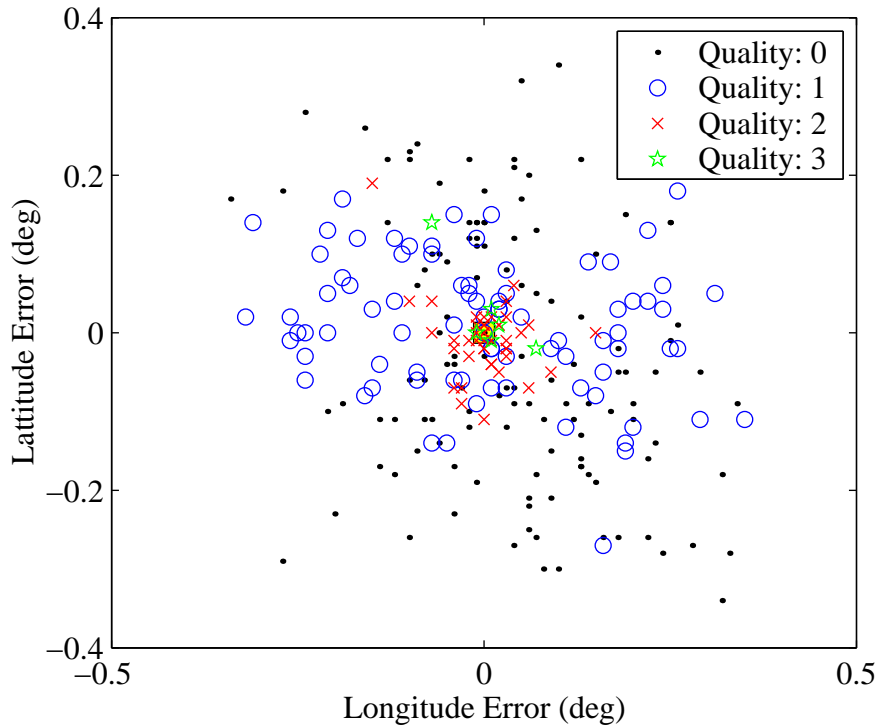


Figure 6.12: Scatter plot of measurement location error using the antenna pattern reconstruction method. The figure shows that measurement location results are highly correlated with the pattern quality.

with a standard deviation of 10.3 km. The mean error of the quality 1 patterns is 15.24 km with a standard deviation of 7.8 km. For quality 2 patterns the mean and standard deviation are 5.4 km and 6.2 km respectively, and for quality 3 they are 4.7 km and 5.5 km.

A further result of the investigation is shown in Figure 6.14, a histogram of the percentage of occurrence of each quality factor, separated by capture type. The figure shows clearly that the 20 second long captures (6 sweeps) outperform the 10 second captures (3 sweeps) in terms of reconstruction quality. The majority of three sweep captures do not include the boresight in the pattern (quality 0), completely discounting their results. The majority of the longer captures provided good

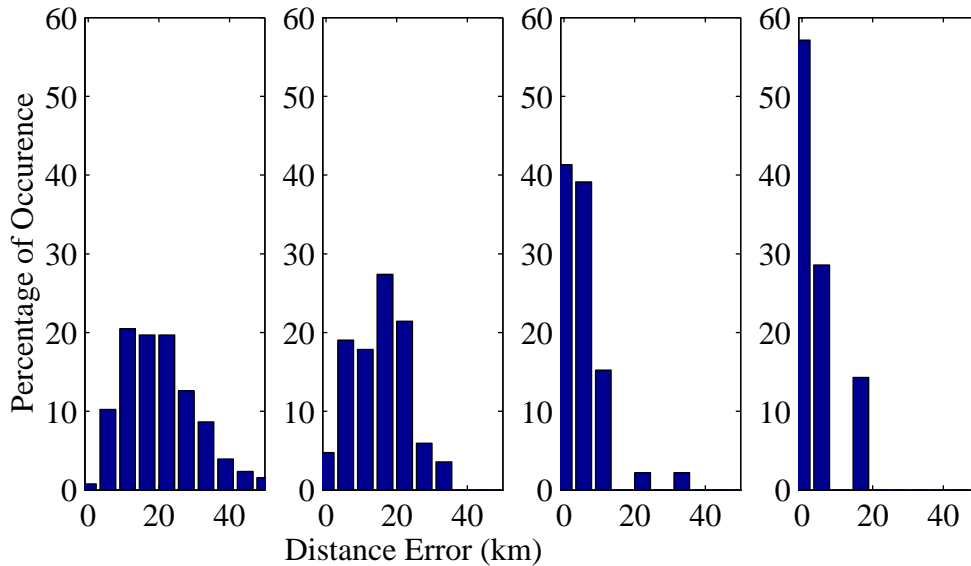


Figure 6.13: Distance error results for each quality rating. Each subplot shows the percentage of occurrence for a given distance. The first plot (far left) represents patterns with a quality rating of 0. The second plot shows reconstructions with a quality of 1. The third plot’s quality is 2, and the fourth plot (far right) shows error for patterns with the highest quality, 3.

reconstruction (quality of 2 or 3) though the high occurrence of poor quality captures suggest that even longer CGS captures are needed to improve the accuracy of estimates.

The combination of these distributions and the associated distance error results show that the duration of CGS captures is the limiting factor in the accuracy of this method. Thus, the method lacks sufficient data to provide accurate, long term monitoring of measurement location. However, the results suggest that future ground stations which are able to provide longer durational captures will be able to accurately measurement location accuracy using the antenna pattern reconstruction method, thus overcoming the power limitations present in other CGS estimation approaches.



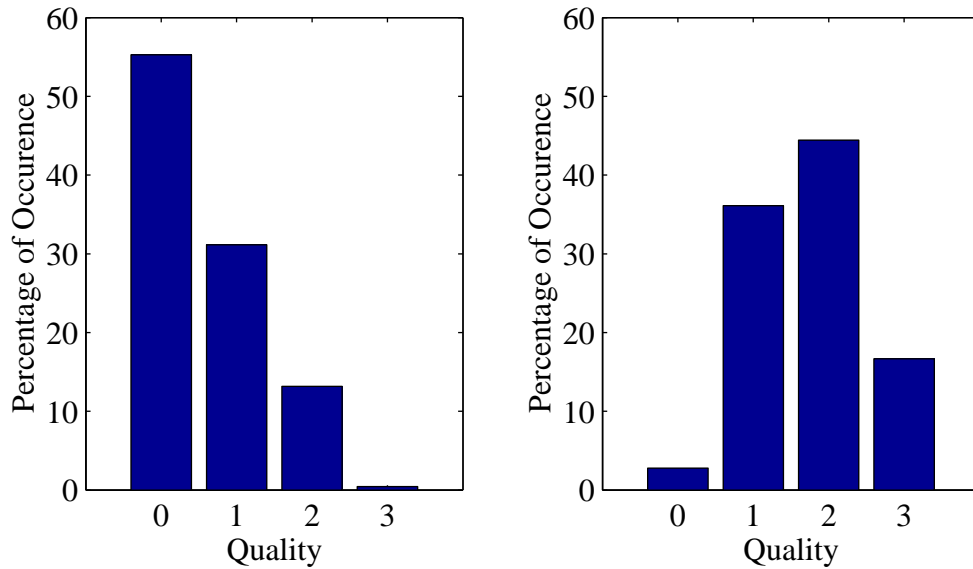


Figure 6.14: Distribution of quality factors for three sweep captures (left) and six sweep captures (right). The distributions clearly show the improved performance of the antenna pattern reconstruction algorithm with the addition of more antenna sweeps (longer capture time).

### 6.3 Summary

The two separate methods of measurement location estimation demonstrate new, applicable techniques for instrument calibration. The image-based approach directly estimates the quality of measurement location calibration by using SeaWinds end data products. The new method developed improves upon the Hsiao gridding technique by using an improved image resolution algorithm and separating the data by orbit, direction, and polarization to better identify the cause of measurement location errors. For the QuikSCAT data shown, the mean error is 5 km, attributed to a  $0.17^\circ$  yaw bias by the satellite. This error is shown by using difference images between various orbit passes and look directions. The second approach, the antenna pattern reconstruction method, uses an indirect approach to estimate location accuracy. Though the results are limited by the accuracy and duration of CGS data captures, when enough data is available, the results correspond well to other

values, including the image-based technique. The data shown for QuikSCAT shows a mean error of 4.7 km for quality 3 captures, confirming the accuracy of the both techniques developed. The antenna pattern reconstruction is also able to establish error bounds on measurement location, the standard deviation of quality 3 captures being 5.5 km.

The effects of measurement location errors are significant. Currently established resolution enhancement techniques for imaging use a pixel size of 2.5 km. Measurement location errors of 5 km, cause pixel magnitudes to be offset by two pixels, blurring images and misrepresenting observed backscatter values. The mislocation of  $\sigma^\circ$  values also effects wind retrieval. Algorithms which use co-located measurements are degraded in performance when the measurements are not truly co-located, the extent of the effect being dependent upon several factors related to geometry.

## Chapter 7

### Correlation of Scatterometer Measurements

Satellite scatterometers have demonstrated an ability to not only estimate ocean wind speed and direction, their original goal, but to also investigate sea ice extent, iceberg location, snow melt cycles, and tropical deforestation [14]. The emergence of additional applications has become a catalyst for development of more capable instruments and new data processing algorithms. New algorithms exploit the spatial overlap and dissimilar geometry of co-located measurements, for new and old instruments alike, to improve the effective measurement resolution [15]. New scatterometer designs seek to increase resolution by providing more surface samples and processing the signal response more effectively [49].

The designs of newer instruments provide dense, overlapping samples of the surface, a significant change from earlier instruments. This introduces several issues which have not been explored in detail previously. A key issue addressed here is correlation between individual measurements. Correlation decreases the number of independent samples obtained by a measurement, degrading data accuracy and precision.

This chapter derives expressions for the correlation of scatterometer measurements and discusses its effect on measurement accuracy. The chapter is organized as follows: Section 7.1 presents principles relevant to the discussion of scatterometer measurements, such as scattering and fading and develops a general signal measurement model. It then derives expressions for multi-measurement statistics. Section 7.2 considers additive noise. The full theory statistically accounts for the combined random fluctuations of additive thermal noise and multiplicative signal fading. Section 7.3 provides analysis of derived coefficients, focusing on a covariance term present in

the correlation and covariance expressions. The section applies the derived results to two pencil-beam instruments to provide general guidelines of how the measurement process effects correlation values. Section 7.4 then uses the results of Sections 7.1 and 7.2 to define the commonly used metric  $K_p$  for multiple pulse measurements. It discusses the effects of correlation on  $K_p$  as well as tradeoffs that exist between pulse correlation, noise power, and measurement precision. Finally, Section 7.5 summarizes findings and concludes.

## 7.1 Interaction and Statistics of Multiple Measurements

Traditionally, consecutive measurements from satellite scatterometers have been assumed to be independent. This assumption is based on the short correlation length of natural surfaces and minimal spatial overlap between measurements. Newly proposed systems which oversample the surface require reconsideration of this assumption. While the spacing between measurements for these instruments is more than the correlation length of the surface, it is not large enough to justify independence of fading between pulses since the measurement footprints significantly overlap. For this reason we consider the relationship between multiple measurements.

### 7.1.1 Surface Scattering for Distributed Targets

When a microwave radar signal impacts a conductive surface a portion of the signal energy is reflected back toward the origin of the incident wave. This reflection is termed backscatter, and can be represented for a point target, by the complex value  $z$ , the electric field (in volts) of the backscatter. The large footprint area of scatterometer measurements causes the transmitted signal to be simultaneously incident on a large number of scatterers, termed a distributed area target. The response from a distributed target can be modeled by the coherent sum of the response from each point scatterer,

$$Z = \sum_i z_i = v_d e^{j\phi_d}, \quad (7.1)$$

with magnitude  $v_d$  which is Rayleigh distributed and phase  $\phi_d$  which is uniformly distributed [55]. Applying the central limit theorem (by assuming that there are a

large number of scatterers in the distributed response) and assuming that no scatterer dominates the overall return, the real and imaginary parts of the individual responses,  $r_i$  and  $q_i$ , may be assumed to be independent, normally distributed random variables with mean zero and variance  $\sigma$  [55]. The expected value of the voltage magnitude is  $\mathcal{E}[v_d] = \sqrt{\frac{\pi}{2}}\sigma$ , where  $\mathcal{E}$  is the expected value operator; the second moment of the voltage magnitude is  $\mathcal{E}[v_d^2] = 2\sigma^2$ . It is assumed that  $v_d$  and  $\phi_d$  are independent for each distributed target considered. This is reasonable considering that most surface features have sub-meter correlation lengths and most scatterometer measurements encompass several kilometers. Stationarity for both magnitude and phase of the distributed targets is also assumed. The normalized radar cross section of the area,  $\sigma^\circ$ , is related to the voltage response by [55]

$$\mathcal{E}[v_d^2] = \mathcal{E}[|Z|^2] = A_d\sigma^\circ, \quad (7.2)$$

where  $A_d$  is the area of the distributed target.  $\sigma^\circ$  is therefore proportional to the variance of real and imaginary parts of the individual scatterers.

Using the properties of a uniform distribution, the correlation between the response of two distributed targets can be written as (see Appendix B.1.1)

$$\mathcal{E}[Z(a)Z^*(b)] = A_d(a)\sigma^\circ(a)\delta(a-b). \quad (7.3)$$

Later it will also be necessary to utilize the fourth order expectation of distributed targets which can be shown to be (see Appendix B.1.2),

$$\begin{aligned} \mathcal{E}[Z(a)Z^*(b)Z(c)Z^*(d)] = & A_d(a)\sigma^\circ(a)\delta(a-b)A_d(c)\sigma^\circ(c)\delta(c-d) \\ & + A_d(a)\sigma^\circ(a)\delta(a-d)A_d(c)\sigma^\circ(c)\delta(b-c). \end{aligned} \quad (7.4)$$

### 7.1.2 Scatterometer Signals

A scatterometer transmits a modulated carrier signal of the form

$$\xi_t(t) = \sqrt{E_t}a(t)e^{j\omega_c t} \quad (7.5)$$

where  $t$  is time,  $E_t$  is the total transmitted energy for a single pulse,  $\omega_c$  is the angular center frequency, and  $a(t)$  is the complex modulation function with

$$\int_0^{T_a} |a(t)|^2 dt = 1 \quad (7.6)$$

and  $a(t) = 0$  for  $t < 0$  and  $t > T_a$ .

Ignoring spreading loss and antenna gain for the moment, the echo return of the scatterometer signal from a single point scatterer can be written as

$$\xi_r(t) = z \left( \sqrt{E_t} a(t - 2r/c) e^{j\omega_c t} e^{-j\omega_d t} e^{j2\omega_c r/c} \right), \quad (7.7)$$

where  $r$  is the range from instrument to the point scatterer and  $\omega_d$  is the Doppler shift of the point,

$$\omega_d = \frac{2\nu_r}{\lambda} \quad (7.8)$$

with  $\nu_r$  being the relative velocity between the instrument and the point scatterer. This expression assumes that changes in spacecraft velocity during the transmission and reception cycle need not be considered in the Doppler shift, which generally holds when pulse periods are less than 1 second and center frequencies are greater than 1 GHz [35]. Accounting for antenna gain and spreading loss terms, the return signal echo for the  $i^{th}$  scatterer can be written as

$$\xi_r(t, i) = z_i \left( \frac{G(i)\lambda}{(4\pi)^{3/2} r^2(i)} \right) \left( \sqrt{E_t} a(t - 2r(i)/c) e^{j\omega_c t} e^{-j\omega_d(i)t} e^{j2\omega_c r(i)/c} \right), \quad (7.9)$$

where  $\lambda$  is the signal's wavelength, and  $G$  is the antenna gain in the direction of the point scatterer.

### 7.1.3 Instrument Measurement

Without some form of Doppler or range filtering, the resolution of a measurement is limited to the size of the antenna footprint, typically described by the antenna pattern 3 dB beam width. Utilizing Doppler and/or range filtering improves the effective resolution of the instrument by separating the antenna footprint into multiple distributed targets [49]. Figure 7.1 illustrates this principle for a general footprint geometry. The large circle represents an antenna footprint and the included

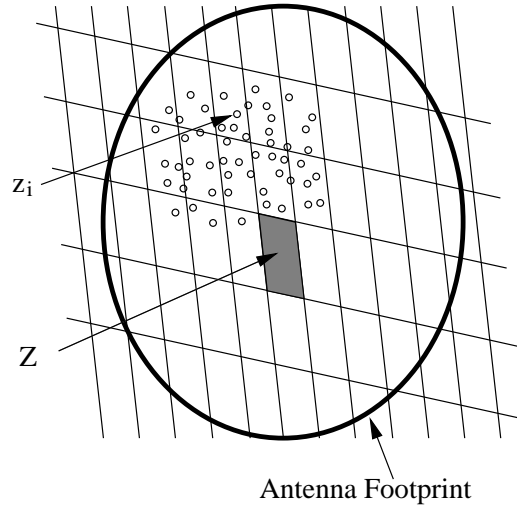


Figure 7.1: Simplified geometry of a scatterometer footprint. Each  $z_i$  represents an individual scatterer.  $Z$  is the total voltage response of one resolution element, consisting of a large numbers of individual scatterers. The elliptical footprint is the 3 dB contour of the illumination pattern.

lines represent an arbitrary resolution grid generated by range and Doppler filtering. The maximum resolution of a scatterometer is a function of pulse length, signal wavelength, frequency modulation, and processing, and constitutes a single resolution element. For scatterometers, this limit is generally on the order of hundreds of meters, allowing the assumption that a large number of scatterers exist in every resolution element and thus the properties of distributed targets is applied.

Using (7.1) the return echo from each resolution element consists of the sum of the individual point scatterers within the element,

$$\xi_r(t, n) = \frac{\sqrt{E_t \lambda}}{(4\pi)^{3/2}} \sum_{i_n} z_{i_n} \frac{G(i_n) a(t - 2r(i_n)/c) e^{j\omega_c t} e^{-j\omega_d(i_n)t} e^{j2\omega_c r(i_n)/c}}{r^2(i_n)}, \quad (7.10)$$

where the sum is over the  $i$  scatterers within the  $n^{th}$  resolution element. For a satellite, the range term is very large in comparison to the change in range for each element. It is therefore assumed that the denominator,  $r^2$ , is constant over the sum for each resolution element and its mean value,  $\bar{r}^2$ , is used. For simplicity, it is also assumed that gain and observed Doppler are constant over each resolution element, and that

the group time delay and phase shift can be sufficiently modeled using the mean range value for each resolution element. Employing an orthogonal  $(x, y)$  coordinate system aligned with the along track and cross track directions of the spacecraft, the return signal for each element is

$$\xi_r(t, x, y) = \frac{\sqrt{E_t \lambda}}{(4\pi)^{3/2} \bar{r}^2} Z(x, y) G(x, y) a(t - 2\bar{r}(x, y)/c) e^{j\omega_c t} e^{-j\omega_d(x, y)t} e^{j2\omega_c \bar{r}(x, y)/c}, \quad (7.11)$$

which is the generalized return signal for a scatterometer.

Scatterometers make measurements of distributed targets in a variety of ways, depending upon requirements for resolution, the instrument modulation function, receiver hardware, and signal processing. In general, instruments use a form of square-law detection so the measurements can be written as

$$M^s = \Omega \left| \Omega \xi_r(t, x, y) \right|^2 \quad (7.12)$$

where  $M^s$  denotes a signal measurement and the  $\Omega$  operator represents a summation, either discrete or continuous, over area and time, as required to describe the resolution filtering desired by the specific instrument. A low resolution measurement utilizing square-law detection and no filtering can be described by

$$M^{as} = \int_t \left| \int_x \int_y \xi_r(t, x, y) dy dx \right|^2 dt, \quad (7.13)$$

the superscript in  $M^{as}$  denoting antenna resolution,  $t$  spans the duration of the return echo and  $x$  and  $y$  span the footprint area. Filtering with maximal resolution over range and Doppler can be modeled as

$$M^{ms} = \left| \int_{\omega} \int_t \int_x \int_y F(t, \omega) \xi_r(t, x, y) dy dx dt d\omega \right|^2 \quad (7.14)$$

where  $F(t, \omega)$  represents the resolution filtering process in time ( $t$ ) and frequency ( $\omega$ ) and consists of a linear operator, usually convolution with a matched filter. Recent pencil beam scatterometers have adopted a one-dimensional range filtering scheme



which can be modeled as

$$M^{fs} = \int_{\omega} \left| \int_t \int_x \int_y F(t, \omega) \xi_r(t, x, y) dy dx dt \right|^2 d\omega, \quad (7.15)$$

the superscript in  $M^{fs}$  denoting a filtered signal measurement.

#### 7.1.4 Measurement Statistics

The general statistical properties of a scatterometer measurement have been calculated for several different instruments and measurement configurations [16, 35, 51]. These studies derived the statistics of single, independent measurements using various measurement forms. It is our desire to extend the theory by considering multiple, spatially overlapping measurements and the correlation between them.

For convenience, the radar calibration parameter,  $X$ , is defined as

$$X = \frac{E_t \lambda^2 G_o^2 A_E}{(4\pi)^3 \bar{r}^4}, \quad (7.16)$$

with  $G_o$  as the peak antenna gain, and  $A_E$  as the effective measurement area,

$$A_E = \frac{1}{G_o^2} \int_x \int_y G^2(x, y) A_d(x, y) dy dx. \quad (7.17)$$

The receive signal term,  $Y$ , is also defined as

$$Y(t, x, y) = \frac{1}{G_o \sqrt{A_E}} G(x, y) a(t - 2\bar{r}(x, y)/c) e^{j\omega_c t} e^{-j\omega_d(x, y)t} e^{j2\omega_c \bar{r}(x, y)/c} \quad (7.18)$$

so that the noise-free receive signal from each resolution element can be written as

$$\xi_r(t, x, y) = \sqrt{XY}(t, x, y) Z(x, y). \quad (7.19)$$

To aid understanding of how the measurement form employed effects the values of signal correlation and covariance, as well as to demonstrate a generalized result, expressions for both the antenna footprint resolution case (7.13) and the one-dimensional filtering case (7.15) are developed. The process developed can be easily expanded to the full resolution case (7.14) as desired.

For (7.13) the expected value of an antenna footprint resolution signal measurement,  $M_a^s$ , is (see Appendix B.2.1)

$$\mathcal{E}[M^{as}] = \mathcal{E} \left[ \int_t \left| \int_x \int_y \xi_r(t, x, y) dy dx \right|^2 dt, \right] = X R^a \quad (7.20)$$

where  $R^a$  is

$$R^a = \int_t \int_x \int_y |Y(t, x, y)|^2 A_d(x, y) \sigma^\circ(x, y) dy dx dt. \quad (7.21)$$

The correlation of two measurements,  $M_k^{as}$  and  $M_l^{as}$ , can then be shown to be (see Appendix B.2.2)

$$\mathcal{E}[M_k^{as} M_l^{as}] = X_k X_l [R_k^a R_l^a + V_{kl}^a] \quad (7.22)$$

with

$$V_{kl}^a = \int_{t_k} \int_{t_l} \int_{x_k} \int_{y_k} \int_{x_l} \int_{y_l} \sigma^\circ(x_k, y_k) \sigma^\circ(x_l, y_l) A_d(x_k, y_k) A_d(x_l, y_l) Y(t_k, x_k, y_k) Y^*(t_l, x_l, y_l) Y(t_l, x_l, y_l) Y^*(t_k, x_k, y_k) dy_l dx_l dy_k dx_k dt_l dt_k. \quad (7.23)$$

The covariance,  $\mathcal{Cov}[M_k^{as} M_l^{as}]$ , of two measurements can also be shown to be (see Appendix B.2.3)

$$\mathcal{Cov}[M_k^{as} M_l^{as}] = X_k X_l V_{kl}^a. \quad (7.24)$$

Similarly, for the one dimensional filtering measurement case (7.15) the expected value of the signal is (see Appendix B.3.1)

$$\mathcal{E}[M^{fs}] = \mathcal{E} \left[ \int_\omega \left| \int_t \int_x \int_y F(t, \omega) \xi_r(t, x, y) dy dx dt \right|^2 d\omega \right] = X R^f \quad (7.25)$$

where  $R^f$  is

$$R^f = \int_\omega \int_t \int_{t'} \int_x \int_y A_d(x, y) \sigma^\circ(x, y) F(t, \omega) F^*(t', \omega) Y(t, x, y) Y^*(t', x, y) dy dx dt' dt d\omega. \quad (7.26)$$

The correlation of two measurements,  $M_k^{fs}$  and  $M_l^{fs}$  is then (see Appendix B.3.2)

$$\mathcal{E}[M_k^{fs} M_l^{fs}] = X_k X_l [R_k^f R_l^f + V_{kl}^f] \quad (7.27)$$

where  $V^f$  is

$$\begin{aligned}
V_{kl}^f = & \int_{\omega_k} \int_{\omega_l} \int_{t_k} \int_{t'_k} \int_{t_l} \int_{t'_l} \int_{x_k} \int_{x_l} \int_{y_k} \int_{y_l} A_d(x_k, y_k) A_d(x_l, y_l) \sigma^\circ(x_k, y_k) \sigma^\circ(x_l, y_l) F(t_k, \omega_k) \\
& F^*(t'_k, \omega_k) F(t_l, \omega_l) F^*(t'_l, \omega_l) Y(t_k, x_k, y_k) Y^*(t'_k, x_l, y_l) Y(t_l, x_l, y_l) Y^*(t'_l, x_k, y_k) \\
& dy_l dy_k dx_l dx_k dt'_l dt_l dt'_k dt_k d\omega_l d\omega_k.
\end{aligned} \tag{7.28}$$

The covariance of two measurements is (see Appendix B.3.3)

$$\text{Cov}[M_k^{fs} M_l^{fs}] = X_k X_l V_{kl}^f. \tag{7.29}$$

It is also frequently assumed that  $\sigma^\circ$  is constant over the measurement area. When true, alternate forms of  $R^a$ ,  $V^a$ ,  $R^f$  and  $V^f$  using a bar, i.e.  $R^a = \sigma^\circ \bar{R}^a$ , are defined to signify such independence.

The expressions in (7.22), (7.24), (7.27), and (7.29) are the desired results. When  $k = l$  the correlation for both (7.22) and (7.27) simplifies to the second moment,

$$\mathcal{E}[(M^s)^2] = X^2[R^2 + V], \tag{7.30}$$

where  $R$  represents either  $R^a$  or  $R^f$  as appropriate, and the covariance equals the variance of the measurement,  $X^2V$  ( $V^a$  or  $V^f$ ). In the case of antenna footprint resolution, the values for the second moment and variance are identical to those shown by Long and Spencer [35]. If  $k = l$  and  $M_k^s$  and  $M_l^s$  ( $M^{as}$  or  $M^{fs}$ ) are completely independent,  $V$  is zero, the covariance is subsequently zero, and the correlation simplifies to the square of the expected value,  $\mathcal{E}^2[M^s] = (XR)^2$ , for both measurement forms.

The derivation of correlation and covariance expressions for two versions of scatterometer measurements, (7.13) and (7.15), demonstrate the effect that various configurations have on the statistical expressions. The two versions can be made equivalent by choosing  $F(t, \omega) = \delta(t - \omega)$  in (7.15) so that  $V^f = V^a$ . This allows the conclusion that the filtered form of instrument measurements (7.15) is sufficiently general to emulate most measurement configurations and thus will be used throughout the remainder of the chapter.

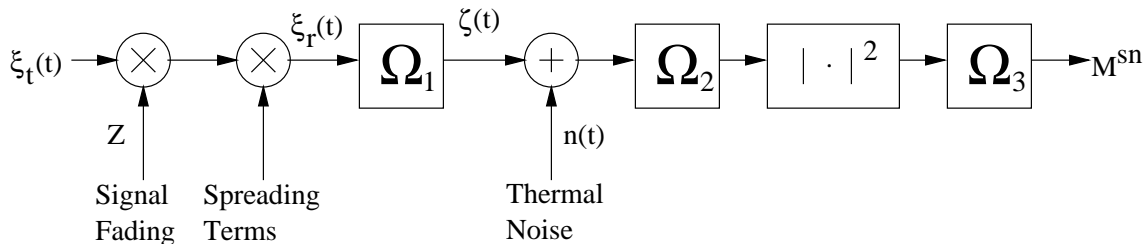


Figure 7.2: Generalized signal flow graph of a scatterometer measurement. The flow graph models the measurement process for backscatter, incorporating additive noise and signal processing to generate the measurement. The  $\Omega$  operators are defined in the text.

## 7.2 Noisy Signal Measurements

The next step in our analysis is to consider random fluctuations caused by sources other than the surface. Consider the general measurement model shown in Figure 7.2, where multiplicative signal fading has already been considered. The output of the first  $\Omega$  operator,  $\Omega_1$ , for our model is

$$\zeta(t) = \int_x \int_y \xi_r(t, x, y) dy dx. \quad (7.31)$$

The second random term in the model is additive noise,  $n(t)$ , which results from radiometric and thermal noise. The total system noise is traditionally measured in terms of brightness temperature,  $T_{sys}$ , and is a linear combination of  $T'_A$ , the radiometric antenna temperature, and  $T'_{rec}$ , the receiver noise temperature independent of the received radiation [54],

$$T_{sys} = T'_A + T'_{rec}. \quad (7.32)$$

Both terms are random variables and are assumed to have Gaussian distributions. For scatterometers,  $T'_{rec}$  is significantly larger than  $T'_A$  and dominates the noise term. Thus for our derivation the overall thermal noise term,  $n(t)$ , is placed as shown in Figure 7.2.

To assess the effects of noise on surface measurements the statistical properties of the noise are defined. First, since the receiver noise dominates, it is assumed

that the additive thermal noise,  $n(t)$ , is a real, zero mean, Gaussian process, independent of the received signal,  $\zeta(t)$ , so that  $\mathcal{E}[\zeta(t)n(t)] = \mathcal{E}[\zeta(t)]\mathcal{E}[n(t)] = 0$ . Second, it is assumed that the instrument receiver measures the signal and noise over a finite bandwidth,  $B_r$ .  $B_r$  is assumed to be larger than the signal bandwidth and that the filters used to constrain the bandwidth are ideal. The filtered noise-only signal,  $\nu(t)$ , is defined as

$$\nu(t) = h(t) * n(t) \quad (7.33)$$

where  $h(t)$  is the impulse response of the band limiting filter.

The noise-only signal,  $n(t)$ , is defined to have a power spectral density of  $n_o/2$  over the measurement bandwidth so that the correlation of the filtered noise is  $\mathcal{E}[\nu(t)\nu^*(t - \tau)] = 2B_r \left(\frac{n_o}{2}\right) \text{sinc}(2B_r[t - \tau])$  where the filter response is determined using the Fourier transform of an ideal low pass filter. For the one dimensional measurement filtering case (7.15) the expected value of a noise-only measurement is

$$\mathcal{E}[M^n] = \mathcal{E} \left[ \int_{\omega} \left| \int_t F(t, \omega) \nu(t) dt \right|^2 d\omega \right] \quad (7.34)$$

$$= \int_{\omega} \int_t \int_{t'} F(t, \omega) F^*(t', \omega) 2B_r \left(\frac{n_o}{2}\right) \text{sinc}(2B_r[t - t']) dt' dt d\omega \quad (7.35)$$

$$= \mathcal{N}_s. \quad (7.36)$$

Using these definitions, the signal plus noise measurement,  $M^{sn}$ , is expressed as

$$M^{sn} = \int_{\omega} \left| \int_t F(t, \omega) [h(t) * (\zeta(t) + n(t))] dt \right|^2 d\omega \quad (7.37)$$

$$= \int_{\omega} \left| \int_t F(t, \omega) [\zeta(t) + \nu(t)] dt \right|^2 d\omega \quad (7.38)$$

with expected value (see Appendix B.4.1)

$$\mathcal{E}[M^{sn}] = XR^f + \mathcal{N}_s. \quad (7.39)$$

It is then shown that the correlation of two noisy measurements,  $M_k^{sn}$  and  $M_l^{sn}$ , is (see Appendix B.4.2)

$$\mathcal{E}[M_k^{sn} M_l^{sn}] = X_k X_l [R_k^f R_l^f + V_{kl}^f] + X_k R_k^f \mathcal{N}_s + X_l R_l^f \mathcal{N}_s + \mathcal{N}_s^2 + \delta(k-l)(2X R^f \mathcal{N}_s + 2\mathcal{N}_s^2), \quad (7.40)$$

and the covariance of the measurements is (see Appendix B.4.3)

$$\mathcal{Cov}[M_k^{sn} M_l^{sn}] = X_k X_l V_{kl}^f + \delta(k-l)(2X R^f \mathcal{N}_s + 2\mathcal{N}_s^2). \quad (7.41)$$

Results are similar for other measurement forms.

The results for the noisy correlation and covariance are similar to those found in the noise free case (7.27) and (7.29). In particular, since noise is assumed to be independent, the covariance of the noisy and noise free cases is identical for  $k \neq l$ . If the measurements are the same ( $k = l$ ) then the covariance contains additional terms which account for the added variance due to noise.

Scatterometers remove the noise induced bias in the signal plus noise expectation (7.39) by subtracting a separate noise-only measurement,  $M^n$ , from the noisy signal measurement. This noise-only measurement is made either by expanding the primary measurement bandwidth and estimating the noise from spectral areas where the signal is not present, or by making a noise-only measurement at a different time than the receive echo signal. The expected value of the noise-only measurement is defined as  $\mathcal{E}[M^n] = \mathcal{N}_n$ .

The unbiased measurement of the signal,  $M^u$ , is

$$M^u = \alpha M^{sn} + \beta M^n \quad (7.42)$$

where  $\alpha$  and  $\beta$  are appropriately chosen so that  $\mathcal{E}[M^u] = X\sigma^\circ$ , which makes the measurement unbiased to noise, i.e.,

$$\alpha = (\bar{R})^{-1} \quad \text{and} \quad \beta = -\frac{\mathcal{N}_s}{\bar{R}\mathcal{N}_n}. \quad (7.43)$$

for all measurement forms.

To determine the correlation and covariance of the unbiased noisy measurement form the correlation between the noisy measurement and the noise-only

measurement is defined as (see Appendix B.5.1)

$$\mathcal{E}[M^{sn}M^n] = XR\mathcal{N}_n + \mathcal{N}_s\mathcal{N}_n, \quad (7.44)$$

and the correlation of two noise-only measurements as (see Appendix B.5.2)

$$\mathcal{E}[M_k^n M_l^n] = \mathcal{N}_n^2 + \delta(k-l)2\mathcal{N}_n^2. \quad (7.45)$$

The correlation of two unbiased measurements is then (see Appendix B.5.3)

$$\mathcal{E}[M_k^u M_l^u] = \frac{X_k X_l}{\overline{R_k R_l}} \left( R_k R_l + V_{kl} + \delta(k-l) \left[ \frac{2R\mathcal{N}_s}{X} + \frac{4\mathcal{N}_s^2}{X^2} \right] \right) \quad (7.46)$$

and the covariance of an unbiased noisy measurement to be (see Appendix B.5.4)

$$\text{Cov}[M_k^u, M_l^u] = \frac{X_k X_l}{\overline{R_k R_l}} \left( V_{kl} + \delta(k-l) \left[ \frac{2R\mathcal{N}_s}{X} + \frac{4\mathcal{N}_s^2}{X^2} \right] \right). \quad (7.47)$$

These results highlight the fact that additive noise effects only the auto-correlation and auto-covariance (variance) statistics of a measurement regardless of measurement form. If the measurements are distinct then the noise is uncorrelated, not only from itself but from the signal as well. The measurement correlation and covariance then depend only upon the random fluctuations of the measured surface and not upon any noise induced variation.

### 7.3 Analysis of the Signal Covariance Expression

To gain an understanding of the signal covariance  $\bar{V}$  is analyzed for two instruments, the SeaWinds scatterometer and a proposed instrument, HYDROS. Both instruments make measurements by conically scanning a pencil-beam antenna about nadir (see Figure 2.3) and generally have the same footprint size of 36 km x 26 km (assuming SeaWinds' outer beam). Both instruments provide two data products: SeaWinds produces a footprint resolution measurement (7.13) and a range filtered measurement (7.15) [51]. HYDROS produces a high resolution, two dimensional filtered product (7.14) and a low resolution, diagnostic product (7.13) [48].

The key difference of the two instruments is their pulse rate. While SeaWinds transmits 1.5 ms pulses every 10.8 ms, each having a bandwidth of 375 kHz,

HYDROS transmits 15  $\mu\text{s}$  pulses every 286  $\mu\text{s}$ , each having a bandwidth of 1 MHz. SeaWinds' rotation rate and PRF locate consecutive pulses 18 km apart in azimuth, consistent with the traditional assumption of independence. HYDROS' rotation rate and PRF locate consecutive pulses 210 meters apart in azimuth, thus bringing this assumption into question.

Both instruments use a linear frequency modulated (LFM), or chirped, pulse. This pulse is modeled as

$$a_k(t) = \frac{1}{\sqrt{T_a}} e^{j(\frac{1}{2})2\pi\mu t^2}, \quad 0 + kT_p \leq t \leq T_a + kT_p, \quad (7.48)$$

where  $\mu$  is the chirp rate and  $T_p$  is the period of the pulse, or pulse repetition increment and assume that each pulse is equivalent in shape and modulation.

### 7.3.1 Footprint Resolution ( $\bar{V}^a$ )

The term  $\bar{V}^a$  which corresponds to the low resolution antenna footprint measurements produced by SeaWinds and HYDROS is considered first. To simplify the expression the generalized radar ambiguity function is introduced [55]

$$\mathcal{X}(t, \omega) = \int_{-\infty}^{+\infty} a(y)a^*(y+t)e^{j\omega y} dy. \quad (7.49)$$

It is noted that  $a(y)$  is zero outside the time limits of the pulse and assume that instrument range gates are sufficiently wide to admit all of the echo signal. This allows the extension of the time limits of  $\bar{V}^a$  to infinity without effecting the total value of the integral. Implementing these changes,  $\bar{V}^a$  can be written as (see Appendix B.6.1)

$$\bar{V}_{kl}^a = \int_{x_k} \int_{y_k} \int_{x_l} \int_{y_l} \mathcal{X}^2(d_r, f_\omega) Q(x_k, y_k) Q(x_l, y_l) B_{kl}(f_\omega) dy_l dx_l dy_k dx_k \quad (7.50)$$

where  $d_r = \frac{2}{c}(r(x_l, y_l) - r(x_k, y_k))$  and  $f_\omega = -[\omega_d(x_l, y_l) - \omega_d(x_k, y_k)]/2\pi$  represent a change of variables for the ambiguity function. The cross-pulse gain product is  $Q(x_k, y_k) = A_d(x_k, y_k)G_k(x_k, y_k)G_l(x_k, y_k)$  and  $B_{kl}(f_\omega)$  is the covariance phase expression defined as

$$B_{kl}(f_\omega) = e^{-jf_\omega T_p(l-k)}. \quad (7.51)$$



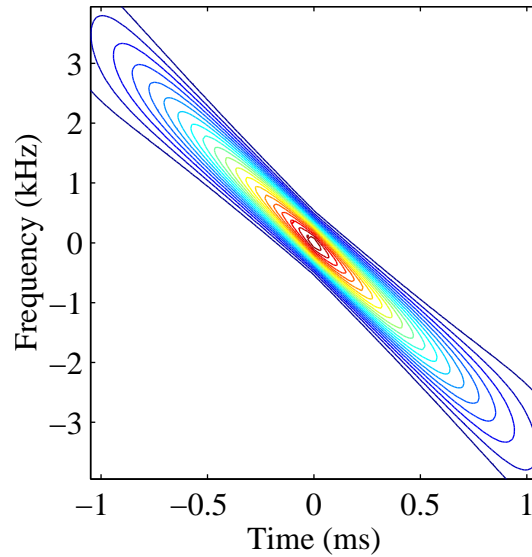


Figure 7.3: Radar ambiguity function for a single LFM pulse with a downchirp.

The characteristics of the radar ambiguity function are determined by the pulse modulation function,  $a(t)$ . For an interrupted continuous wave pulse the ambiguity function has a triangular shape in the time dimension, and a sinc-like shape in the frequency dimension. The ambiguity function for a linear frequency modulated (LFM) pulse is often referred to as a “knife blade” due to its sharp diagonal peak. The major axis of the blade is sloped in the time-frequency plane, with the slope determined by the chirp rate. The width of the blade in the time dimension is determined by the duration of the pulse and the width of the response in the frequency direction is proportional to the reciprocal of the pulse repetition period, see Figure 7.3.

The relatively high chirp rates for both SeaWinds and HYDROS cause the major axis of the razor blade to be almost vertical, HYDROS more so than SeaWinds, in the time-frequency plane, so that the ambiguity function is nominally invariate for small frequencies and a delta function in time.

The second term in (7.50), the cross-pulse gain product,  $Q(x, y)$ , is a product of the antenna patterns of the two pulses, multiplied by the differential measurement area. If the two pulses are identical then  $Q(x, y) = A_d(x, y)G^2(x, y)$ , if they have no overlap then  $Q(x, y) = 0$ . For most previous instruments, including SeaWinds, the large spacing between pulses reduces  $Q$  and minimizes  $\bar{V}^a$ .

The third term in (7.50), the covariance phase  $B_{kl}$ , is also a major contributor to measurement correlation. This can be illustrated by assuming, for the moment, that  $G(x, y)$  is an ideal footprint,

$$G(x, y) = \begin{cases} 1, & -X/2 \geq x \geq X/2 \quad \text{and} \quad -Y/2 \geq y \geq Y/2, \\ 0, & \text{else,} \end{cases} \quad (7.52)$$

so that  $\bar{V}^a$  can be expressed as (see Appendix B.8)

$$\bar{V}_{kl}^a = \int_{-X}^X \int_{-Y}^Y (X - |r_d|)(Y - |f_\omega|) \Re\{B_{kl}(f_\omega)\} \mathcal{X}^2(r_d, f_\omega) dr_d df_\omega, \quad (7.53)$$

where  $\Re$  references the real part of  $B_{kl}$ . Note that  $\bar{V}^a$  is always real and conforms with previously derived results for  $k = l$  [35].

The covariance phase, or more precisely the real part of the phase, is a sinc function, where  $B_d$  is the Doppler bandwidth of the return echo. If  $B_d T_p \geq 1$ , then  $B_{kl} = \delta(k - l)$  and each measurement is independent. This is the case for SeaWinds. For HYDROS at  $90^\circ$  azimuth,  $B_d T_p \approx 0.55$ . This translates to a correlation value of 30% for consecutive pulses. Results for other values of  $l - k$  at  $90^\circ$  are shown in Figure 7.4.

Using  $B_{kl}(f_\omega)$  the level of pulse correlation for a particular sensor can rapidly be assessed. For large Doppler bandwidths and pulse periods measurements are independent. The reduction of either the pulse period or the Doppler bandwidth increases the level of measurement correlation, as evidenced by the HYDROS design.

### 7.3.2 Range Resolution ( $\bar{V}^f$ )

Similar analysis can be used for evaluation of the covariance expression for range filtered measurements,  $\bar{V}^f$ . While the processing is slightly different, the

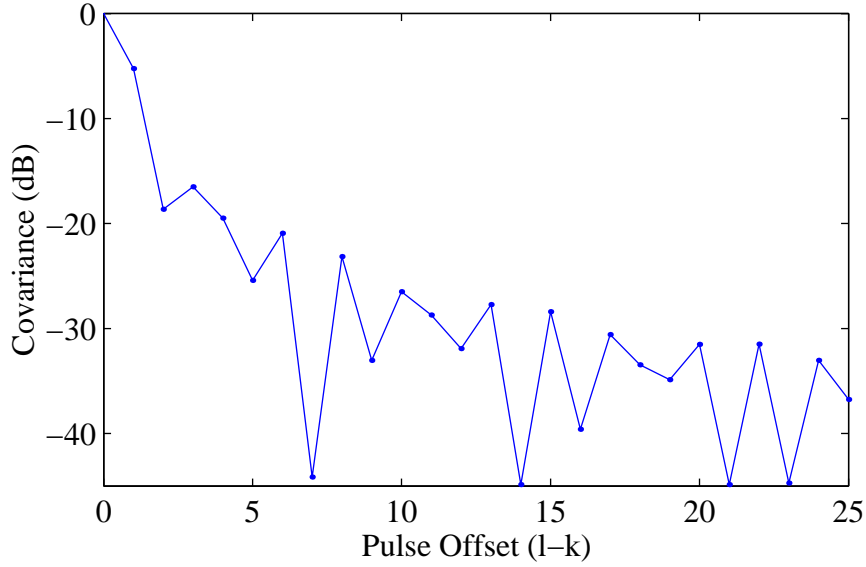


Figure 7.4: Plot of  $\bar{V}_{kl}^a$  at  $90^\circ$  azimuth as a function of  $l - k$  for the HYDROS instrument. The figure shows that consecutive pulses have a covariance of 0.30 and pulses offset by more than 2 pulses are essentially independent.

results of measurement correlation are similar. One key issue is the orientation of measurements as the antenna rotates about nadir. Antenna resolution measurements experience only fractional variations of Doppler bandwidth as a function of azimuth. Conversely, the Doppler bandwidth varies significantly with azimuth angle when using range resolved measurements. Figure 7.5 illustrates this phenomenon for three different azimuth angles. At  $90^\circ$  azimuth the bandwidth of each range measurement is equivalent to that of the footprint, at  $0^\circ$  the Doppler bandwidth is minimal. The rotation of range resolved measurements effects the behavior of  $B_{kl}(k)$  with the decreased bandwidth of forward looking azimuths causing the sinc function to expand, increasing measurement correlation length.

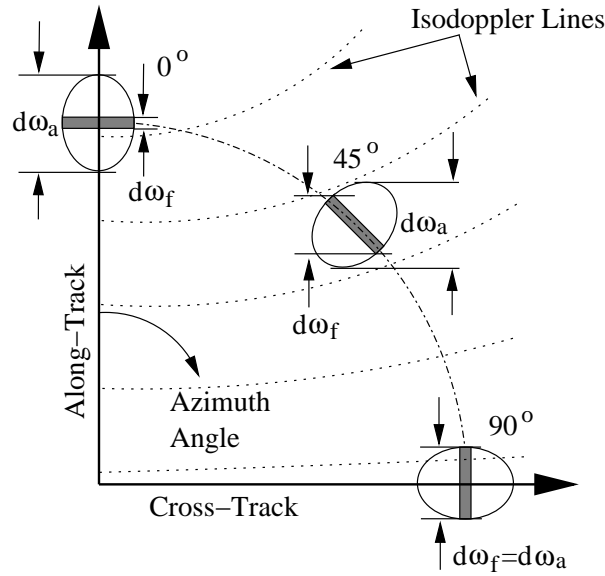


Figure 7.5: Illustration of the effect antenna rotation has on the Doppler bandwidth of antenna footprint and range resolved measurements. At  $0^\circ$  the bandwidth of an antenna footprint ( $d\omega_a$ ) measurement is maximum and a range resolved ( $d\omega_f$ ) measurement is minimal. At  $90^\circ$  the bandwidth of both measurements are equal.

#### 7.4 Multiple Pulse Measurements and the Effects of Correlation

The accuracy of scatterometer measurements is commonly described by the normalized standard deviation of the measurement, termed  $K_p$ , [16]

$$K_p = \frac{\sqrt{\mathcal{V}\text{ar}[\sigma_{meas}^\circ]}}{\sigma^\circ} = \sqrt{\frac{\mathcal{V}\text{ar}[M^u]}{(X\sigma^\circ)^2}}. \quad (7.54)$$

As part of the analysis of multiple pulses, the statistics of multiple pulse measurements is also considered. The pulses are summed either incoherently or coherently. Incoherent measurements are made by summing the squared response of each individual pulse in the measurements. Coherent processing is performed by combining pulses before the squaring operation, similar to synthetic aperture radar (SAR) processing. To determine the statistics of multiple pulse measurements  $K_p$  is evaluated to account for this processing.

### 7.4.1 Incoherent Measurements

To evaluate  $K_p$  for an incoherent multiple pulse measurement  $M^m$  is defined as the mean of  $N_p$  single  $M^u$  measurements, processed using either footprint (7.13) or range filtering resolution (7.15)

$$M^m = \frac{1}{N_p} \sum_{k=1}^{N_p} M_k^u = \frac{1}{N_p} \sum_{k=1}^{N_p} \alpha M_k^{sn} + \beta M_k^n. \quad (7.55)$$

Then,

$$\mathcal{E}[M^m] = \mathcal{E}[M^u] = X\sigma^\circ. \quad (7.56)$$

Using (7.47), the variance of  $M^m$  is (see Appendix B.7.1)

$$\mathcal{V}\text{ar}[M^m] = \mathcal{E}[(M^m)^2] - \mathcal{E}^2[M^m] \quad (7.57)$$

$$= \frac{1}{N_p^2} \sum_{l=1}^{N_p} \sum_{k=1}^{N_p} \mathcal{C}\text{ov}[M_k^u M_l^u] \quad (7.58)$$

$$= \frac{1}{N_p^2} \sum_{l=1}^{N_p} \sum_{k=1}^{N_p} \mathbf{K}_{kl} \quad (7.59)$$

where  $\mathbf{K}$  is a covariance matrix with  $\mathcal{C}\text{ov}[M_k^u M_l^u]$  at the  $kl^{th}$  entry. If all of the pulses are independent, then  $\mathbf{K}$  is a diagonal matrix with zero entries for all off-diagonal elements. If the  $N_p$  pulses have some degree of correlation,  $\mathbf{K}$  is still diagonally symmetric, but the off-diagonal terms may be non-zero. It can also be shown that the correlation of two incoherent multi-pulse measurements is (see Appendix B.7.2)

$$\mathcal{E}[M_k^m M_l^m] = \frac{1}{N_p^2} \sum_{k=k_a}^{k_b} \sum_{l=l_a}^{l_b} \mathbf{R} + \mathbf{K} \quad (7.60)$$

where  $\frac{X_k X_l}{R_k R_l} (R_k R_l)$  is the  $(k, l)^{th}$  entry of  $\mathbf{R}$ , and that the covariance of two measurements is (see Appendix B.7.3)

$$\mathcal{C}\text{ov}[M_k^m M_l^m] = \frac{1}{N_p^2} \sum_{k=k_a}^{k_b} \sum_{l=l_a}^{l_b} \mathbf{K} \quad (7.61)$$

According to (7.47) and (7.50) it is possible that some of the off-diagonal elements of  $\mathbf{K}$  are negative, though the covariance is always positive. This suggests that it is possible to reduce the overall variance of multiple pulse measurements by

sampling at an appropriate rate, allowing negative values in  $\mathbf{K}$  to offset positive values. This ability to minimize measurement variance through negatively correlated pulses is limited to instruments with short pulse periods ( $T_p$ ) and small  $N_p$  as dictated by  $B_{kl}(k)$ .

As  $\mathbf{K}$  relates to the multi-pulse expression for  $K_p$  it is valuable to explore the behavior of  $\mathbf{K}$  relative to key instrument parameters. First let  $K_p(N_p)$  be

$$K_p(N_p) = \sqrt{\frac{\sum_{l=1}^{N_p} \sum_{k=1}^{N_p} \mathbf{K}_{kl}}{N_p^2 \mathbf{m}^T \mathbf{m}}} \quad (7.62)$$

where the numerator is the Frobenius norm, with

$$\mathbf{m} = \frac{1}{N_p} [X \sigma_1^\circ \ X \sigma_2^\circ \ \dots \ X \sigma_{N_p}^\circ]^T. \quad (7.63)$$

This allows for determination of the effectiveness of using multiple pulse measurements using

$$J_{K_p}(N_p) = \frac{K_p(N_p)}{K_p(1)}, \quad (7.64)$$

the ratio of the multi-measurement  $K_p$  normalized by the single measurement  $K_p$ . In doing so, it is assumed that the means of the measurements are statistically identical. If the  $N_p$  pulses are all independent,  $J_{K_p}(N_p)$  is  $1/\sqrt{N_p}$ . If the pulses are completely dependent (i.e. identical),  $\mathbf{K}$  is a matrix with equal elements and  $J_{K_p}(N_p) = 1$ . In general, the tradeoff for using  $N_p$  pulses is reduced spatial resolution. Oversampling seeks to reduce  $K_p$  using large  $N_p$  without significantly degrading resolution.

$K_p$  is a function of the signal to noise ratio (SNR). The multiple pulse covariance matrix can be expressed as

$$\mathbf{K} = \mathbf{K}_V + s\mathbf{I} \quad (7.65)$$

where  $\mathbf{K}_V$  is the contribution to  $\mathbf{K}$  from the random fading in the signal,  $\mathbf{I}$  is an identity matrix, and the scalar  $s$  represents the contribution from additive noise [see (7.44)],

$$s = \frac{2R\mathcal{N}_s}{X} + \frac{4\mathcal{N}_s^2}{X^2} \quad (7.66)$$

For high SNR,  $s$  is small and  $\mathbf{K} \approx \mathbf{K}_V$ . For low SNR,  $s$  is large and  $\mathbf{K} \approx s\mathbf{I}$ , reducing covariance but not necessarily improving  $K_p$ . This introduces the tradeoff between the correlation of the pulses and the operating SNR.

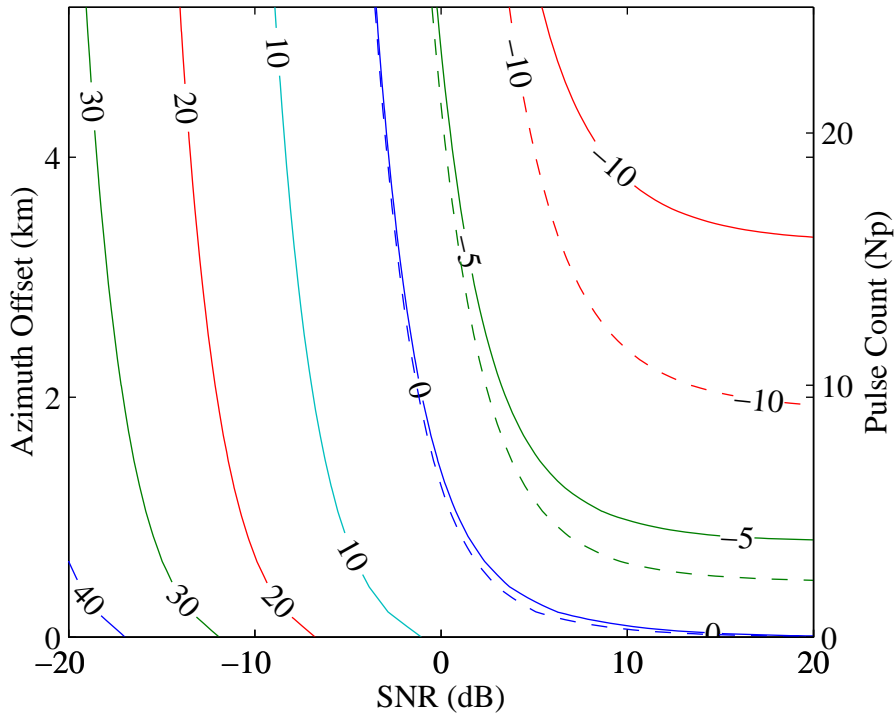


Figure 7.6: Contour plot of normalized variance ( $K_p^2$ ) as a function of SNR and azimuth offset (pulse count) in decibels ( $20\log_{10}K_p$ ), for HYDROS at  $90^\circ$  azimuth angle. The left axis is azimuth offset, the spacing between the first and last pulses in the sum, in kilometers, and the right axis is the corresponding number of pulses included in the variance sum (7.59). The solid lines represent the variance for HYDROS pulses, the dashed lines represent measurement variance if the pulse were independent pulses.

Figure 7.6 illustrates the tradeoff between measurement correlation and SNR for HYDROS. The data is derived from Figure 7.4, the 90° azimuth calculation of signal covariance. The figure plots normalized measurement variance as a function of azimuth offset (pulse count) and SNR. The figure shows that combining several pulses improves  $K_p$ , particularly at high SNR. It also shows that for large  $N_p$  a proportionally greater benefit can be derived from improving SNR rather than increasing  $N_p$ . Finally, it shows that for small SNR changes in SNR have little effect of measurement correlation.

#### 7.4.2 Coherent Measurements

The other option in multiple pulse measurement is the coherent combination of multiple pulses. The disadvantage of this procedure is the significant increase in signal processing complexity. The advantages of this SAR-like processing is the improvement in signal variance and resolution by both range and frequency filtering [49]. While significantly more complicated to implement, coherent processing can incorporate the information gained from measurement correlation, allowing for extraction of the maximum number of looks from the measurement. This can be used to provide maximum resolution or be averaged to minimize measurement  $K_p$ . The variance of incoherent measurements is proportional to  $1/N_p$  while the variance of coherent processing is proportional to  $1/N_p^2$  [55].

#### 7.5 Summary

General expressions for correlation and covariance between pulses are derived for a scatterometer measurements. These expressions can be adapted to specific instruments. Expressions for several different types of measurements for signal-only, signal plus noise, and noise-only are shown. A numerical evaluation of the signal covariance parameter,  $\bar{V}$ , is presented for two scatterometer designs, showing basic behavior of correlation and covariance between pulses as a function of pulse offset, pulse width and Doppler bandwidth. The effects of correlation on signal variance and  $K_p$  are demonstrated for the incoherent case. It is shown that the  $K_p$  for multiple pulses is always less than or equal to the  $K_p$  for a single pulse measurement. It is



concluded that correlation between measurements for high PRF instruments must be considered in the design process. Correlation can be minimized through proper selection of pulse rates and measurement dimensions. Measurement variance can be improved and correlation reduced by combining multiple pulses, both incoherently and coherently to make single backscatter measurements of the surface.



## Chapter 8

### Simulating Measurement Variations

Development of scatterometer instruments and data processing algorithms relies heavily on simulation. In particular, modeling and simulation of random fluctuations in the measurements is a critical portion of assessing the performance of a design. As previously noted, variations for scatterometers occur in two forms. The first is fading due to the coherent summation of responses from multiple surface scatterers. Fading is multiplicative in nature and is related to the magnitude of the surface response. The second random variation is additive noise caused by a variety of thermal and environmental factors [55].

Previous simulation models couple the two variation sources, fading and noise, into one equivalent term, e.g. [34]. While this assumption may be appropriate in some circumstances, developing scatterometer applications benefit from improved simulation models. In particular, the two sources of variation, while independent in origin, are correlated by the non-linear, square law processing used by most instruments. Further, proper definition and determination of signal-to-noise ratios (SNR) is difficult when using a single variation term. Complex models which properly account for these variations have been created for some instruments. However, they are instrument specific and extremely time consuming to develop. This limits their utility in simulations designed to use data from multiple instruments.

To facilitate development of new instrument designs and additional scatterometer data applications an improved statistical model for simulating scatterometer data is proposed. The proposed model is specific enough, by accounting for fading and noise separately, to accurately simulate data variations, yet general enough to be quickly and easily adapted to any microwave scatterometer configuration. Example

applications for the model include development of sample backscatter fields for wind estimation, image enhancement, and polar climate studies [11, 14, 15].

The presentation of the model is organized as follows: Section 8.1 develops a general framework of scatterometer measurements. It discusses causes and effects of variation in a general measurement formulation. Section 8.2 then presents the statistical simulation model, applying it to the measurement scheme of Section 8.1 as well as externally derived results. Finally, Section 8.3 summarizes findings and concludes.

### 8.1 Data Collection

Scatterometers operate by transmitting pulses of microwave energy and measuring the amount of energy which returns to the instrument. The measurement of returning backscatter is directly related to the normalized radar cross section ( $\sigma^\circ$ ) of the surface [55]. Similar to Section 7.1.1, the voltage response of each measurement,  $Z$ , is modeled as a complex, random variable having a Rayleigh distributed magnitude and a uniformly distributed phase and  $\sigma^\circ$  is related to the voltage response through the expected value squared [55],

$$A_d \sigma^\circ = \mathcal{E}[|Z|^2]. \quad (8.1)$$

Section 7.2 discusses signal corruption from additive noise. Noise comes from multiple sources, most notably from internal thermal excitement of the instrument electronics and radiometric radiation incident on the instrument antenna. Since the magnitude of the internal thermal noise is the most significant, all additive variation is modeled as coming from this source. Thermal noise in the receiver bandwidth is zero mean and normally distributed with a white spectrum.

A variety of instrument measurement configurations have been used for past instruments [16, 35, 39, 51, 65]. For this presentation the simulation model is developed using the general measurement scheme used in [35], similar to (7.12), and described by Figure 8.1. Application of the model to other measurement forms is then demonstrated.

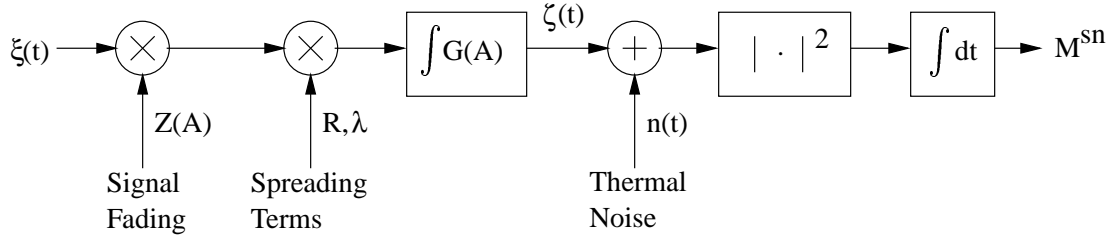


Figure 8.1: Simplified signal flow model for scatterometer measurements. See text for definition of terms.

A transmitted microwave signal,  $\xi(t)$ , scatters off the surface having response  $Z$ . In course of flight the signal spreads as a function of instrument-to-surface range,  $r$ , and wavelength,  $\lambda$ . The received response is integrated over its area,  $A$ , with weighting equivalent to the gain of the antenna,  $G$ . Thermal noise,  $n(t)$ , is modeled internal to the instrument by placing it after the antenna gain filtering. In the final step of processing, the received signal is squared to create a power signal and integrated to obtain the total measurement energy.

Mathematically, the transmitted signal is defined using (7.5),

$$\xi(t) = \sqrt{E_t} a(t) e^{j\omega_c t} \quad (8.2)$$

where  $E_t$  is the total transmitted energy,  $a(t)$  is the pulse modulation function, and  $\omega_c$  the angular center frequency. The received signal,  $M^{sn}$ , is then written as

$$M^{sn} = \int_{T_s} \left| \left[ \int_A \frac{\xi(t) Z(A) \lambda G(A)}{(4\pi)^{3/2} r^2(A)} dA \right] + n(t) \right|^2 dt \quad (8.3)$$

$$= \int_{T_s} |\zeta(t) + n(t)|^2 dt \quad (8.4)$$

where  $\zeta(t)$  denotes the signal portion of the measurement (enclosed in brackets in (8.3) and shown in Figure 8.1). By using the bulk range,  $\bar{r}$ , in the denominator, assuming that all filters are ideal, and  $\sigma^\circ$  is constant over the area of integration, and defining the variance of the noise as  $n_o/2$ , it can be shown that [65]

$$\mathcal{E}[M^{sn}] = X \sigma^\circ R + 2B_s T_s \frac{n_o}{2} \quad (8.5)$$

where  $X$ ,  $A_E$ , and  $R$  are described by (7.16), (7.17), and (7.21). The receiver bandwidth,  $B_s$ , and the time of integration,  $T_s$ , are assumed wide enough to fully capture the signal.

Scatterometers remove the bias caused by the noise by making a separate, noise-only measurement,  $M^n$ , so that [55]

$$M^u = \varsigma M^{sn} + \varphi M^n \quad (8.6)$$

where  $M^u$  is the unbiased measurement. Given that  $\mathcal{E}[M^n] = 2B_n T_n n_o / 2$ , where  $B_n$  and  $T_n$  are the noise-only bandwidth and integration time,  $\varsigma$  and  $\varphi$  are defined ( $\varsigma = R^{-1}$ ,  $\varphi = -\frac{B_s T_s}{R B_n T_n}$ ) so that  $\mathcal{E}[M^u] = X \sigma^\circ$ .

## 8.2 Modeling Scatterometer Measurement Variation

A commonly used metric to express measurement variability is  $K_p$ , the normalized standard deviation of the measurements, defined as

$$K_p = \frac{\sqrt{\mathcal{V}\text{ar}[\sigma_{meas}^\circ]}}{\mathcal{E}[\sigma^\circ]}. \quad (8.7)$$

A generally used form of  $K_p$  is

$$K_p = \alpha(\sigma^\circ)^2 + \beta(\sigma^\circ) + \gamma \quad (8.8)$$

where  $\alpha$  is related to signal variations,  $\gamma$  is related to noise variations, and  $\beta$  is a cross correlation term [11, 16, 34]. The  $\alpha$ ,  $\beta$ , and  $\gamma$  coefficients depend on the instrument design and measurement signal-to-noise ratio.

Past simulation models have simulated noisy  $\sigma^\circ$  measurements using

$$z = X \sigma^\circ (1 + K_p \nu) \quad (8.9)$$

where  $\nu$  is a zero-mean Gaussian random variable [34]. An estimate of  $\sigma^\circ$  is then

$$\hat{\sigma}^\circ = \frac{z}{X}. \quad (8.10)$$

This model, while simple and widely used, lumps the variations of both the multiplicative signal fading and the additive noise into one variable,  $\nu$ . For some applications

this model is adequate. However, it is difficult to separate the two independent variations and thus handle SNR design tradeoffs and measurement correlation effects.

The proposed model accounts for these issues by modeling a scatterometer measurement as the sum of the mean backscatter,  $m = X\sigma^\circ$ , and two random variables,

$$z = m + Ax + By \quad (8.11)$$

where  $A$  and  $B$  are instrument specific coefficients, and  $x$  and  $y$  are zero mean, unit variance, Gaussian distributed random variables. The two random variables  $x$  and  $y$  have a correlation coefficient

$$\mathcal{E}[xy] = \rho \quad (8.12)$$

where  $0 \leq \rho \leq 1$ . While the origins of  $\zeta(t)$  and  $n(t)$  are independent, the power-law squaring procedure used in processing correlates the signals. The  $\rho$  term accounts for this.

It is noted that modeling of the signal fluctuation,  $x$ , as Gaussian may not always be a valid assumption. Scatterometers integrate the squared signal over a particular time and bandwidth. Application of the Central Limit Theorem suggests that the Gaussian approximation is valid when the time bandwidth product approaches 10 or greater [55]. For most previous instruments, this product has been in the hundreds, easily justifying the assumption, though there have been some exceptions due to the processing used [23]. Newer instruments use high pulse rates which can lower the time bandwidth product to levels where this assumption becomes questionable. In this case, the distribution of  $x$  can be modified appropriately.

To adapt the model to a particular instrument, values for  $A$ ,  $B$ , and  $\rho$  must be determined. While expressions for  $K_p$  have been reported for several instruments, only two examples are presented here. In general, the  $A$  term accounts for the variance of the measurements due to fading, and the  $B$  term accounts for the noise in the signal, both in  $M^{sn}$  and  $M^n$ . Since  $x$  and  $y$  are zero mean, the expected value of the model measurement is  $\mathcal{E}[z] = m$ .

For the measurement scheme developed in [35], the variance of an unbiased measurement has the form of (8.8) and can be expressed as

$$\mathcal{V}\text{ar}[M^u] = \left(\frac{X\sigma^\circ}{R}\right)^2 \left(V + SU + 2S^2[I(2T_s B_s) + I(2T_n B_n)]\right) \quad (8.13)$$

where  $V$  is the normalized signal variance,  $S$  is the noise-to-signal ratio,  $U$  is the signal-noise cross-correlation function, and  $I$  is a special function that starts at 1 and converges to the inverse of its arguments as it increases.

The simulation model can be adapted to this scenario by choosing

$$A = \frac{X\sigma^\circ\sqrt{V}}{R} \quad (8.14)$$

and

$$B = \left(\frac{X\sigma^\circ S}{R}\right) \sqrt{2[I(2T_s B_s) + I(2T_n B_n)]} \quad (8.15)$$

with

$$\rho = \frac{U}{2\sqrt{2V[I(2T_s B_s) + I(2T_n B_n)]}}. \quad (8.16)$$

It should be noted, that while the  $B$  term in (8.15) appears to be dependent upon the return signal magnitude, the noise-to-signal term,  $S$ ,

$$S = \frac{1}{X\sigma^\circ} \left(2T_s B_s \frac{n_o}{2}\right) \quad (8.17)$$

cancels out the signal values, resulting in  $B$  being dependent only on the noise (8.15), i.e.

$$B = \left(\frac{2T_s B_s n_o / 2}{R}\right) \sqrt{2[I(2T_s B_s) + I(2T_n B_n)]}. \quad (8.18)$$

Spencer *et al.* [51] derived the basic statistics for the SeaWinds instrument, showing the variance (in simplified form) to be

$$\mathcal{V}\text{ar}[M^u] = (X\sigma^\circ)^2 \left(\frac{1}{BT_s} + \frac{2S}{BT_n} + \frac{S^2}{BT_n}\right) \quad (8.19)$$

where  $B$  is the bandwidth of both the signal and noise measurements. This variance form is similar to that of the Active Microwave Instrument (AMI) on the ERS-1



satellite [17]. The model is adapted to [51] using

$$A = \frac{X\sigma^\circ}{\sqrt{BT_s}} \quad (8.20)$$

$$B = \frac{X\sigma^\circ S}{\sqrt{BT_n}} = \frac{BT_s n_o}{\sqrt{BT_n}} \quad (8.21)$$

$$\rho = \sqrt{\frac{T_s}{T_n}}. \quad (8.22)$$

In both adaptations it can be seen that  $\rho$  is non-negative since all of the terms are positive. Additionally, in [35]  $U^2 \approx 4V/B_s T_s$ , allowing  $\rho$  to satisfy its definition. The second adaptation [51] also satisfies  $\rho \leq 1$  since  $T_n > T_s$  for SeaWinds.

The separation of signal and noise components in the model allows for significant simplification in the control of simulated signal-to-noise ratios. In both cases illustrated, the  $A$  parameter depends only upon the signal and the  $B$  parameter depends only upon the noise. The signal-to-noise ratio is thus the ratio of  $A$  to  $B$  scaled appropriately to account for the other terms. Similarly,  $S \propto B/A$ .

A final consideration in the development of the statistical model is its simulation of correlation between measurements. This topic has previously been irrelevant due to small measurement overlap and low sampling rates of instruments. Recent designs which oversample the surface now require its consideration. Using the results of Chapter 7, the correlation between measurements (8.6) can be shown to be

$$\begin{aligned} \mathcal{E}[M_k^u M_l^u] &= \frac{X_k X_l \sigma_k^\circ \sigma_l^\circ}{R_k R_l} \left( R_k R_l + W + \right. \\ &\quad \left. \delta(k-l) [SU + 2S^2(I(2B_s T_s) + I(2B_n T_b))] \right) \end{aligned} \quad (8.23)$$

where  $W$  is the fading covariance between the two measurements. When  $k = l$ ,  $W = V$ . Comparing this to the new model,

$$\begin{aligned} \mathcal{E}[z_k z_l] &= \mathcal{E}[(m_k + A_k x_k + B_k y_k)(m_l + A_l x_l + B_l y_l)] \\ &= m_k m_l + A_k A_l \mathcal{E}[x_k x_l] + A_k B_l \mathcal{E}[x_k y_l] \\ &\quad + B_k A_l \mathcal{E}[y_k x_l] + B_k B_l \mathcal{E}[y_k y_l], \end{aligned} \quad (8.24)$$

which requires additional consideration for the two random terms,  $x$  and  $y$ . First,  $y$  is chosen to be independent, identically distributed so that  $\mathcal{E}[y_k y_l] = \delta(k-l)$ . This

models the behavior of thermal noise which is independent from one pulse to another. Conversely, the fading between pulses is correlated with

$$\mathcal{E}[x_k x_l] = \frac{W}{\sqrt{V_k V_l}}. \quad (8.25)$$

The correlation expression is then

$$\begin{aligned} \mathcal{E}[z_k z_l] &= m_k m_l + \left( \frac{W}{\sqrt{V_k V_l}} \right) A_k A_l \\ &+ \delta(k - l) B_k B_l + \rho_{kl} A_k B_l + \rho_{lk} A_l B_k \end{aligned} \quad (8.26)$$

where

$$\rho_{kl} = \mathcal{E}[x_k y_l] \quad (8.27)$$

is the cross-correlation coefficient. Assuming that both measurements,  $x_k$  and  $x_l$ , have an identical time-bandwidth product,  $\rho_{kl}$  for the scheme in [35] is

$$\rho_{kl} = \delta(k - l) \frac{U}{2\sqrt{2V[I(2T_s B_s) + I(2T_n B_n)]}}, \quad (8.28)$$

which is a consistent extension of the single measurement definition of  $\rho$ .

### 8.3 Summary and Application

Simulation of variations in scatterometer measurements is an essential part of performance assessment of data applications. The proposed model simply and accurately produces simulated measurements for these purposes. The model can be easily adapted to most existing instruments and is capable of handling measurement correlation in developing instruments. By separately handling the two components in the measurement variance the model accurately describes their effects and might be used to better describe the signal-to-noise performance of a particular algorithm or application. While the model does not simulate every nuance of a particular instrument, it generates values which have statistically equivalent means, variances, and covariances and therefore is useful in application development and simulation.

## Chapter 9

### Summary and Conclusion

The preceding pages have demonstrated several advancements in the field of satellite scatterometry. The first topic addressed was calibration of the SeaWinds instrument using the calibration ground station. As a ground station calibration approach has never been fully investigated, a methodology was developed for the extraction of calibration parameters using CGS data. The methodology discussed the required steps and tradeoffs involved for calibrating SeaWinds with the CGS. Following the methodology a specific parameter separation approach for the SeaWinds CGS was developed and implemented. The approach detailed the extraction of possible parameters and investigated the observability and identifiability of each. After the approach was defined, algorithms were implemented and results obtained. Initial calibration results proved better than expected. They showed that the CGS is capable of fulfilling its calibration role and that the spaceborne instrument is operating well within expectations. Comprehensive results revealed several limitations of the SeaWinds design and the CGS implementation regarding the extension of instrument operation.

The second topic addressed was the development of new approaches for measurement location calibration. Two were presented, one which improved upon an existing algorithm, and one which is a new development. Both approaches are able to estimate location errors to within a few kilometers. The CGS-based approach and the coastal imaging approach represent methods which successfully estimate desired parameters and can be expanded to obtain more information.

The third topic addressed was the theoretical analysis of scatterometer measurement correlation. Previously this issue has been irrelevant due to the low

overlap factor of scatterometer measurements. Newly proposed instruments which seek to improve spatial resolution significantly oversample the surface and thus require consideration of correlation issues. Statistical expressions were derived for several measurement designs and configurations and analysis of design tradeoffs was presented.

The fourth topic covered was the development of a simulation model for scatterometer application development. Scatterometer data has two random components, multiplicative fading and additive noise. The components are frequently correlated due to instrument processing. Previously no models existed which could be easily adapted to multiple platforms and still provide accurate simulation of these variations. The model developed provides a simple interface for the generation of simulated data sets and the ability to accurately reference the interaction between random variables.

## **9.1 Contributions**

Corresponding to the four topics covered by the dissertation many contributions have been made to the field of satellite scatterometry.

### **9.1.1 Ground Station Calibration**

Calibration ground stations have been a part of the instrument calibration plan for several scatterometers. However, specific abilities and limitations have never been fully considered for the a CGS design, let alone SeaWinds' CGS which is significantly different than past ground station realizations. This dissertation fills this need through the development of a methodology for the SeaWinds CGS. Since the methodology was developed after the construction of the CGS the methodology considers only the limitations already present in the design. However, the methodology was developed so that future ground station realizations can benefit from the successes and shortcomings of the SeaWinds CGS. Future designs will be able to better focus on specific parameters of interest by making educated decisions related to CGS performance.

The second contribution of the CGS analysis is the quantitative calibration results provided to the scientific community, specifically NASA/JPL. The results showed that in general QuikSCAT and SeaWinds are well calibrated and operate within specification. The data showed that SeaWinds timing, while within specification, is not precise enough to allow significant calibration extension. Sensitivity analysis showed that the lack of timing and power precision limited the ground station's ability to estimate attitude. The prescribed sensitivity limitations, the accuracy of attitude estimates, and the precision of power values all correspond to the same levels of variation. These inaccuracies, while small and within specified levels, precluded precision estimation of several parameters. An initial 1 second bias was discovered and corrected for QuikSCAT. A subsequent bias of 8 ms for QuikSCAT and 14 ms for SeaWinds was also shown. These results set limitations for higher resolution data applications through the relationship with measurement location. They also highlight areas of emphasis for next generation designs. A summary of calibration results is provided in Table 5.3.

While the development of the simulation model is subordinate to CGS objectives, the model is the backbone of the approach and represents a third contribution related to the CGS analysis. The simulation model is not only invaluable for assessing instrument performance using the CGS. The simulation model is also useful for the development of other calibration approaches independent of a ground station. The model facilitates the development of the antenna pattern reconstruction approach and can also assist in an extension of the coastal validation technique to estimate attitude. In its current state the software model is tailored to SeaWinds, though it can be adapted to future instruments, allowing future approaches and future instruments to implement the model and develop new techniques for calibration analysis.

### 9.1.2 Measurement Location Calibration

Measurement location calibration has become a popular topic with the emergence of backscatter imaging as a viable application. To date most of the approaches to calibration have focused on low level parameters such as timing and attitude. While this calibration is important, it is also necessary to observe the performance of high level parameters which directly effect scientific analysis such as measurement location. Two separate, new, and original contributions have been made to location calibration. The two approaches represent significant achievement in this emerging field. The coastal validation method make several improvements on the existing Hsiao approach. Through the use of difference imaging, SIR resolution enhancement and coastal truth data the method shows that accurate location values can be determined. The antenna pattern reconstruction method proves that the CGS is not only a valuable choice in low level calibration but is also able to assist in measurement location estimation. Subject to the constraints of capture duration the method demonstrates a high level of precision and accuracy. While the coastal imaging approach is more closely tied to application, it is also more limited by the constraints of resolution and temporal instrument stability. Both methods produced consistent results for SeaWinds measurement location. They demonstrated that the measurements have a mean error of 5 km, well within instrument specifications, but significant for new applications such as high resolution imaging.

### 9.1.3 Multiple Measurement Statistics

The contribution made by the dissertation culminates the continuing study of measurement variance, particularly the  $K_p$  parameter. Previous works have developed expressions for  $K_p$  for various measurement configurations. This work expands the applicability of  $K_p$  to new measurement issues. The expressions and analysis presented allow new designs, such as HYDROS, and new applications to further improve the performance and resolution of spaceborne scatterometry by improving the understanding of tradeoffs involved in instrument design.

#### **9.1.4 Noise Modeling**

Simulation of scatterometer data is essential to the development of new instruments and new applications - the accuracy of simulation in many cases limits the accuracy of the design. Previous simulation models exist in one of two categories. First, several models exist which are appropriately accurate, but are highly instrument specific. These models are valuable for a specific instrument but are not easily adapted to other platforms. Other models exist which are adaptable, but do not accurately model both the additive noise and the multiplicative fading which exists in instrument data. The noise model developed here bridges the gap between these two models. It requires some instrument customization yet provides a high level of simulation accuracy. The simple implementation allows designers to understand how tradeoffs in design parameters effect overall instrument performance.

### **9.2 Future Work**

While this work attempts to cover the issues addressed as completely as possible, several important areas for future research exist.

#### **9.2.1 Future Calibration Ground Stations**

The theory and analysis presented here relating to the SeaWinds Calibration Ground Station can be used to improve the design for future instruments. Three possibilities are proposed. The first possibility is a low budget, low capability ground station. The extreme precision of the blind analysis is directly attributed to the GPS timing reference and precision oscillators based on a GPS controlled phase-locked loop. A low cost ground station having a nominal precision front end receiver with a GPS timing and frequency reference is one option. This configuration is able to validate basic instrument operation and be able to precisely calibrate timing and frequency. Recorded power values have nominal precision and attitude estimates are limited for this design.

The second possibility of future ground stations is to replicate the current configuration with several improvements. The primary limitation of the CGS design

is its short capture time and inability to uniquely identify individual pulses. The effect of short capture time is visible in the antenna pattern reconstruction method for measurement location, and to a lesser degree, in attitude and power estimation. The capability of capturing more sweeps of the instrument antenna would improve sensitivity to small changes in attitude and power. This conclusion is particularly true for instruments which have higher pulse rates, thus improving azimuthal sampling of the instrument antenna pattern. For a CGS of this type to be effective complimentary changes must also be implemented in instrument design. The asynchronous polling timing systems used by the SeaWinds instruments are detrimental to CGS-based attitude calibration. In addition, better antenna pattern measurements must be made so that power can be more accurately simulated. The conditions of this CGS implementation are strict, but are necessary to improve the precision over current estimates.

The third foreseeable realization of calibration ground stations is the option of multiple locations. Current emphasis on attitude estimation suggests a small, closely spaced, constellation of 3-5 ground stations. Several issues related to this type of configuration must be addressed, specifically coordination of data sets and the sensitivity of the configuration. While this type of arrangement improves the ground sensitivity of attitude variations it still mandates improved reporting of instrument performance, both in timing and transmitted power.

### **9.2.2 Measurement Location Tools**

Development of specific measurement location calibration tools is in its infancy, particularly as it relates to imaging. Results obtained suggest that techniques of this kind possess the possibility to estimate measurement location more accurately through improved image resolution data separation and coastal comparisons.

Model perturbations for attitude estimates using the simulation model are a distinct possibility. The antenna reconstruction method already uses the model and is shown to have better performance than direct CGS estimates. Precision is limited because the mapping is underdetermined - the three degrees of attitude freedom are



mapped to a two dimension coordinate system. However, by limiting the realm of possible attitude values using other methods this approach is potentially viable.

### **9.2.3 Noise Model Application**

The construction and validation of the simulation noise model presents an opportunity for a wide variety of new applications. The noise model was envisioned during an attempt to accurately generate noise for simulations of the SIR algorithm. Now that random fading is separable from additive noise an assessment of the behavior of the SIR algorithm is now tractable. This includes modeling the behavior of spectral noise amplification and the effect of fading independent of the additive noise.

The noise model also can be used to improve other applications such as high resolution wind calculation. New applications are seeking to estimate wind at scales of 5 km and even 2.5 km as opposed to the 25 km wind grid generated for SeaWinds [30,31]. This improved resolution requires better simulation of the effects of noise and the separation of fading from noise. The developed noise model can facilitate this development.



## APPENDICES



## Appendix A

### Issues Related to SeaWinds CGS Calibration

This appendix contains two points of analysis related to the implementation of the calibration methodology for SeaWinds. The first section discusses internal calibration and stability of the CGS. The second section presents results related to blind calibration.

#### A.1 Ground Station Self-Calibration

An essential first step in obtaining calibration results from the CGS is to assess accuracy and stability of the CGS. The SeaWinds CGS operates autonomously using a network of computer workstations which predict capture times, prepare hardware for capture, perform captures, and process data. The technical foundation of the ground station is an RF receiver, a GPS receiver, and calibrated noise source. The GPS receiver provides timing information to the workstation and triggers data capture. It also provides a stable reference for CGS phase locked loop oscillators. Internal power calibration is governed by a NIST standardized noise source.

When received by the CGS, the signal first passes through the radome and into the antenna. The radome is constructed of composite fiberglass and has a loss figure of less than 0.01 dB. The antenna is a circularly polarized corrugated horn antenna, having an aperture of 12 cm. It is designed to have a large beamwidth so that the effects of CGS related pointing errors are limited. Testing has shown the antenna to have a peak directivity of 20.09 dB, with a 3 dB beam width greater than 13°. Over the duration of a capture the CGS antenna is held stationary to mitigate vibrations. During this time the change in pointing towards SeaWinds due to spacecraft motion is nominally 3.2°, depending on capture geometry, resulting in

a maximum change in antenna gain of 0.35 dB. Once the signal passes through the antenna it is amplified and mixed down in a series of stages. The overall gain of the stages is 56.24 dB, calculated using the internal noise source. The variation of the internal system is less than 0.01 dB. Finally, the signal is digitally sampled by an analog-to-digital (A/D) converter. Discounting antenna pointing errors, the data recorded by the CGS is accurate to within 0.07 dB. Assuming CGS pointing accuracy within  $1^\circ$ , power measurements reported by the CGS are determined to have an accuracy of 0.15 dB.

The center frequency of the signal received by the CGS, nominally 13.402 GHz, varies due to the Doppler effect of the moving satellite with a range of  $\pm 500$  kHz. The CGS mixes received signals down in a series of steps, 13.007 GHz and 360 MHz, resulting in a center frequency of 35 MHz. The signal is then digitally sampled at a rate of 41.5 MHz and decimated by a factor of 8, resulting in a center frequency of 1.3125 MHz and an effective sampling rate of 5.1875 MHz. CGS filters limit the bandwidth of the signal to 2 MHz. Each of the mixing stages are disciplined with a 10 MHz GPS-based reference signal. The accuracy of the GPS oscillator is 1 part in  $10^{12}$ , resulting in negligible CGS induced frequency errors.

Data capture begins when the analog-to-digital (A/D) converter is triggered by a signal from the GPS, and is accurate to within 20 ns. The time precision of the CGS is  $0.193 \mu\text{s}$ , the inverse of the sampling rate. Since the A/D is tied directly to the GPS, no other significant timing factors exist.

An important portion of CGS validation is the stability of measurements over time, especially considering that the location of the CGS changed midway through its mission. Timing and frequency are directly tied to the GPS signal, allowing us to assume stability over time and between White Sands and Provo. However, power stability must be evaluated since there is no external power reference. Power is monitored by measuring the statistical properties of the signal from the CGS noise source over time. The CGS is also able to make noise measurements of uncalibrated warm and cold loads, an RF foam absorber in the radome and zenith measurements of the sky. The power of the noise at the system input is equal to  $kTB$ , Boltzman's

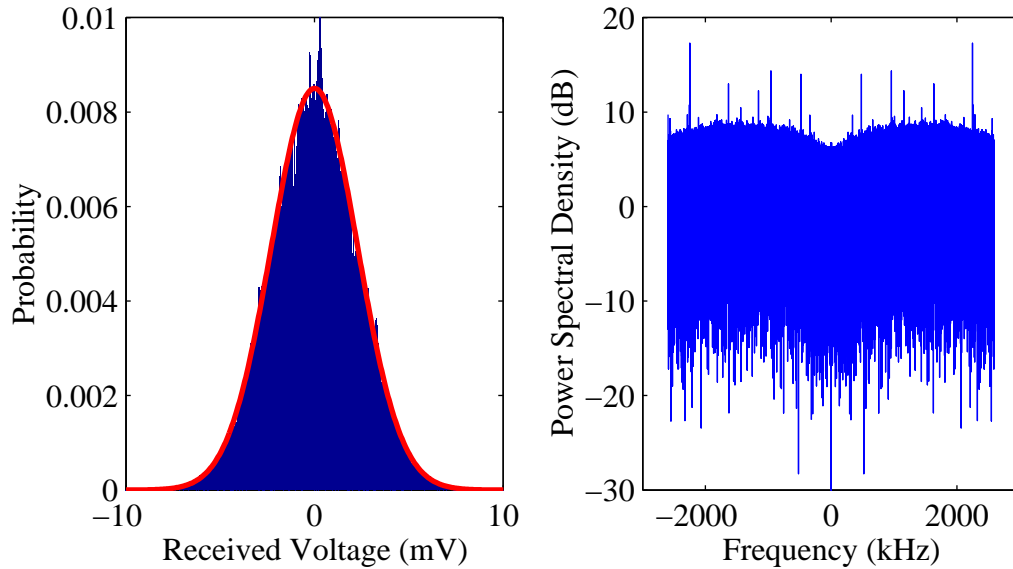


Figure A.1: (left) Histogram of a noise source sample recorded by the CGS. A Gaussian curve of equivalent mean and variance is superimposed for reference. (right) Power spectral density of the data. The spectrum of the data follows the response of the CGS's 2 MHz Butterworth filter.

constant multiplied by the noise temperature (either sky or noise source) and the system bandwidth. Accounting for system gains, at room temperature (298 K) the noise power received at the CGS is -81.5 dBm.

Figure A.1 shows a histogram and power spectral density of a 0.2 second sample from the calibrated noise source, a Gaussian curve with equivalent mean and variance is superimposed on the histogram. The figure shows that the noise has a Gaussian distribution with a minor exception around the mean suggesting a slight A/D induced skew. Since this error is at low voltage levels it does not significantly effect power values of measured pulses. The received spectrum resembles the passband of the 2 MHz Butterworth filter which is part of the CGS receiver. Noise samples taken from other sources, such as the warm and cold loads, display similar characteristics.

A simpler, albeit less controlled, method of obtaining noise-only information is to use actual CGS captures and measure the noisy samples between pulses.

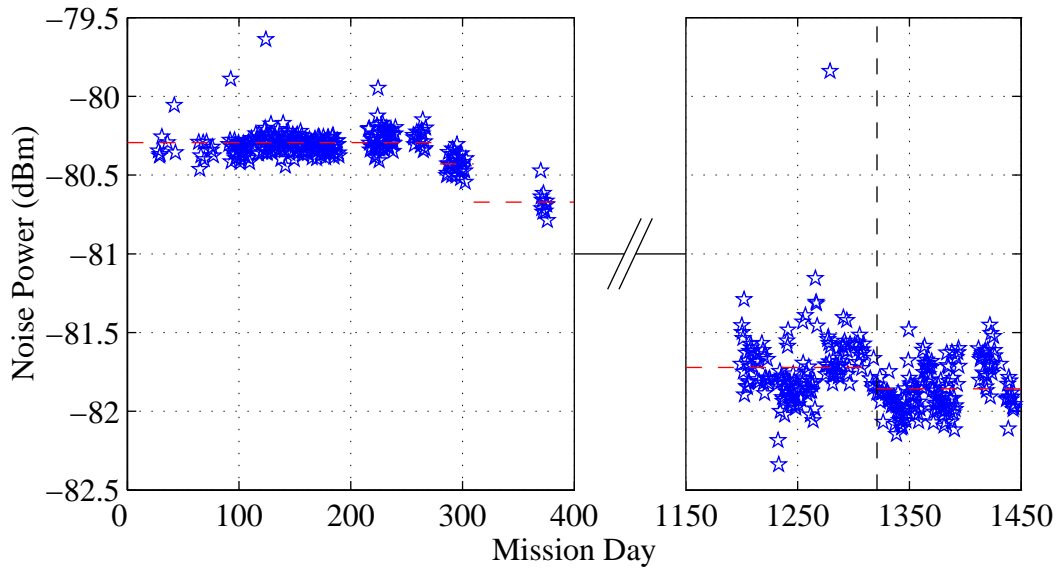


Figure A.2: Noise power as a function of mission day. Noise power is calculated using (A.1) from samples taken between received pulses. The figure uses the convention of mission day, the days since the CGS went into operation at QuikSCAT’s launch. The gap in data between day 400 and day 1150 represents the time when the CGS was not capturing data. Up to day 1150 the CGS was located in White Sands, New Mexico, after day 1150 the CGS was located in Provo, Utah. The vertical line at day 1321 corresponds to SeaWinds’ turn on, January 28, 2003, when the CGS ceased to capture QuikSCAT data and began to track SeaWinds.

This method is equivalent to a zenith, or cold sky noise-only measurement. SeaWinds’ has a PRI of 5.4 ms and pulse width of 1.5 ms leaving 3.9 ms of noise-only measurements between pulses. Distributions using this data are similar to the noise source data shown in Figure A.1.

One drawback of noise samples taken from data captures is the possibility of multipath contamination. Multipath occurs when transmitted SeaWinds pulses bounce off another terrestrial object and reflect into the CGS receiver. Since a multipath signal is not received directly from the satellite, it corrupts the true measurement as well as the measured noise. It has been shown that multipath for the CGS is not an issue, with a maximum possible power value of -140 dBm [5].



Figure A.2 shows the recorded noise power for each CGS capture as a function of mission day. Noise power,  $P_n$ , is determined using

$$P_n = \hat{\sigma}_n^2 \left( \frac{Y_{cgs}}{Z_{ad}} \right) \quad (\text{A.1})$$

where  $\hat{\sigma}_n^2$  is the variance of the noise voltage for the capture,  $Z_{ad}$  is the impedance of the A/D, and  $Y_{cgs}$  is a gain conversion constant for the CGS, described in Table 5.1. The figure shows that the mean noise power for the first 300 days of the CGS mission is -80.2 dB. After this point, the noise power diminishes, to almost -82 dB by mission day 1450, or June 1, 2003. (Mission day is defined as the number of days since the launch of QuikSCAT and the turn on of the CGS.) A subsequent comparison of other noise-only data also indicates a decrease of 1.7 dB in noise power. While of some concern, the results are not unexpected considering the age and movement of the ground station. This degradation does not effect the ability of the CGS to calibrate SeaWinds as comparable decreases in SeaWinds power measurements are compensated for.

## A.2 Blind Calibration Results

The second section of this appendix reports the results for blind CGS parameter estimation discussed in Section 5.3. Results are separated into three sections: timing, frequency and power.

### A.2.1 Timing Calibration

Results of pulse width estimation using a split gate filter are shown in Figure A.3. The histogram shows the distribution of pulse width estimates as a function of CGS samples. The figure shows that the pulse width distribution is approximately Gaussian, with a mean of 7754.92 samples and a standard deviation of 1.18 samples. This translates to a mean pulse width of 1.494924 ms and a deviation of 230 ns.

Pulse width estimates are separated into several categories to investigate dependencies on multiple issues. Dependencies include beam (inner or outer), pass direction (the instrument approaching the CGS or receding from it), and orbit type

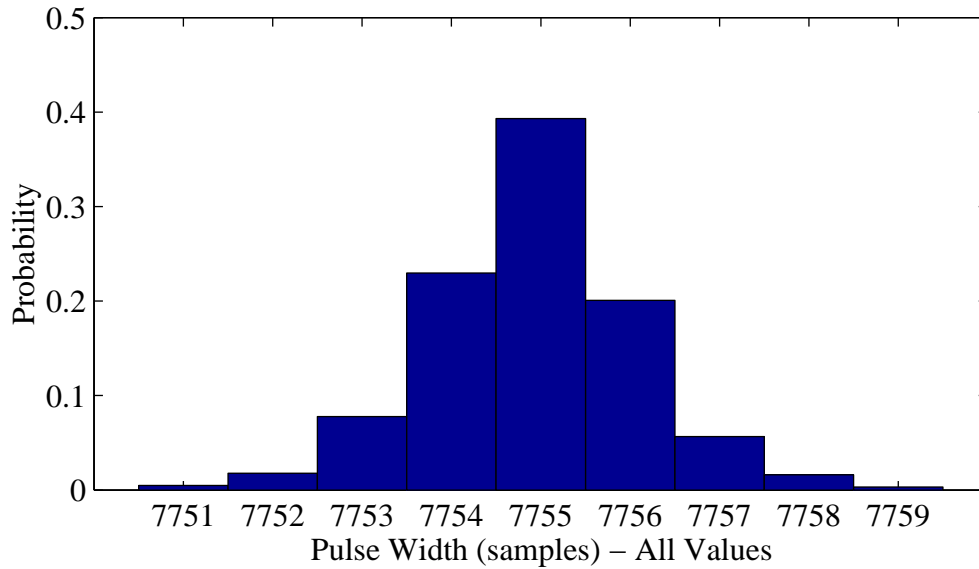


Figure A.3: Histogram showing the distribution of pulse width estimation. The mean value of all data is 7754.92 A/D samples (1.494924 ms). The standard deviation is 1.18 samples (230 ns).

(ascending or descending). Figure A.4 shows a breakdown of pulse width statistics for these three subcategories. Overall, the measurements display consistency, with no visible anomalies.

From the above results, it is concluded that the pulse width of SeaWinds is 1.494924 ms. While the standard deviation of the measurements might reflect actual pulse variation, it approaches the realizable precision of the CGS and thus is attributed to A/D sampling. The remaining variation is caused by additive noise in the recorded signal.

The other timing parameter of interest is pulse repetition increment. Figure A.5 shows the results of PRI estimation for a single instrument pass as a function of the SNR of the two pulses used in the estimate. The plus symbols (+) represent a PRI estimate error of greater than  $5 \mu\text{s}$ , and an asterisk (\*) represents an estimate error of more than  $20 \mu\text{s}$ . The figure confirms the results of the arrival time simulation shown in Figure 5.8 which display a similar dependence on SNR.

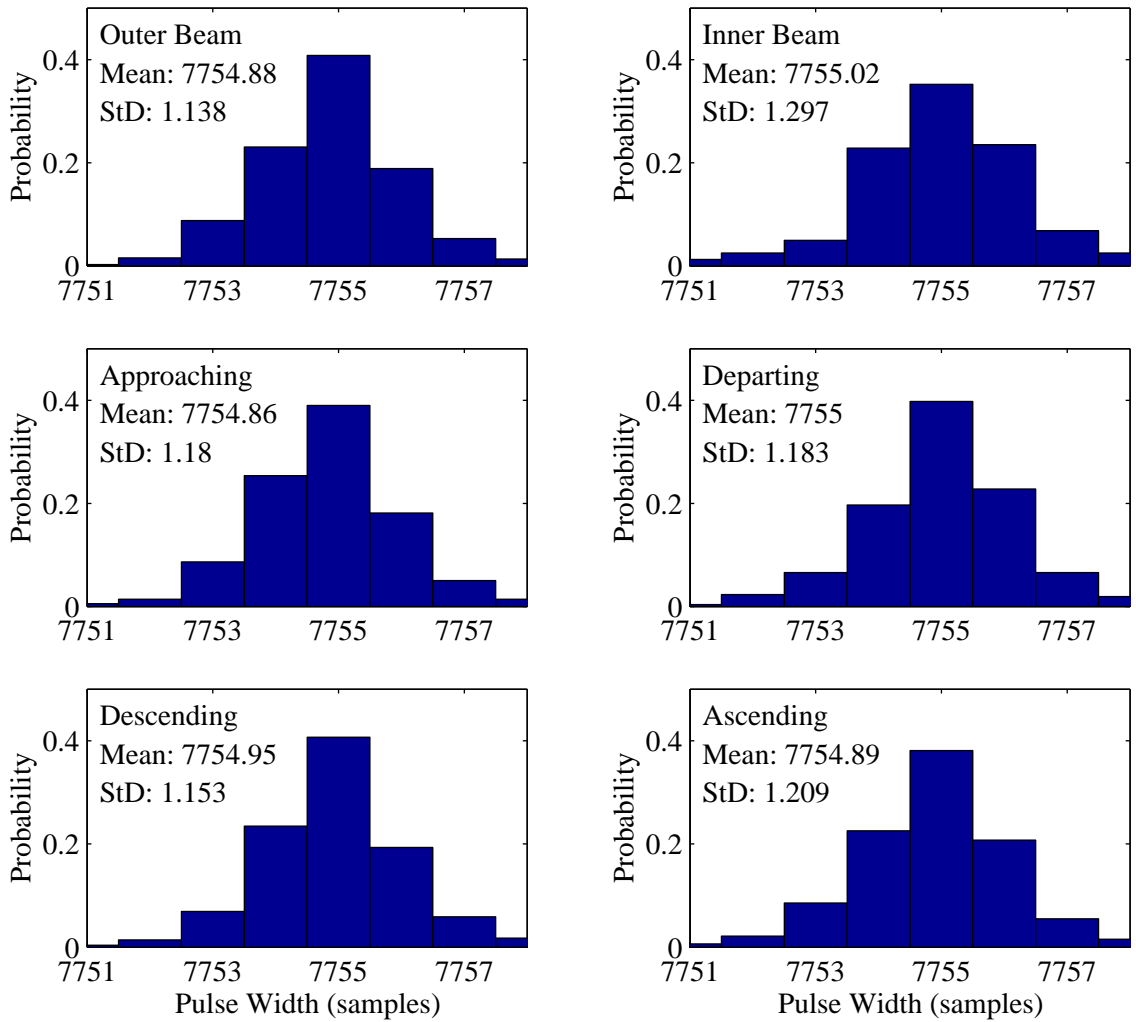


Figure A.4: Multiple histograms showing distributions of pulse width for various conditions such as beam, orbit type, and pass direction.

Next, Figure A.6 shows a histogram of PRI estimates from a single instrument pass. Estimates of PRI are obtained by finding the time difference between every combination of pulse with an SNR above 15 dB as described in Section 5.3. In this case two 20 second captures are shown (an outer beam only pass geometry). The abscissa of the plot is the variation from the mean estimate, 5.389527 ms, displayed in nanoseconds. The ordinate is the derived probability of the estimate.

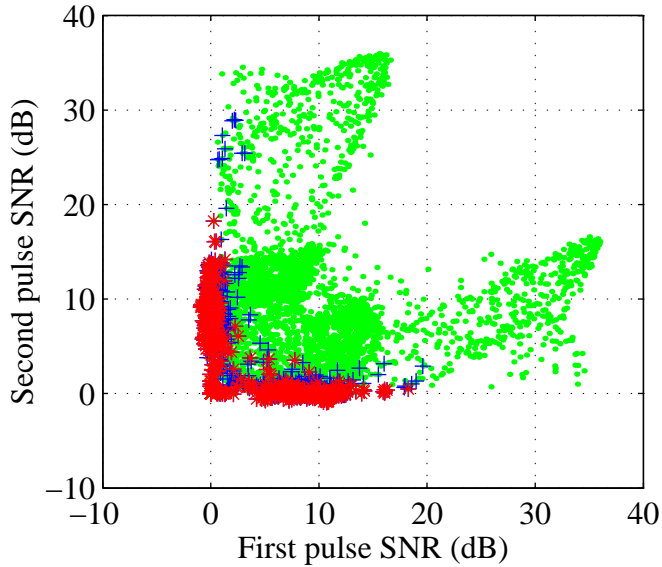


Figure A.5: Scatter plot showing the effect of SNR on PRI estimates. Each point represents a single PRI estimate using consecutive pulses. The pulses (+) represent pulses where the PRI differs from the mean by more than 5 $\mu$ s. The stars (\*) represent pulses where the PRI estimate differs by more than 20 $\mu$ s.

The derived distribution is clearly bi-modal, caused by instrument movement during capture. As the instrument approaches the CGS the range shortens slightly from pulse to pulse, thus decreasing the PRI. Conversely, as the satellite recedes from the CGS the range and PRI increase. This effect is also seen with pulse width estimates in Figure A.4, though to a much smaller extent. Each of the peaks in Figure A.6 display a low variance, demonstrating the accuracy of arrival time estimates and PRI differencing using large pulse multiples.

Figure A.7 next shows the mean PRI estimate for each instrument pass as a function of mission day using the same criteria as Figure A.6. The mean value of the PRI shown is 5.389527 ms with a deviation of 35 ns. The figure not only confirms the PRI stability of both QuikSCAT and SeaWinds, but also reiterates timing stability of the CGS.

Finally, Figure A.8 separates the data used in Figure A.7 into approaching and receding captures, performing separate estimates. The figure clearly shows the

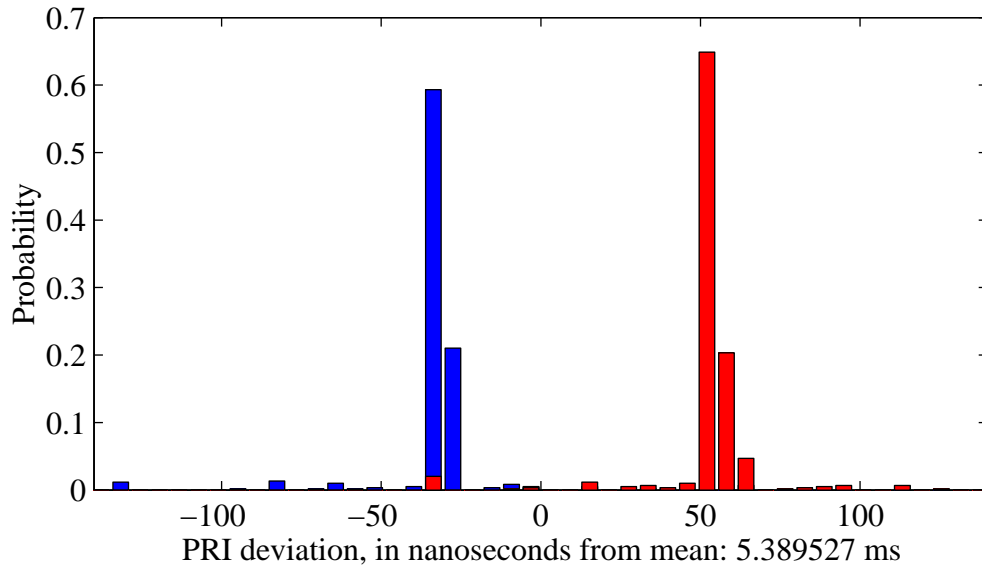


Figure A.6: Histogram of PRI estimates for one data capture. The data is centered about the mean of is 5.389527 ms. The histogram is highly bimodal showing the difference in PRI between approaching and receding captures. Approaching captures shorten the PRI, while receding captures lengthen the PRI. The variance of each mode is 30 ns.

differentiation between the two pass directions. The mean value of the approaching PRI is 5.389471 ms with a standard deviation of 34 ns, the mean value of the receding PRI is 5.389604 ms, a difference of 133 ns. The standard deviation of the receding PRI is 31 ns.

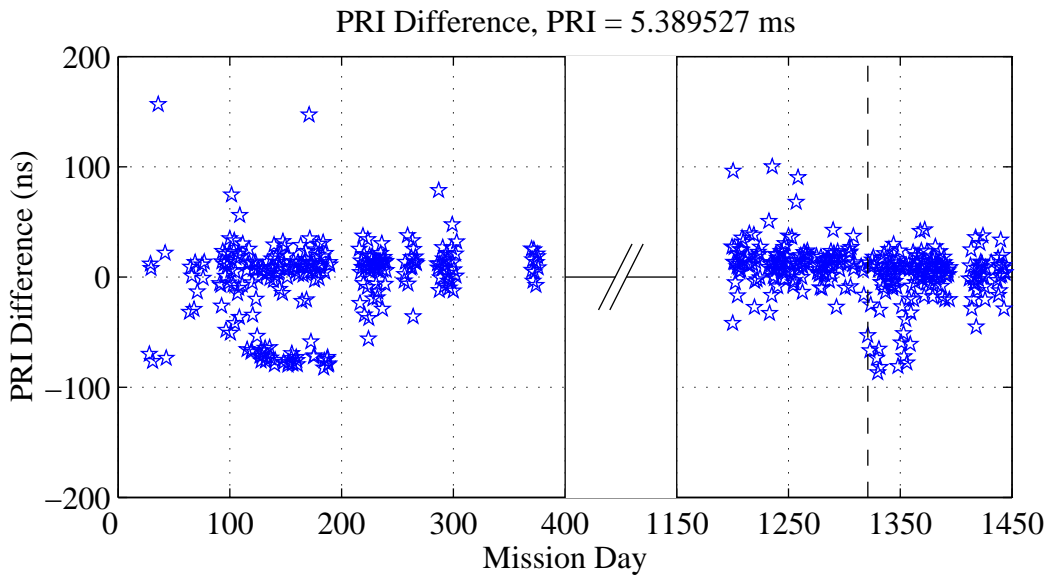


Figure A.7: Difference of the mean capture PRI from the overall mean of 5.389527 ms as a function of mission day. The figure demonstrates the stability of the PRI for both instruments.

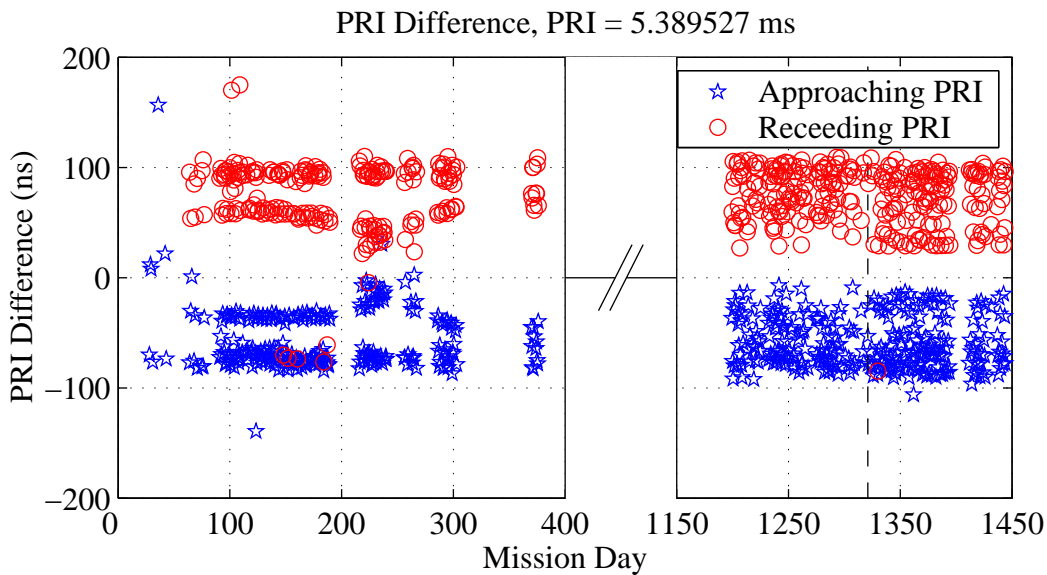


Figure A.8: PRI difference separated by pass direction. The figure demonstrates the effect of pass direction on the PRI, a difference of 133 ns. It also shows a slight degradation of timing accuracy for the CGS in Provo, Utah as compared with its location in White Sands, New Mexico. The cause of this difference is uncertain.

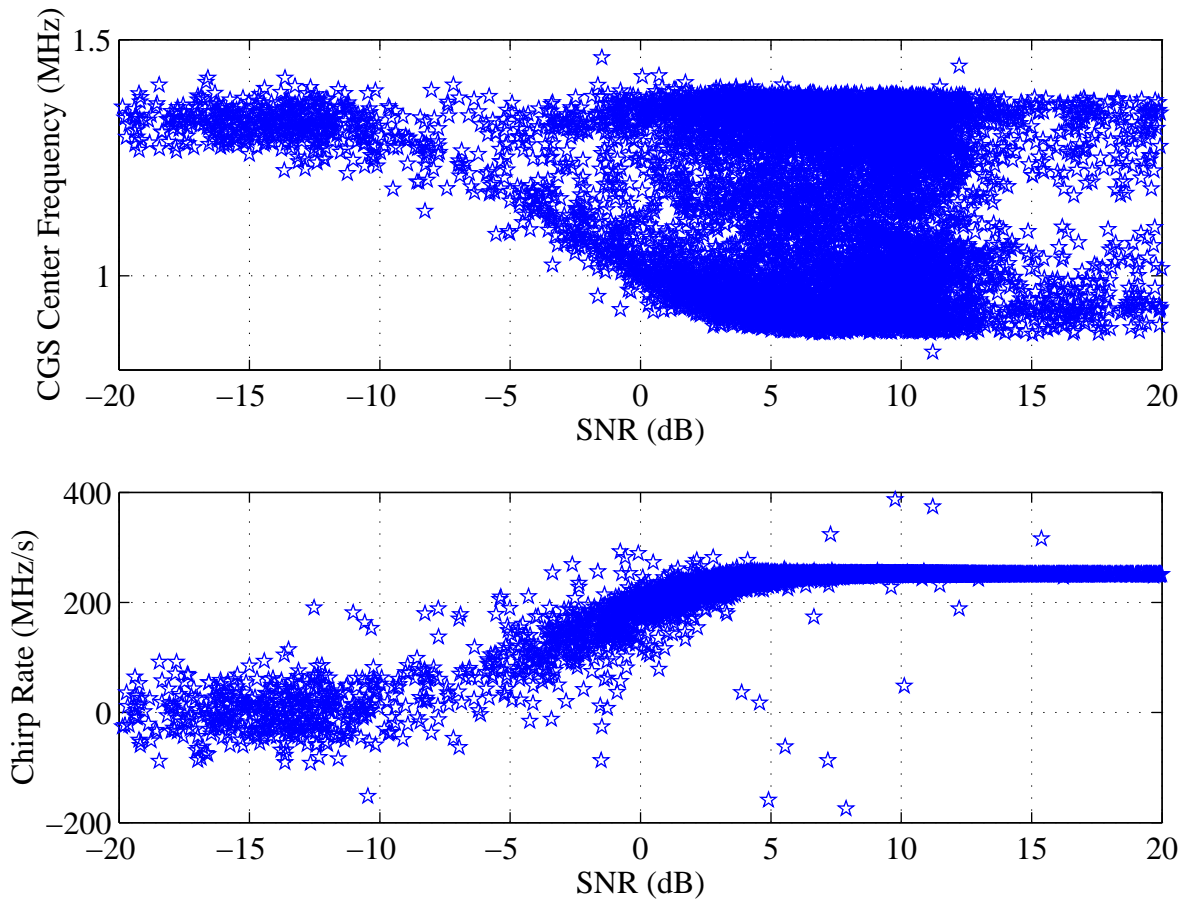


Figure A.9: Scatter plot of estimated carrier frequency and chirp rate as a function of SNR. The top plot shows that the carrier frequency does not converge to a single value since each pulse has a variable frequency. The chirp rate is fixed and thus converges. The results compare well to simulations shown in Figure 5.9.

### A.2.2 Frequency Calibration

The next group of calibration parameters are related to frequency, in particular the center frequency of the signal and the rate of the LFM chirp. Figure A.9 shows a scatter plot of center frequency and chirp rate estimates for the entire QuikSCAT and SeaWinds CGS data set. The data confirms the effectiveness of the Tretter algorithm and the accuracy of the data simulation. The data shows that the chirp rate estimates have very little variance at high SNR and trend to zero at low

SNR, as expected. The results of the carrier offset do not converge due to the Doppler induced variable received center frequency.

The average CGS capture yields 12 sweeps, or rotations of the SeaWinds antenna across the CGS location. In general, the first six sweeps have a larger frequency magnitude than do the last six sweeps due to the Doppler compensation. While the mean value of the 12 sweeps approaches the SeaWinds carrier frequency the geometry of each capture and the pulses selected for analysis impose limitations on the precision of this technique. Using this generalization, Figure A.10 shows the mean carrier frequency of each pass as a function of mission day. The figure shows results for all pulses and for those with high SNR ( $> 10$  dB). The figure shows first, that the carrier frequency for both instruments is stable and consistent, and second, that power limitations have little effect on mean estimates due to the unbiased nature of the algorithm. The mean for the QuikSCAT White Sands portion is 1.329 MHz, for the QuikSCAT BYU portion it is 1.325 MHz and for SeaWinds it is 1.317 MHz. The standard deviation of each is approximately 32 kHz. The difference between these estimates and the specification of 1.3125 MHz is 16.9 kHz, 12.9 kHz, and 4.9 kHz respectively, converting to carrier frequencies of 13.402017 GHz, 13.402013 GHz, and 13.402005 GHz.

The other frequency parameter of interest is the rate of the chirp. Figure A.11 plots the estimated chirp rate as a function of pulse count for a sample CGS capture. The data in the figure confirms conclusions gained from simulation, that the chirp rate estimates are effected by pulse SNR, and that low SNR pulses tend to decrease the estimate value.

Figure A.12 shows the mean chirp rate value of each CGS capture as a function of mission day, for both the power limited pulses ( $> 10$  dB SNR) and all pulse cases. The figure shows that the chirp rate estimate is extremely accurate and follows well with expected theory. The mean value for the QuikSCAT White Sands segment is 250.747 MHz/s. For QuikSCAT at BYU it is 250.747 MHz/s and for SeaWinds it is 250.743 MHz/s.



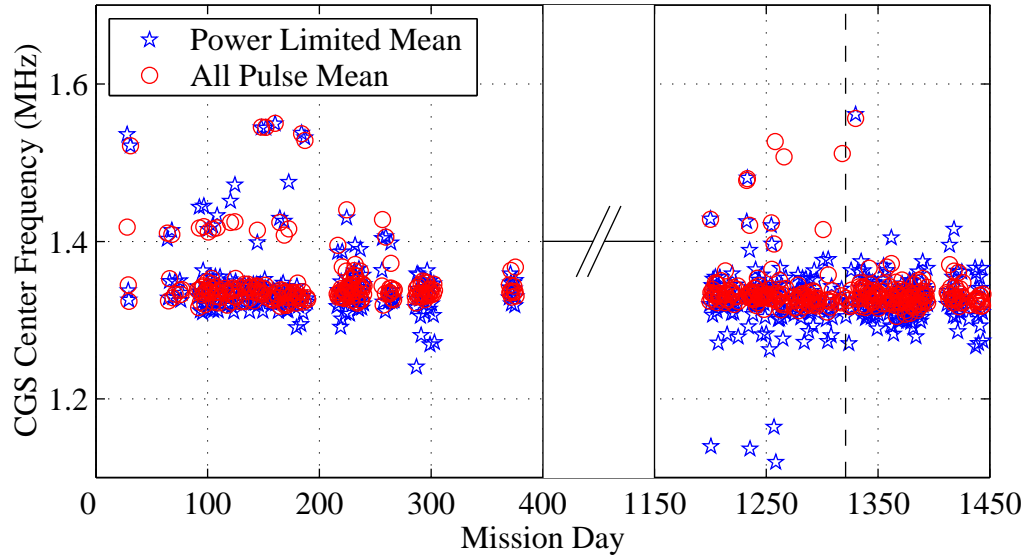


Figure A.10: CGS reported center frequency as a function of mission day. The figure shows that limiting the SNR of the pulses does not improve performance. It also shows that SeaWinds and QuikSCAT are operating at essentially the same center frequency.

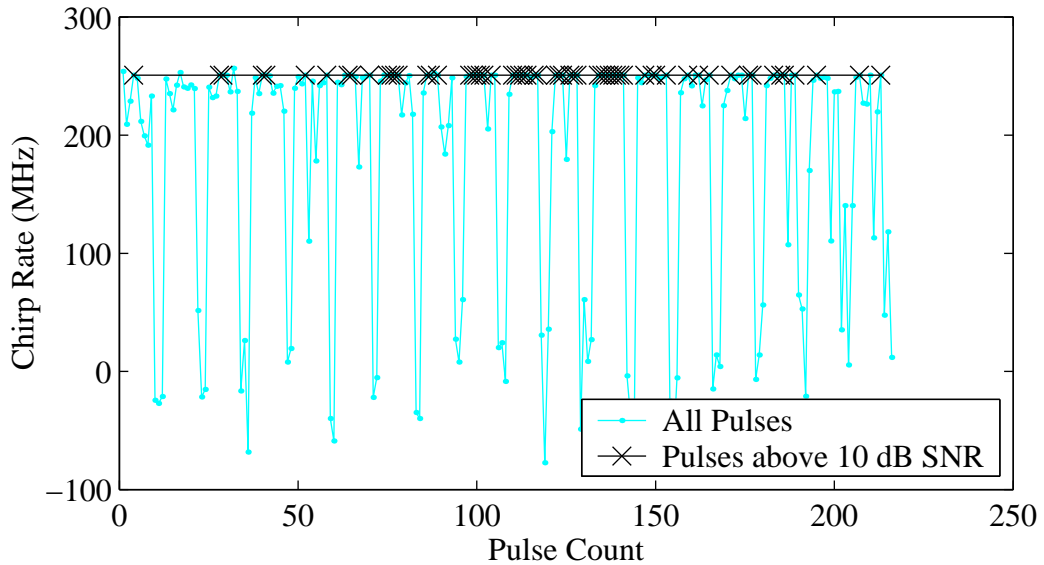


Figure A.11: Example of chirp rate estimation. Limiting SNR improves accuracy of the algorithm.

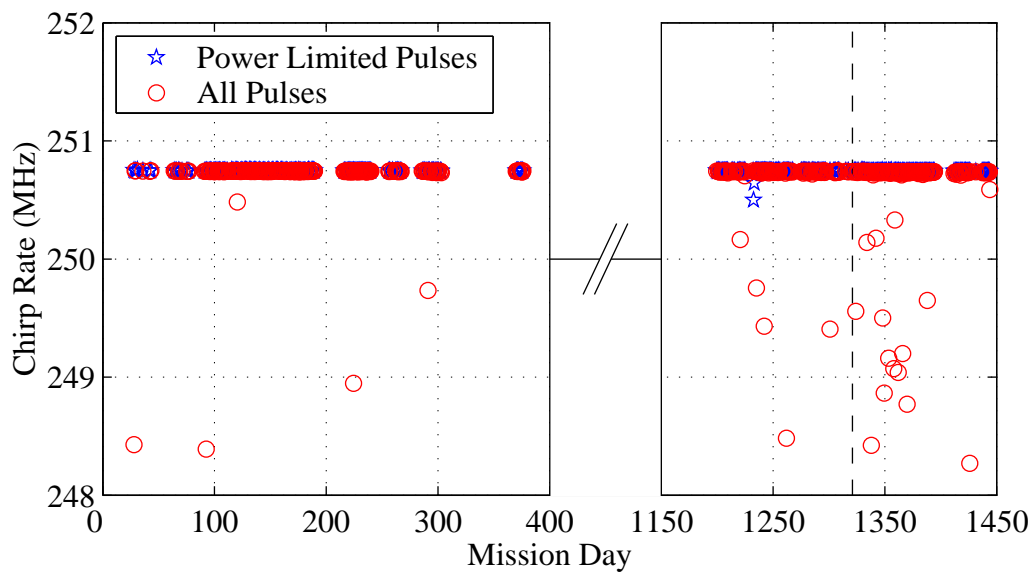


Figure A.12: Chirp rate as a function of mission day. The figure demonstrates the excellent stability of the chirp generation over the length of the missions and across platforms.

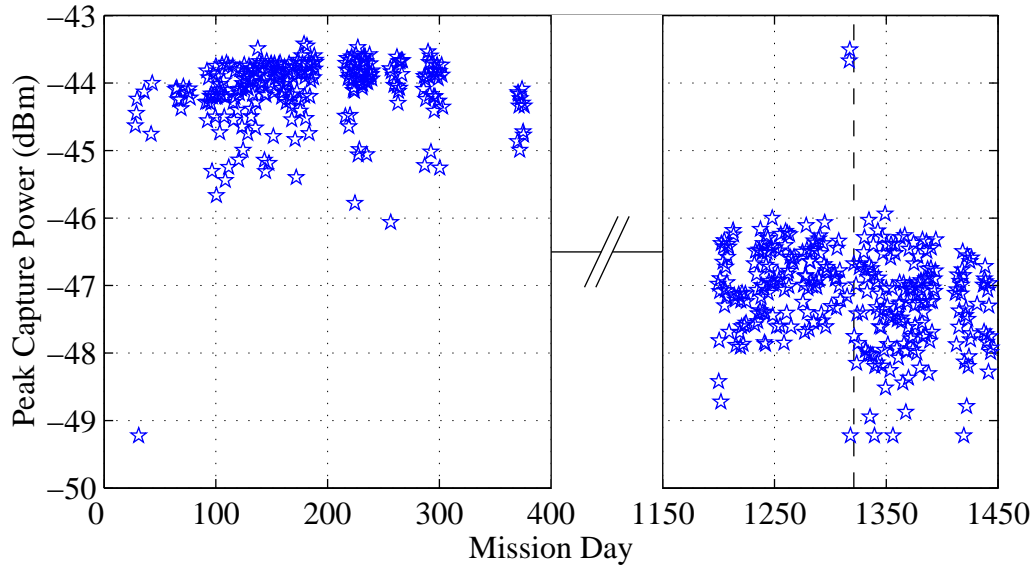


Figure A.13: Peak power of each capture as a function of mission day. The figure shows the degradation of power at the Provo, Utah location of the CGS when compared to the White Sands location. This degradation is also observed in the noise only values (see Figure A.2).

### A.2.3 Power Calibration

Figure A.13 shows the peak received power at the CGS for each pass as a function of mission day. When compared to the noise power (Figure A.2) several observations are made. First, the drop in the noise power is also apparent in the signal power data, confirming the diminishing gain of the CGS. It is concerning that the drop in signal power is more pronounced than the noise power, having a peak to peak drop of 2.5 dB, compared to a 1.7 dB drop in the noise power. This difference of 0.7 dB is cause for concern. Unless the CGS system is non-linear, identical drops in power should be observed in both the noise and signal power measurements. The difference exceeds the determined tolerances of CGS power accuracy. While the possibility of non-boresight pointing for all of the Utah captures exists, it seems an unlikely separation.

The second observation from the figure is the comparison to calculated values. The peak power received for QuikSCAT is -43.4 dBm, corresponding well with the calculated maximum of -43.01 dBm. Compensating for reduced CGS power, SeaWinds peak power is -44.32 dB. A third observation from Figure A.13 is the consistency between QuikSCAT and SeaWinds values. While the power drops off over time, the figure displays little difference in power between the two instruments indicating excellent cross platform performance.

Along with calculation of transmit power, identification of power differences between captures, orbit locations, and polarizations is desired, which is indicative of overall stability of the instrument transmitter. Both satellites have orbits which provide two CGS captures each day. The CGS observes the instrument as it is going north in the first half of the orbit (ascending) or as it is going south in the second half of the orbit (descending). For QuikSCAT, the first capture of each day is a descending pass and the second capture of the day is an ascending pass. For SeaWinds the first CGS capture is an ascending pass, and the second capture is a descending pass.

Figure A.14 shows the maximum power data separated into pass type. The figure shows that there is no distinguishable difference in power between ascending and descending passes for either instrument. For QuikSCAT the mean difference is -0.18 dB (ascending is greater), for SeaWinds the difference is 0.19 dB. The median difference for both instruments is less than 0.1 dB.

The other power analysis of interest is the comparison of polarizations, referred to as beam balancing. Beam balancing constitutes a significant portion of SeaWinds post-launch calibration, with the CGS making a valuable contribution. Since the CGS has a circularly polarized antenna it is unable to uniquely differentiate between the H-pol and V-pol pulses. It is, however, able to use orbit ephemeris and capture timing to determine which beam is observed. The first capture is usually the outer beam, since it crosses first. Though the possibility certainly exists to confuse the two beams, capture timing is precise enough to minimize these chances. Figure A.15 shows the peak received power for each SeaWinds CGS pass separated into outer beam (V-pol) and inner beam (H-pol) captures. The data illustrate a distinct difference in

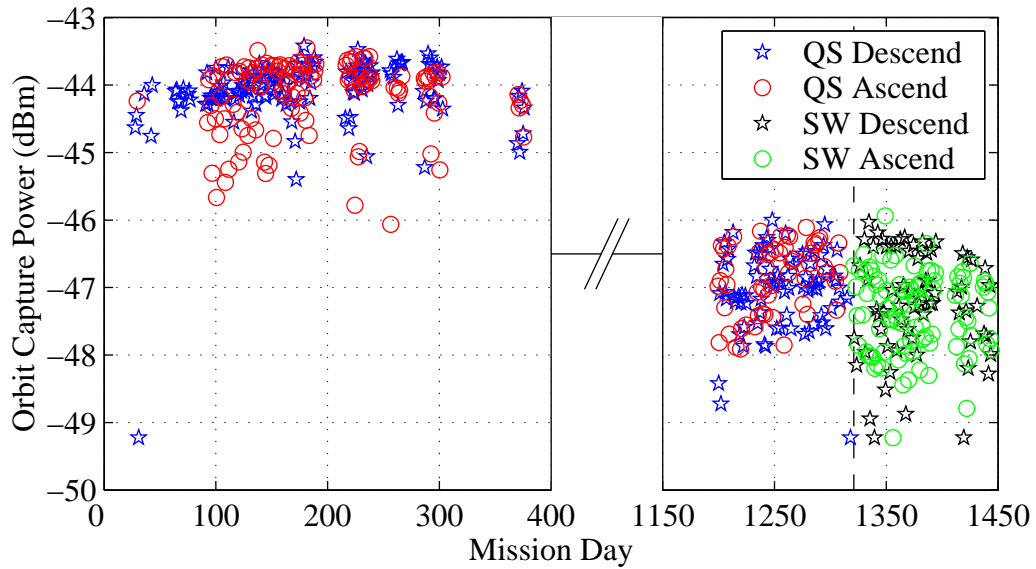


Figure A.14: Peak received power as a function of mission day, separated into orbit passes. The figure shows no distinguishable evidence of a bias between ascending passes and descending passes.

received power. The maximum value for QuikSCAT's outer beam is -43.22 dB and is -43.64 for the inner beam. The maximum for SeaWinds' outer beam is -45.81 dBm and is -45.72 for the inner beam, -44.11 dBm and -44.02 dBm when compensated for CGS power degradation. While these values show a discrepancy between beams, some of the difference is caused by different gain and power coefficients. As noted in Table 5.2, the peak gain of each antenna is slightly different for both instruments as is internal instrument amplification and atmospheric loss. Second, the single peak value received at the CGS over two years of data is a poor metric for estimating determining beam balance. It is therefore necessary to recognize the limitations of power estimates.

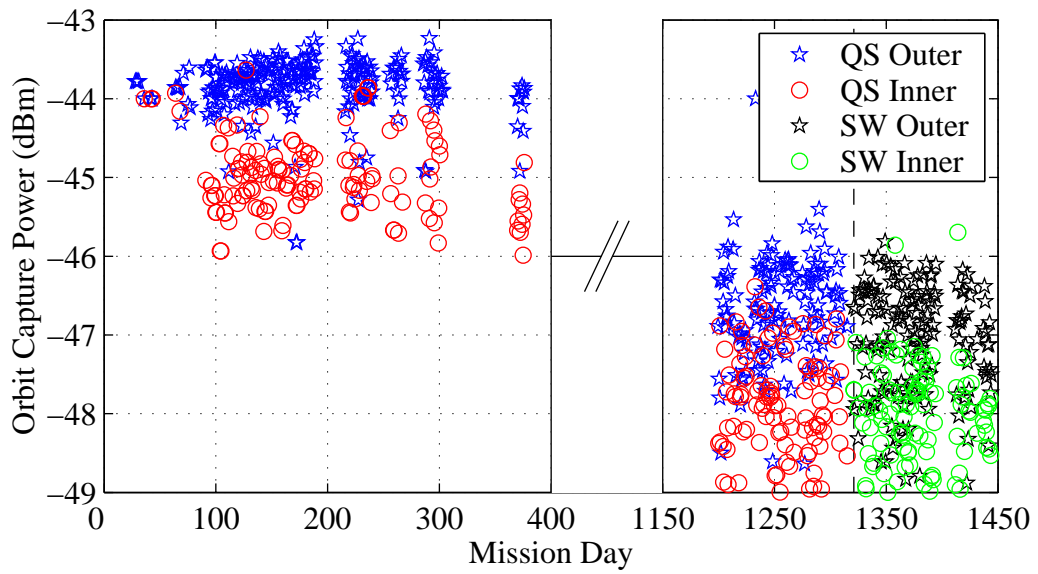


Figure A.15: Peak received power as a function of mission day, separated by beam (polarization). The figure shows a distinguishable difference between the outer beam (V-pol) and inner beam (H-pol).

## Appendix B

### Derivation of Multiple Measurement Statistics

This appendix includes detailed derivations used in Chapter 7.

#### B.1 Expectation of Surface Backscattered Voltage

##### B.1.1 Second-Order Expectation

Using the properties of a uniform distribution we see that

$$\begin{aligned}\mathcal{E}[Z(a)Z^*(b)] &= \mathcal{E}[v_d(a)v_d(b)]\mathcal{E}[e^{j[\phi_d(a)-\phi_d(b)]}] \\ &= \mathcal{E}[v_d(a)v_d(b)]\delta(a-b) \\ &= \mathcal{E}[v_d^2(a)]\delta(a-b) \\ &= A_d(a)\sigma_d^\circ(a)\delta(a-b).\end{aligned}\tag{B.1}$$

##### B.1.2 Fourth-Order expectation

To show that

$$\begin{aligned}\mathcal{E}[Z(a)Z^*(b)Z(c)Z^*(d)] &= A_d(a)\sigma^\circ(a)\delta(a-b)A_d(c)\sigma^\circ(c)\delta(c-d) \\ &\quad + A_d(a)\sigma^\circ(a)\delta(a-d)A_d(c)\sigma^\circ(c)\delta(b-c)\end{aligned}\tag{B.2}$$

where the complex random variable  $Z$  is

$$Z(a) = v_d(a)e^{-j\phi_d(a)} = r_a + jq_a\tag{B.3}$$

and  $r$  and  $q$  are independent, zero mean, real Gaussian random variables we note that

$\mathcal{E}[Z(a)Z^*(b)Z(c)Z^*(d)]$  is real valued and that

$$\mathcal{E}[q_a q_b r_c r_d] = \mathcal{E}[r_a r_b q_c q_d].\tag{B.4}$$

Since  $q$  and  $r$  are independent, identically distributed random variables, this property holds for all permutations of  $q$  and  $r$ . Using the well-known properties of Gaussian random variables and (B.1) we see that

$$\mathcal{E}[r_a r_b r_c r_d] = \mathcal{E}[r_a r_b] \mathcal{E}[r_c r_d] + \mathcal{E}[r_a r_c] \mathcal{E}[r_b r_d] + \mathcal{E}[r_a r_d] \mathcal{E}[r_b r_c], \quad (\text{B.5})$$

$$\mathcal{E}[q_a r_b] = \mathcal{E}[r_a q_b] = 0, \quad (\text{B.6})$$

and thus

$$\mathcal{E}[r_a r_b] = \mathcal{E}[q_a q_b] = \frac{1}{2} A_d(a) \sigma^\circ(a) \delta(a - b). \quad (\text{B.7})$$

From these properties, we obtain,

$$\begin{aligned} \mathcal{E}[Z(a)Z^*(b)Z(c)Z^*(d)] &= \mathcal{E}[(r_a + jq_a)(r_b - jq_b)(r_c + jq_c)(r_d - jq_d)] \\ &= \mathcal{E}[r_a r_b r_c r_d] - j\mathcal{E}[r_a r_b r_c q_d] + j\mathcal{E}[r_a r_b q_c r_d] + \mathcal{E}[r_a r_b q_c q_d] \\ &\quad - j\mathcal{E}[r_a q_b r_c r_d] - \mathcal{E}[r_a q_b r_c q_d] + \mathcal{E}[r_a q_b q_c r_d] - j\mathcal{E}[r_a q_b q_c q_d] \\ &\quad + j\mathcal{E}[q_a r_b r_c r_d] + \mathcal{E}[q_a r_b r_c q_d] - \mathcal{E}[q_a r_b q_c r_d] + j\mathcal{E}[q_a r_b q_c q_d] \\ &\quad + \mathcal{E}[q_a q_b r_c r_d] - j\mathcal{E}[q_a q_b r_c q_d] + j\mathcal{E}[q_a q_b q_c r_d] + \mathcal{E}[q_a q_b q_c q_d] \\ &= \mathcal{E}[r_a r_b r_c r_d] + \mathcal{E}[r_a r_b q_c q_d] - \mathcal{E}[r_a q_b r_c q_d] + \mathcal{E}[r_a q_b q_c r_d] \\ &\quad + \mathcal{E}[q_a r_b r_c q_d] - \mathcal{E}[q_a r_b q_c r_d] + \mathcal{E}[q_a q_b r_c r_d] + \mathcal{E}[q_a q_b q_c q_d] \\ &= 2(\mathcal{E}[r_a r_b] \mathcal{E}[r_c r_d] + \mathcal{E}[r_a r_c] \mathcal{E}[r_b r_d] + \mathcal{E}[r_a r_d] \mathcal{E}[r_b r_c]) \\ &\quad + 2(\mathcal{E}[r_a r_b] \mathcal{E}[q_c q_d] + \mathcal{E}[r_a q_c] \mathcal{E}[r_b q_d] + \mathcal{E}[r_a q_d] \mathcal{E}[r_b q_c]) \\ &\quad - 2(\mathcal{E}[r_a q_b] \mathcal{E}[r_c q_d] + \mathcal{E}[r_a r_c] \mathcal{E}[q_b q_d] + \mathcal{E}[r_a q_d] \mathcal{E}[q_b r_c]) \\ &\quad + 2(\mathcal{E}[r_a q_b] \mathcal{E}[q_c r_d] + \mathcal{E}[r_a q_c] \mathcal{E}[q_b r_d] + \mathcal{E}[r_a r_d] \mathcal{E}[q_b q_c]) \\ &= 2\mathcal{E}[r_a r_b] \mathcal{E}[r_c r_d] + 2\mathcal{E}[r_a r_c] \mathcal{E}[r_b r_d] + 2\mathcal{E}[r_a r_d] \mathcal{E}[r_b r_c] \\ &\quad + 2\mathcal{E}[r_a r_b] \mathcal{E}[q_c q_d] - 2\mathcal{E}[r_a r_c] \mathcal{E}[q_b q_d] + 2\mathcal{E}[r_a r_d] \mathcal{E}[q_b q_c] \\ &= 4\mathcal{E}[r_a r_b] \mathcal{E}[r_c r_d] + 4\mathcal{E}[r_a r_d] \mathcal{E}[r_b r_c] \\ &= A_d(a) \sigma^\circ(a) \delta(a - b) A_d(c) \sigma^\circ(c) \delta(c - d) \\ &\quad + A_d(a) \sigma^\circ(a) \delta(a - d) A_d(c) \sigma^\circ(c) \delta(b - c). \end{aligned} \quad (\text{B.8})$$



## B.2 Single Pulse, Antenna Resolution, Signal-only Measurements

### B.2.1 Expected Value

We show that  $\mathcal{E}[M^{as}] = X R^a$  as follows:

$$\begin{aligned}
 \mathcal{E}[M^{as}] &= \mathcal{E} \left[ \int_t \left| \int_x \int_y \xi_r(t, x, y) dy dx \right|^2 dt \right] \\
 &= \mathcal{E} \left[ \int_t \left( \int_x \int_y \sqrt{X} Y(t, x, y) Z(x, y) dy dx \right) \right. \\
 &\quad \left. \left( \int_{x'} \int_{y'} \sqrt{X} Y^*(t, x', y') Z^*(x', y') dy' dx' \right) dt \right] \\
 &= X \int_t \int_x \int_y \int_{x'} \int_{y'} Y(t, x, y) Y^*(t, x', y') \mathcal{E}[Z(x, y) Z^*(x', y')] dy' dx' dy dx dt \\
 &= X \int_t \int_x \int_y |Y(t, x, y)|^2 A_d(x, y) \sigma^\circ(x, y) dy dx dt \\
 &= X R^a.
 \end{aligned} \tag{B.9}$$

### B.2.2 Correlation

We show that  $\mathcal{E}[M_k^{as} M_l^{as}] = X_k X_l [R_k^a R_l^a + V_{kl}^a]$  as follows:

$$\begin{aligned}
 \mathcal{E}[M_k^{as} M_l^{as}] &= \mathcal{E} \left[ \left( \int_{t_k} \left| \int_{x_k} \int_{y_k} \xi_r(t_k, x_k, y_k) dy_k dx_k \right|^2 dt_k \right) \right. \\
 &\quad \left. \left( \int_{t_l} \left| \int_{x_l} \int_{y_l} \xi_r(t_l, x_l, y_l) dy_l dx_l \right|^2 dt_l \right) \right]
 \end{aligned}$$

$$\begin{aligned}
&= \mathcal{E} \left[ X_k X_l \int_{t_k} \int_{t_l} \left( \int_{x_k} \int_{y_k} Y(t_k, x_k, y_k) Z(x_k, y_k) dy_k dx_k \right) \right. \\
&\quad \left( \int_{x'_k} \int_{y'_k} Y^*(t_k, x'_k, y'_k) Z^*(x'_k, y'_k) dy'_k dx'_k \right) \\
&\quad \left( \int_{x_l} \int_{y_l} Y(t_l, x_l, y_l) Z(x_l, y_l) dy_l dx_l \right) \\
&\quad \left. \left( \int_{x'_l} \int_{y'_l} Y^*(t_l, x'_l, y'_l) Z^*(x'_l, y'_l) dy'_l dx'_l \right) dt_l dt_k \right] \\
&= X_k X_l \int_{t_k} \int_{t_l} \int_{x_k} \int_{y_k} \int_{x'_k} \int_{y'_k} \int_{x_l} \int_{y_l} \int_{x'_l} \int_{y'_l} Y(t_k, x_k, y_k) Y^*(t_k, x'_k, y'_k) \\
&\quad Y(t_l, x_l, y_l) Y^*(t_l, x'_l, y'_l) \mathcal{E}[Z(x_k, y_k) Z^*(x'_k, y'_k) Z(x_l, y_l) Z^*(x'_l, y'_l)] \\
&\quad dy'_l dx'_l dy_l dx_l dy'_k dx'_k dy_k dx_k dt_l dt_k \\
&= X_k X_l \int_{t_k} \int_{t_l} \int_{x_k} \int_{y_k} \int_{x'_k} \int_{y'_k} \int_{x_l} \int_{y_l} \int_{x'_l} \int_{y'_l} A_d(x_k, y_k) \sigma^\circ(x_k, y_k) \\
&\quad \delta(x_k - x'_k) \delta(y_k - y'_k) A_d(x_l, y_l) \sigma^\circ(x_l, y_l) \delta(x_l - x'_l) \delta(y_l - y'_l) \\
&\quad Y(t_k, x_k, y_k) Y^*(t_k, x'_k, y'_k) Y(t_l, x_l, y_l) Y^*(t_l, x'_l, y'_l) \\
&\quad dy'_l dx'_l dy_l dx_l dy'_k dx'_k dy_k dx_k dt_l dt_k \\
&\quad + X_k X_l \int_{t_k} \int_{t_l} \int_{x_k} \int_{y_k} \int_{x'_k} \int_{y'_k} \int_{x_l} \int_{y_l} \int_{x'_l} \int_{y'_l} A_d(x_k, y_k) \sigma^\circ(x_k, y_k) \\
&\quad \delta(x_k - x'_l) \delta(y_k - y'_l) A_d(x_l, y_l) \sigma^\circ(x_l, y_l) \delta(x'_k - x_l) \delta(y'_k - y_l) \\
&\quad Y(t_k, x_k, y_k) Y^*(t_k, x'_k, y'_k) Y(t_l, x_l, y_l) Y^*(t_l, x'_l, y'_l) \\
&\quad dy'_l dx'_l dy_l dx_l dy'_k dx'_k dy_k dx_k dt_l dt_k
\end{aligned}$$

$$\begin{aligned}
&= X_k X_l \int_{t_k} \int_{t_l} \int_{x_k} \int_{y_k} \int_{x_l} \int_{y_l} A_d(x_k, y_k) \sigma^\circ(x_k, y_k) A_d(x_l, y_l) \sigma^\circ(x_l, y_l) \\
&\quad Y(t_k, x_k, y_k) Y^*(t_k, x_k, y_k) Y(t_l, x_l, y_l) Y^*(t_l, x_l, y_l) \\
&\quad dy_l dx_l dy_k dx_k dt_l dt_k \\
&+ X_k X_l \int_{t_k} \int_{t_l} \int_{x_k} \int_{y_k} \int_{x_l} \int_{y_l} A_d(x_k, y_k) \sigma^\circ(x_k, y_k) A_d(x_l, y_l) \sigma^\circ(x_l, y_l) \\
&\quad Y(t_k, x_k, y_k) Y^*(t_k, x_l, y_l) Y(t_l, x_l, y_l) Y^*(t_l, x_k, y_k) \\
&\quad dy_l dx_l dy_k dx_k dt_l dt_k \\
&= X_k X_l \left( \int_{t_k} \int_{x_k} \int_{y_k} A_d(x_k, y_k) \sigma^\circ(x_k, y_k) Y_k(t_k, x_k, y_k) Y_k^*(t_k, x_k, y_k) \right. \\
&\quad \left. dy_k dx_k dt_k \right) \left( \int_{t_l} \int_{x_l} \int_{y_l} A_d(x_l, y_l) \sigma^\circ(x_l, y_l) \right. \\
&\quad \left. Y_l(t_l, x_l, y_l) Y_l^*(t_l, x_l, y_l) dy_l dx_l dt_l \right) \\
&+ X_k X_l \int_{t_k} \int_{t_l} \int_{x_k} \int_{y_k} \int_{x_l} \int_{y_l} A_d(x_k, y_k) A_d(x_l, y_l) \sigma^\circ(x_k, y_k) \sigma^\circ(x_l, y_l) \\
&\quad Y(t_k, x_k, y_k) Y^*(t_k, x_l, y_l) Y(t_l, x_l, y_l) Y^*(t_l, x_k, y_k) \\
&\quad dy_l dx_l dy_k dx_k dt_l dt_k \\
&= X_k X_l [R_k^a R_l^a + V_{kl}^a] \tag{B.10}
\end{aligned}$$

### B.2.3 Covariance

We show that  $\text{Cov}[M_k^{as} M_l^{as}] = X_k X_l V_{kl}^a$  as follows:

$$\begin{aligned}
\text{Cov}[M_k^{as} M_l^{as}] &= \mathcal{E}[(M_k^{as} - \mathcal{E}[M_k^{as}])(M_l^{as} - \mathcal{E}[M_l^{as}])] \\
&= \mathcal{E}[M_k^{as} M_l^{as}] - \mathcal{E}[M_l^{as}] \mathcal{E}[M_k^{as}] - \mathcal{E}[M_k^{as}] \mathcal{E}[M_l^{as}] + \mathcal{E}[\mathcal{E}[M_k^{as}] \mathcal{E}[M_l^{as}]] \\
&= X_k X_l R_k^a R_l^a + X_k X_l V_{kl}^a - X_k X_l R_k^a R_l^a - X_k X_l R_k^a R_l^a + X_k X_l R_k^a R_l^a \\
&= X_k X_l V_{kl}^a. \tag{B.11}
\end{aligned}$$



$$\begin{aligned}
&= X_k X_l \int_{\omega_k} \int_{\omega_l} \int_{t_k} \int_{t'_k} \int_{t_l} \int_{t'_l} \int_{x_k} \int_{x_l} \int_{y_k} \int_{y_l} A_d(x_k, y_k) \sigma^\circ(x_k, y_k) A_d(x_l, y_l) \sigma^\circ(x_l, y_l) \\
&\quad F(t_k, \omega_k) F^*(t'_k, \omega_k) F(t_l, \omega_l) F^*(t'_l, \omega_l) Y(t_k, x_k, y_k) Y^*(t'_k, x_k, y_k) Y(t_l, x_l, y_l) \\
&\quad\quad\quad Y^*(t'_l, x_l, y_l) dy_k dx_k dt_k dt'_k dy_l dx_l dt_l dt'_l d\omega_l d\omega_k \\
&+ X_k X_l \int_{\omega_k} \int_{\omega_l} \int_{t_k} \int_{t'_k} \int_{t_l} \int_{t'_l} \int_{x_k} \int_{x_l} \int_{y_k} \int_{y_l} A_d(x_k, y_k) \sigma^\circ(x_k, y_k) A_d(x_l, y_l) \sigma^\circ(x_l, y_l) \\
&\quad F(t_k, \omega_k) F^*(t'_k, \omega_k) F(t_l, \omega_l) F^*(t'_l, \omega_l) Y(t_k, x_k, y_k) Y^*(t'_k, x_l, y_l) Y(t_l, x_l, y_l) \\
&\quad\quad\quad Y^*(t'_l, x, y) dy_k dx_k dt_k dy'_k dx'_k dt'_k dy_l dx_l dt_l dt'_l d\omega_l d\omega_k \\
&= X_k X_l [R_k^f R_l^f + V_{kl}^f]. \tag{B.13}
\end{aligned}$$

### B.3.3 Covariance

We show that  $\text{Cov}[M_k^{fs} M_l^s] = X_k X_l V_{kl}^f$  as follows:

$$\begin{aligned}
\text{Cov}[M_k^{fs} M_l^{fs}] &= \mathcal{E}[(M_k^{fs} - \mathcal{E}[M_k^{fs}])(M_l^{fs} - \mathcal{E}[M_l^{fs}])] \\
&= (X_k X_l R_k^f R_l^f + X_k X_l V_{kl}^f) - X_k R_k^f X_l R_l^f - X_k R_k^f X_l R_l^f + X_k R_k^f X_l R_l^f \\
&= X_k X_l V_{kl}^f. \tag{B.14}
\end{aligned}$$

## B.4 Single Pulse, Range Resolution, Signal Plus Noise Measurements

### B.4.1 Expected Value

We show that  $\mathcal{E}[M^{sn}] = X R^f + \mathcal{N}_s$  for the range resolution case as follows:

$$\begin{aligned}
\mathcal{E}[M^{sn}] &= \mathcal{E} \left[ \int_{\omega} \left| \int_t F(t, \omega) [\zeta(t) + \nu(t)] dt \right|^2 d\omega \right] \\
&= \mathcal{E} \left[ \int_{\omega} \left( \int_t F(t, \omega) \zeta(t) dt \int_{t'} F^*(t', \omega) \zeta^*(t') dt' + \int_t F(t, \omega) \nu(t) dt \right. \right. \\
&\quad \left. \int_{t'} F^*(t', \omega) \zeta^*(t') dt' + \int_t F(t, \omega) \zeta(t) dt \int_{t'} F^*(t', \omega) \nu^*(t') dt' \right. \\
&\quad \left. \left. + \int_t F(t, \omega) \nu(t) dt \int_{t'} F^*(t', \omega) \nu^*(t') dt' \right) d\omega \right]
\end{aligned}$$

$$\begin{aligned}
&= \mathcal{E} \left[ \int_{\omega} \int_t \int_{t'} F(t, \omega) \zeta(t) F^*(t', \omega) \zeta^*(t') dt' dt d\omega \right] \\
&+ \mathcal{E} \left[ \int_{\omega} \int_t \int_{t'} F(t, \omega) \nu(t) F^*(t', \omega) \zeta^*(t') dt' dt d\omega \right] \\
&+ \mathcal{E} \left[ \int_{\omega} \int_t \int_{t'} F(t, \omega) \zeta(t) F^*(t', \omega) \nu^*(t') dt' dt d\omega \right] \\
&+ \mathcal{E} \left[ \int_{\omega} \int_t \int_{t'} F(t, \omega) \nu(t) F^*(t', \omega) \nu^*(t') dt' dt d\omega \right] \\
&= \mathcal{E} \left[ \int_{\omega} \int_t \int_{t'} F(t, \omega) \zeta(t) F^*(t', \omega) \zeta^*(t') dt' dt d\omega \right] \\
&+ \mathcal{E} \left[ \int_{\omega} \int_t \int_{t'} F(t, \omega) \nu(t) F^*(t', \omega) \nu^*(t') dt' dt d\omega \right] \\
&= XR^f + \mathcal{N}_s. \tag{B.15}
\end{aligned}$$

#### B.4.2 Correlation

We show that  $\mathcal{E}[M_k^{sn} M_l^{sn}] = X_k X_l R_k^f R_l^f + X_k X_l V_{kl}^f + X_k R_k^f \mathcal{N}_s + X_l R_l^f \mathcal{N}_s + \mathcal{N}_s^2 + \delta(k-l)(2XR^f \mathcal{N}_s + 2\mathcal{N}_s^2)$  for the range resolution case as follows:

$$\begin{aligned}
\mathcal{E}[M_k^{sn} M_l^{sn}] &= \mathcal{E} \left[ \left( \int_{\omega_k} \left| \int_{t_k} F(t_k, \omega_k) [\zeta_k(t_k) + \nu(t_k)] dt_k \right|^2 d\omega_k \right) \right. \\
&\quad \left. \left( \int_{\omega_l} \left| \int_{t_l} F(t_l, \omega_l) [\zeta_l(t_l) + \nu(t_l)] dt_l \right|^2 d\omega_l \right) \right] \\
&= \mathcal{E} \left[ \int_{\omega_k} \int_{\omega_l} \int_{t_k} \int_{t'_k} \int_{t_l} \int_{t'_l} F(t_k, \omega_k) F^*(t'_k, \omega_k) F(t_l, \omega_l) F^*(t'_l, \omega_l) \right. \\
&\quad \left. [\zeta_k(t_k) + \nu(t_k)] [\zeta_k^*(t'_k) + \nu^*(t'_k)] [\zeta_l(t_l) + \nu(t_l)] [\zeta_l^*(t'_l) + \nu^*(t'_l)] dt'_l dt_l dt'_k dt_k d\omega_l d\omega_k \right]
\end{aligned}$$

$$\begin{aligned}
&= \int_{\omega_k} \int_{\omega_l} \int_{t_k} \int_{t'_k} \int_{t_l} \int_{t'_l} F(t_k, \omega_k) F^*(t'_k, \omega_k) F(t_l, \omega_l) F^*(t'_l, \omega_l) \\
&\quad \mathcal{E} \left[ \zeta_k(t_k) \zeta_k^*(t'_k) \zeta_l(t_l) \zeta_l^*(t'_l) + \zeta_k(t_k) \zeta_k^*(t'_k) \nu(t_l) \zeta_l^*(t'_l) \right. \\
&\quad + \zeta_k(t_k) \zeta_k^*(t'_k) \zeta_l(t_l) \nu^*(t'_l) + \zeta_k(t_k) \zeta_k^*(t'_k) \nu(t_l) \nu^*(t'_l) \\
&\quad + \nu(t_k) \zeta_k^*(t'_k) \zeta_l(t_l) \zeta_l^*(t'_l) + \nu(t_k) \zeta_k^*(t'_k) \nu(t_l) \zeta_l^*(t'_l) \\
&\quad + \nu(t_k) \zeta_k^*(t'_k) \zeta_l(t_l) \nu^*(t'_l) + \nu(t_k) \zeta_k^*(t'_k) \nu(t_l) \nu^*(t'_l) \\
&\quad + \zeta_k(t_k) \nu^*(t'_k) \zeta_l(t_l) \zeta_l^*(t'_l) + \zeta_k(t_k) \nu^*(t'_k) \nu(t_l) \zeta_l^*(t'_l) \\
&\quad + \zeta_k(t_k) \nu^*(t'_k) \zeta_l(t_l) \nu^*(t'_l) + \zeta_k(t_k) \nu^*(t'_k) \nu(t_l) \nu^*(t'_l) \\
&\quad + \nu(t_k) \nu^*(t'_k) \zeta_l(t_l) \zeta_l^*(t'_l) + \nu(t_k) \nu^*(t'_k) \nu(t_l) \zeta_l^*(t'_l) \\
&\quad \left. + \nu(t_k) \nu^*(t'_k) \zeta_l(t_l) \nu^*(t'_l) + \nu(t_k) \nu^*(t'_k) \nu(t_l) \nu^*(t'_l) \right] \\
&\quad dt'_l dt_l dt'_k dt_k d\omega_l d\omega_k \\
&= \int_{\omega_k} \int_{\omega_l} \int_{t_k} \int_{t'_k} \int_{t_l} \int_{t'_l} F(t_k, \omega_k) F^*(t'_k, \omega_k) F(t_l, \omega_l) F^*(t'_l, \omega_l) \\
&\quad \mathcal{E} \left[ \zeta_k(t_k) \zeta_k^*(t'_k) \zeta_l(t_l) \zeta_l^*(t'_l) + \zeta_k(t_k) \zeta_k^*(t'_k) \nu(t_l) \nu^*(t'_l) \right. \\
&\quad + \nu(t_k) \zeta_k^*(t'_k) \nu(t_l) \zeta_l^*(t'_l) + \nu(t_k) \zeta_k^*(t'_k) \zeta_l(t_l) \nu^*(t'_l) \\
&\quad + \zeta_k(t_k) \nu^*(t'_k) \nu(t_l) \zeta_l^*(t'_l) + \zeta_k(t_k) \nu^*(t'_k) \zeta_l(t_l) \nu^*(t'_l) \\
&\quad \left. + \nu(t_k) \nu^*(t'_k) \zeta_l(t_l) \zeta_l^*(t'_l) + \nu(t_k) \nu^*(t'_k) \nu(t_l) \nu^*(t'_l) \right] \\
&\quad dt'_l dt_l dt'_k dt_k d\omega_l d\omega_k
\end{aligned}$$

$$\begin{aligned}
&= \int_{\omega_k} \int_{\omega_l} \int_{t_k} \int_{t'_k} \int_{t_l} \int_{t'_l} F(t_k, \omega_k) F^*(t'_k, \omega_k) F(t_l, \omega_l) F^*(t'_l, \omega_l) \\
&\quad \left[ \mathcal{E}[\zeta_k(t_k) \zeta_k^*(t'_k) \zeta_l(t_l) \zeta_l^*(t'_l)] + \mathcal{E}[\zeta_k(t_k) \zeta_k^*(t'_k)] \mathcal{E}[\nu(t_l) \nu^*(t'_l)] \right. \\
&\quad + \mathcal{E}[\zeta_k^*(t'_k) \zeta_l^*(t'_l)] \mathcal{E}[\nu(t_k) \nu(t_l)] + \mathcal{E}[\zeta_k^*(t'_k) \zeta_l(t_l)] \mathcal{E}[\nu(t_k) \nu^*(t'_l)] \\
&\quad + \mathcal{E}[\zeta_k(t_k) \zeta_l^*(t'_l)] \mathcal{E}[\nu^*(t'_k) \nu(t_l)] + \mathcal{E}[\zeta_k(t_k) \zeta_l(t_l)] \mathcal{E}[\nu^*(t'_k) \nu^*(t'_l)] \\
&\quad + \mathcal{E}[\nu(t_k) \nu^*(t'_k)] \mathcal{E}[\zeta_l(t_l) \zeta_l^*(t'_l)] + \mathcal{E}[\nu(t_k) \nu^*(t'_k)] \mathcal{E}[\nu(t_l) \nu^*(t'_l)] \\
&\quad \left. + \mathcal{E}[\nu(t_k) \nu(t_l)] \mathcal{E}[\nu^*(t'_k) \nu^*(t'_l)] + \mathcal{E}[\nu(t_k) \nu^*(t'_k)] \mathcal{E}[\nu^*(t'_k) \nu(t_l)] \right] \\
&\quad dt'_l dt_l dt'_k dt_k d\omega_l d\omega_k \\
&= X_k X_l [R_k^f R_l^f + V_{kl}^f] + X_k R_k^f \mathcal{N}_s + X_l R_l^f \mathcal{N}_s + \mathcal{N}_s^2 + \delta(k-l) \\
&\quad \left( \int_{\omega_k} \int_{\omega_l} \int_{t_k} \int_{t'_k} \int_{t_l} \int_{t'_l} F(t_k, \omega_k) F^*(t'_k, \omega_k) F(t_l, \omega_l) F^*(t'_l, \omega_l) \right. \\
&\quad \left[ \mathcal{E}[\zeta_k^*(t'_k) \zeta_l^*(t'_l)] \mathcal{E}[\nu(t_k) \nu(t_l)] + \mathcal{E}[\zeta_k^*(t'_k) \zeta_l(t_l)] \mathcal{E}[\nu(t_k) \nu^*(t'_l)] \right. \\
&\quad + \mathcal{E}[\zeta_k(t_k) \zeta_l^*(t'_l)] \mathcal{E}[\nu^*(t'_k) \nu(t_l)] + \mathcal{E}[\zeta_k(t_k) \zeta_l(t_l)] \mathcal{E}[\nu^*(t'_k) \nu^*(t'_l)] \\
&\quad \left. \left. + \mathcal{E}[\nu(t_k) \nu(t_l)] \mathcal{E}[\nu^*(t'_k) \nu^*(t'_l)] + \mathcal{E}[\nu(t_k) \nu^*(t'_k)] \mathcal{E}[\nu^*(t'_k) \nu(t_l)] \right] \right. \\
&\quad \left. dt'_l dt_l dt'_k dt_k d\omega_l d\omega_k \right) \\
&= X_k X_l R_k^f R_l^f + X_k X_l V_{kl}^f + X_k R_k^f \mathcal{N}_s + X_l R_l^f \mathcal{N}_s + \mathcal{N}_s^2 + \delta(k-l) \\
&\quad \int_{\omega_k} \int_{\omega_l} \int_{t_k} \int_{t'_k} \int_{t_l} \int_{t'_l} F(t_k, \omega_k) F^*(t'_k, \omega_k) F(t_l, \omega_l) F^*(t'_l, \omega_l) \\
&\quad \left[ \left[ \mathcal{E}[\zeta_k^*(t'_k) \zeta_k(t_l)] \mathcal{E}[\nu(t_k) \nu(t'_l)] + \mathcal{E}[\zeta_k(t_k) \zeta_k^*(t'_l)] \mathcal{E}[\nu(t'_k) \nu(t_l)] \right. \right. \\
&\quad \left. \left. + \mathcal{E}[\nu(t_k) \nu(t_l)] \mathcal{E}[\nu(t'_k) \nu(t'_l)] + \mathcal{E}[\nu(t_k) \nu(t'_l)] \mathcal{E}[\nu(t'_k) \nu(t_l)] \right] \right. \\
&\quad \left. dt'_l dt_l dt'_k dt_k d\omega_l d\omega_k \right] \\
&= X_k X_l R_k^f R_l^f + X_k X_l V_{kl}^f + X_k R_k^f \mathcal{N}_s + X_l R_l^f \mathcal{N}_s \\
&\quad + \mathcal{N}_s^2 + \delta(k-l) (2X R^f \mathcal{N}_s + 2\mathcal{N}_s^2). \tag{B.16}
\end{aligned}$$



### B.4.3 Covariance

We show that  $\mathcal{Cov}[M_k^{sn} M_l^{sn}] = X_k X_l V_{kl}^f + \delta(k-l)(2X R^f \mathcal{N}_s + 2\mathcal{N}_s^2)$  for the range resolution case as follows:

$$\begin{aligned}
\mathcal{Cov}[M_k^{sn} M_l^{sn}] &= \mathcal{E}[(M_k^{sn} - \mathcal{E}[M_k^{sn}])(M_l^{sn} - \mathcal{E}[M_l^{sn}])] \\
&= X_k X_l R_k^f R_l^f + X_k X_l V_{kl}^f + X_k R_k^f \mathcal{N}_s + X_l R_l^f \mathcal{N}_s + \mathcal{N}_s^2 \\
&\quad + \delta(k-l)(2X R^f \mathcal{N}_s + 2\mathcal{N}_s^2) - [X_k R_k^f + \mathcal{N}_s][X_l R_l^f + \mathcal{N}_s] \\
&\quad - [X_k R_k^f + \mathcal{N}_s][X_l R_l^f + \mathcal{N}_s] + [X_k R_k^f + \mathcal{N}_s][X_l R_l^f + \mathcal{N}_s] \\
&= X_k X_l V_{kl}^f + \delta(k-l)(2X R^f \mathcal{N}_s + 2\mathcal{N}_s^2). \tag{B.17}
\end{aligned}$$

## B.5 Single Pulse, Range Resolution, Unbiased Measurements

### B.5.1 Correlation Between Noise and Noisy Measurement

We show that  $\mathcal{E}[M^{sn} M^n] = X R^f \mathcal{N}_n + \mathcal{N}_s \mathcal{N}_n$ , for the range resolution case as follows:

$$\begin{aligned}
\mathcal{E}[M^{sn} M^n] &= \mathcal{E} \left[ \int_{\omega_s} \left| \int_{t_s} F(t_s, \omega_s) [\zeta(t_s) + \nu(t_s)] dt_s \right|^2 \int_{\omega_n} \left| \int_{t_n} F(t_n, \omega_n) \nu(t_n) dt_n \right|^2 d\omega_n d\omega_s \right] \\
&= \mathcal{E} \left[ \int_{\omega_s} \int_{\omega_n} \int_{t_s} \int_{t'_s} \int_{t_n} \int_{t'_n} F(t_s, \omega_s) F^*(t'_s, \omega_s) F(t_n, \omega_n) F^*(t'_n, \omega_n) [\zeta(t_s) + \nu(t_s)] \right. \\
&\quad \left. [\zeta^*(t'_s) + \nu(t'_s)] [\nu(t_n) \nu(t'_n)] dt'_n dt_n dt'_s dt_s d\omega_n d\omega_s \right] \\
&= \int_{\omega_s} \int_{\omega_n} \int_{t_s} \int_{t'_s} \int_{t_n} \int_{t'_n} F(t_s, \omega_s) F^*(t'_s, \omega_s) F(t_n, \omega_n) F^*(t'_n, \omega_n) \\
&\quad \mathcal{E} \left[ \zeta(t_s) \zeta^*(t'_s) \nu(t_n) \nu(t'_n) + \nu(t_s) \nu(t'_s) \nu(t_n) \nu(t'_n) \right] \\
&\quad dt'_n dt_n dt'_s dt_s d\omega_n d\omega_s \\
&= X R^f \mathcal{N}_n + \mathcal{N}_s \mathcal{N}_n. \tag{B.18}
\end{aligned}$$

### B.5.2 Correlation of Measured Noise

We show that  $\mathcal{E}[M_k^n M_l^n] = \mathcal{N}_n^2 + \delta(k-l)2\mathcal{N}_n^2$  for the range resolution case as follows:

$$\begin{aligned}
\mathcal{E}[M_k^n M_l^n] &= \mathcal{E} \left[ \int_{\omega_k} \left| \int_{t_k} F(t_k, \omega_k) \nu(t_k) dt_k \right|^2 \int_{\omega_l} \left| \int_{t_l} F(t_l, \omega_l) \nu(t_l) dt_l \right|^2 d\omega_k d\omega_l \right] \\
&= \int_{\omega_k} \int_{\omega_l} \int_{t_k} \int_{t'_k} \int_{t_l} \int_{t'_l} F(t_k, \omega_k) F^*(t'_k, \omega_k) F(t_l, \omega_l) F^*(t'_l, \omega_l) \\
&\quad \mathcal{E} \left[ \nu(t_k) \nu(t'_k) \nu(t_l) \nu(t'_l) \right] dt'_l dt_l dt'_k dt_k d\omega_k d\omega_l \\
&= \mathcal{N}_n^2 + \delta(k-l) 2\mathcal{N}_n^2. \tag{B.19}
\end{aligned}$$

### B.5.3 Correlation

We show that  $\mathcal{E}[M_k^u M_l^u] = \frac{X_k X_l}{\bar{R}_k^f \bar{R}_l^f} \left( R_k^f R_l^f + V_{kl}^f + \delta(k-l) \left[ \frac{2R^f \mathcal{N}_s}{X} + \frac{4\mathcal{N}_s^2}{X^2} \right] \right)$  for the range resolution case as follows:

$$\begin{aligned}
\mathcal{E}[M_k^u M_l^u] &= \mathcal{E}[(\alpha_k M_k^{sn} + \beta_k M_k^n)(\alpha_l M_l^{sn} + \beta_l M_l^n)] \\
&= \mathcal{E} \left[ \frac{M_k^{sn} M_l^{sn}}{\bar{R}_k^f \bar{R}_l^f} - \frac{\mathcal{N}_s M_k^{sn} M_l^n}{\bar{R}_k^f \bar{R}_l^f \mathcal{N}_n} - \frac{\mathcal{N}_s M_l^{sn} M_k^n}{\bar{R}_k^f \bar{R}_l^f \mathcal{N}_n} + \frac{\mathcal{N}_s^2 M_k^n M_l^n}{\bar{R}_k^f \bar{R}_l^f \mathcal{N}_n^2} \right] \\
&= \frac{X_k X_l R_k^f R_l^f + X_k X_l V_{kl}^f + X_k R_k^f \mathcal{N}_s + X_l R_l^f \mathcal{N}_s + \mathcal{N}_s^2}{\bar{R}_k^f \bar{R}_l^f} \\
&\quad + \frac{\delta(k-l)(2X R^f \mathcal{N}_s + 2\mathcal{N}_s^2)}{\bar{R}_k^f \bar{R}_l^f} - \frac{\mathcal{N}_s(X_k R_k^f \mathcal{N}_n + \mathcal{N}_s \mathcal{N}_n)}{\bar{R}_k^f \bar{R}_l^f \mathcal{N}_n} \\
&\quad - \frac{\mathcal{N}_s(X_l R_l^f \mathcal{N}_n + \mathcal{N}_s \mathcal{N}_n)}{\bar{R}_k^f \bar{R}_l^f \mathcal{N}_n} + \frac{\mathcal{N}_s^2(\mathcal{N}_n^2 + \delta(k-l)2\mathcal{N}_n^2)}{\bar{R}_k^f \bar{R}_l^f \mathcal{N}_n^2} \\
&= \frac{X_k X_l}{\bar{R}_k^f \bar{R}_l^f} \left( R_k^f R_l^f + V_{kl}^f + \delta(k-l) \left[ \frac{2R^f \mathcal{N}_s}{X} + \frac{4\mathcal{N}_s^2}{X^2} \right] \right). \tag{B.20}
\end{aligned}$$

### B.5.4 Covariance

We show that  $\text{Cov}[M_k^u M_l^u] = \frac{X_k X_l}{\bar{R}_k \bar{R}_l} \left( V_{kl}^f + \delta(k-l) \left[ \frac{2R^f \mathcal{N}_s}{X} + \frac{4\mathcal{N}_s^2}{X^2} \right] \right)$  as follows:

$$\begin{aligned}
\text{Cov}[M_k^u, M_l^u] &= \mathcal{E}[(M_k^u - \mathcal{E}[M_k^u])(M_l^u - \mathcal{E}[M_l^u])] \\
&= \mathcal{E}[M_k^u M_l^u - X_k \sigma_k^\circ M_l^u - X_l \sigma_l^\circ M_k^u + X_k X_l \sigma_k^\circ \sigma_l^\circ] \\
&= \mathcal{E}[M_k^u M_l^u] - X_k \sigma_k^\circ X_l \sigma_l^\circ - X_l \sigma_l^\circ X_k \sigma_k^\circ + X_k X_l \sigma_k^\circ \sigma_l^\circ
\end{aligned}$$

$$\begin{aligned}
&= \frac{X_k X_l}{\bar{R}_k^f \bar{R}_l^f} \left( R_k^f R_l^f + V_{kl}^f + \delta(k-l) \frac{2R^f \mathcal{N}_s}{X} + \delta(k-l) \frac{4\mathcal{N}_s^2}{X^2} \right) - X_k \sigma_k^\circ X_l \sigma_l^\circ \\
&= \frac{X_k X_l}{\bar{R}_k^f \bar{R}_l^f} \left( V_{kl}^f + \delta(k-l) \left[ \frac{2R^f \mathcal{N}_s}{X} + \frac{4\mathcal{N}_s^2}{X^2} \right] \right). \tag{B.21}
\end{aligned}$$

## B.6 Analysis of Signal Covariance Expressions

### B.6.1 Footprint Resolution $\bar{V}^a$

Implementing the definitions of  $a$  and  $Y$ , we simplify the expression of  $\bar{V}^a$  as follows:

$$\begin{aligned}
\bar{V}^a &= \int_{t_k} \int_{t_l} \int_{x_k} \int_{y_k} \int_{x_l} \int_{y_l} A_d(x_k, y_k) A_d(x_l, y_l) Y(t_k, x_k, y_k) Y^*(t_k, x_l, y_l) \\
&\quad Y(t_l, x_l, y_l) Y^*(t_l, x_k, y_k) dy_l dx_l dy_k dx_k dt_l dt_k. \\
&= \frac{1}{G_o^4 A_E^2} \int_{x_k} \int_{y_k} \int_{x_l} \int_{y_l} A_d(x_k, y_k) A_d(x_l, y_l) G_k(x_k, y_k) G_l(x_k, y_k) G_k(x_l, y_l) G_l(x_l, y_l) \\
&\quad \left( \int_{t_k} a(t_k - 2\bar{r}(x_k, y_k)/c) a^*(t_k - 2\bar{r}(x_l, y_l)/c) e^{-j[\omega_d(x_k, y_k) - \omega_d(x_l, y_l)]t} dt_k \right) \\
&\quad \left( \int_{t_l} a(t_l - 2\bar{r}(x_l, y_l)/c) a^*(t_l - 2\bar{r}(x_k, y_k)/c) e^{-j[\omega_d(x_l, y_l) - \omega_d(x_k, y_k)]t_l} dt_l \right) dy_l dx_l dy_k dx_k \\
&= \frac{1}{G_o^4 A_E^2} \int_{x_k} \int_{y_k} \int_{x_l} \int_{y_l} A_d(x_k, y_k) A_d(x_l, y_l) G_k(x_k, y_k) G_l(x_k, y_k) G_k(x_l, y_l) G_l(x_l, y_l) \\
&\quad \left( \int_{t_k} a(t_k - 2\bar{r}(x_k, y_k)/c) a^*(t_k - 2\bar{r}(x_l, y_l)/c) e^{-j[\omega_d(x_k, y_k) - \omega_d(x_l, y_l)]t_k} dt_k \right) \\
&\quad \left( \int_{[t_k + (l-k)T_p]} a([t_k + (l-k)T_p] - 2\bar{r}(x_l, y_l)/c) a^*([t_k + (l-k)T_p] - 2\bar{r}(x_k, y_k)/c) \right. \\
&\quad \left. e^{-j[\omega_d(x_l, y_l) - \omega_d(x_k, y_k)][t_k + (l-k)T_p]} dt_k \right) dy_l dx_l dy_k dx_k
\end{aligned}$$

$$\begin{aligned}
&= \frac{1}{G_o^4 A_E^2} \int_{x_k} \int_{y_k} \int_{x_l} \int_{y_l} A_d(x_k, y_k) A_d(x_l, y_l) G_k(x_k, y_k) G_l(x_k, y_k) G_k(x_l, y_l) G_l(x_l, y_l) \\
&\quad \left( \int_{t_k} a(t_k - 2\bar{r}(x_k, y_k)/c) a^*(t_k - 2\bar{r}(x_l, y_l)/c) e^{-j[\omega_d(x_k, y_k) - \omega_d(x_l, y_l)]t} dt_k \right) \\
&\quad \left( \int_{t_k} a(t_k - 2\bar{r}(x_l, y_l)/c) a^*(t_k - 2\bar{r}(x_k, y_k)/c) e^{-j[\omega_d(x_l, y_l) - \omega_d(x_k, y_k)]t_k} \right. \\
&\quad \quad \left. (e^{-j[\omega_d(x_l, y_l) - \omega_d(x_k, y_k)](l-k)T_p}) dt_k \right) dy_l dx_l dy_k dx_k \\
&= \frac{1}{G_o^4 A_E^2} \int_{x_k} \int_{y_k} \int_{x_l} \int_{y_l} A_d(x_k, y_k) A_d(x_l, y_l) G_k(x_k, y_k) G_l(x_k, y_k) \\
&\quad G_k(x_l, y_l) G_l(x_l, y_l) e^{-j[\omega_d(x_l, y_l) - \omega_d(x_k, y_k)](l-k)T_p} \\
&\quad \left( \int_{t_k} a(t_k - 2\bar{r}(x_k, y_k)/c) a^*(t_k - 2\bar{r}(x_l, y_l)/c) e^{-j[\omega_d(x_k, y_k) - \omega_d(x_l, y_l)]t_k} dt_k \right)^2 \\
&\quad dy_l dx_l dy_k dx_k \\
&= \frac{1}{G_o^4 A_E^2} \int_{x_k} \int_{y_k} \int_{x_l} \int_{y_l} A_d(x_k, y_k) A_d(x_l, y_l) G_k(x_k, y_k) G_l(x_k, y_k) \\
&\quad G_k(x_l, y_l) G_l(x_l, y_l) B_{kl}(f_\omega) \mathcal{X}^2(d_r, f_\omega) dy_l dx_l dy_k dx_k \\
&= \frac{1}{G_o^4 A_E^2} \int_{x_k} \int_{y_k} \int_{x_l} \int_{y_l} Q(x_k, y_k) Q(x_l, y_l) B_{kl}(f_\omega) \mathcal{X}^2(d_r, f_\omega) dy_l dx_l dy_k dx_k \quad (\text{B.22})
\end{aligned}$$

where  $d_r = \frac{2}{c}(r(x_l, y_l) - r(x_k, y_k))$ ,  $f_\omega = -[\omega_d(x_l, y_l) - \omega_d(x_k, y_k)]/2\pi$ ,  $Q(x, y) = A_d(x, y)G_k(x, y)G_l(x, y)$ , and  $B_{kl}(f_\omega) = e^{-jf_\omega T_p(l-k)}$ .

## B.7 Derivation of Multiple Measurement Statistics

### B.7.1 Incoherent Variance

We can show that  $\mathcal{V}\text{ar}[M^m] = \frac{1}{N_p^2} \int_{l=1}^{N_p} \int_{k=1}^{N_p} \mathbf{K}_{kl}$  as follows:

$$\begin{aligned}
\mathcal{V}\text{ar}[M^m] &= \mathcal{E}[(M^m)^2] - \mathcal{E}^2[M^m] \\
&= \mathcal{E}\left[\left(\frac{1}{N_p} \sum_{k=1}^{N_p} M_k^u\right)^2\right] - \mathcal{E}^2\left[\frac{1}{N_p} \sum_{k=1}^{N_p} M_k^u\right] \\
&= \frac{1}{N_p^2} \sum_{k=1}^{N_p} \sum_{l=1}^{N_p} \mathcal{E}[M_k^u M_l^u] - \frac{1}{N_p^2} \sum_{k=1}^{N_p} X \sigma_k^\circ \sum_{l=1}^{N_p} X \sigma_l^\circ
\end{aligned}$$

$$\begin{aligned}
&= \frac{1}{N_p^2} \sum_{k=1}^{N_p} \sum_{l=1}^{N_p} \frac{X_k X_l}{\bar{R}_k \bar{R}_l} \left( V_{kl} + \delta(k-l) \frac{2R\mathcal{N}_s}{X} + \delta(k-l) \frac{4\mathcal{N}_s^2}{X^2} \right) \\
&= \frac{1}{N_p^2} \sum_{l=1}^{N_p} \sum_{k=1}^{N_p} \mathcal{Cov}[M_k^u M_l^u] \\
&= \frac{1}{N_p^2} \sum_{l=1}^{N_p} \sum_{k=1}^{N_p} \mathbf{K}_{kl}. \tag{B.23}
\end{aligned}$$

### B.7.2 Incoherent Correlation

We can show that  $\mathcal{E}[M_k^m M_l^m] = \frac{1}{N_p^2} \sum_{k=k_a}^{k_b} \sum_{l=l_a}^{l_b} \mathbf{R} + \mathbf{K}$  as follows:

$$\begin{aligned}
\mathcal{E}[M_k^m M_l^m] &= \frac{1}{N_p^2} \sum_{k=k_a}^{k_b} \sum_{l=l_a}^{l_b} \mathcal{E}[M_k^u M_l^u] \\
&= \frac{1}{N_p^2} \sum_{k=k_a}^{k_b} \sum_{l=l_a}^{l_b} \frac{X_k X_l}{\bar{R}_k \bar{R}_l} \left( R_k R_l + V_{kl} + \delta(k-l) \frac{2R\mathcal{N}_s}{X} + \delta(k-l) \frac{4\mathcal{N}_s^2}{X^2} \right) \\
&= \frac{1}{N_p^2} \sum_{k=k_a}^{k_b} \sum_{l=l_a}^{l_b} \mathbf{R} + \mathbf{K} \tag{B.24}
\end{aligned}$$

where  $\frac{X_k X_l}{\bar{R}_k \bar{R}_l} (R_k R_l)$  is the  $kl^{th}$  entry of  $\mathbf{R}$  and  $k_b - k_a = N_p$  and  $l_b - l_a = N_p$ .

### B.7.3 Incoherent Covariance

We can show that  $\mathcal{E}[M_k^m] M_l^m = \frac{1}{N_p^2} \sum_{k=k_a}^{k_b} \sum_{l=l_a}^{l_b} \mathbf{K}$  as follows:

$$\begin{aligned}
\mathcal{Cov}[M_k^m M_l^m] &= \mathcal{E}[M_k^m M_l^m] - \mathcal{E}[M_k^m] \mathcal{E}[M_l^m] \\
&= \frac{1}{N_p^2} \sum_{k=k_a}^{k_b} \sum_{l=l_a}^{l_b} \mathcal{E}[M_k^u M_l^u] - \frac{1}{N_p^2} \sum_{k=k_a}^{k_b} X \sigma_k^\circ \sum_{l=l_a}^{l_b} X \sigma_l^\circ \\
&= \frac{1}{N_p^2} \sum_{k=k_a}^{k_b} \sum_{l=l_a}^{l_b} \frac{X_k X_l}{\bar{R}_k \bar{R}_l} \left( V_{kl} + \delta(k-l) \frac{2R\mathcal{N}_s}{X} + \delta(k-l) \frac{4\mathcal{N}_s^2}{X^2} \right) \\
&= \frac{1}{N_p^2} \sum_{l=l_a}^{l_b} \sum_{k=k_a}^{k_b} \mathcal{Cov}[M_k^u M_l^u] \\
&= \frac{1}{N_p^2} \sum_{l=l_a}^{l_b} \sum_{k=k_a}^{k_b} \mathbf{K}_{kl} \tag{B.25}
\end{aligned}$$

where  $k_b - k_a = N_p$  and  $l_b - l_a = N_p$ .

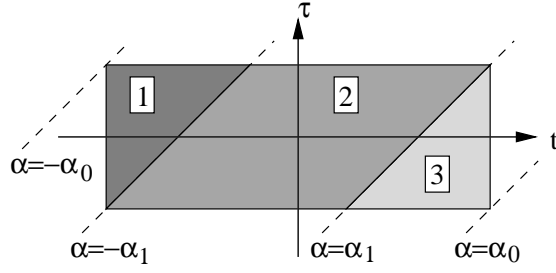


Figure B.1: Double integral simplification.

## B.8 Double Integral Simplification

It can be shown that the double integral

$$D = \int_{-a}^a \int_{-b}^b f(t - \tau) dt d\tau \quad (\text{B.26})$$

can be written as

$$D = 2b \int_{b-a}^{a-b} f(\alpha) d\alpha + \int_{a-b}^{a+b} (a+b-\alpha)[f(\alpha) + f(-\alpha)] d\alpha. \quad (\text{B.27})$$

In the special case that  $a = b$  we can write

$$\int_{-a}^a \int_{-b}^b f(t - \tau) dt d\tau = \int_{a-b}^{a+b} (2a - \alpha)[f(\alpha) + f(-\alpha)] d\alpha. \quad (\text{B.28})$$

Further, if  $f(\alpha) = f^*(-\alpha)$  and  $a = b$  we can write

$$\int_{-a}^a \int_{-a}^a f(t - \tau) dt d\tau = 2 \int_0^{2a} (2a - \alpha) \Re\{f(\alpha)\} d\alpha, \quad (\text{B.29})$$

To prove (B.27) let  $\alpha = t - \tau$ ,  $\alpha_1 = a + b$ , and  $\alpha_0 = a - b$ . Using Figure B.1 we see that  $D$  can be split into integrals over the three indicated regions, so that

$$\begin{aligned} D &= \int_{-a}^a \int_{-b}^b f(t - \tau) dt d\tau \\ &= 2 \int_{-\alpha_0}^{-\alpha_1} f(\alpha) \left[ b \frac{\alpha + \alpha_0}{\alpha_0 - \alpha_1} \right] d\alpha \quad \text{Region 1} \end{aligned}$$

$$+ 2 \int_{-\alpha_1}^{\alpha_1} f(\alpha) b \, d\alpha \quad \text{Region 2}$$

$$+ 2 \int_{\alpha_1}^{\alpha_0} f(\alpha) \left[ b \frac{\alpha_0 - \alpha}{\alpha_0 - \alpha_1} \right] d\alpha \quad \text{Region 3}$$

$$\begin{aligned}
&= \int_{-a-b}^{b-a} f(\alpha)(a+b+\alpha) \, d\alpha + 2b \int_{b-a}^{a-b} f(\alpha) \, d\alpha + \int_{a-b}^{a+b} f(\alpha)(a+b-\alpha) \, d\alpha \\
&= 2b \int_{b-a}^{a-b} f(\alpha) \, d\alpha + \int_{a-b}^{a+b} [f(\alpha) + f(-\alpha)](a+b-\alpha) \, d\alpha. \quad (\text{B.30})
\end{aligned}$$





## Bibliography

- [1] “SeaWinds experiment: Experiment function requirements,” Internal Report, NASA Jet Propulsion Laboratory, Tech. Rep., April 1994.
- [2] J. T. Adams, “QuikSCAT / SeaWinds calibration ground station (QSCGS) design review,” Internal Report, NASA Jet Propulsion Laboratory, Tech. Rep., June 1998.
- [3] J. T. Adams, “Ground calibration of an orbiting spacecraft radar transmitter,” Master’s thesis, University of California at Los Angeles, 1999.
- [4] J. T. Adams and J. P. Lux, “Ground calibration of an orbiting spacecraft transmitter,” in *2000 IEEE Aerospace Conference Proceedings*, vol. 5, March 2000, pp. 37–49.
- [5] A. Anderson, “Analysis and usage of the QuikSCAT calibration ground station,” Master’s thesis, Brigham Young University, 2001.
- [6] I. Ashcraft and D. G. Long, “Azimuth variation in microwave backscatter over the Greenland ice sheet,” in *Proc. IEEE Geosci. Remote Sensing Symposium*, Sydney, Australia, July 2001, pp. 1779–1781.
- [7] I. S. Ashcraft and D. G. Long, “The spatial response function of SeaWinds backscatter measurements,” in *Proceedings of SPIE, Earth Observations Systems VIII*, vol. 5151, August 2003.
- [8] R. Atlas, S. Bloom, R. Hoffman, E. Brin, J. Ardizzone, J. Terry, D. Bungato, and J. C. Jusern, “Geophysical validation of NSCAT winds using atmospheric data and analyses,” *Journal of Geophysical Research*, vol. 104, no. C5, pp. 11 405–11 424, May 1999.

- [9] E. P. Attema, "The Active Microwave Instrument on-board the ERS-1 satellite," *Proc. IEEE*, vol. 79, no. 6, pp. 791–799, June 1991.
- [10] I. Birrer, E. Bracalente, G. Dome, J. Sweet, and G. Berthold, " $\sigma^0$  signature of the Amazon rain forest obtained from the Seasat scatterometer," *IEEE Trans. Geosci. Remote Sensing*, vol. GE-20, no. 1, pp. 11–17, January 1982.
- [11] C.-Y. Chi and F. K. Li, "A comparative study of several wind estimation algorithms for spaceborne scatterometers," *IEEE Trans. Geosci. Remote Sensing*, vol. 26, no. 2, pp. 115–121, March 1988.
- [12] R. Crapolicchio and P. Lecomte, "ERS-2 scatterometer calibration and long-loop performance since launch," in *Proceedings of a Joint ESA Workshop on Emerging Scatterometer Applications - From Research to Operations*, vol. ESA SP-424, Noordwijk, Netherlands, October 1998.
- [13] P. M. Djuric and S. M. Kay, "Parameter estimation of chirp signals," *IEEE Trans. Acoust., Speech, Signal Processing*, vol. 38, no. 12, pp. 2118–2126, December 1990.
- [14] M. R. Drinkwater and C. C. Ling, "Introduction to the special section on emerging scatterometer applications," *IEEE Trans. Geosci. Remote Sensing*, vol. 38, pp. 1763–1764, 2000.
- [15] D. S. Early and D. G. Long, "Image reconstruction and enhanced resolution imaging from irregular sampling," *IEEE Trans. Geosci. Remote Sensing*, vol. 39, no. 2, pp. 291–302, February 2001.
- [16] R. Fisher, "Standard deviation of scatterometer measurements from space," *IEEE Trans. Geosci. Electron.*, vol. GE-10, April 1972.
- [17] P. L. Frison and E. Mougin, "Use of ERS-1 wind scatterometer data over land surfaces," *IEEE Trans. Geosci. Remote Sensing*, vol. 34, no. 2, pp. 550–560, March 1996.

- [18] R. M. Gray and L. D. Davisson, *An Introduction to Statistical Signal Processing*, 1999. [Online]. Available: <http://www-isl.stanford.edu/gray/sp.html>
- [19] J. P. Guignard and J. Louet, "ERS-1 AMI in-flight calibration and performance verification," in *Proc. IEEE Geosci. Remote Sensing Symposium*, Houston, TX, May 1992.
- [20] V. Hsiao. (2001, January) Personal Communication.
- [21] L. Isaksen and A. Stoffelen, "ERS scatterometer wind data impact on ECMWF's tropical cyclone forecasts," *IEEE Trans. Geosci. Remote Sensing*, vol. 38, no. 4, pp. 1885–1892, July 2000.
- [22] J. W. Johnson, L. A. Williams, E. M. Bracalente, F. Beck, and W. L. Grantham, "Seasat-A satellite scatterometer instrument evaluation," *IEEE J. Oceanic Eng.*, vol. OE-5, no. 2, pp. 138–144, April 1980.
- [23] P. E. Johnson, "Uncertainties in oceanic microwave remote sensing: the radar footprint, the wind-backscatter relationship, and the measurement probability density function," Ph.D. dissertation, Brigham Young University, 1999.
- [24] E. D. Kaplan, *Understanding GPS: Principles and Application*. Boston: Artech House, Inc., 1996.
- [25] R. G. Kennett and F. K. Li, "Seasat over-land scatterometer data, part i: Overview of the Ku-band backscatter coefficients," *IEEE Trans. Geosci. Remote Sensing*, vol. 27, no. 5, pp. 592–605, September 1989.
- [26] P. Lecomte, "The ERS scatterometer instrument and the on-ground processing of its data," in *Proceedings of a Joint ESA Workshop on Emerging Scatterometer Applications - From Research to Operations*, vol. ESA SP-424, Noordwijk, Netherlands, October 1998.
- [27] P. Lecomte and E. P. Attema, "Calibration and validation of the ERS-1 wind scatterometer," in *Proceedings of the First ERS-1 Symposium*, November 1992.

- [28] P. Lecomte and W. Wagner, "ERS wind scatterometer commissioning and in-flight calibration," in *Proceedings of a Joint ESA Workshop on Emerging Scatterometer Applications - From Research to Operations*, vol. ESA SP-424, Noordwijk, Netherlands, October 1998.
- [29] W. T. Liu, "Progress in scatterometer application," *Journal of Oceanography*, vol. 58, pp. 121–136, 2002.
- [30] D. G. Long, "High resolution wind retrieval from SeaWinds," in *Proc. IEEE Geosci. Remote Sensing Symposium*, Sydney, Australia, July 2001, pp. 2187–2189.
- [31] D. G. Long, "High resolution wind retrieval from SeaWinds," in *Proc. IEEE Geosci. Remote Sensing Symposium*, Toronto, Canada, July 2002, pp. 751–753.
- [32] D. G. Long and M. R. Drinkwater, "Cryosphere applications of NSCAT data," *IEEE Trans. Geosci. Remote Sensing*, vol. 37, no. 3, pp. 1671–1684, May 1999.
- [33] D. G. Long, M. R. Drinkwater, B. Holt, S. Saatchi, and C. Bertoia, "Global ice and land climate studies using scatterometer image data," *EOS, Transaction of the American Geophysical Union*, vol. 82, no. 43, p. 503, Oct 2001.
- [34] D. G. Long and J. M. Mendel, "Identifiability in wind estimation from scatterometer measurements," *IEEE Trans. Geosci. Remote Sensing*, vol. 29, no. 2, pp. 268–274, March 1991.
- [35] D. G. Long and M. W. Spencer, "Radar backscatter measurement accuracy for a spaceborne pencil-beam wind scatterometer with transmit modulation," *IEEE Trans. Geosci. Remote Sensing*, vol. 35, no. 1, pp. 102–114, January 1997.
- [36] D. G. Long, P. K. Yoho, A. Anderson, J. P. Lux, J. Adams, and F. Cheng, "QuikSCAT calibration results using the calibration ground station," in *SeaWinds Cal/Val Workshop Meeting*, Pasadena, CA, Nov. 1999.

- [37] T. K. Moon and W. C. Stirling, *Mathematical Methods and Algorithms for Signal Processing*. Upper Saddle River, NJ: Prentice Hall, 2000.
- [38] R. K. Moore and J. Young, "Active measurement from space of sea surface winds," *IEEE J. Oceanic Eng.*, vol. OE-2, pp. 309–317, 1977.
- [39] F. M. Naderi, M. H. Freilich, and D. G. Long, "Spaceborne radar measurement of wind velocity over the ocean - an overview of the NSCAT scatterometer system," *Proc. IEEE*, vol. 79, no. 6, pp. 850–866, June 1991.
- [40] S. Nghiem, W. Liu, W.-Y. Tsai, and X. Xie, "Flood mapping over the Asian continent during the 1999 summer monsoon season," in *Proc. IEEE Geosci. Remote Sensing Symposium*, Honolulu, Hawaii, July 2000, pp. 2027–2028.
- [41] P. Z. Peebles, *Radar Principles*. New York: John Wiley and Sons, Inc., 1998.
- [42] H. R. Raemer, *Radar Systems Principles*. Boca Raton, FL: CRC Press, 1997.
- [43] Q. P. Remund, D. G. Long, and M. R. Drinkwater, "An iterative approach to multi-sensor sea ice classification," *IEEE Trans. Geosci. Remote Sensing*, vol. 38, no. 4, pp. 1843–1856, July 2000.
- [44] D. Russell. (1999, October) Personal Communication.
- [45] C. C. Schmullius, "Monitoring siberian forests and agriculture with the ERS-1 wind scatterometer," *IEEE Trans. Geosci. Remote Sensing*, vol. 35, no. 5, pp. 1363–1366, Sept 1997.
- [46] M. W. Spencer. (1999) Jet Propulsion Laboratory. [Online]. Available: <http://photojournal.jpl.nasa.gov/catalog/PIA02458>
- [47] M. W. Spencer, "A methodology for the design of spaceborne pencil-beam scatterometer systems," Ph.D. dissertation, Brigham Young University, 2001.
- [48] M. W. Spencer. (2003, May) Personal Communication.

- [49] M. W. Spencer, W. Y. Tsai, and D. G. Long, "High-resolution measurements with a spaceborne pencil-beam scatterometer using combined range/doppler discrimination techniques," *IEEE Trans. Geosci. Remote Sensing*, vol. 41, no. 3, pp. 567–581, March 2003.
- [50] M. W. Spencer, C. Wu, and D. G. Long, "Tradeoffs in the design of a spaceborne scanning pencil beam scatterometer: Application to SeaWinds," *IEEE Trans. Geosci. Remote Sensing*, vol. 35, no. 1, pp. 115–126, January 1997.
- [51] M. W. Spencer, C. Wu, and D. G. Long, "Improved resolution backscatter measurements with the SeaWinds pencil-beam scatterometer," *IEEE Trans. Geosci. Remote Sensing*, vol. 38, no. 1, pp. 89–104, January 2000.
- [52] S. A. Tretter, "Estimating the frequency of a noisy sinusoid by linear regression," *IEEE Trans. Inform. Theory*, vol. IT-31, no. 6, pp. 832–835, November 1985.
- [53] W. Y. Tsai, J. E. Graf, C. Winn, J. N. Huddleston, S. Dunbar, M. H. Freilich, F. J. Wentz, D. G. Long, and W. L. Jones, "Postlaunch sensor verification and calibration of the NASA scatterometer," *IEEE Trans. Geosci. Remote Sensing*, vol. 37, no. 3, pp. 1517–1542, May 1999.
- [54] F. Ulaby, R. Moore, and A. Fung, *Microwave Remote Sensing: Active and Passive*. Norwood, Massachusetts: Artech House, Inc., 1986, vol. 1.
- [55] F. Ulaby, R. Moore, and A. Fung, *Microwave Remote Sensing: Active and Passive*. Norwood, Massachusetts: Artech House, Inc., 1986, vol. 2.
- [56] Unknown. (1999) Jet Propulsion Laboratory. [Online]. Available: <http://winds.jpl.nasa.gov/missions/quikscat/seawinds-img.html>
- [57] M. Wright, "Direct search methods: Once scorned, now respectable," in *Proceedings of the 1995 Dundee Biennial Conference in Numerical Analysis*, 1995, pp. 191–208.

- [58] P. K. Yoho, "Calibration of the SeaWinds scatterometer using the SeaWinds Calibration Ground Station," Internal Report, NASA Jet Propulsion Laboratory, Tech. Rep., September 2003.
- [59] P. K. Yoho, A. Anderson, and D. G. Long, "Model-based SeaWinds on QuikSCAT ground station calibration analysis," in *USNC/URSI National Radio Science Meeting*, Salt Lake City, UT, July 17 2000.
- [60] P. K. Yoho, A. Anderson, D. G. Long, J. P. Lux, J. Adams, and F. Cheng, "SeaWinds on QuikSCAT calibration using a calibration ground station," in *Proc. IEEE Geosci. Remote Sensing Symposium*, Honolulu, Hawaii, July 2000, pp. 1039–1042.
- [61] P. K. Yoho and D. G. Long, "Improved timing calibration of QuikSCAT," in *Proc. IEEE Geosci. Remote Sensing Symposium*, Sydney, Australia, July 2001, pp. 1591–1593.
- [62] P. K. Yoho and D. G. Long, "Model-based ground station calibration for SeaWinds on QuikSCAT," in *Proceedings of the SPIE International Symposium on Optical Science and Technology*, vol. 4483, July 2001, pp. 117–126.
- [63] P. K. Yoho and D. G. Long, "Validation of SeaWinds on QuikSCAT cell location," in *Proc. IEEE Geosci. Remote Sensing Symposium*, Sydney, Australia, July 2001, pp. 508–510.
- [64] P. K. Yoho and D. G. Long, "Calibration capabilities of the SeaWinds CGS," *To Be Submitted IEEE Trans. Geosci. Remote Sensing*, 2003.
- [65] P. K. Yoho and D. G. Long, "Correlation and covariance of satellite scatterometer measurements," *In Review IEEE Trans. Geosci. Remote Sensing*, 2003.
- [66] P. K. Yoho and D. G. Long, "An improved simulation model for spaceborne scatterometer measurements," *IEEE Trans. Geosci. Remote Sensing*, vol. 41, no. 11, pp. 2692–2695, November 2003.

- [67] Y. Zhao, A. K. Liu, and D. G. Long, "Validation of sea ice motion from QuikSCAT with those from SSM/I and buoy," *IEEE Trans. Geosci. Remote Sensing*, vol. 40, no. 6, pp. 1241–1246, June 2002.